NSTX-U FY2014 Year End Report

J. Menard, M. Ono, and the NSTX-U Research Team
September 10, 2014 – Version 11

Table of contents

Executive Summary of NSTX-U Year-End Report

- **Executive Summary for FY2014 Notable Outcomes**
  - *Objective 1.1a "Carry out scenario modeling and research planning to ensure a strong NSTX-U research program in FY 2015"*

    Time-dependent simulations of non-inductive current ramp-up and sustainment have been performed with TRANSP using the free-boundary equilibrium solver ISOLVER for the first time. These advanced simulations with TRANSP evolve plasma pressure profiles and heating and current drive sources self-consistently. This self-consistent treatment is particularly important for the neutral beam (NBI) calculations, since NBI provides the primary external heating and non-inductive source of current in these NSTX-U discharges. These simulations support the planned sequential usage of ECH, HHFW, and NBI to support non-inductive ramp-up in NSTX-U.

  - *Objective 1.1b "Analyze experimental data from FES major facilities to investigate and quantify plasma response to non-axisymmetric (3D) magnetic fields in tokamaks, in support of the FES joint research target"*

    The NSTX-U team continued active collaboration with DIII-D and C-Mod to support JRT14, contributing strong numerical capabilities for 3D plasma response physics as well as unique high-beta NSTX/ST data. Significant progress was made in the areas of modeling and validation for: (1) linear/perturbed versus non-linear plasma response, (2) ideal vs. kinetic response, and also for (3) 3D neoclassical transport of angular momentum and (4) divertor heat and particle flux modifications by 3D fields.

  - *Outcome 3.2 "Expand engagement with university scientists to enhance the NSTX-U program"*

    In order to generate ideas for increasing University engagement in the NSTX-U program, during the spring and summer of 2014, the NSTX-U Program coordinated 3 meetings with all 22 FES-funded NSTX-U collaboration grantees. Collaboration grantees were asked to participate in brainstorming to develop "Ideas to enhance participation in NSTX-U research and/or program by U.S. Universities, early-career researchers, students". Input was also solicited from the PPPL Advisory Board and NSTX-U PAC-35. The most impactful/compelling ideas developed include: Expanding Early Career Research (ECR) awards to University Scientists/Research Professors, supporting students with coordinated senior projects and targeted run-time, implementing enhanced collaboration tools (remote control rooms), implementing an "NSTX-U Innovative Research Award (NIRA)" with funding targeting primarily university researchers, consideration of direct financial support for start-up and initial salary for tenure-track professor positions – in particular for universities in close geographic proximity to NSTX-U/PPPL, and to more strongly engage University Principal Investigators and researchers in the management of the NSTX-U scientific program. At the present time there is no path to expand ECR awards, and resources are very limited to fund NIRA or tenure track positions. However, the NSTX-U Program organization will be restructured in early FY15 to ensure every topical science group has representation from at least one funded University collaborator. This restructuring will more than triple the number of University researchers explicitly engaged in the management of the NSTX-U scientific program. Increased student support, targeted run-time, and enhanced collaboration tools will be considered later in FY15 once the NSTX-U facility and research program are fully operational again.

- **Executive Summary for Facility and Diagnostics**
  - NSTX Upgrade Project Accomplishments

    - **New Center Stack Upgrade:** After completing the TF bundle in FY2013, the winding of the OH coil over the full TF bundle commenced in FY2014. After the OH winding was completed, a VPI of the entire TF-OH center-bundle was successfully completed. The TF and OH coils were electrically tested to full test voltage. The Center-Stack Casing with the welding of the 700 inconel studs for mounting the carbon tiles to the walls is complete. The inner poloidal field (PF) coils were manufactured and are being prepared for mounting onto the casing. The completed OH/TF bundle and CS casing will be transported to the NSTX-U for final assembly. Delivery of the completed CS Assembly is scheduled for the fall of 2014.

    - **Second Neutral Beam Injection System Upgrade:** The 2nd NBI beam-line (BL) refurbishment and relocation have been completed and the jobs closed. The installation of the support structure and alignment of the BL has been completed. The refurbished 90 inch flange, ion dump, calorimeter, and bending magnet were installed on the BL. The three NB Ion Sources were installed on the BL2 platform and vacuum connections completed. Power system progress includes the completion of all major cabling required to fully connect the N4ABC power systems from the TFTR area to the NTC location via the TFTR Test Cell (TTC) Basement. Fabrication of the NBI armor to be located inside the VV is complete. Assembly and installation of the NBI armor quadrants is complete. The Bay H port cover modification for the armor is also complete. Pending appropriate approvals, the Beam 2 CD-4 of 40 kV beam fired into the Armor has been scheduled for the end of December or first of January depending on availability of beam conditioning time with NTC closed.

    - **Power systems and RF:** The TFTR-era motor generator weld cracks were repaired. This motor generator repair brings the motor generator to its original specifications, and the repair will enable the full field and current operation of NSTX-U. To handle increased disruption loads in NSTX-U, compliant connectors between the feed-throughs and antenna straps were designed, tested and installed on the 12-strap high-harmonic fast-wave antenna.

  - *Facility Milestone F(14-1): Complete installation and testing of refurbished D-Site Rectifier Firing Generators*

    Precise control of thyrister firing angles by the FCPC firing generators (FGs) has always been necessary for NSTX operations, and becomes more critical for the new 8-parallel, 130kA TF system configuration. The new Firing Generator (FG) delivers firing pulses with far greater resolution, precision, and repeatability. In FY 2014, 32 dual-output firing generators (enough to drive the 64 power supply sections needed for the NSTX-U FY15 experimental run, with spares) were installed and tested in the FCPC rectifiers.

  - *Diagnostic Milestone D(14-1) Complete the Multi-Pulse Thomson Scattering (MPTS) diagnostic in-vessel hardware modifications*

    Modifications to the Multi-Pulse Thomson Scattering (MPTS) diagnostic required for the NSTX Upgrade were designed, and fabrication and installation of the needed components is progressing well. Installation and commissioning of the reconfigured MPTS diagnostic will be completed prior to the start of the first NSTX-U experimental campaign in 2015.

- **Executive Summary of Research Results – FY14 Milestones**
  - *R(14-1): Assess access to reduced density & collisionality in high-performance scenarios*

    In order to assess access to reduced density and collisionality in high-performance scenarios in NSTX-U, equilibria were computed with the free-boundary TRANSP code and the no-wall and ideal-wall n = 1 stability limits are computed with the DCON code. This analysis indicates core fast-ion diffusion can reduce fast-ion pressure peaking at low density and increase ideal-wall stability limits. RWM analysis with the MISK code finds that as collisionality is reduced in experiments with greater stabilization by kinetic resonances, there is a decrease in resonant field amplification (RFA) amplitude indicating the plasma is becoming more stable. MARS-K analysis of rotating kink/tearing modes indicates that high rotation and increased fast ion pressure fraction - both typically encountered at reduced density - can reduce the ideal-wall limit and trigger tearing modes as beta is increased toward the reduced limit. Density feedback control and control of the rotation magnitude and profile using the more tangential NBI and the proposed Non-Axisymmetric Control Coils (NCC) will be very important tools for accessing the lowest density and collisionality in NSTX-U. Stellarator optimizers coupled to 3D perturbed equilibria and rotation damping models are now being utilized to further optimize the NCC physics design.

  - *R(14-2): Develop models for *AE mode-induced fast-ion transport*

    Two complementary approaches have been developed to compute the fast ion response to a given set of instabilities, namely: through quasi-linear theory and via a reduced, "probabilistic" model for fast ion evolution in phase space. The first approach is based on the 1.5-dimensional quasi-linear theory of energetic particle profile relaxation following radial transport induced by instabilities. Inclusion of this model in TRANSP will be considered after completion of the validation work. A second approach employs a probability distribution to advance an ensemble of particles in phase space coordinates following a Monte-Carlo scheme. This model is being implemented in the NUBEAM module of TRANSP, and it will be used to quantitatively assess AE effects on fast ion confinement and NB current drive for both NSTX and (predicted) NSTX-U scenarios with different levels of AE activity.

  - *R(14-3): Develop advanced axisymmetric control in sustained high performance plasmas*

    Advancement in axisymmetric control development was made in 4 topical areas: i) model based β_N+l_i control and β_N+q_0 control using TRANSP as a "flight simulator", ii) model based full q-profile control development, iii) model based rotation profile control development, and iv) studies of the neoclassical toroidal viscosity (NTV) from the proposed NCC coils. For activities i-iii, the "expert file" mechanism within TRANSP is now used in which external blocks of FORTRAN code can be called at appropriate times during the execution of TRANSP. TRANSP is now fully functional as a tool for control development and controllers for current and rotation profile control have been rapidly developed for NSTX-U. The development of control within the TRANSP framework allows sophisticated control models to be developed with minimal physics model development on the part of the control engineer and should also be directly applicable to controller development for ITER and FNSF. For activity iv), a key advantage of the proposed NCC coil set found for NSTX-U is the ability to independently control the resonant and non-resonant components of NTV torque for rotation damping and rotation profile control.

Executive Summary for Additional Research Highlights

- Executive Summary of Research Highlights for Boundary Physics

  - NSTX-U researchers published results in Physical Review Letters in which it was shown that edge instabilities consistent with Kinetic Ballooning Modes (KBM) limit the increase of the pedestal temperature. These first of its-kind detailed measurements on this edge instability on Alcator C-Mod were made possible using a suite edge diagnostics and a magnetic probe placed near the separatrix.

  - On NSTX, fast measurements of Edge Localized Mode (ELM) events with the Beam Emission Spectroscopy (BES) diagnostics are being used to identify possible patterns in the time-series data. In particular, hierarchical clustering – best known from genomics for connecting gene expression and functional pathways – is being used to identify ELM groups with high similarity, and results will be compared to non-linear ELM evolution models.

  - The M3D-C1 MHD stability code has recently been used to compute plasma response to 3D fields from the proposed NSTX-U NCC coils with application to resonant magnetic perturbation (RMP) ELM control, and has also been used for computing fast-ion loss from plasma-amplified 3D fields form the midplane coils on NSTX. Computed neutron rate drops from reduced fast-ion confinement from NSTX 3D fields are in good agreement with measurement.

  - Improvements to the proposed NSTX-U lower outboard divertor cryo-pump geometry have been identified and can provide: reduced interference with divertor diagnostic views, increased clearance from the vacuum vessel for improved tile bake-out capability, and improved overall consistency with engineering constraints - all while maintaining adequate projected pumping capabilities.

  - A new technique for inferring neutral density profiles from the tangentially viewing Edge Neutral Density Diagnostic (ENDD) has been developed and applied to discharges from the 2010 run campaign. This new method is a hybrid approach in which a DEGAS-2 neutral transport simulation is used to augment the experimental procedure, extending the spatial range over which useful densities can be obtained.

  - UEDGE modeling of snowflake divertor configurations for NSTX-U find highly radiating, partially detached divertor conditions are accessible at relatively low core/separatrix densities, and also provide a “gradual” detachment as density is increased. This favorable result is attributed to improved neutral confinement as flux surfaces are tilted with respect to the target as the strike-point radius is increased. UEDGE modelling for ST-FNSF shows that long-legged super-X-like snowflake divertors can achieve outer strike-point detachment.

- Executive Summary of Research Highlights for Materials and PFC R&D

  - Li evaporation and the strong enhancement of the Li sputter yield at elevated temperatures observed on low-flux experiments indicate that the maximum Li temperature permitted on future fusion devices may be unacceptably low. However, thin Li films on TZM molybdenum substrates were recently studied in the high-power-density Magnum-PSI linear plasma device and compared to SDTrimSP simulations of sputtering and evaporation. Measured Li erosion rates were lower by a factor > 1000 from the predictions and modifications to the Li erosion model are being developed to interpret this strongly suppressed Li yield. For example, momentum-loss-induced increases of the potential drop in the pre-sheath may help trap Li near the material surface. These results imply that temperature limits for lithium-coated PFCS in a fusion reactor environment may be significantly higher than previously envisioned.

  - Deuterium retention in ultrathin lithium films (three monolayers thick) on molybdenum substrates was studied in ultrahigh vacuum environments to elucidate the chemistry at the Mo-Li interface. Experiments conducted on ultrathin oxidized lithium films indicated that the amount of D retained in the lithium oxide film was 2.5 times higher than the amount of D retained as LiD in the metallic Li film. However, lithium oxide retains D as LiOD, which is less thermally stable than LiD. These results highlight the importance of maintaining a metallic Li layer and shows that oxygen can be detrimental to D retention in Li films on TZM at elevated temperatures.

  - The Materials Analysis and Particle Probe (MAPP) is a unique diagnostic that allows in-situ analysis of samples exposed to tokamak plasmas. Testing of MAPP prior to installation on NSTX-U continued on the Lithium Tokamak eXperiment (LTX) during the past year. Samples of plasma-facing component (PFC) materials that included stainless steel and a molybdenum alloy (TZM) were coated by evaporation of lithium from a reservoir inside LTX. A series of X-ray photoelectron spectroscopy (XPS) measurements were taken over a span of several days, and changes in the fractions of lithium compounds on the samples were monitored and provided information on the “passivation” of lithium coatings on PFCs, which is an important indicator of plasma performance. Activities related to the installation of MAPP on NSTX-U included a successful “fit-up” of the analysis chamber and bellows drive on a lower dome port, progress on remote control of the surface analysis diagnostic, and implementation of safety interlock systems for the X-ray source and microchannel plate detectors.

- Executive Summary of Research Highlights for Macroscopic Stability

  - Validated and benchmarked calculations of kinetic resistive wall mode (RWM) stability are important for disruption avoidance in ITER and other high performance tokamaks by providing a confidently predicted RWM stable operating region. Kinetic RWM calculations were benchmarked between three leading codes: MARS-K, MISK, and PENT. Good agreement was found between the code calculations for two Solov'ev analytical equilibria and a projected ITER equilibrium, including the most important stabilizing kinetic effect: resonances between the plasma rotation and frequencies of thermal particle's motion. Systematic comparison and numerical benchmarking has also been successfully carried out among three different approaches in neoclassical toroidal viscosity (NTV) theory using IPEC-PENT, MARS-Q, and MARS-K.

  - A dedicated experiment was recently run on DIII-D to test kinetic RWM stabilization physics proposed in several NSTX publications with the goal of unifying the physics understanding of kinetic RWM marginal stability conditions between devices. The experiment was successful and analysis of the data is ongoing, but substantial progress has already been made in comparing experimental observations and kinetic RWM stability analysis between the devices. In particular, kinetic RWM stabilization theory is broad enough to explain the observed RWM destabilization in both devices, and an important complementarity has been found in the analysis to date that are part of the underlying theory: stabilization can be dominated by bounce orbit resonance in DIII-D for higher rotation plasmas, but is dominated by ion precession drift resonance in NSTX.

  - The impact of toroidal rotation and drift-kinetic effects on the tokamak ideal wall mode stability limit was considered theoretically and compared to experiment for the first time. It was shown that high toroidal rotation can be an important destabilizing mechanism primarily through the angular velocity shear, and that drift-kinetic damping can potentially stabilize rotation-driven instabilities. These results were obtained using the unique parameter regime accessible in NSTX of high toroidal rotation speed relative to the thermal and Alfven speeds and high kinetic pressure relative to the magnetic pressure. The inclusion of rotation and kinetic effects was found to significantly improve agreement between measured and predicted stability characteristics.

  - NSTX-U MHD researchers have developed a rotation feedback controller that will use the six neutral beam sources and, for the first time, non-resonant Neoclassical Toroidal Viscosity (NTV) induced torque as actuators. The controller uses the momentum force balance equation to evolve for the plasma rotation frequency, and the model for the NTV torque was developed from a substantial database of NSTX experimental results and related theoretical analyses. Rotation variation experiments on KSTAR have shown that regardless of whether rotation is increasing or decreasing – as will naturally occur repeatedly in a plasma rotation controller with an NTV actuator – the steady-state rotation profile is the same at each level of the applied 3D field current. This substantially increases confidence that the planned non-resonant NTV actuation will allow successful plasma rotation control in NSTX-U with closed-loop feedback.

  - Stellarator optimizers coupled to 3D perturbed equilibria and NTV rotation damping models (using IPEC-PENT) are now being utilized to optimize NCC design. The IPECOPT code utilizes experimentally validated models: the IPEC code computes the perturbed equilibrium

model, the PENT code then calculates the NTV torque based on this perturbed equilibrium, and the IPECOPT code reuses the optimization machinery of STELLOPT, including a choice of the Levenberg-Marquardt, Genetic Algorithms, Differential Evolution, or Particle Swarm techniques. IPECOPT has already proven very useful in identifying 3D field patterns capable of localizing NTV torque to either the core or edge regions of the plasma.

- Substantial progress was made in developing new disruption mitigation systems. NSTX-U researchers successfully built and tested an electromagnetic MGI (EM-MGI) valve for installation on NSTX-U, and also developed the concept of an Electromagnetic Particle Injector (EPI) for very rapid mass delivery. For the EM-MGI valve, very fast valve opening times have been achieved, and pressure rise-times in dedicated laboratory tests using nitrogen fill gas are consistent with the expected thermal velocity transit time. For the EPI concept, preliminary calculations indicate such a system could accelerate multi-gram payloads to velocities on the order of 1-2 km/s in less than 2 ms in a linear rail gun accelerator. The EPI system is fully electromagnetic, with no mechanical moving parts, which ensures high reliability after a period of long standby, as needed for satisfying the demanding needs of a prompt-acting reactor disruption mitigation system as may be required for ITER.

➢ Executive Summary of Research Highlights for Transport and Turbulence

- Because of the strong toroidal rotation, large larmor radius, and strong toroidicity and shaping in ST plasmas, it is crucial, while highly challenging, to use global gyrokinetic simulations to address turbulence and transport physics. Nonlinear global gyrokinetic simulations of an NSTX L-mode plasma using the GTS code have shown, for the first time, that a drift wave Kelvin-Helmholtz mode can be destabilized by strong toroidal rotation shear. This shear flow mode is characterized by finite parallel wave-number and broader poloidal wavenumber spectrum than the ITG mode, which is also found to be present in the L-mode. The ITG and KH modes can co-exist and can produce a significant ion thermal transport relevant to the experimental level in the outer core region.

- In H-mode plasma regimes with higher beta and collisionality, linear and non-linear simulations find micro-tearing modes to be the dominant driver for anomalous electron thermal transport. In such regimes where a single micro-instability is dominant, reduced models for transport can be tested in time-dependent integrated models such as TRANSP. Under such conditions, the Rebut-Lallia-Watkins (RLW) electron thermal diffusivity model, which is based on microtearing-induced transport, was used to predict the time-evolving electron temperature across most of the profile. The results indicate that RLW does a good job of predicting Te for times and locations where microtearing was determined to be important, but not as well when microtearing was predicted to be stable or subdominant.

- NSTX-U researchers contributed to analysis and gyrokinetic simulations of the DIII-D National Fusion Science Campaign experiment “Controlling H-mode particle transport with ECH”. Gyrokinetic simulations show density gradient driven trapped electron modes (TEM) are the only unstable drift modes in the inner half-radius, and particle transport driven by TEM increases strongly with electron temperature when local ECH is applied, reducing the core electron density gradient. Despite a reduction in density gradient, the growth rates increase due to doubling of Te/Ti, which reduces the threshold density gradient of the TEM. This research supports future studies of density profile control in NSTX-U using RF heating.

- Executive Summary of Research Highlights for Energetic Particles

  - At frequencies up to the Toroidal Alfvén Eigenmode (TAE) range, stability boundaries for AEs, Energetic Particle modes (EPMs), and other kink-like instabilities have been empirically characterized in terms of fast ion to Alfvén velocity ratio and fast-ion to total plasma pressure (or beta) ratio. Overall, it is found that TAE avalanches are present for fast-ion beta fractions > 0.3 and quiescent plasmas only for fractions < 0.3. A more quantitative assessment of TAE stability, including saturation level, is under way by studying the multi-mode scenarios commonly observed on NSTX through the M3D-K code. Preliminary results show strong modification of the mode dynamics, including frequency chirping and amplitude modulation, when multiple modes are included self-consistently in the simulations.

  - For a series of NSTX discharges at low current, high-harmonic fast-wave (HHFW) heating is found to simultaneously suppress fishbone instabilities and toroidal and global Alfven Eigenmodes (TAE/GAE). The delay in suppression after start of HHFW heating suggests that it either takes time to modify the fast-ion distribution responsible for exciting TAEs/GAEs, or there are variations in the equilibrium plasma parameters, during this interval, which affect the AE stability. These instability suppression mechanisms are under active investigation.

  - In support of the development of reduced models for fast ion transport, two complementary approaches have been developed to compute fast ion response to a given set of instabilities. The first approach is based on the 1.5-dimensional quasi-linear theory of energetic particle profile relaxation following radial transport induced by instabilities. A second approach employs a probability distribution to advance an ensemble of particles in phase space coordinates following a Monte-Carlo scheme. This model is being implemented in the NUBEAM module of TRANSP, and it will be used to quantitatively assess AE effects on fast ion confinement and NB current drive for both NSTX and (predicted) NSTX-U scenarios with different levels of AE activity.

  - A new 3D "halo" model in was implemented in TRANSP enabling more accurate interpretation and simulations of charge-exchange-based diagnostics. The effects of so-called halo neutrals are important, since halo density can be of the same order of the NB neutral density. The new model has been compared with the FIDASim code and a broader assessment of the two methods is ongoing to quantify the effects of different cross-section libraries available in TRANSP on NB deposition and simulation of charge-exchange reactions.

- Executive Summary of Research Highlights for Wave Heating and Current Drive

  - The fraction of the high-harmonic fast-wave power lost to the scrape-off layer has been evaluated in 3D AORSA calculations for the first time (using 81 toroidal modes to reconstruct the full antenna spectrum). The computed losses are comparable to those of the dominant mode (2D, one single toroidal mode), and the transition in SOL power losses as a function of the density in front of the antenna is reproduced, although it is less pronounced due to the contribution of the several toroidal modes. Full 3D simulations find that the absorbed power in the SOL is largest near the last-closed-flux surface and near the front of the antenna, as experimentally observed. Full wave simulations have been also used to predict that plasmas in NSTX-U will have a wider density range for which SOL losses are low.

- Executive Summary of Research Highlights for Solenoid-Free Plasma Start-up

  - Free-boundary TRANSP has been used to model non-inductive plasma start-up evolution self-consistently for the first time. Simulations indicate that 1MW of electron-cyclotron (EC) heating, at 28GHz in O-mode, can rapidly heat typical plasmas generated by coaxial helicity injection (CHI). The plasma rapidly becomes over-dense to EC penetration so that only the first 100-150ms of discharge after the startup – depending on plasma conditions - offer adequate conditions for optimal heating with EC. Simulations also indicate that high-harmonic fast-wave (HHFW) can only be coupled to the CHI target plasma with additional EC heating. The combination of EC and HHFW is predicted to heat the plasma up to 3-4keV, and it delays the current decrease of the CHI. HHFW also triggers the L-H transition contributing to an increase in the bootstrap current. The use of RF is required to prepare the plasma for Neutral Beam Injection (NBI) heating and current drive with minimal losses. Simulations indicate that in this low-density plasma, the contribution of HHFW and bootstrap current sustains about 350kA of non-inductive current. In these conditions, the neutral beams are well confined and penetrate into the H-mode plasma with minimal losses. With 10MW of NBI distributed on the two beam-lines, the current is ramped-up to 900kA in approximately 2.5s.

  - Resistive MHD simulations using the NIMROD code have been used to model CHI start-up in NSTX to improve understanding of the physics of injection, flux-surface closure, and current drive for CHI plasmas, and to extend these results to NSTX-U. An important result is the observation that closed flux surfaces during transient CHI can be explained through 2-D Sweet-Parker type reconnection, and 3-D non-axisymmetric modes do not appear to play a dominant role. There are similarities between the transient Sweet-Parker reconnection found for CHI and that reported in forced-reconnection laboratory plasmas. The simulations reproduce several experimental trends including the finding that closed flux fraction increases with the rate of injector voltage and current turn-off, and that narrower injector flux footprint widths increase the magnitude of the closed flux fraction.

- Executive Summary of Research Highlights for Advanced Scenarios and Control

  - Advances in axisymmetric control were made using TRANSP as a “flight simulator” to develop simultaneous beta and current profile control algorithms for NSTX-U, and also to develop rotation profile control algorithms. TRANSP is now fully functional as a tool for control development, and this framework allows sophisticated control models to be developed with minimal physics model development on the part of the control engineer.

  - NSTX-associated researchers continued to collaborate on control topics on the DIII-D tokamak including real-time control of the novel snowflake divertor configurations demonstrating sustained high performance in advanced tokamak plasmas with large flux expansion. In a second experiment, real-time control of the detachment front was demonstrated with application to mitigate high divertor heat fluxes in ITER and FNSF.

  - Non-linear vertical displacement event simulations and also halo-current modeling for NSTX-U have been initiated via new collaboration activities with General Atomics.

Summary of FY2014 Notable Outcomes:

Objective 1.1a *"Carry out scenario modeling and research planning to ensure a strong NSTX-U research program in FY 2015"*

Time-dependent simulations of non-inductive current ramp-up and sustainment have been performed with TRANSP, using the free-boundary equilibrium solver ISOLVER. Compared to previous work, where the free boundary TSC (Tokamak Simulator Code) was used, using TRANSP represents a significant improvement in the predictive capabilities. Previous simulations were using analytic heating and current drive profiles, together with assumptions on the thermal transport in all phases of the discharge. The most recent simulations with TRANSP do evolve plasma pressure profiles and heating and current drive sources self-consistently. This is important for the neutral beam (NBI) calculations, since NBI provides the main and most significant source of current in these NSTX-U discharges. The beam pressure significantly affects the plasma shape evolution and the MHD stability. The deposition profiles need therefore to be calculated self consistently. This is done in TRANSP with the Monte Carlo code NUBEAM.

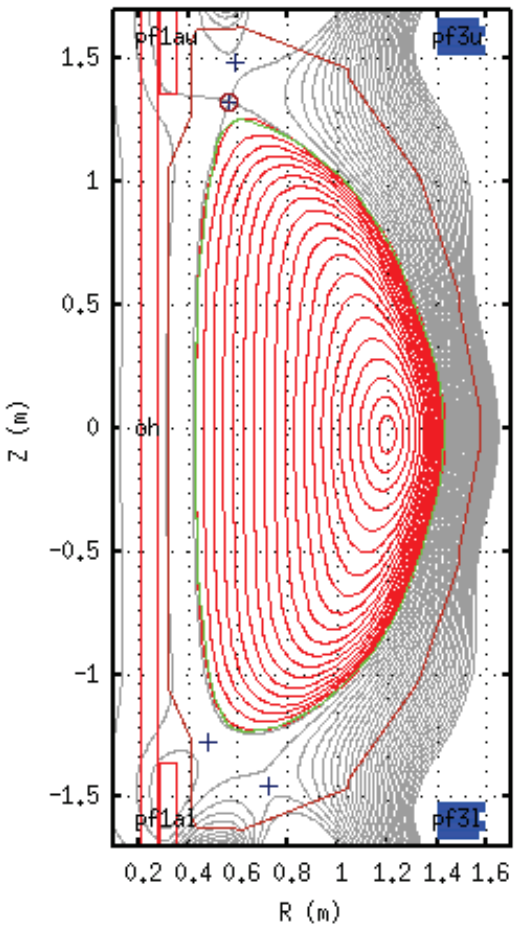

Figure NO1.1A-1. *NSTX-U equilibrium, calculated with Isolver, at t = 3.5s, with plasma current 0.9MA, plasma elongation of κ~ 2.50 and triangularity of δ~0.75.*

Self-consistent evolution of the plasma equilibrium and profiles, with correct accounting of the heating and current drive sources is particularly and mostly important in the early ramp-up phase. During this phase, in fact, the evolution of the plasma parameters is strongly sensitive to the assumptions and self-consistency is necessary to accurately predict the evolution of the current profile and minimize artifacts like the formation of a current hole, which was found in previous simulations that were using analytic heating and current drive profiles.

Large aspect ratio discharges from NSTX (A~1.7) have been used as a reference to extrapolate to NSTX-U. Figure NO1.1A-1 shows the equilibrium in the flattop, for a simulation of fully non-inductive ramp-up and sustainment of 0.9MA with 10MW of NBI, whose waveforms are shown

in Figure 2. Simulations use analytic density profiles with shape that reproduces typical L-mode and H-mode profiles in NSTX. The density amplitude is rescaled to satisfy constant Greenwald fraction between 0.5 and 1.0. During the RF phase the ion and electron temperature evolution is predicted using the Multi-Mode transport model (MMM), which is found to reproduce amplitude and peaking of the electron temperature profile within 10% in NSTX RF heated discharges. During the NBI phase the ion temperature is assumed to follow Neoclassical transport, while the electron temperature profiles are prescribed in shape and amplitude. It is found in fact that no transport model can reproduce both amplitude and peakedness of NSTX beam discharges within 20%.

The ramp-up evolution consists of two phases: RF heating and current drive during the first 500ms and Neutral Beam injection after that. The use of RF is needed to prepare the plasma to the Neutral Beam Injection with minimal losses. Simulations indicate that 1MW of EC heating, at 28GHz in O-mode, can heat rapidly typical plasmas generated by coaxial helicity induction (CHI). The electron temperature increases from the 10-20eV typical of CHI plasmas to about 1keV in less than 30ms (see Section X). The Electron Cyclotron waves propagation is computed with the ray-tracing code TORAY-GA, which is implemented in TRANSP. The plasma rapidly becomes overdense to EC penetration so that only the first 100-150ms of discharge after the startup offer adequate conditions for optimal heating with EC. Regardless, the use of EC is deemed necessary for HHFW coupling in a CHI-initiated plasma. Figure NO1.1A-2 shows a simulation where HHFW is injected at about 40ms and stepped up to 4MW during the EC heating time window. Simulations also indicate that HHFW cannot be coupled to the CHI target plasma without EC heating.

The combination of EC and HHFW heats the plasma up to 3-4keV and it delays the current decrease of the CHI, sustaining a non-inductive current of about 350kA. HHFW also triggers the L-H transition contributing to an increase in the bootstrap current. Under these conditions, the neutral beams are well confined and penetrate into the H-mode plasma with minimal losses. With 10MW of NBI distributed on the two beamlines and operating at 90% of the Greenwald density, the current is ramped-up to 900kA in about 2.5s, with about 50% of the current provided by the bootstrap mechanism.

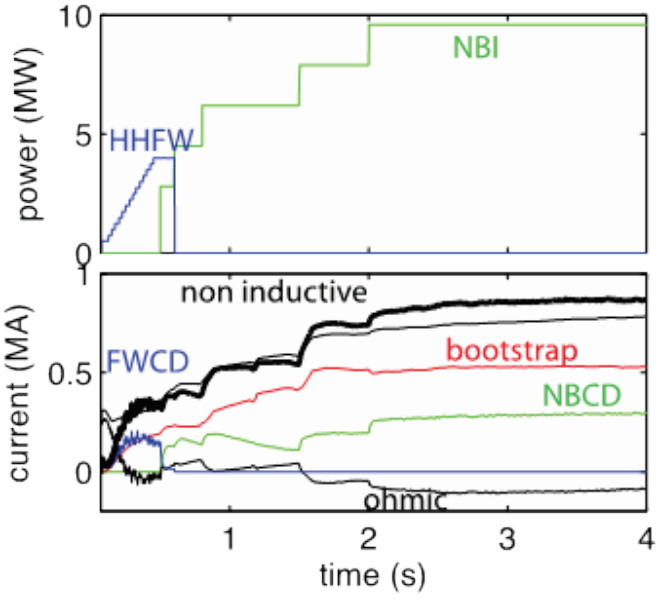

***Figure NO1.1A-2**. Injected power (top) and currents (bottom).*

Objective 1.1b *"Analyze experimental data from FES major facilities to investigate and quantify plasma response to non-axisymmetric (3D) magnetic fields in tokamaks, in support of the FES joint research target"*

FY2014 Joint Research Target: Validate plasma response to non-axisymmetric magnetic fields in tokamaks

Milestone Description: *Conduct experiments and analysis to investigate and quantify plasma response to non-axisymmetric (3D) magnetic fields in tokamaks. Effects of 3D fields can be both beneficial and detrimental and research will aim to validate theoretical models in order to predict plasma performance with varying levels and types of externally imposed 3D fields. Dependence of response to multiple plasma parameters will be explored in order to gain confidence in predictive capability of the models.*

NSTX-U team continued the active collaboration with DIII-D and CMOD to support JRT14, with the strong numerical capabilities on 3D plasma response physics as well as with the access to unique ST regime and NSTX data. Significant progress has been made particularly from research in the areas of modeling and validation across (1) linear vs. non-linear response, (2) ideal vs. kinetic response, and also for effects on (3) neoclassical transport and (4) divertor heat flux by 3D fields. The progress for each topic is summarized as follows.

Modeling and validation of linear vs. non-linear plasma response

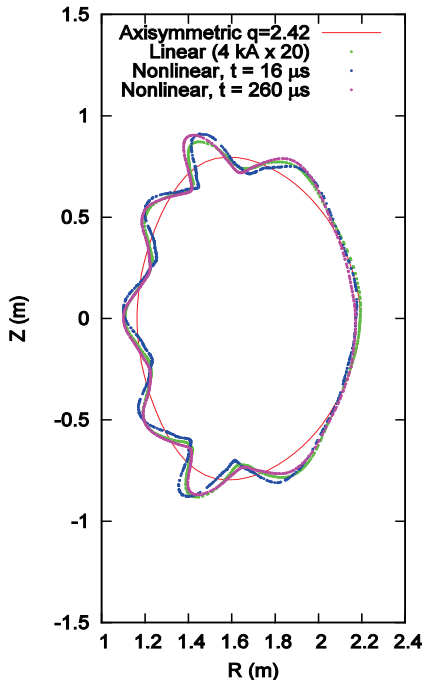

Figure JRT14-1. *Linear and non-linear M3D-C1 modeling for plasma displacement.*

An ongoing theoretical initiative to benchmark 3D equilibrium codes is closely related to this Joint Research Target., eleven codes including several stellarator codes are being benchmarked to each other, with a focus on the n=3 fields used for ELM suppression in DIII-D. Particularly the difference among linear and non-linear codes is of interest, as the linear assumption can break down easily in the edge for n>1. However, M3D-C1 calculations find that linear and nonlinear solutions for the displacement of the q = 2.42 surface are in good agreement, despite the fact that there is a substantial region near the plasma edge where the linear solution predicts overlap of flux surfaces. This suggests that the breakdown of the linear approximation does not contribute significantly to the disagreement between the VMEC and perturbative 3D equilibrium calculations such as IPEC and MARS-K. The most likely cause of the disagreement is the absence of localized screening currents at low order rational surfaces in the VMEC solutions. This is supported by recent M3D-C1 calculations of 3D equilibria for rotating and nonrotating plasmas. The rotation leads to the persistence of localized currents at rational surfaces. There is a corresponding effect on the calculated displacement on the inboard side, with the amplitude of

the displacement significantly larger in the rotating plasma. Calculations with the NSTAB code provide further support for this picture. NSTAB is believed to have improved handling of localized currents relative to VMEC. The NSTAB calculations find a displacement amplitude on the inboard side significantly larger than that of VMEC, despite the fact that the NSTAB calculation is a fixed boundary calculation, imposing the VMEC boundary on the NSTAB calculation.

Modeling and validation of ideal vs. kinetic plasma response

3D fields can modify the kinetic motion of particles along the field lines and thus change plasma response. The kinetic effects are expected to be more important in higher beta plasmas near or beyond the stability boundary, and thus for the n=1 or the low n plasma response that has less stable in general. The correlation between the stability and plasma response, and the importance of the kinetic effects, has been successfully shown by MISK code applications to resonant field amplification (RFA) experiments, where the RFA amplitude as a function of β/li was shown to be inversely proportional to the kinetic potential energy [JRT14-1]. In order to make quantitative calculations, MARS-K code has been successfully modified for this purpose and applied to DIII-D and NSTX. The importance of the self-consistent calculations was highlighted by comparison between SXR measurement in DIII-D [JRT14-2] and MARS-K prediction for internal displacements, which agree to each other and both showed the substantial change of the internal structure. This successful validation potentially provides the full, quantitative resolution of RFA phenomena for the first time. In details, it was shown that the most important kinetic effects arise from thermal particles, rather than energetic particles or fluid rotation in DIII-D.

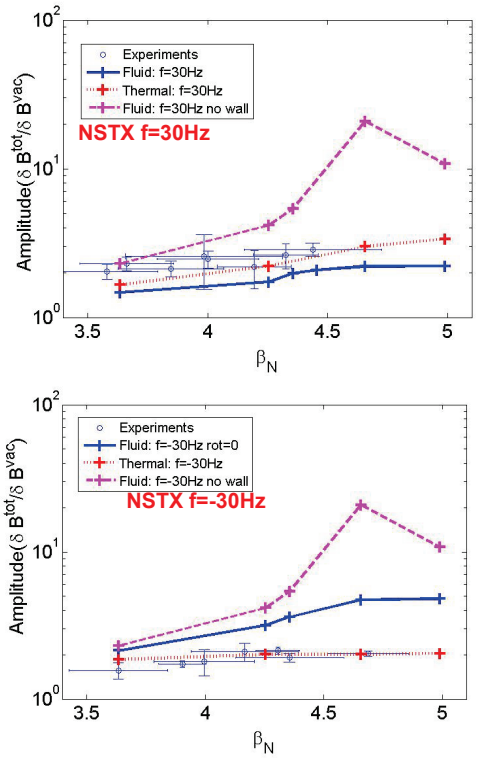

Figure JRT14-2*. The amplitude of plasma response to co-rotating field (Top) and counter-rotating field (Bottom) measured at the magnetic sensor is plotted as the function of β_N for fluid and kinetic plasma response.*

However, MARS-K applications, to a rotating RFA experiment in NSTX performed in 2009 [JRT14-3] show that the kinetic effects can interplay in more complicated fashion. First the plasma response can be strongly coupled to the resistive wall, as the period of 30Hz applied external fields is close to the NSTX wall time ~ 5ms, and thus even the fluid plasma response is largely suppressed with wall comparing with the no-wall case. However, the fluid cases show a large phase shift when $\beta_N \gtrsim \beta_N^{NW}$, differently from the small phase shift observed in NSTX experiments. Only the full kinetic plasma response gives an agreement of the phase shift as well as the amplitude to measurements as shown in Figure JRT14-2. Also, since the fluid rotation in

NSTX plasma is much stronger than DIII-D plasma, it is important to consider this effect in the kinetic plasma response calculation. The study indicates that the fluid rotation could cause the destabilizing effect of the plasma, as is consistent with the results in a NSTX Ideal Wall Mode study [JRT14-4]. In both experiments, the perturbed energy analysis shows the modification of plasma response is mainly contributed by the precession, bounce, and transit resonances of thermal ions.

Effects on neoclassical transport by 3D fields

The study of 3D momentum (NTV) transport has been very active along with continuous upgrade and cross-code benchmark. Mainly three types of NTV codes are being tested and applied; (1) Regime-combined codes with simplified collisional operator, such as PENT, MISK, MARS-K, (2) Regime-connected codes with pitch-angle collisional operator such as MARS-Q and NTVTOK, (3) First-principle particle codes such as POCA and XGC0. Briefly, PENT, MISK, and MARS-K results were shown equivalent [JRT14-5, JRT14-6], and MARS-Q and POCA showed consistent trends but can differ by several factors in low collisionality and high rotation. This cross-code benchmarking will be extended to NTVTOK, which is a geometrically generalized version of MARS-Q, and also to XGC0, which is being utilized for 3D neoclassical transport. Note the transport modeling needs 3D plasma response, and thus is separable while the self-consistent calculation between the two can be achieved. MARS-K is presently unique for this aspect as described in the previous paragraph, but the validity of perturbative vs. self-consistent modeling should be thoroughly investigated further.

For the 3D plasma response experiments newly preformed in DIII-D, particularly PENT code with IPEC field has been used to predict and analyze NTV. In the n=2 error field correction to minimize rotation degradation, IPEC-PENT predicted a simple sinusoidal variation of NTV as a function of I-coil connecting phase as shown in Figure JRT14-3, in spite of complications in I-coil fields and non-linear NTV physics. While the amplitudes differ by a factor of 3, the sinusoidal trend was confirmed by experiments. Interestingly, this prediction based on NTV is shown to correlate with the coupling to the dominant mode, implying the Kink-coupling plays an important role in both plasma response and NTV. However, the similarity between the dominant modes for response and NTV is perhaps manifested due to the limitation in the coils. In the non-axisymmetric control coil (NCC) design for NSTX-U, stellarator optimizers have been successfully combined with IPEC-PENT and utilized to investigate such an NTV-dominant mode in the core without the coil constraints. In the n=3 application, the optimizer surprisingly found the pitch-crossing field lines, which are nearly orthogonal to the response-dominant mode. This differentiation depending on the constraint in the coils or core-to-edge NTV should be further discussed and studied, within and even beyond the scope of this JRT in the future.

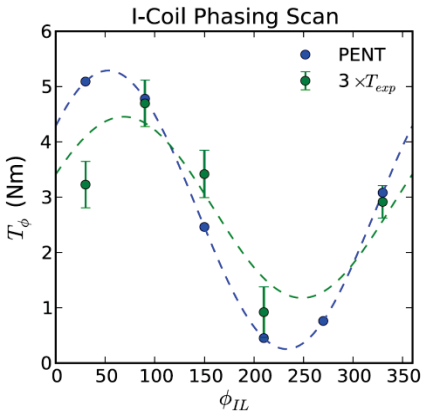

Figure JRT14-3. *NTV torque variation as a function of I-coil phasing by PENT modeling and experiments.*

Effects on divertor heat flux by 3D fields

The applied 3D fields can also alter the divertor flux and transport, which therefore can be used to validate the plasma response modeling against the experiments. This is being addressed through energy and particle transport modeling to test the consistency of various magnetic response models with both pedestal and divertor measurements. NSTX demonstrated that detached divertor plasma can be re-attached by applied 3D fields. The cause of this re-attachment is believed to be hot and dense plasma particles from the pedestal region though magnetic lobes from the split separatrix. This hypothesis is currently being studied through plasma-neutrals modeling using the EMC3-EIRENE transport code, based on various 3D equilibrium codes to account for the changed magnetic topology caused by the 3D fields. EMC3-EIRENE simulations have been performed using the vacuum approximation. Figure JRT14-4 shows heat flux profiles without (a) and with (b) 3D fields applied for several upstream densities. In the axisymmetric case the peak head flux is reduced with increasing upstream density, reaching a low level characteristic of detached conditions. At an intermediate density, the heat flux is increased at larger radii, consistent with a transition to a conduction limited regime in the flux tubes near the strike point allowing perpendicular diffusion to have a larger effect, transporting energy and particles to the outer flux tubes. When 3D fields are applied the heat flux is only reduced near the strike point, while in the outer peaks the heat flux is not reduced, or is even increased. The outer peaks are connected to hotter regions of the plasma inside of the unperturbed separatrix, and do not transition to the condution limited or detached regimes over this density range. The flux tubes connected to the primary peak do reach the conduction-limited regime, which again allows for perpendicular diffusion to transport particles to larger radii and causes a smoothing of the secondary peaks.

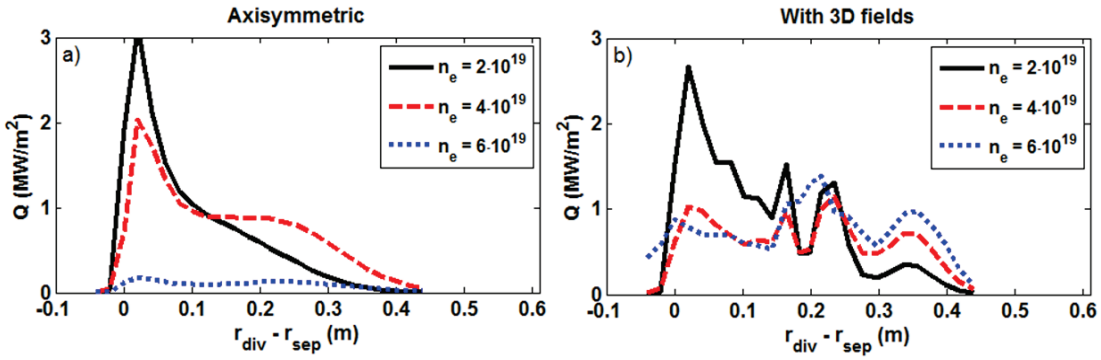

Figure JRT14-4. *Heat flx profiles calculated by EMC3-EIRENE for several upstream densities without (a) and with (b) 3D field applied.*

Progress has also been made with regard to the role of plasma response in the formation of strike point splitting when external 3D fields are applied. In the case of L-mode, it can be explained with the conventional picture of screening effect by response fields and the subsequent field penetration. When the response fields, measured by magnetic probes, are screening the applied fields, splitting is barely observed. After the loss of screening (signified by the local zeroing of rotation profile) occurs, splitting becomes strong and the phase deviation of response fields is also observed. This observation is simultaneously supported by the rise of edge rotation, which is

regarded as a typical signature of field stochastization in the edge region. However this story does not appear to apply to H-mode and the messages are complicated. First, for the low density H-mode, the core rotation profile is not significantly affected but the edge rotation increase is quite consistently observed when the splitting is formed. However, for the high density H-mode, a global NTV type rotation braking is observed with the appearance of splitting and the edge rotation also decreases. Detailed study on the physical processes responsible for the splitting phenomena in relation to the plasma response is in progress, but there are a few candidate parameters under investigation; collisionality (ν_e*), plasma shape (δ), and β_N. So far, survey of data seems to indicate higher values of each of these parameters are favorable to produce clear splitting, but more work is needed to confirm the role of the parameters in the plasma response to the applied 3D fields.

References

[JRT14-1] J.W. Berkery et al, Phys. Plasmas **21**, 056112 (2014)
[JRT14-2] M.L. Lanctot et al., Phys. Plasmas **17**, 030701 (2010)
[JRT14-3] J.-K. Park et al, Phys, Plasmas **16**, 082512(2009)
[JRT14-4] J.E. Menard et al., "Rotation and Kinetic Modifications of the High-beta Tokamak Ideal Wall Limit", submitted to Phys. Rev. Lett. (2014)
[JRT14-5] J.W. Berkery et al., Phys. Plasmas **21**, 052505 (2014)
[JRT14-6] Z. Wang et al., Phys. Plasmas **21,** 042502 (2014)

Outcome 3.2 *"Expand engagement with university scientists to enhance the NSTX-U program"*

With the resumption of research operations on the Upgraded NSTX in the spring of 2015, it is anticipated there will be increased interest in collaboration on NSTX-U – in particular from U.S. university researchers. Such increased interest has already been demonstrated with the recent FES NSTX-U solicitation for collaboration by Universities and Industry. In particular, there were 38 individual Records of Discussion completed for submission with formal proposals – as compared to 26 during the previous corresponding solicitation, i.e. a roughly ~50% increase in collaboration interest. Since funding for NSTX-U collaboration has not increased proportionate to the increased level of interest, alternative mechanisms are being sought to increase participation by University researchers – including students. In order to generate ideas for increasing University engagement through means other than increased funding, during the spring and summer of 2014, the NSTX-U Program coordinated 3 meetings with 22 FES-funded NSTX-U collaboration grantees. Collaboration grantees were asked for brainstorming on "Ideas to enhance participation in NSTX-U research and/or program by U.S. Universities, early-career researchers, students". The feedback received can be organized into two main categories of ideas – ideas for: (1) FES, and (2) NSTX-U / PPPL.

Ideas for FES:

1. Stabilize funding to prevent loss of personnel and to enable engaging graduate students in research. Fluctuations in funding can be quite harmful – especially for smaller groups with little funding margin.
2. FES-related DOE solicitations should explicitly encourage student research. It was noted that the 2013 NSTX-U Collaboration Solicitation does not explicitly encourage student research. In contrast, NSF-DOE Basic Plasma Science solicitations do explicitly encourage support for education – this is an important criterion in proposal review. It was recommended that additional funding for students be provided.
3. Expand Early Career Research (ECR) awards to University Scientists and/or Research Professors. Early Career Awards have proven very effective for initiating long term collaboration with major facilities, and current DoE solicitations for early career researchers only cover tenure track faculty (up to $150k/yr). Many university researchers are encouraged to be PIs on collaboration proposals, but cannot apply for these awards. Extending ECR to research faculty positions could: (a) foster new strong collaborations with universities, (b) perhaps lead to formation of new tenure-track positions. It should be noted that FES has previously inquired about such expansion within the Office of Science, but there is/was reluctance to expand ECR awards to non-tenure-track positions.

Ideas for NSTX-U/PPPL:

1. Identify graduate and undergraduate 'independent research' projects to be done for academic credit, and coordinate / identify topics across major research facilities, and solicit interested students from range of Universities. In terms of scope, these would be like a senior thesis or have a similar time-commitment, i.e. a 6 – 12 month project. Thus, these projects would be more in-depth / extensive than a SULI/NUF summer project which is typically 8-10 weeks.

2. Host student visits to national facilities during operations to help advertise the NSTX-U research environment and also provide a context for students with their peers.
3. Set aside run-time explicitly for exploratory ideas – in particular targeting students, early career researchers, and groups outside main-line fusion.
4. Have a "fellow/scholar" program for mid-career research collaborators to aid in promotions at home institution. To facilitate this, provide small seed funding for travel can help support students in projects affiliated with NSTX-U from their home institutions.
5. Actively encourage proposals from University Researchers to DoE, NSF, etc. that **directly benefit NSTX-U** – such encouragement could also target other activities at PPPL
6. Direct PPPL funding of small, targeted 1-year NSTX-U subcontracts with University Researchers. This benefits researchers by raising their stature, both within and outside of the University, while also providing exposure to increased opportunities. Such contracts could act as a stepping stone to full DoE Grants.
7. Develop/utilize remote experimental collaboration IT/software capabilities to enhance participation of off-site researchers.
8. Allocate space for a "diagnostic test laboratory" (NOTE: this will be included as part of PPPL "campus plan")

Using this input we identified leading candidate ideas to enhance NSTX-U attractiveness:

1. Implement all 3 ideas for FES - stabilize funding (in progress), encourage student participation in collaboration solicitations, non-tenure-track ECR (difficult)
2. Support several NSTX-U/PPPL ideas:
    a. Students: senior projects, visits/travel, targeted run-time
    b. Universities: joint proposals, short-term direct grants, enhanced collaboration tools (remote control room)
3. The most compelling idea from the NSTX-U Programmatic standpoint would be the implementation of an award primarily for universities researchers. In particular – implement a "NSTX-U Innovative Research Award (NIRA)". Such an award would:
    a. Target innovative / breakthrough R&D, emphasizing high-impact science and/or address critical NSTX-U / ITER / FNSF needs.
    b. Encourage early-career and student participation and leadership
    c. Be funded from (supplemented) NSTX-U science budget at a level of $0.5-1M / year
    d. Have a typical award level of up to ~100-200k / year for up to 3 years, with awards granted up to twice per year with annual progress reviews and funding renewals.
    e. Proposal review would be led by NSTX-U management (Program and Project) combined with a small standing committee comprised of members of the NSTX-U team without conflicts of interest. The FES NSTX-U program manager would provide final review and concurrence.

This set of ideas was presented to NSTX-U PAC-35, and the PAC responded very favorably and commented that:

> *"The PAC applauds the concerted effort to engage NSTX-U collaborators in a fruitful planning discussion on expanding engagement with university scientists. While this is a specific request from FES to the NSTX-U program, it is in fact a larger fusion community issue. The PAC was informed that the planning discussion was organized through three meetings jointly with 22 FES-funded NSTX-U collaboration grantees (university, laboratory, industry). The specific suggestions identified for possible FES and PPPL action are good examples that are either essential to stabilize or to improve the environment for university collaborations on NSTX-U (J. Menard overview presentation slides 40-43)"*

and

> *"The PAC agrees the NSTX-U Innovative Research Award (NIRA) is a good idea that should be implemented. We were informed through the question-answer period that university-based collaborations involving NSTX-U research are already substantial, e.g., totaling 76 individuals. Hence, if targeted exclusively to university researchers, the NIRA would increase university collaborations 10-20% beyond that which is currently underway. The PAC advises that in considering support for collaborative Ph.D. student research, duration of more than three years might be necessary to make such support tenable."*

The PAC-35 also provided ideas of its own, and noted that:

"Looking beyond the specific suggestions presented to the PAC toward the larger community issue, establishing a university program dependent primarily on collaboration at a major fusion user facility is compelling but very challenging. There are few such programs in existence in the U.S. fusion program. The PAC suggests that PPPL and/or FES could help facilitate the establishment of such university-based collaborative programs, keeping in mind the following considerations:

- *The base for stable university collaboration is a tenured faculty member(s) who is responsible for the supervision of Ph.D. education. This base is often greatly enhanced by the addition of professional scientists/engineers. The faculty member(s) must be vested in the students' research activities.*
- *Tenure promotions typically demand demonstration of scientific leadership in addition to scientific productivity. Structuring the scientific management of the NSTX program to include university faculty/researchers would help demonstrate scientific leadership and integrate university participation with less concern for additional financial support, i.e., the university faculty member(s) becomes an integrated, co-leader of the Research team. We note that university scientists already hold leadership positions in the Topical Science Groups.*
- *Competition for tenured faculty positions is fierce. Guaranteed financial support for startup and initial salary can significantly influence hiring decisions. This model has been successful in other research communities and other fusion projects, e.g., MAST/Culham and its nearby universities. PPPL and/or FES could seek to establish tenure-track positions through such support, perhaps targeting universities in close geographic proximity to facilitate graduate student educational needs. (Proximity is not likely essential, however.)*

The three points above only touch on the essential criteria for successful and sustainable university participation at FES user facilities. We recommend that PPPL/NSTX help drive a national conversation on the role of universities in fusion and plasma physics research, together with other laboratories and universities."

Summary for Notable Outcome 3.2:

The most impactful ideas developed included: Expanding Early Career Research (ECR) awards to University Scientists/Research Professors, supporting students with coordinated senior projects and targeted run-time, implementing enhanced collaboration tools (remote control rooms), implementing a "NSTX-U Innovative Research Award (NIRA)", and consideration of direct financial support for start-up and initial salary for tenure-track professor positions, in particular for universities in close geographic proximity. These ideas were presented to FES at the NSTX-U Q3 review and will be presented / advocated again at future meetings with FES. However, at the present time, there is no path within the Office of Science to expand ECR awards to non-tenure-track researchers, and resources are very limited to fund NIRA or direct-fund tenure-track positions from the NSTX-U science budget. However, the NSTX-U Program organization will be restructured in early FY15 to improve coordination among the topical science groups and to ensure every topical science group has representation from at least one funded University collaborator. This restructuring will more than triple the number of University researchers explicitly engaged in the management of the NSTX-U scientific program. Increased student support, targeted run-time, and enhanced collaboration tools will be considered later in FY15 once the NSTX-U facility and research program are fully operational again.

NSTX-U FY2014 Year End Report: Facility and Diagnostics

In FY 2014, the NSTX-U team continued to make a good progress on the NSTX Upgrade Project during the extended outage as described below. The NSTX-U Facility Operations team maintained the NSTX-U device, auxiliary systems, and site infrastructure to support the planned research efforts when NSTX-U starts plasma operations in FY2015. The team also initiated the preparation for the NSTX-U facility commissioning and subsequent plasma operations. Onsite support for equipment provided by other collaborating institutions was provided through the collaboration diagnostic interface budget. There were a number of important facility operation related enhancements carried out in FY 2014 which are needed to take full advantage of the NSTX-U device capabilities. With the enhanced plasma control requirements for longer duration plasmas expected in NSTX-U, an upgrade to the existing plasma control system is being implemented as part of the base program. In addition due to the aging D-site rectifier infrastructure and greater demands expected for NSTX-U, refurbishments of the TF and PF rectifiers (i.e., firing generators) were implemented by the base program. The TFTR-era motor generator with weld cracks was also repaired. The motor generator repair brought the motor generator to its original specifications, and the repair will enable the full operation of NSTX-U. The in-vessel installation for the modifications to the Multi-Pulse Thomson Scattering (MPTS) diagnostic required for the NSTX-U was completed in FY 2014 as described in Diagnostic Milestone Report D(14-1). The work is now shifted to ex-vessel work scopes in preparation for the NSTX-U operation. The recent NSTX-U Test Cell aerial view taken in August 2014 is shown in Fig. FD-1. The preparation of the NSTX-U commissioning and plasma operation has begun. To provide capabilities needed to carry out the NSTX-U scientific research, the NSTX Team identified high priority facility and diagnostic enhancements for post upgrade operations as the part of the successful DOE NSTX-U Five Year Plan Review conducted in May 21 – 23, 2013. These included diagnostics and physics capabilities provided by NSTX Research Team members from U.S. laboratories other than PPPL.

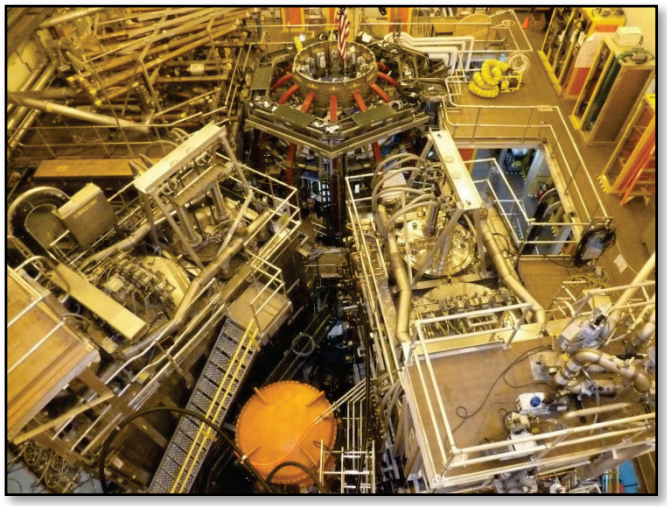

Fig. FD-1. *Aerial view of the NSTX-U Test Cell. The newly installed 2nd NBI beam box can be seen in the foreground.*

Facility and Diagnostic Milestones for FY2014

Facility Milestone F(14-1): Complete installation and testing of refurbished D-Site Rectifier Firing Generators. (Target date: April 2014, Completed: April 2014)

Description: The refurbished D-site rectifier firing generators will be installed and tested to support integrated systems testing of the D-site FCPC power systems.

Milestone F(14-1) Report: The D-site rectifiers (Transrex AC/DC Convertors of the NSTX Field Coil Power conversion System (FCPC)) provide a pulsed power capability of 1800 MVA for 6 seconds every 300 seconds. The modular converter concept of 74 identical, electrically isolated 6-pulse "power supply sections" was originally used on TFTR and then 68 of them were adapted to NSTX-U which has a more complex topology including anti-parallel and three wire configurations. Precise control of thyrister firing angles by the FCPC firing generators (FGs) has always been necessary for NSTX operations, and becomes more critical for the new 8-parallel, 130kA TF system configuration. The new Firing Generator (FG) delivers firing pulses with far greater resolution, precision, and repeatability. In FY 2014, 32 dual-output firing generators (enough to drive the 64 power supply sections needed for the NSTX-U FY15 experimental run, with spares) were installed and tested in the FCPC rectifiers. Chassis and parts for the additional seven firing generators are on hand in the electronics shop.

Diagnostic Milestone D(14-1): Complete the Multi-Pulse Thomson Scattering (MPTS) diagnostic in-vessel hardware modifications (Target date: April 2014, Completed: April 2014)

Description: To support post upgrade operation the MPTS diagnostic in-vessel hardware modifications will be completed to be ready for a system test and calibration of the diagnostic.

Milestone D(14-1) Report: Modifications to the Multi-Pulse Thomson Scattering (MPTS) diagnostic required for the NSTX Upgrade were designed, and fabrication and installation of the needed components is progressing. The larger diameter of the center stack in NSTX-U requires re-aiming of the MPTS laser beams to avoid striking the center stack, which would cause damage to it as well as an unacceptable level of scattered laser light in the vacuum vessel. Re-aiming of the laser beams requires several other changes to the MPTS diagnostic configuration: 1) a new laser beam dump is provided on a new vacuum vessel port (located at Bay L) on the opposite side of the vacuum vessel from the laser input port; 2) the laser input port on the vacuum vessel is moved several centimeters on the vacuum vessel and re-aimed to achieve the needed laser beam path; and 3) the MPTS light collection optics are modified and re-aimed to provide high-resolution imaging of the re-aimed laser beam. Design of the reconfigured MPTS system to meet these requirements is complete. The MPTS diagnostic in-vessel hardware modifications were completed to be ready for a system

test and calibration of the diagnostic. Fabrication of the ex-vessel components for the laser input flight tube and the light collection optics box (COB) is complete. Fabrication and procurement of the laser exit flight tube and associated components is underway. The new path of the laser beam through the vacuum vessel has been established. Work continues on the partially assembled COB with hopes to proceed to alignment and radial-array calibration before closure of the vacuum vessel. Installation and commissioning of the reconfigured MPTS diagnostic will be completed prior to the start of the first NSTX-U experimental campaign in 2015.

NSTX Upgrade Project Accomplishments - The NSTX Upgrade (NSTX-U) Project which has two major components, new center stack, and 2nd NBI, has made excellent progress in FY 2014. The Upgrade Project activities ramped up rapidly in all areas and are currently on pace to be completed in the early spring of 2015 well ahead of the Sept 2015 CD-4 completion target date.

New Center Stack Upgrade - The new center-stack part of the NSTX Upgrade Project has multiple elements including the fabrication of the new center-stack, the structural enhancements to the device for the ~ 4x increased electromagnetic forces, and the associated sub-system enhancements to supported the doubling of the TF current and 5 sec plasma pulse length. The new center-stack is connected to the outer TF through 36 U-shaped TF Flex Buses. A detailed center-stack drawing is shown in Fig. FD-2. The NSTX Upgrade Project has continue to work on the critical path fabrication of the center-stack (CS) components in FY 2014 including successful completion of the OH winding and its vacuum pressure impregnation (VPI). The CS component manufacturing stages are shown in Fig. FD-3. After completing the TF bundle in FY 2013, the winding of the OH coil over the full TF bundle has commenced in FY 2014. In Fig. FD-3(a), the OH winding activity is shown. After the OH winding is complete, a VPI of the entire TF-OH center-bundle was successfully completed. The The TF and OH coils were electrically tested to full test voltage. The completed TF-OH bundle is shown in Fig. FD-3(b). In parallel, the Center-Stack Casing with the welding of the 700 inconel studs for mounting the carbon tiles to the walls is completed. The carbon tiles (PFC) are being mounted with surface diagnostics to the casing walls as shown in Fig. FD-3(c). The inner poloidal field (PF) coils were manufactured and they are being prepared for mounting on to the casing as shown in Fig. FD-2. The completed OH/TF bundle and CS casing will be transported to the NSTX-U for final assembly. Delivery of the completed CS Assembly is scheduled for the fall of 2014.

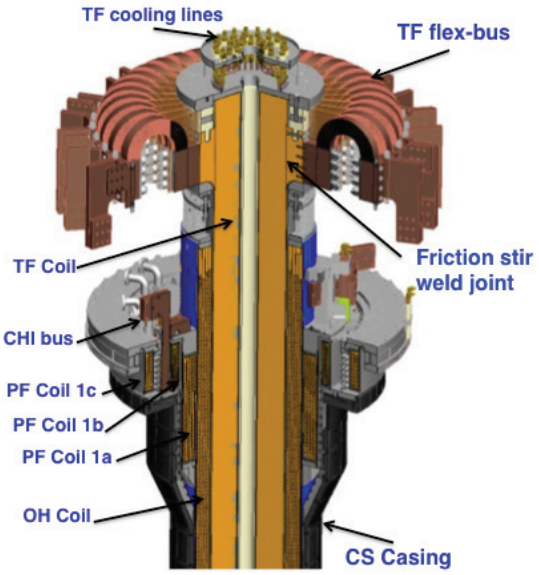

Fig. FD-2. *A schematic of the new center-stack and the TF joint area.*

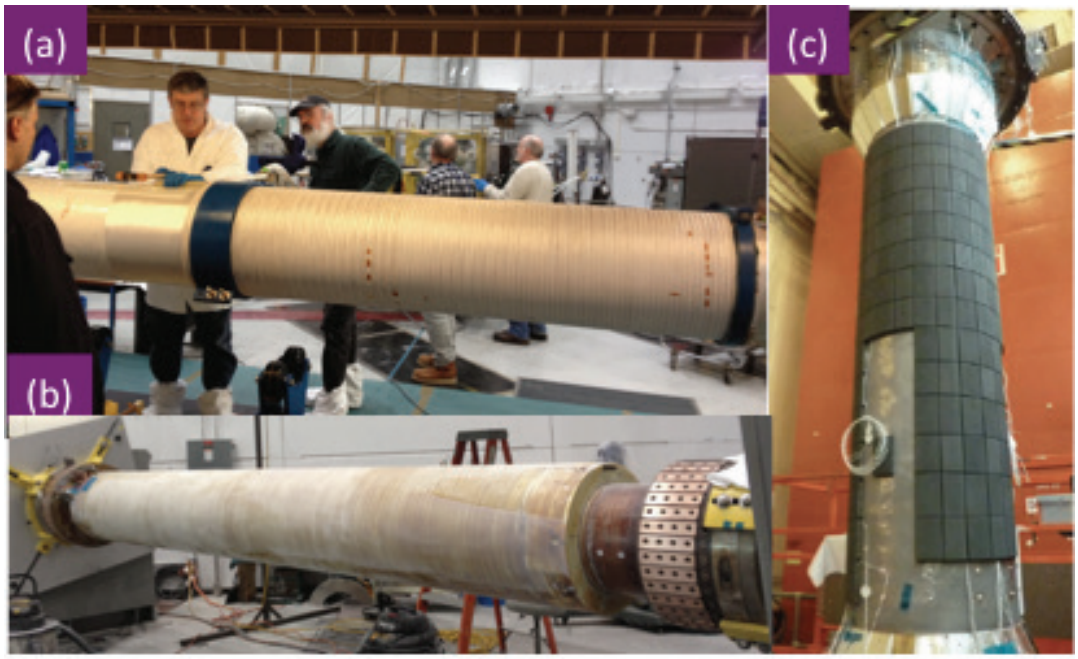

Fig. FD-3. *Center-stack component manufacturing. (a) OH coil being wound over the TF bundle. (b) Completed TF-OH bundle after VPI. (c) Graphite tiles and censors being installed center-stack casing.*

For the NSTX-U Center Stack, accommodations were needed to allow the toroidal field (TF) and Ohmic heating (OH) coils to move independently. While there are several ways that such differential coil movement (slip) might be accomplished, a decision was made to try to provide a 0.1" air gap between the TF and OH coils to accommodate their free movement during coil energizing and heating. It should be noted that a configuration without an air gap is also feasible and was the original TF/OH design concept presented at the NSTX-U Project Conceptual Design Review (CDR) where the OH would be directly wound on the TF with a slip plane to provide independent motion. However, it was decided that an air gap would result in the simplest operation in that there would not be a need for controlling the temperature of the TF and OH separately during coil operation. To achieve the air gap, water-soluble "Aquapour" was applied between the TF and OH coils with the intent of removing it with water after vacuum pressure impregnation (VPI) of the OH coil. In addition to the air gap, a layer of Teflon tape was applied to the inside of the OH coil to reduce the chances of VPI penetrating into the Aquapour region and to provide a slip plane if the air gap was not achieved. During the OH VPI process, the epoxy material (CTD-425) evidently saturated the Aquapour (resulting in a polymer that we refer to as "Aquament"), making water-based removal infeasible. The impact of leaving the Aquament in place on the NSTX-U operations and programmatic goals was evaluated. Based on the analyses of the NSTX-U plasma scenarios, it was concluded with a high degree of confidence that all of the NSTX-U physics objectives can be met and achieve the technical parameters stated in the Project Execution Plan (PEP) with Aquament in place. For certain operating scenarios, we might need to ensure a temperature differential is maintained. Important NSTX-U research goals such as achieving current profile equilibration (i.e., physics steady-state) at I_P = 2 MA can be met for broad range of plasma confinement time and plasma densities. The achievement of 1T, 2MA,

and 5 sec discharges as noted in PEP is projected to be achievable for confinement slightly above ITER scaling values (H_{98} = 1.05) with sufficient density control ($n_e/n_{Greenwald}$ = 0.5) and for a wide range of densities for higher confinement multiplier $H_{98} \geq 1.2$. While the presence of the Aquament will require the operational temperature constraints, it has the advantage of providing robust centering support for OH with respect to TF and naturally maintaining the pre-loading of Belleville washers against the OH launching loads. Based on our analysis of the current situation and options, it was concluded that the best option is to proceed with the final center-stack assembly without further Aquament removal attempts in order to achieve CD-4 and the start of NSTX-U plasma operation in FY 2015. The final center-stack assembly is now proceeding

Second Neutral Beam Injection System Upgrade - The 2nd NBI upgrade scope is to add a complete, functional second beam-line (BL) to NSTX-U at aiming tangency radii of 110, 120 and 130 cm compared to 50, 60, 70 cm for the present 1st NBI. This task largely utilizes the existing TFTR NBI infrastructure. The 2nd NBI tasks include the TFTR NBI BL tritium decontamination, refurbishments, sources, relocation, services, power and controls, and NSTX-U Test Cell (NTC) arrangements, as well as Vacuum Vessel modifications, the NBI and TVPS Duct, and NBI armor.

The 2nd NBI BL refurbishment and relocation have been completed and the jobs closed. The BL box and lid were moved into the NTC and reassembled. The installation of the support structure and alignment of the BL has been completed. The refurbished 90 inch flange, ion dump, calorimeter, and bending magnet were installed on the BL. The source platform has been fully decontaminated and installed. Relocation also included moving three High Voltage Enclosures (HVEs) from the TTC Basement into the NTC. This year, the High Voltage Transmission Lines were refurbished and relocated to the NTC where they were installed on the HVE and Source connections. The three NB Ion Sources were installed on the BL2 platform and vacuum connections completed. The BL2 and its sources are ready for vacuum pumpdown.

The BL services include deionized water, vacuum, liquid nitrogen (LN) and liquid helium (LHe) cryogenics, SF6, feedstock gas, and pneumatics. Progress includes the fabrication, installation and completion of the LN manifolds in the NTC and on the BL, as well as fabrication of LHe lines and valve manifolds in the NBI shops. All of the LN and LHe cryogenics piping installations have been completed. Leak-checking of cryo lines is completed. Pumpdown of vacuum jackets for operations has started. The deionized water system installation has been completed. The deionized water pump subcontract to upgrade the ion source and ion dump water pumps is completed and the pumps have been installed. The water system is ready for filling and operation. Vacuum system installation is in progress. SF6 system installation is in progress. Pneumatic systems are completed. BL Platform design is complete and installation is imminent. BL2 turbopump installation is imminent.

Power system progress includes the completion of all major cabling required to fully connect the N4ABC power systems from the TFTR area to the NTC location via the TFTR Test Cell (TTC) Basement. The high voltage triax cable has been terminated and installed in HVEs and Modulator/Regulators. Reactivation of the low voltage Filament, Arc, and Decel power supplies

for BL2 has been completed. Reactivation of bending magnets and the Accel line ups is imminent. Fiber optics cabling has been terminated and tested. Due to technical complications fiber optic rework was required and new tooling used to improve results. Rework is completed on the BL2-C system, partially completed on the BL2-B system, and in progress on BL2-A.

Major progress on controls continues. Cabling has been run to the NB racks in the galleries. BL2 tray and cable installation is in progress. The Local Control Centers for N4ABC have been addressed to add NI electronics and LabView software controls. Power supply controls have been updated in the Switchyard, Surge Rooms, Mod/Regs, and Decels. Three Gradient Grid Dividers have been fabricated for the Mod/Regs and installed. LabView programming is complete and ready for testing. Final controls installation was put on hold due to resource limitations, but work has resumed as planned and supports startup as scheduled. Additional resources were added. The LCCs have been in use to support power supply reactivation and testing. Controls cabling displaced by moving racks to galleries for BL1 has been installed. BL2 controls cabling and wiring is in progress.

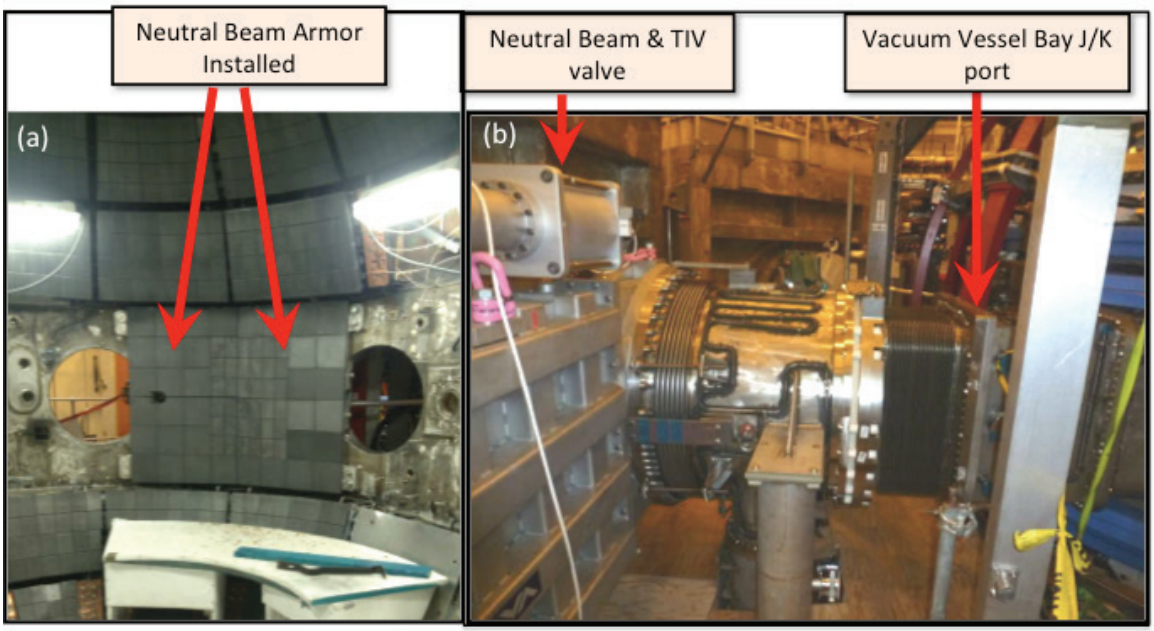

Fig. FD-4. *Final installation of 2nd NBI components: (a) Neutral beam armor spanning space between Bay G and I mid-plane ports . (b) Transition section including torus pumping system.*

Fabrication of the NBI armor to be located inside the VV is complete. The carbon tiles have been machined. The backing plates have been fabricated and the assembly and brazing are also completed. Final structural welding is complete in the VV. Assembly and installation of the NBI armor quadrants is complete. The Bay H port cover modification for the armor is also complete. The lift fixture to install Bay H port cover was used successfully to install the port and the installation and final connections are complete. All work for the Armor has been completed and the job has been closed. Final installation photos of these components are shown in Figure FD-4.

The Duct and VV modification at Bay JK has been completed. A new Bay JK "bay window" or cap was required for accommodating the strongly tangential aiming angles. The opening for the new cap was cut on the VV and the welding of the new Bay JK cap and Bay J port flange onto the VV has been completed. The JK reinforcement installation in the VV is complete. The sFLIP diagnostic port reinforcement near Bay J has been completed. The Bay K port extension required to clear the TF outer leg has been installed. The rectangular bellows for the NBI duct has been fabricated and leak checked. The major flanges and structures for the duct have been fabricated and welding is complete. Shield installation is completed. Since the original vacuum vessel duct and the torus vacuum pump system (TVPS) located in Bay L were removed, and the TVPS was incorporated into the NBI transition duct for NSTX-U. The VV leg strut had to be modified for angle and reinstalled to avoid spatial interference with the TVPS turbomolecular pump tables. The leg modification has been completed. The RWM coils for J-K as well as A-L have been redesigned, fabricated, and installed.

The Torus Vacuum Pump System (TVPS) ducts have been installed on the NBI duct and final duct installation onto the VV and BL2 was completed. The TVPS turbopump and RGA table installation has been completed. Instrumentation has been completed. Leakchecking of the duct components was successfully performed.

The NTC required extensive rearrangements to create the floor space for the BL. All rearrangements have been completed. New platforms have been installed; some additional platforms will be installed when final configurations of supports are known. The TVPS racks have been moved to the gallery area. The North door shield wall will be relocated to the gallery.

With the successful completion of the above tasks, preoperational testing of BL systems and N4ABC power and controls has started to properly commission subsystems and confirm readiness for operations. This testing has begun in earnest in FY2014 and flows into startup operations based on project schedules. At present the cryogenics startup is scheduled for October 2014. Due to safety precautions, the BL2 pumpdown is scheduled after installation of the VV CS and closure of the VV at the end of November. The Beam PTP low voltage conditioning is scheduled to follow in early December. Pending appropriate approvals, the Beam 2 CD-4 of 40 kV beam fired into the Armor has been scheduled for the end of December or first of January depending on availability of beam conditioning time with NTC closed.

TF and OH Power Systems for NSTX Upgrade - NSTX Upgrade requires an increase in the TF field. Thus the TF feed was designed to a rating of 1kV, 129.8kA for 7.45 seconds every 2400 seconds. Also the design is such that the pulse period can be reduced to 1200 seconds in the future by providing additional power cabling in the power loop. The NSTX rating was 1kV, 71.2kA for 1.3 seconds every 300 seconds. To meet the upgrade requirements, four additional branches are added to the existing four branches. The existing four TF Safety Disconnect Switches (SDS) will continue to be used with two parallel branches through each SDS. Extensive power cabling reconfiguration has been undertaken in the TF wing of Field Coil Power Conversion (FCPC) building. Ninety-six (about 6200 feet) TFTR-era cables are being

disconnected, removed, and scrapped. Hundreds of cables (about 5800 feet) are to be pulled and installed. Also additional cables from the Transition area to the NSTX test cell are to be provided for TF circuit. In FY 2014, all the installation work is completed.

New accurate fiber optic DCCTs (+/-150kA) will be provided to measure the TF current. The PF1A circuit is redesigned without the ripple suppression reactors, which were used with the previous PF1A coils. These ripple reduction reactors (the original PLT TF coils) will now be used in the upgraded OH circuit as the branch DC current limiting reactors (CLR) and the power cabling will be modified as needed. The existing OH power supply is designed to have the capability of 6kV, +/-24kA and meets the new requirements based on PSCAD analysis.

Rectifier Control System Upgrades - The D-site rectifiers (Transrex AC/DC Convertors) of the NSTX Field Coil Power conversion System (FCPC) has the capability to provide a pulsed power of 1800 MVA for 6 seconds every 300 seconds. The modular converter concept of 74 (1kV, 24kA), electrically isolated 6-pulse "power supply sections" was originally used on TFTR and two 1kV, 5kA supplies used for TFTR HF, out of which 65 of them were then adapted to NSTX-U which has a more complex topology including anti-parallel and three wire configurations. In order to extend the useful operational life of this system, which has remained largely unchanged since 1984, it is necessary to replace key elements of the FCPC controls. The elements to be redesigned are the Firing Generators, the Fault Detectors, the electromagnetic relays which provide the interlock logic in the "Hardwired Control System (HCS)", and the HCS to Fault Detector interface. The rationale for this refurbishment is based on the facts that many parts are nearing end-of-life due to age and wear, replacement parts are rare or unavailable, and that performance can be improved to meet the NSTX-U requirements using more modern control equipment. Precise control of thyrister firing angles by the FCPC firing generators has always been necessary for NSTX operations, and becomes more critical for the new 8-parallel, 130kA TF system configuration. In addition, the ability to separately control the "A" and "B" sections of each power supply unit allows for more efficient utilization of the available sections. The new Firing Generator (FG) was given the highest priority task [see Milestone F(13-1)] and, compared to the original FG, will deliver firing pulses with far greater resolution, precision, and repeatability, and can receive and process separate commands to the A and B sections as noted above. After successfully testing the FG prototype, the new FGs have been installed in 32 (thirty-two) rectifiers that are used for the Upgrade. The new Fault Detector (FD) provides the same functionality as the existing FD in terms of faults detected, but includes an improved external interface compatible with the present NSTX data acquisition system. The implementation of the new FD was considered a lower priority than the FG, but testing of the FD prototype has been completed in conjunction with the new FG in a Transrex rectifier. The final design of the new FD has been completed and documented, but a new set of FD's will not be assembled and installed at this time. The electromagnetic relay logic in the Hardwired Control System (HCS-Relays) in the TF & OH circuits is being replaced with PLC-based interlock logic. This will provide enhanced reliability via the elimination of old electromagnetic devices, and will provide an interface to the NSTX data acquisition system which will indicate the status of all interlock logic criteria. This includes the implementation of PLC compatible I/O modules in each

Transrex power supply of the TF & OH circuits, interfacing the FD, and connecting to the PLC. Thus the PLC will provide the Permissive interlock & Level 1 Series fault to the Rectifiers. Also by re-designing this Level 1 Series system response time to invoke a fault has been reduced from nearly 90 milliseconds to under 4 milliseconds The original Level 1 Fault Parallel system will continue to be used in the original state thereby, providing effective redundancy for the controls. The HCS system for the PF coils also will be converted to PLC in the future. A unique new TF turn-to-turn fault detection system has been designed and the Final Design Review successfully completed. The system will be installed prior to the end of the calendar year 2014. A new Digital Coil Protection System has been designed and it is being installed. All the power system upgrade installation work has been completed except the completion of the PLC wiring. Testing will start soon after completing this work as well as PSRTC & DCPS.

HHFW Heating and Current Drive Systems - The NSTX RF heating and current drive (CD) systems will consists of the existing 6 MW high harmonic fast wave (HHFW) system [10.3] and the new ECH/EBW system, which is an important element of the NSTX five year facility upgrade plan. The HHFW system is expected to perform better with higher toroidal field of NSTX-U. After the initial HHFW operation with the NSTX-U plasmas, an upgrade of the HHFW antennas is envisioned to increase the heating power and heating / CD efficiency. As a part of the NSTX-U five year plan, a MW-class ECH/EBW system is planned. The ECH/EBW system is particularly crucial for the non-inductive start-up research where it can be effectively bridge the temperature gap between the CHI based start-up plasmas which tends to be below 50 eV and the HHFW heating and CD regime which tends to be above ~ 200 eV. It is estimated that about 0.5 to 1 MW to ECH/EBW power would be sufficient to heat the CHI plasmas to ~ 200 eV range. The ECH/EBW system could also provide an efficient off-axis CD needed for advanced ST operations.

HHFW Antenna Upgrade - In the HHFW area, while the system is basically unchanged, the HHWF feed-thru conductor must be modified to be able to handle the higher disruption loads (~ x4) in NSTX-U. To handle those disruption loads, compliant connectors will be designed, tested and installed between the feed-throughs and antenna straps for the NSTX-U operations. In order to increase the power from the existing 12-strap HHFW antenna, RF voltage stand-off was tested on an RF test stand with the new compliant feeds. The test demonstrated the rf voltage stand-off of 46 kV which is about twice the value required. The HHFW antennas with the compliant feeds and improved back plate grounding were installed in NSTX is shown in Fig. FD-5. The tests also showed RF-induced arc-prone areas behind the back-plate. RF probes and tile sensors were also installed. The in-vessel installation work for HHFW was completed. The remaining test cell work is to install the external pipe connections and external cable installation for the rf probes and tile sensors.

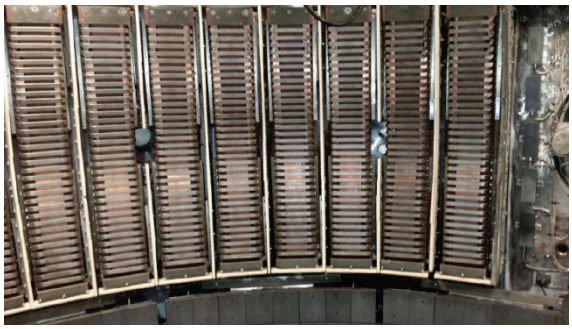

Fig. FD-5. *Enhanced HHFW antenna installed in NSTX-U with compliant feeds and improved back-plate grounding.*

CHI Upgrades – In the past, the TSC code was used to develop initial plasma start-up scenarios for future experiments, which has shown that the NSTX-U coil configurations will easily support plasma start-up to well over the 400 kA required to couple a CHI started discharge to non-inductive current ramp-up. The free boundary TRANSP code now begins to be used to model the evolution of the CHI started plasma and to study the effect of ECH heating on these target plasmas. These simulations show that 1MW of EC heating, at 28GHz in O-mode, can rapidly heat typical plasmas generated by CHI. The electron temperature increases from about 10-20eV typical of CHI plasmas to about 1keV in less than 30ms. For non-inductive current ramp-up, simulations indicate that HHFW cannot be coupled to the CHI target plasma without EC heating. Non-inductive ramp-up of low-current inductively generated plasmas has been carried out, as this is the first step in developing current ramp-up scenarios for CHI-generated targets. Start-up modeling with NIMROD has been carried out using two approaches. In the first method, a simplified model is used to understand basic physics. In the second approach, actual coil currents from a CHI-started discharge from NSTX are used to develop a realistic model of NSTX-CHI discharges. This year we also finished the design of the CHI system for QUEST and have started procuring hardware for implementing CHI capability on QUEST later this year. The US side is responsible for providing the primary insulators, which is currently being fabricated and is planned to be delivered to QUEST during October. The US will also provide the capacitor bank and the gas injection system, both of which are being fabricated at the University of Washington. We also identified suitable electrode configurations for a ST-FNSF, one of which has design features of the electrode configuration that will be tested on QUEST. These are described in the section on Solenoid-free plasma start-up.

Macro-stability Tools - While NSTX-U is a modification of NSTX, changes to the device conducting structure (e.g. new 2nd NBI port structure), mid-plane RWM control coils, and equilibria require re-computation of n = 1 active RWM control performance using proportional gain, and RWM state space control. The upgrade also adds new capability, such as independent control of the 6 RWM coils. This new capability, combined with the upgrade of the RWM state space controller will also allow simultaneous n = 1 and n = 2 active control, along with n = 3 dynamic error field correction. Finally, the active control performance of the proposed off-mid-plane non-axisymmetric control coils (NCC) also needs to be evaluated. A significant increase in controllable β_N is expected with the RWM state space control in NSTX-U, as was found for NSTX.

Disruption Mitigation Systems - A key issue for ITER, and the tokamak/ST line of fusion devices in general, is the avoidance and mitigation of disruptions. Most of the disruptions are expected to be mitigated by massive gas injection (MGI). In support of the planned Massive Gas Injection Experiments on NSTX-U, the University of Washington has successfully built and tested an electromagnetic Massive Gas Injection (MGI) valve for installation on NSTX-U. The operating principle of the valve is similar to the valve that is being planned for ITER. Both off - line tests as well as experiments on NSTX-U using this valve, and future improvements to the valve design will help inform the final design for the ITER valve. Fabrication of the first valve for installation on the upper divertor has been completed. This valve will be installed before the upper TF flags are installed on NSTX-U during mid-November. The necessary peer reviews for

the installation of the upper and lower divertor valves on NSTX-U has been completed. The lower divertor valve and the mid-plane MGI valves will be installed on NSTX-U early in 2014. The valve is at present undergoing off-line tests at the Univ. of Washington. After these tests are completed later this year, three such valves will be built for installation on NSTX-U. The UW group also developed the concept for an Electromagnetic Particle injector in much more detail than described in the 2013 report. The system accelerates a cylindrical boron nitrite projectile filled with impurity dust (boron nitride of beryllium powder for reactor applications, boron nitride, carbon or lithium, in the case of NSTX-U), accelerates it about 1 km/s in less than 2ms in a liner rail gun accelerator and injects it into the target plasma. Such a system has the potential to satisfy the 10 ms response time that may be required for a reactor DM system, as it is not limited by the slow thermal speed of gas molecules. The revised design is much simpler, and it takes advantage of the ambient magnetic fields in a reactor environment to improve its efficiency. The system is compact. An off-line test of the concept, followed by experiments on NSTX-U should be technically feasible by the end of 2017.

Boundary Physics Tools - The base line PFCs for the initial NSTX-U operation is graphite tiles. Because of the increased plasma heat loads due to the increased NBI heating power and pulse duration, it was decided to enhance the protection of the CHI Gap. "CHI Gap" is the region between the NSTX-U inner and outer vacuum vessels, above or below the CHI insulators. Also because of the new PF 1C coil, which is placed in the CHI Gap region, an improved protection was deemed necessary. Control room observations showed that when the strike-point was placed in this region, severe contamination of the plasma could occur. This problem was anticipated to be much more severe in NSTX-U, where the horizontal inner target is narrower by a factor of two. Hence, the graphite tiles on both the inner and outer divertors will be extended downwards, coming in close contact to the PF-1C coil casing and stainless steel outer vessel flanges and shielding these components from plasma contact. This narrower and deeper CHI gap will protect the vessel and PF-1C coil from excessive heat flux and protect the plasma from metal contamination, while continuing to provide the capability for CHI operations. The final tile installation is planned in the fall after the installation of the new center-stacl.

Fueling Tools - NSTX-U plasma operations will require the capability for gas injection from numerous locations. The gas injection systems on NSTX were not adequate to meet the physics program needs of NSTX-U as improvements are needed in the area of divertor heat flux mitigation, and increased levels of gas injection from high-field side to meet the up to 10s discharge pulses planned for in NSTX-U. These are briefly summarized.

For normal inductive plasma operation, NSTX-U will rely on three outboard gas injectors as on NSTX. However, Injectors 2 and 3 are being relocated to bays I and G as their original locations on the vessel were eliminated by the modifications providing the 2nd neutral beam port. NSTX relied on two high-field side gas injectors, one injecting near the midplane and one injecting at the "shoulder" of the center stack near the PF-1aU coil. These were used for H-mode triggering, and the high-field mid-plane injector was routinely used on most of the H-mode discharges. In NSTX-U, the system will have the capability for injection from two mid-plane locations and two "shoulder" locations at the top of the center stack. At each location, these injectors will be

toroidally displaced by 180 degrees. Furthermore, for both the midplane and shoulder locations, one installation will have a larger diameter tube, while the other installation will have a small diameter tube; this variation in tube size will provide a measure of control over the flow rates. The higher gas delivery capability from these injectors may be required during Li conditioned operation on NSTX-U as the injectors on NSTX were at some times (such as during the diffusive Li coating experiments) were found to be inadequate to maintain the required electron densities in NSTX.

For CHI start-up, in addition to the existing gas injector on bay K bottom, a Tee will be added at Bay G bottom port, which is the location of lower divertor Penning gauge, and this too used to provide more control and improved toroidal gas injection symmetry.

The glow discharge conditioning (GDC) system will use one of the mid-plane injectors as on NSTX. The boronization system, based on deuterated Tri-Methyl-Boron (dTMB) in a He carrier gas, is being significantly modified, by adding a new gas delivery system with improved safety features. In addition to the mid-plane injection, provisions will be provided for gas injection from both the upper and lower divertor regions. This is based on results from DIII-D that suggest that spatially distributed injectors will provide more uniform coverage of the boron coatings.

For divertor heat flux mitigation studies, NSTX relied on a single low-conductance gas injection location beneath the lower divertor plate on Bay-E. Initial NSTX-U capabilities will replace this injector with two high-conductance injectors in the lower divertor, separated by 180 degrees toroidally. This capability can be extended to additional toroidal angles, and to the upper divertor, in subsequent years once experience is gained with the new system.

A supersonic gas injector (SGI) has been developed for fueling and diagnostic applications on NSTX. It is comprised of a graphite converging-diverging Laval nozzle and a commercial piezoelectric gas valve mounted on a movable probe at a low field side mid-plane port location. The SGI flow rate is up to 4 x 10^{21} particles/s, comparable to conventional NSTX gas injectors. The nozzle operates in a pulsed regime at room temperature and a reservoir gas pressure up to 0.33 MPa. The deuterium jet Mach number of about 4, and the divergence half-angle of 5^{o} - 25^{o} have been measured in laboratory experiments simulating NSTX environment. The SGI has been used for fueling of ohmic and 2-6 MW NBI heated L- and H-mode plasmas. Fueling efficiency in the range 0.1 - 0.3 has been obtained from the plasma electron inventory analysis. In NSTX, long-pulse discharge scenarios with controlled ion inventory have been demonstrated via the use SGI fueling and lithium-coatings for ion pumping. It is planned to continue using the SGI routinely in support of plasma operations on NSTX-U. In initial years, H-mode fueling scenarios with SGI fueling will be developed. A primary benefit of the SGI is a precise control of injected gas inventory. The SGI can support H-mode density limit and pedestal studies, as well as perturbative transport experiments. In later years, it is planned to integrate the SGI in a feedback-control loop for active density control with PCS. Another gas fueling method that is envisioned for NSTX-U is a cryogenic supersonic gas injection (also referred to as molecular beam injection). Recent fueling experiments at HL-2A and LTX indicated that molecular clusters obtained via cryogenic gas cooling could penetrate deeper into the plasma due to a much higher

neutral density in a cluster jet and smaller ionization cross-sections of molecular clusters, thereby improving fueling efficiency of the supersonic gas injection even further.

Preparations for NSTX-U Lithium Operations - The safe handling of lithium is essential for supporting the technologies required for lithium conditioning of plasma-facing components (PFCs) and ELM control. Critical to this effort is a well-equipped workspace, and the NSTX-U Lithium Research and Development Laboratory at C-Site has been upgraded to fulfill this need. The LRDL has a large glove box with two stainless steel chambers that was previously used with a static dry argon fill. The glove box has been made to operate with full capabilities, including an evacuated transfer chamber and argon circulation through a drying train with a molecular sieve. Previously, the cleaning of components that involved lithium had to be performed in fume hood in another laboratory. With the installation of a new metal fume hood in the LRDL, lithium can now be safely loaded into apparatus for use on NSTX-U and cleaned afterwards in the same room. The 44" wide opening ("sash width") of the fume hood provides a large space for chemical handling. The exhaust duct also has two valves ("valterra valves") for connecting other chambers that require external venting. The new LRDL facilities are included in the revised procedures that are being prepared for lithium handling on NSTX-U.

Lithium Granule Injector for ELM Control - The lithium granular injector for ELM pacing which was successfully demonstrated on EAST will be available for NSTX-U. The NSTX-U lithium granule injector (LGI) for ELM control has been completed in FY 2011. The LGI system was shipped to the Chinese Academy of Science, institute of Plasma Physics and installed on the EAST Tokamak. The NSTX-U LGI system is capable of injecting horizontally redirected spherical Lithium granules (0.6 mm) at speeds approaching 100 m/s. The dropping rates (pacing frequencies) of 500 Hz have been achieved in the laboratory test. A dropper apparatus allows the granule size to be changed between discharges. After an extended shake-down period, the injector was used to trigger/pace ELMs in EAST H-modes. Using Li granules with diameters of several tenths of a millimeter injected at speeds of several tens of meters per second, ELMs were triggered at high efficiency. Pacing frequencies ranging between 10's to 100's of Hertz were observed. It is anticipated that much higher pacing frequencies can eventually be achieved using similar injector technology. The JET group is interested in the NSTX-U granular injector using beryllium granules for ELM pacing with application to ITER. A similar LGI system was also sent to RFX in Italy and successfully commissioned. An NSTX-U lithium dropper was also shipped to DIII-D for divertor recycling control and produced intriguing H-mode confinement and enhanced pedestal results. In preparation for the NSTX-U operation, LGI parts including a high-speed rotary feedthrough for the LGI "paddle" that propels the lithium granules into the plasma have been obtained. The feedthrough has a special "ferrofluid" vacuum seal that enables lithium granule injection in the kilohertz range required for ELM pacing. An LGI with this ferro-fluidic seal is being assembled for use on NSTX-U in FY15.

Lithium Evaporator and Upgraded Lithium Coating Systems - With encouraging results in NSTX, the NSTX lithium evaporator (LITER) system is planned for NSTX-U from "Day 1". The LITER system is essentially a temperature controlled stainless steel container filled with liquid lithium (LL), with a nozzle to direct the lithium vapor for coating PFCs at desired locations. The nozzle is typically aimed toward the middle of the inner divertor to maximize the lithium

deposition on the divertor plates. Two LITERS units were used for better toroidal PFC coverage of lithium on NSTX. The units each have a 90 g lithium capacity. The LITER consists of a main reservoir oven and an output duct to allow insertion in a PFC gap in the upper divertor region. Two heaters were used on each LITER, one heater on the output duct and one heater on the main reservoir. The heater on the main reservoir was typically operated to maintain the LL temperatures of 600–650 °C which enables an adequate lithium evaporation rate, as this rate increases rapidly with temperature. The heater on the output duct was operated about 50–100 °C hotter than the heater on the main reservoir to reduce lithium condensation on the output duct aperture. Typical evaporation rates have been in the range of 1 to 40 mg/min. The lithium evaporation typically takes place between plasma discharges to obtain the desired level of lithium coating on the PFCs, which could be in the range of 30 – 500 nm thick. In NSTX, nearly 1,000 g of lithium was delivered onto the PFCs during the last experimental campaign in FY 2010-2011. For the initial NSTX-U lithium capability, the baseline is the dual upper and lower aiming evaporators and a new Li granular injector on the mid-plane. The two downward-oriented lithium evaporators (LITERs) were removed from the upper dome ports when the upgrade began in 2011. The torus interface valves and shutters were left in place. The LITERs and their probe drives were inventoried in their storage locations, and the port areas were checked for interferences that might have resulted from upgrade activities around the NSTX-U upper domes.

A design is being developed for an upper aiming evaporator to cover the upper divertor region. The mini Li evaporator concept requires a lithium dropper as a source to fill a Li crucible which is then inserted into the edge of NSTX-U well outboard of the SOL, and heated to above 700 °C to cause rapid evaporation of the Li powder. Electron beam heating is the leading candidate for a heat source. Due to the high temperature, all Li is promptly evaporated to the upper vessel. This has advantages of requiring no shutters after evaporation. Since the evaporator is outside of the plasma volume, the discharge can commence without retracting the evaporator. This reduces the time between the end of the evaporation and the start of the discharge ensuring minimal passivation of the fresh lithium. A candidate mid-plane port has been identified as a possible location for the upward evaporator on NSTX-U.

Liquid lithium technology development - Several laboratory-scale research and development efforts are underway to support the NSTX-U lithium operations. These range from maintaining and improving existing infrastructure to support lithium wall conditioning via evaporations to the development of new liquid lithium technologies for evaluation in future upgrades to the NSTX-U PFCs. Lithium development capabilities in the Lithium Technology and Development Laboratory (LTDL) have recently been improved. The LTDL glove box has been recently refurbished to support lithium loading procedures for the LITER evaporation system. The refurbishment includes repair of the recirculation system and a thorough check of the H2O and O2 scrubbing systems. In addition, a fume-hood and wet-chemistry capabilities have been improved and procedures are being developed to exploit these capabilities. In particular, these facilities will be utilized to improve the liquid lithium loading of plasma targets being used to support Magnum-PSI collaboration work. These targets are loaded with liquid lithium in a glove-box environment with wetting promoted via mechanical action. The addition of a wet-chemistry lab will enable performing pre-treatment of the substrate materials to remove oxide layers that have previously been demonstrated to inhibit wetting requiring mechanical action if the procedure

is attempted at low temperature (T<400C). After loading with liquid lithium, a protective diffusion barrier is applied to the samples allowing transport without exposing the lithium to atmosphere. The procedure was carried out successfully leading to experiments on cup targets in the Magnum-PSI facility in the Netherlands. These tests will be used to inform on the design of advanced, pre-filled liquid metal targets for consideration as part of the NSTX-U high-Z divertor upgrades. While more conventional lamellae designs are planned for the first row of high-Z, a more aggressive technology could be utilized further outboard that makes use of pre-filled liquid lithium to ensure sufficient reservoir of lithium for physics studies while avoiding extended periods of lithium evaporation. Development of the liquid lithium test loop continues with the design of an argon enclosure to hold the loop. The work has begun redesigning the enclosure to provide an argon environment around the loop. The internal interlock system has been successfully tested with gallium as a surrogate metal and the system only awaits the completion of the argon enclosure.

NSTX-U Diagnostic System Status and Plans - The NSTX-U diagnostic installation has been an active area of NSTX-U operational preparation. A list of the existing diagnostic systems which are expected to be available for NSTX-U within the first year of operation is shown in the Table FD-1 except for the poloidal FIR high-k scattering system which is expected in FY 2016. We note that at least half of those diagnostic systems have strong collaboration components. The in-vessel diagnostic installation and related calibration tasks have been complete. The main focus now is the external installations. We shall briefly describe some noteworthy activities in FY 2014 for major diagnostic systems in the following sections.

MHD/Magnetics/Reconstruction
- Magnetics for equilibrium reconstruction
- *Halo current detectors*
- *High-n and high-frequency Mirnov arrays*
- Locked-mode detectors
- RWM sensors

Profile Diagnostics
- MPTS (42 ch, 60 Hz)
- T-CHERS: $T_i(R)$, $V_\phi(r)$, $n_C(R)$, $n_{Li}(R)$, (51 ch)
- P-CHERS: $V_\theta(r)$ (71 ch)
- *MSE-CIF (18 ch)*
- *MSE-LIF (20 ch)*
- *ME-SXR (40 ch)*
- Midplane tangential bolometer array (16 ch)

Turbulence/Modes Diagnostics
- *Poloidal FIR high-k scattering (installed in 2016)*
- *Beam Emission Spectroscopy (48 ch)*
- Microwave Reflectometer,
- *Microwave Polarimeter*
- Ultra-soft x-ray arrays – multi-color

Energetic Particle Diagnostics
- *Fast Ion D_α profile measurement (perp + tang)*
- Solid-State neutral particle analyzer
- Fast lost-ion probe (energy/pitch angle resolving)
- Neutron measurements

Edge Divertor Physics
- Gas-puff Imaging (500kHz)
- Langmuir probe array
- Edge Rotation Diagnostics (T_i, V_ϕ, V_{pol})
- *1-D CCD H_α cameras (divertor, midplane)*
- *2-D divertor fast visible camera*
- Metal foil divertor bolometer
- AXUV-based Divertor Bolometer
- IR cameras (30Hz) (3)
- *Fast IR camera (two color)*
- Tile temperature thermocouple array
- *Divertor fast eroding thermocouple*
- Dust detector
- Edge Deposition Monitors
- Scrape-off layer reflectometer
- Edge neutral pressure gauges
- *Material Analysis and Particle Probe*
- *Divertor VUV Spectrometer*

Plasma Monitoring
- FIReTIP interferometer
- Fast visible cameras
- Visible bremsstrahlung radiometer
- *Visible and UV survey spectrometers*
- *VUV transmission grating spectrometer*
- *Visible filterscopes (hydrogen & impurity lines)*
- Wall coupon analysis

Table FD-1 - Initial NSTX-U Diagnostic Systems

Soft X-ray Diagnostics – A new set of x-ray based diagnostics including core and edge tangential Multi-energy Soft X-ray system (ME-SXR), the midplane tangential Transmission Grating Imaging Spectrometer (TGIS), and the poloidal Ultrasoft X-ray arrays (USXR) are being prepared by the Johns Hopkins University (JHU) group. When installed the core ME-SXR system will provide a total of 100 channels of soft X-ray detection covering the entire outboard midplane plasma with a spatial resolution of ~3cm. The edge ME-SXR system will add another 100 channels covering with high resolution of ~1cm the plasma pedestal and the outer periphery ($0.6< r/a <1.1$ approximately). Designs for the new port-mounted ME-SXR system were completed in early summer, with an expected delivery of the machined hardware this fall. The new amplification and readout electronic systems have already been delivered. The compact JHU-designed electronic systems have also been adopted for use in the NSTX-U SSNPA system by UCI and in the NSTX-U diode bolometer system by PPPL Additionally, a novel, highly integrated and modular microcomputer-based system for ME-SXR data acquisition, which can amplify, read and digitize 100 ME-SXR channels using a single electronics unit, and send the digitized data to a remote computer through a single Ethernet connection, instead of hundreds of analog connections was developed. This innovation has potential to dramatically lower the cost and complexity of future soft X-ray diagnostics for NSTX-U and other fusion experiments. The data from the ME-SXR system will be used as input to the new JHU-developed neural network analysis code that will provide electron temperature profiles with frame rate of ~10 kHz, on a routine between-shot basis. Furthermore, in conjunction with the laser blow-off diagnostic currently under development at the Lawrence Livermore National Laboratory, the ME-SXR system will enable an accurate and routine diagnostic of the impurity transport in NSTX-U. Finally, the ME-SXR system will be used for fast, non-magnetic boundary position measurements, and will enable studying the use non-magnetic sensing for equilibrium boundary detection and for feedback position control in fusion experiments.

The current mid-plane tangential TGIS diagnostic has been upgraded with a faster detector which will increase frame rates from ~2.5Hz to ~50Hz, and is being readied for installation before NSTX-U research operations. A new detection system based on a direct-detection VUV/XUV CCD for increased sensitivity was also tested on LTX, where it has been successfully used to study the plasma recycling with solid and liquid lithium surfaces. In NSTX-U, the TGIS with direct-detection CCD will significantly reduce the complexity of the current diagnostic, as well as provide space and spectrally resolved impurity emission measurements with improved SNR. With the addition of a new post-doctoral researcher, the JHU group is now also evaluating the use of a similar direct-detection TGIS for the diagnostic of the upper divertor on NSTX-U. The measurements from the divertor TGIS will provide spatially and spectrally resolved profiles of the radiated power, which will be used in conjunction with the OEDGE and DIVIMP codes for validation of divertor physics models, for spectroscopic estimates of the electron temperature, and for assessment of the impurity content and transport.

Motional Stark Effect – Collisional Induced Fluorescence - With a doubling of the magnetic field as part of the NSTX upgrade the Motional Stark Effect measurement based on Collisionally Induced Fluorescence (MSE-CIF) collection optics can be optimized to increase the throughput.

With the higher field, this will change the optimal aperture width and polarization fraction for maximizing the signal-to-noise. We will use our design codes to re-optimize the aperture width. The MSE-CIF system will start with 18 sightlines and will have real-time capability (rt-MSE). In FY 2014 the testing and optimizing of the algorithms for rt-MSE was done and is nearly complete. In preparation for operation of NSTX-U in FY15, in-vessel spatial calibration was complete. Final calibration of the polarimeter will be completed after replacement of the vacuum interface window.

Motional Stark Effect – Laser Induced Fluorescence - The Motional Stark Effect measurement based on Laser Induced Fluorescence (MSE-LIF) will provide measurements of the field line pitch angle profile without requiring injection of the heating neutral beam needed for the present MSE system on NSTX-U, which is based on collisionally induced fluorescence (MSE-CIF). It will therefore provide critical data for measuring RF-driven current in NSTX-U without the competing effect of current driven by the heating neutral beam. Also, direct reconstruction of the total plasma pressure profile should be possible from its capability to make local measurements of the total magnetic field in the plasma. Combining this measurement with the comprehensive thermal profile measurements already available on NSTX-U, the fast-ion pressure profile can be inferred and compared to prediction to determine the influence of Alfvén Eigenmodes and other MHD activity on fast-ion confinement. Furthermore, the data from the two MSE systems, MSE-CIF and MSE-LIF, can be combined to calculate the radial electric field profile, an important element in plasma transport research. The first 12 fiber-optic bundles consisting of 24 sightlines (2 sightlines per bundle) were installed. The final four bundles were received and will be installed by the end of FY 2014. The spatial calibration for the complete set of 32 sightlines has been completed. Al the detectors and most of the filters for the system were received. The remaining filters are scheduled to arrive in early FY15. All 32 sightlines should be operational by the end of FY15.

CHERS - The following diagnostics for charge-exchange recombination spectroscopy (CHERS) have been reinstalled on NSTX-U in preparation for the beginning of operations in FY-15: CHERS (toroidal and poloidal), Edge Rotation Diagnostic (ERD, toroidal and poloidal) and Real-Time Velocity (RTV). Some of the viewing optics for the poloidal CHERS system have been modified to correct issues observed during NSTX operations, namely the occasional variation of lens aperture possibly caused by transient EM forces acting on the aperture mechanism. For all systems, the spectrometers have been re-aligned to optimize their spectral response. Both spatial and intensity calibrations have been performed. A final check of the calibration of the toroidal systems (CHERS and RTV) is planned after replacement of the faulty window hosting the "active" CHERS/RTV views at Bay B. An upgrade of the Operating System has been completed for all the acquisition PC's and testing/debugging of the acquisition software is under way.

Far Infrared Tangential Interferometer/Polarimeter – UC Davis is in the process of reconfiguring and upgrading the Far Infrared Tangential Interferometer/Polarimeter (FIReTIP) and high-k scattering systems on NSTX-U. In addition to providing time-resolved electron density data, the newly refurbished FIReTIP instrument will play a key role in NSTX-U's first density feedback control system, as well as providing density calibration for Thomson scattering. The seven-channel FIReTIP system employed previously on NSTX is being reconfigured into a three-channel system. Channel 1 will be employed for core plasma density monitoring as well as density feedback control and density calibration of the Thomson scattering system, while subsequent channels (as the necessary vacuum windows are installed) will monitor core and edge fluctuations. The optically-pumped FIR lasers that comprise the heart of the FIReTIP system will be located outside the NSTX-U test cell in the mezzanine area. This has necessitated the fabrication of long lengths of over-moded waveguide to transport the FIReTIP beams to the NSTX-U vacuum vessel, and the design and construction of a 3-level tower arrangement in the mezzanine area which will house not only the FIReTIP lasers, but also the CO_2 laser and CO_2-pumped FIR laser that provides the high-k illumination source. Constraints imposed by the new location of FIReTIP channel 1 has necessitated the design and fabrication of internal retro-reflectors (decision pending on subsequent chords). As internally-mounted retro-reflectors are subject to high levels of mechanical vibrations (attached, as they are, to the vacuum vessel rather than placed on a vibration isolation mount external to the vessel), this has required the design and fabrication of a vibration monitoring system. This system will consist of a heterodyne HeNe interferometer coupled to a field programmable gate array (FPGA) to provide real-time vibration compensated density information for use in density feedback control. Installation of the reconfigured FIReTIP system (laser tower, waveguides, optics, mixers, etc.) will take begin in late 2014, with Channel 1 to be operational for first research plasmas in early 2015. UC Davis has successfully overhauled the CO_2 and three CO_2-pumped FIR lasers that generate the FIReTIP beams. Dielectric-coated waveguides have been developed to couple the beams to/from the NSTX-U vacuum vessel, as well as flanges to both support the waveguides and ensure low-loss coupling between sections. The 3-level laser tower has been completed, and is due to be installed on NSTX-U in late 2014 along with the optics, phase comparator electronics, digitizers etc. that make up the full system. Chord #1 is expected to be operational for first research plasmas in early 2015, with additional chords to follow in succeeding years.

Turbulence Diagnostics - For turbulence diagnostics systems, the high-k scattering system detector array presently located at Bay K will have to be relocated to Bay L after the 2nd NBI installation at Bay K. By re-aiming the microwave beam, it is possible to measure both the radial and poloidal components of the high-k turbulence. The existing 280 GHz system will be replaced by a ~600 GHz system. The higher frequency system is designed to improve high-k resolution and SNR. For low-k turbulence, the beam emission spectroscopy (BES) system with a new generation of BES detector has been developed by the University of Wisconsin group. The group is planning to expand the BES system from 28 spatial channels to 48 channels for NSTX-U. A 288 GHz polarimetry system for magnetic fluctuation measurements is presently being tested on DIII-D. For the edge region, the gas puff imaging (GPI) diagnostic will be implemented.

High-k Scattering System - The 280 GHz high-k tangential scattering system of NSTX will be replaced by a 693 GHz poloidal scattering system being developed by UC Davis for NSTX-U, thereby considerably enhancing planned turbulence physics studies by providing a measurement of the k_θ-spectrum of both ETG and ITG modes. The probe beam in this case will enter the plasma from a port on Bay G while a tall exit window located on Bay L will be employed to collect the poloidally-scattered beams and image them onto an array of waveguide mixers. The diagnostic will begin operation in 2016 with a 4-channel array and will be extended to 8 or more channels in subsequent years. The reduced wavelength will result in less refraction and extend the poloidal wavenumber coverage from the previous 7 cm-1 up to > 40 cm-1. Measuring the kθ spectrum as well as kr spectrum is crucial for identifying the source of turbulence, since the 2D k-spectra driven by different instabilities have difference anisotropies. More importantly, the peak of the 2D k-spectrum has to be measured so that the turbulence amplitude can be experimentally correlated to observed plasma transport. The unique property of this new high-k scattering system is that it uses only one microwave launching system but is able to achieve four scattering configurations, which are sensitive to different regions of the 2D k-spectrum owing to the large magnetic shear in NSTX-U. The probe beams are tilted toroidally with respect to the scattered beams for positive and negative radial scattering. In the poloidal scattering arrangement, the first scheme has scattered beams going upward in the positive Z direction (upward scattering) while the other schem has scattered beams going downward in the negative Z direction (downward scattering). A total of four scattering schemes is thus possible with different combinations of toroidal and poloidal tilt angles. The simulation is performed using predicted profiles for a high-performance NSTX-U H-mode plasma. The anisotropy in the 2D k-spectrum of ETG turbulence, i.e. the existence of ETG streamers, can be determined by comparing the k-spectrum measured by the different schemes. Furthermore, a range of k_θ and k_r can be scanned by varying launching and receiving optics to map a wide range of 2D k-spectrum. UC Davis has successfully overhauled a CO_2 and CO_2-pumped FIR laser which will serve as the 693 GHz probe source. Corrugated waveguides are being remachined to couple the probe beam to the NSTX-U vacuum vessel. Design of the launch optics is near completion, while that of the receive optics will commence once the first waveguide mixer array has been fabricated and optically characterized. The diagnostic will begin operation in 2016 with a 4-channel array and will be extended to 8 or more channels in subsequent years.

Beam Emission Spectroscopy - The Beam Emission Spectroscopy (BES) diagnostic on NSTX-U, based upon observing the Dα emission of collisionally-excited neutral beam particles, will enable direct spatially-resolved measurements of longer wavelength density fluctuations in the plasma core, providing valuable insights into the suppression of ion turbulence and the attainment of near-neoclassical ion confinement on NSTX-U. The BES diagnostic together with the existing microwave tangential scattering diagnostic (which measures medium to short wavelength turbulence) will provide the most comprehensive turbulence diagnostic set available. The BES diagnostic also enhances measurements of the spatial structure of fast-ion-driven instabilities such as the TAE and BAAE observed on NSTX. BES measurements therefore contribute to several NSTX-U research areas, including turbulence and transport, waves and energetic particles, and boundary physics. Specific scientific applications include investigations of turbulence, turbulent flows, zonal flows, energetic particle modes, and Edge Localized Modes. University of

Wisconsin has previously developed an advanced 24-channel Beam Emission Spectroscopy (BES) diagnostic system on NSTX. For NSTX-U, an expansion of BES to 48 detection channels will be implemented to improve the scientific productivity of the BES system on NSTX-U. All 48 detectors are presently at PPPL, and alignment and installation activities are ongoing. A new fiber assembly for 2D BES measurements spanning the pedestal region has been designed. The UW Physical Sciences Lab has nearly finished fabricating the 2D assembly. .

Microwave Fluctuation Diagnostics – A number of microwave based fluctuation diagnostics are planned buy the UCLA group. The 16 channel reflectometer systems for the study of MHD mode activity including fast-ion driven modes are in process of reinstallation. These systems were transferred to MAST over the last year to test feasibility of Doppler Back Scattering (DBS) measurements on an ST. This collaboration was successful with an Invited Talk at the 2014 High temperature Plasma Diagnostics Conference. The vacuum interface is now at PPPL awaiting installation on Bay J. UCLA is also in process of developing a 4 -channel higher -frequency (82-86GHz) reflectometer system which will allow higher densities (~$1x10^{14}$ cm^{-3} to be probed. The current plan is to install this on the second UCLA port on Bay J using a quasi-optical configuration. This will allow not only additional reflectometery data at higher density, but also preliminary DBS measurements. It may also be possible to pursue the cross polarization scattering technique to probe magnetic fluctuations (preliminary testing was also performed on MAST and a diagnostic development program is underway at DIII-D with Terry Rhodes the Principal Investigator). The polarimeter has returned from DIII-D (Jie Zhang obtained his PhD degree on December 2013). However, based on the DIII-D experience (primarily S/N) UCLA plans to upgrade the polarimeter prior to installation on NSTX-U. Discussions are also underway for UCLA to provide some initial 288GHz interferometry data for Thomson calibration purposes during the first period of plasma operation. This would require temporary reinstallation of the "old" NSTX 288GHz interferometer which is currently being utilized on LTX.

Magnetics For Equilibrium Reconstruction, Boundary Control, and RWM Suppression - NSTX had a comprehensive set of magnetic diagnostics, including ~ 45 poloidal flux loops, ~ 60 magnetic field sensors for constraining equilibrium reconstruction codes such as EFIT, and 48 in-vessel sensors for measuring and controlling resistive wall modes. These sensor systems will be retained on NSTX-U, but with some significant improvements. In particular, the density of poloidal magnetic field probes flux loops in the divertor region will be increased, in anticipation of improving the magnetic reconstruction of snowflake divertor configurations. Furthermore, a second vertical array of poloidal field sensors will be installed on the center column, increasing the redundancy of these critical measurements. Finally, the density of poloidal magnetic flux loops in the vicinity of the divertor coil mandrels will be increased, allowing better reconstruction of the eddy currents induced in these support structures.

Boundary Physics Diagnostics - The NSTX facility has been investing strongly in boundary physics related diagnostics in the past several years, and a major activity has been to insure that port space is available on NSTX-U to accommodate them. There are over 20 boundary physics diagnostic systems on NSTX-U and additional ones are being readied. They include Gas-Puff Imaging (500kHz), a new poloidal Langmuir probe array, Edge Rotation Diagnostics (T_i, V_ϕ, V_{pol}), 1-D CCD H_α cameras (divertor and midplane), 2-D fast visible cameras for divertor and overall plasma imaging, divertor bolometer, IR cameras (30Hz), fast IR camera (two color), tile temperature thermocouple array, divertor fast eroding thermocouples, dust detector, Quartz Microbalance Deposition Monitors, scrape-off layer reflectometer, edge neutral pressure gauges, Material Analysis and Particle Probe (MAPP), Divertor Imaging Spectrometer, Lyman Alpha (Ly_a) Diode Array, visible bremsstrahlung radiometer, visible and UV survey spectrometers, VUV transmission grating spectrometer, visible filterscopes (hydrogen & impurity lines), and wall coupon analysis. Major upgraded boundary physics diagnostics are described in more detail below.

Material Analysis Particle Probe (MAPP) - A major NSTX-U PMI diagnostic addition is the Material Analysis Particle Probe (MAPP) by Purdue University. MAPP is an in-vacuo inter-shot diagnostic capable of correlating surface chemistry evolution with plasma response to PMI conditioning. MAPP utilizes multiple surface-science measurement techniques to characterize a sample material exposed to NSTX-U conditions and assess plasma-surface interactions near the divertor strike point. A unique sample head has been designed for MAPP to allow simultaneous exposure of up to four samples to plasma discharges. The surface of each sample is positioned (via shims or custom machining) colinear to the top surface of the retaining stems in order to avoid self sputtering. Independently controlled heaters are contained beneath each sample and radiative and conductive cross-talk heating is reduced using perforated sample stems and vertical heat baffle shields. Following plasma exposure, samples are retracted *in-vacuo* into an adjoining chamber, where a variety of analysis techniques are performed during the in-between shot window. Analysis techniques include X-ray photoelectron spectrscopy (XPS) – used to assess the chemical interactions of the top ~10 nm, ion scattering spectroscopy (ISS) – interrogates the top 1-2 monolayers to determine surface chemical composition, and direct recoil spectroscopy (DRS) – uniquely capable of measuring the surface hydrogen content in samples. In addition, thermal desorption spectroscopy (TDS) can be performed at the end of each day in order to measure and quantify bulk deuterium retention. The MAPP has been installed and tested on LTX . Activities related to the installation of MAPP on NSTX-U included a successful “fit-up” of the analysis chamber and bellows drive on a lower dome port. Progress was also made on remote control of the surface analysis diagnostic. For XPS, this included the safety interlock systems and providing power for the X-ray source and microchannel plate detectors. Remote control was also implemented for scanning the electrostatic analyzer voltage for determining electron energies. For TDS, remote control is operational for the residual gas analyzer and the four sample heaters, whose temperatures can be set separately. A remotely-controllable ion source was also implemented, and initial tests have been performed for “depth profile” with ion bombardment.

Divertor Spectrometers and Two-Color Fast Infrared Camera - A new set of diagnostics for divertor and plasma-surface interaction studies as well as upgrading of existing divertor diagnostics were being prepared. The LLNL upgraded spectroscopic complex would enable new and improved impurity erosion measurements with lithium-coated graphite and high-Z plasma-facing components, as well as divertor impurity radiation distribution and divertor parameter control. New capabilities include a vacuum-ultraviolet divertor spectrometer (SPRED) to monitor impurity emission in the divertor. The divertor SPRED spectrometer has been upgraded with a new detector, and a port design has been completed. Another new capability is the CIDTEC camera system equipped with an image splitter. The radiation-hardened camera can withstand high X-ray and neutron environment and unlike other conventional diagnostic cameras can be placed within a few feet from NSTX-U. The LLNL group previously used the system for molybdenum erosion studies in Alcator C-Mod tokamak. The new image splitter enables simultaneous measurements of emission in the same divertor region from two impurities. The opens up a large number of new measurement opportunities, e.g., simultaneous monitoring adjacent impurity ion spices, helium line ratio technique, impurity emission relative to recycling emission, and others. The camera is presently being tested on the LTX tokamak. In addition to the above mentioned diagnostis, 1) 30 spectrally filtered edge impurity emission system (EIES) detectors; 2) the Lyman-alpha diode array (LADA) divertor radiometer; 3) the ultraviolet-visible-near-infrared spectrometers VIPS and DIMS; 4) Upgraded one-dimensional filtered camera arrays with divertor and midplane views; and 5) Near-infrared divertor spectrometer were being prepared. A new spectroscopic diagnostic complex for divertor detachment control is being developed for NSTX-U. Several new diagnostics will provide spatially resolved information on divertor electron temperature, density and impurity distribution in real time, so that the signals can be fed into the plasma control system for real-time feedback control of deuterium or impurity seeding. The new diagnostics include a fast camera, an imaging divertor spectrometer, and upgrades to existing dignostics (such as e.g. divertor SPRED) for real-time detection.

Dual-band high-speed IR Thermography - Another important divertor diagnostic developed on NSTX is a two-color or dual-band (DB) device developed for application to high-speed IR thermography by ORNL. Temperature measurement with two-band infrared imaging has the advantage of being mostly independent of surface emissivity, which may vary significantly for an LLD as compared to that of an all-carbon first wall. In order to take advantage of the high-speed capability of the existing IR camera (1.6-6.3 kHz frame rate), a commercial visible-range optical splitter was extensively modified to operate in the medium wavelength (MWIR) and long wavelength IR (LWIR). This two-band IR adapter utilizes a dichroic beamsplitter which reflects 4-6 micron wavelengths and transmits 7-10 micron wavelength radiation, each with > 95% efficiency and projects each IR channel image side-by-side on the camera's detector. The DBIR system was successfully operated in FY 2010 and provided surface temperature data for lower divertor plates for heat flux calculation, and a duplicate of high speed DBIR system to monitor upper divertor plates is being implemented for NSTX-U. The ORNL boundary physics group has designed and implemented a wide angle, 30 Hz infrared camera system on NSTX in FY 2011. A dual-band adapter was also implemented for variable surface emissivity due to lithium films. This system was designed as part of a Princeton University student's first year experimental project. The optical relay system is being modified and a system calibration is in progress for NSTX-U. The University of Tennessee Knoxville (UTK) group, in close collaboration with the

ORNL group, also comprises the staged installation of two new infrared cameras, to extend the pre-existing thermography imaging coverage. The cameras will be installed at Bay G bottom and Bay J equatorial ports to provide measurement to couple with the spectroscopy lines of sights (i.e. upper divertor and center stack). Both cameras will be equipped with a fast-dual-band adapter, for the simultaneous acquisition of imaged in the medium (4-6μm) and long wavelength (7-10 μm) infrared. In addition, two ORNL eroding thermocouples at the PFC tile surface were installed and instrumented. These thermocouples, which have a design response time ~ 1 ms are intended to be used in the future for feedback control of PFC surface temperature in NSTX-U.

The (UTK) group is also preparing a multi-channel spectroscopic diagnostic that will provide spatially and temporally resolved measurement of visible and UV emission from near-wall regions, permitting to characterize the near-wall processes by monitoring the abundance of atomic (e.g. C, Li, O) and molecular species, (Li_2, CD, LiD, Li oxides) within a single plasma discharge and throughout the campaign. The spectroscopic diagnostic design is complete and vacuum interface elements for Bay G lower and Bay J mid-plane ports have been acquired and are ready for installation. The main items of optic lines (objectives, collection optics, spectrometer, and camera) have been purchased and assembling is progressing.

A Divertor Imaging Radiometer for spectrally resolved measurements of the radiated power by Johns Hokins will extend the multi-energy concept to divertor diagnostic by performing absolute measurements of the radiated power in tens of spectral bins covering the range from several eV to few hundred eV (VUV to XUV). The radiometer will use dual transmission gratings in conjunction with a direct detection CCD camera and will view the divertor from the outboard side, with vertically spaced lines of sight from the X-point region to the strike-point region. The instrument will have ≥2 cm space resolution and ≥10 ms time resolution. The proposed diagnostic will provide, for the first time in a tokamak, measurements of the spectrally resolved radiated power from the divertor and will enable determination of the radiating impurity type and charge state distribution over the range of temperatures expected for the NSTX-U divertor. This in turn will provide information on the radiating efficiency and transport of *injected* impurities for radiative divertor studies, as well as information on *intrinsic* impurities and associated radiation. In addition, the proposed diagnostic will be used to calibrate and validate the advanced divertor modeling codes used at NSTX-U. We will also study using the radiometer in conjunction with divertor emission modeling for a spectroscopic diagnostic of the electron temperature and cross-field particle transport in the divertor. Even if approximate, such measurements will be useful for the NSTX-U divertor research.

Laser blow-off impurity injection system - Injection of neutral atoms into the core plasma from the edge can be an inefficient process due to shielding of the core by the SOL and divertor. When injected by simple gas puffing into the boundary plasma, a large gas puffing source may be required in order to overcome this inefficiency and deposit impurity atoms into the core sufficient for detection by charge-exchange and filtered emission imaging diagnostics. Creation of a highly directional burst of low energy neutrals can be accomplished, however, by quickly vaporizing a thin film deposited on a glass substrate using a laser, known as the laser blow-off injection. This type of system has been demonstrated in the past on plasma test stands and tokamaks and used in impurity transport studies. The LLNL group is now working on developing and installing a laser

blow-off impurity injection system on NSTX-U. The system comprises of a 10-hZ, 1 J, Q-switched Nd-YAG laser, beam delivery optics, and a target chamber that will be mounted on the NSTX-U vacuum vessel. The laser blow-off impurity injection system will be used for low- and high-Z impurity transport studies in the core, pedestal, and edge of NSTX-U plasmas, and for benchmarking predictions of the edge impurity transport codes, such as the LLNL fluid code UEDGE and turbulence code BOUT++.

Divertor Thomson scattering diagnostic - A conceptual design for a divertor Thomson scattering (DTS) diagnostic has been developed for NSTX-U to operate in parallel with the existing multipoint Thomson scattering (MPTS) system. Higher projected peak heat flux in NSTX-U will necessitate application of advanced magnetics geometries and divertor detachment. Interpretation and modeling of these divertor scenarios will depend heavily on local measurement of electron temperature, T_e, and density, n_e, which DTS provides in a passive manner. The DTS design for NSTX-U adopts major elements from the successful DIII-D DTS system including 7-channel polychromators measuring T_e to 0.5 eV. If implemented on NSTX-U, the divertor TS system would provide an invaluable diagnostic for the boundary program to characterize the edge plasma. The conceptual design has been detailed and presented at the High Temperature Plasma Diagnostics conference in June 2014.

Pulse Burst Laser System - During FY 2014, under the DoE early career research project, the PI (with the support of NSTX-U) had PSL (from University of Wisconsin) complete the phase I of the design of the Pulse Burst Laser System. The laser will be capable of three modes of operation with different repetition rates: (1) The base mode, whereby single laser pulses are generated with a repetition rate of 30 Hz; (2) The fast-burst mode whereby following interruption of the base mode, a burst of pulses is generated at constant frequency in the range of 10 kHz to 15 kHz for a minimum of 5 ms and (3) The slow-burst mode whereby following interruption of the base mode, a burst of pulses is generated at constant frequency of 1 kHz for a minimum of 50 ms. The base and fast-burst modes are required. It is hoped that the slow-burst mode can also be achieved. At the end of this conceptual design, a review was carried out and was deemed satisfactory. The PI is now proceeding to phase II during which the laser system will be fabricated.

Energetic Particle Diagnostics - In the energetic particle (EP) research area, in addition to the perpendicular and newly implemented tangential fast ion D-alpha (FIDA) diagnostics, additional SSNPA (Solid-State Neutral Particle Analyzer) channels will be implemented since the scanning NPA was removed. Additional diagnostics for EP studies on NSTX-U include neutron rate counters, a scintillator-based Fast Lost-Ion Probe (sFLIP), installed on the vessel wall, and a new charged fusion product (CFP) profile diagnostic. The 16 channel reflectometry will be also installed for the energetic particle mode measurements.

Energetic Particle Distribution Diagnostics - On NSTX-U the radial fast ion profile is characterized through the FIDA and ssNPA systems. A vertical FIDA system measures fast ions with small pitch, corresponding to trapped or barely passing (co-going) particles. A new tangential FIDA system measures co-passing fast ions with pitch *~0.4* at the magnetic axis up to *1* at the plasma edge. Both FIDA systems have time resolution of *10* ms, spatial resolution ≈*5* cm and energy resolution ≈*10* keV. An upgraded solid-state Neutral Particle Analyzer (ssNPA) will provide energy-integrated measurement of trapped fast ions, with a lower energy threshold

E_{min}~*20* keV, from 5 radii. The ssNPA system will mainly work in current-mode to get fast time response. The sampling rate is ≈ *1* MHz. Two ssNPA channels will also incorporate pulse-counting mode capability to obtain energy spectra with ~*10* keV energy resolution and ~*10* ms temporal resolution. The fast-ion distribution function F is a complicated function of energy, pitch angle, space, and time. Successful reconstruction of F requires multiple measurements with a variety of techniques. The vertical FIDA system is a working diagnostic that has been producing valuable data for several years. Only minor changes to this diagnostic are proposed. The tangential FIDA system is patterned after the vertical FIDA diagnostic. Although it has not collected data during plasma operations, its installation is complete. Both FIDA systems were calibrated. An adjustment of the tangential view was completed. The SSNPA diagnostic will be displaced from its present location by the new beam-line. A new SSNPA diagnostic will be designed and installed to measure trapped fast ions at several radial locations. The solid state neutral particle analyzer (SSNPA) arrays for NSTX-U were designed. All components were purchased. The mechanical assemblies have been installed in the vessel. The electronics are currently being tested.

Additional diagnostics for EP studies on NSTX-U include neutron rate counters, a new CFP profile diagnostic, and a scintillator-based Fast Lost Ion probe (sFLIP) installed on the vessel wall. Neutron counter measurements are strongly weighted toward the higher-energy portion of the distribution function, with no pitch angle dependence. For example, an increased count rate during HHFW injection is a straightforward indicator of the formation of tails in the fast ion distribution above the NB injection energy. The neutron diagnostic system is being upgraded to expand the system from two to four fission chambers. This upgrade will extend the dynamic range of the system and increase its fault tolerance. In addition, a new neutron source for absolute neutron rate calibrations is being purchased to replace a legacy TFTR-era source that is now too weak to be useful for in-vessel calibrations. Furthermore, a preliminary plan has been developed for long term stability measurements of the neutron system using a low emissivity neutron source.

Similarly to neutron counters, the CFP diagnostic in collaboration with Florida International University would provide direct measurements of the fusion reactivity. Because both protons and tritons are largely unconfined for NSTX-U parameters, fusion products are eventually detected outside the plasma volume. By knowing the magnetic field geometry, their orbit can be tracked back in the plasma. Such orbits are equivalent to curved sightlines for each detector, so that multiple signals can be inverted to infer a radial profile of the high-energy fast ions. A 4-channel CFP prototype has been tested in FY2013 on the MAST device (see the Energetic Particle Research Section). The 3 MeV protons and 1 MeV tritons produced by DD fusion reactions in MAST have been clearly observed. Given the successful observations on MAST, a similar small system (4 - 6 channels) with improved energy resolution is currently being designed at FIU with the plan to install and test it in NSTX-U in 2015. The data obtained on NSTX-U will be used in a proposal for a future 16-channel system for NSTX-U.

A scintillator-based Fast Lost Ion probe (sFLIP) contributes to the NB characterization by providing energy and pitch resolved spectra of lost fast ions, e.g. from prompt losses, as the NB

tangency radius is varied. sFLIP is being upgraded with a faster CCD detector capable of frame rates up to 100 kHz. A set of photo-multiplier tubes is also being installed on sFLIP for energy and pitch integrated measurements at rates up to 250 kHz from 6-10 sub-regions of the sFLIP scintillator plate. Major modifications to the vacuum vessel and two large diagnostic ports to accommodate the new neutral beam lines for NSTX-U has resulted in displacement of the scintillator Fast Lost Ion Probe (sFLIP) from the port it had used during NSTX operations. A suitable alternate port for this diagnostic was identified, and that port was enlarged and substantially reinforced to accommodate the diagnostic. The diagnostic assembly itself will also be reconfigured to fit in the new location, while at the same time extending its range of pitch angle acceptance.

Energetic-Particle-Induced Mode Diagnostics - A recently-developed UCLA 16-channel comb quadrature reflectometry system has been utilized on NSTX to study the eigenmode structure of fast-ion driven Alfven as well as other MHD modes. This unique system has also provided a wealth of additional information including investigation of three-wave coupling processes and identification of the potential role of Compressional Alfven Eigenmodes (CAEs) in contributing to core anomalous transport. In order to prepare for higher density operation in NSTX-U it is proposed to expand operation to 100GHz through the installation of 8 additional channels. This upgrade to 24 channels will allow detailed eigenmode structure measurements in high performance NSTX-U plasmas. Similarly to NSTX, several arrays of high-frequency Mirnov coils will provide routine measurements of the fluctuations spectrum on NSTX-U. Two sets of coils are toroidally displaced to enable the computation of the toroidal mode number of the modes from the phase of the complex spectrum. A reduced set of coils is displaced poloidally to provide information on the poloidal mode structure. The bandwidth of the magnetic fluctuation measurements will be extended on NSTX-U from the present 2-2.5 MHz up to 4 MHz, to account for the expected frequency up-shift of the modes as the toroidal field is increased. Another quantity of great relevance for EP studies is the radial structure of *AE modes. Several complementary systems will be available to this end on NSTX-U, including beam emission spectroscopy (BES) arrays, reflectometers, interferometers, polarimeters, and X-ray detectors. A proposal for installing a Doppler back-scattering (DBS) system will be also considered based on the available funds (see below). The BES system will provide low-k density fluctuation measurements near the mid-plane for normalized radii $0.1<r/a<1$. The number of channels will be increased from 32 up to 64 to simultaneously sample a wide region of the plasma. The measurement region will extend poloidally to cover a ~10 cm broad strip along the mid-plane. Further improvements may include a toroidally-displaced set of viewing channels, possibly limited to the edge region, to measure background emission (in the absence of the 2nd NB source) or the toroidal mode number of the instabilities. Density fluctuations are also derived from a multi-channel reflectometer system. The 16 channels available on NSTX will be complemented by 8 new channels at higher frequency, which will enable fluctuation measurements up to densities ~10^{20} m^{-3}. Line-integrated measurements of density fluctuations will also be available from 3-4 far-infrared interferometer with sampling frequency ~4MHz. Beside density fluctuations, other quantities such as magnetic field and velocity fluctuations are important for a thorough identification and characterization of the different instabilities. A new radial polarimeter

system will provide direct measurement of magnetic fluctuations along the mid-plane. Pending incremental funding for diagnostics development, flow fluctuations will be measured through a millimeter-wave Doppler back-scattering (DBS) system operating in the 80-100 GHz frequency range. This new measurement capability represents an alternative, substantially independent tool for identifying fast-ion modes that would significantly strengthen comparison with theory, expanding previous internal measurements of fast-ion modes previously restricted to perturbed density on NSTX. Additional information on fluctuations with frequency < 100 kHz will be provided by a multi-energy SXR array with two toroidally displaced sets of views. Spatial resolution varies from ~1cm at the outboard mid-plane (R>150 cm) to ~3 cm in the core and inboard mid-plane region (40<R<140 cm). Faster measurements with up to ~500 MHz bandwidth will be available from a system of two poloidal SXR arrays. Each array contains 16 channels viewing poloidally through two variable selected filters, with 2-3 cm resolution. Alfven Eigenmode Antenna for AE Stability Measurements - Simple antennae have been used in several machines (JET, C-Mod) to study TAE stability. The linear damping rate can be measured by sweeping the antenna frequency through the mode frequency. It will be useful to extend these studies to low aspect ratio tokamaks (MAST and NSTX). This would also help to validate ITER projections by challenging our fundamental understanding of the physics in the drive and stability of these modes. For low aspect ratio the antenna can also be used to study higher frequency Alfvén modes such as GAE and CAE. The "MHD active spectroscopy" plan begins with relatively simple antenna design. As operational experience builds up, more ambitious designs will be tried. In years 1&2 several proto-type antenna designs will be evaluated to optimize the coupling to TAE and CAE. The NSTX-U prototype AE antenna system consists of up to 4 compact modules, each of which is a single, 5-turn 'window-frame' coil, similar in principle to those used on JET, C-Mod and MAST. In parallel, the external power supplies for driving the antenna, the coupling networks and control hardware and software will be developed. While the highest priority will be to develop the capability to study TAE, time will also be devoted to evaluating the antenna and coupling network at frequencies up to 2MHz, as will eventually be needed for Global and Compressional Alfvén eigenmode studies. A four-element *AE antenna was designed and installed on NSTX-U to test selectivity of the toroidal / poloidal mode number, as well as improving the coupling of the antenna to the modes. The low power (≈1kW) experiments will provide important information on antenna coupling and natural damping rates for each of the eigenmodes. This information will be used to determine the potential benefits of higher power experiments. If the natural eigenmode damping rates are small, there is the possibility of driving them to amplitudes where stochastic heating of thermal ions occurs.

NSTX-U Plasma Operation Start-Up Planning - Making the transition from engineering project management to operations engineering requires certain considerations. For example, sound project management will lead to the successful completion of a system to all of its technical requirements, but may not consider important concerns such as that system's operation in concert with other systems, staging the pre-operational and subsequent integrated system testing, establishing and controlling interrelated subsystem operating limits, maintaining interrelated safety interlock and equipment protection circuitry, maintaining configuration control during repairs/maintenance, proper analysis of hazards before beginning work, training and work authorizations for engineers/operators/technicians, managing personnel access to the various

experimental areas, defining expected personnel conduct while in these areas, and managing temporary modifications.

The NSTX-U project has addressed the above considerations with a network of administrative and technical procedures to assign operational roles, coordinate operations-related activities and machine configurations, and maintain a safe work environment. This includes the authorization of allowable operating parameters for a given machine configuration, and the system for the establishment/testing of all coil protection systems for those parameters.

The NSTX-U integrated system testing, commissioning, and start-up will follow the same process as the NSTX initial start-up in 1999, and each subsequent return to operations after an extended outage where machine upgrades were implemented. There are four components to NSTX-U post-construction start-up:

Activity Certification Committee (ACC) Review:

1. Operational Readiness Assessment (ORA)
2. Completion of sub-system preoperational testing (PTP's)
3. Run start-up procedure (OP-NSTX-02) including integrated system testing (ISTP)

The NSTX-U Activity Certification Committee (ACC), comprised of representatives from PPPL Engineering, Physics, Safety, and the DOE Princeton Area Office (PAO), reviews newly installed sub-systems and collateral devices with regard to personnel, environmental, and machine safety. The ACC will perform physical walk-downs of equipment and document reviews in developing a findings report to be submitted to the PPPL Deputy Director of Operations and the NSTX-U Operations Manager. After submittal of the ACC report and any associated open items, non-compliances or safety concerns, the PAO will conduct an Operational Readiness Assessment (ORA) before the project may move to start-up.

By this time, the sub-system cognizant engineers will have developed and are performing their pre-operational test procedures (PTP's). The NSTX-U Start-Up procedure (OP-NSTX-02) will coordinate and document the completion of the various sub-system PTP's, interlock and equipment protection test procedures, and all safety system checks. OP-NSTX-02 concludes with the NSTX-U Integrated System Test Procedure (ISTP-01) which establishes, tests, and documents the allowable NSTX-U operating parameters. ISTP-01 must be re-performed for any changes in those operating parameters.

We are formulating the operational plan toward full operational capability for NSTX-U. A draft plan is shown based on assessment of physics needs for first year of operations. The 1st year goal is to operate NSTX-U with the electromagnetic forces (I_pB_T) at halfway between NSTX and NSTX-U limits and 50% of the NSTX-U design-point of heating of any coil. This still allows

NSTX to operate at $B_T \sim 0.8$ T, $I_p \sim 1.6$ MA, and the maximum flat-top duration of 3.5 s in the first year which is far beyond the achieved NSTX parameters. The device will be inspected and refurbished as needed at the end of the each operating year. For the second year, the toroidal magnetic field will be increased to its full field value of 1 T but keeping the heating of the coil to 75% of the design-point of any coil. This will allow 3 sec discharges at full field and current. The same limits should allow the full 5 sec discharges at $B_T \sim 0.8$ T, $I_p \sim 1.6$ MA. The device will be brought to full operational capability in the third year of NSTX-U operation.

NSTX-U FY2014 Year End Report: Research Results

In FY2014, the NSTX-U research team contributed experimental data and analysis in support of the 2014 DOE Joint milestone*: "Conduct experiments and analysis to investigate and quantify the plasma response to non-axisymmetric (3D) magnetic fields in tokamaks. The effects of 3D fields can be both beneficial and detrimental and the research will aim to validate theoretical models in order to predict plasma response to varying levels and types of externally imposed 3D fields. The dependence of the response to multiple plasma parameters will be explored in order to gain confidence in the predictive capability of the models."*

The NSTX-U contributions to the 2014 Joint Milestone are described briefly above and also in a separate longer report. Summary descriptions of the results of research milestones are provided below. Descriptions of additional selected research highlights are also provided.

FY2014 Research Milestone R(14-1): Assess access to reduced density and collisionality in high-performance scenarios (Target - September 2014. Completed – September 2014)

Milestone Description: *The high performance scenarios targeted in NSTX-U and next-step ST devices are based on operating at lower Greenwald density fraction and/or lower collisionality than routinely accessed in NSTX. Collisionality plays a key role in ST energy confinement, non-inductive current drive, pedestal stability, resistive wall mode (RWM) stability, neoclassical toroidal viscosity that affects plasma torque balance, and plasma response and transport with 3D fields. Lower density and/or higher temperature are required to access lower ν*. Potential means identified in NSTX to access lower ν* included high harmonic fast wave heating, reduced fueling and/or Li pumping. However, while D pumping from lithium has been observed, additional gas fueling was typically required to avoid plasma disruption during the current ramp and/or in the high β phase of the highest performance plasmas of NSTX. The goal of this milestone is to identify the stability boundaries, characterize the underlying instabilities responsible for disruption at reduced density, and develop means to avoid these disruptions in NSTX-U. In support of this goal, tearing mode, RWM, neoclassical toroidal viscosity transport, disruption physics, and scrape-off-layer current (SOLC) in low density and collisionality will be investigated through analysis of NSTX data. This analysis will be used to project to NSTX-U scenarios and will include analysis of the potential impact of proposed/new non-axisymmetric control coils (NCC), and related research will also be carried out in other devices such as DIII-D, KSTAR, and MAST. These physics studies will be utilized to prepare for high-performance scenarios using methods such as current ramp-rate (li and q(r) evolution), H-mode transition timing, shape evolution, heating/beta evolution and control, optimized tearing mode and RWM control, rotation control, error field correction, fueling control (SGI, shoulder injector), and optimized Li pumping. This milestone will also aid development of MISK, VALEN, IPEC, and 3D transport models, as well as TRANSP and TSC integrated predictive models for NSTX-U and next-step STs.*

Milestone R(14-1) Report:

In order to assess access to reduced density and collisionality in high-performance scenarios in NSTX-U we endeavored to identify the stability boundaries in this parameter space by exploring a range of equilibrium scenarios in NSTX-U. Equilibria were computed with free-boundary TRANSP, and the no-wall and ideal-wall n = 1 stability limits are computed with the DCON code. Figure R14-1-1 shows one such exploration of n=1 stability vs. confinement multiplier and Greenwald fraction for a nearly 100% non-inductive NSTX-U case with fast ion diffusion of 0 m^2/s and $1 m^2/s$ [R14-1-1].

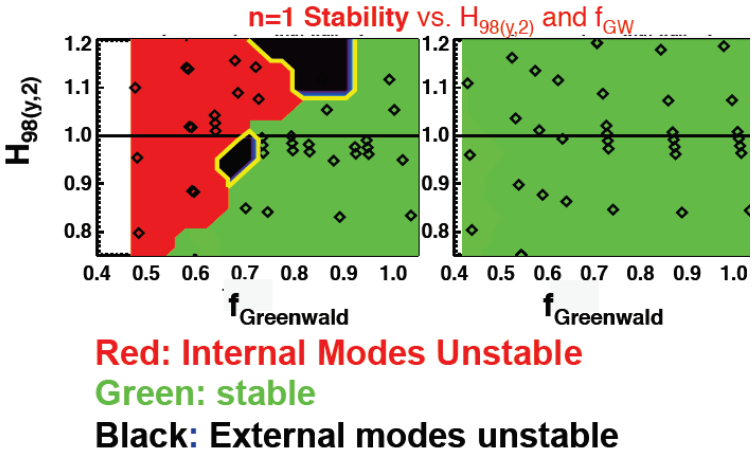

Figure R14-1-1. *n=1 stability vs. $H_{98(y,2)}$ confinement multiplier and Greenwald fraction for a nearly 100% non-inductive NSTX-U case with fast ion diffusion of a) 0 m^2/s and b) $1 m^2/s$. From Reference [R14-1-4].*

Another exploration of the stability boundaries at reduced collisionality was performed by examining the trends of resistive wall mode (RWM) stability with on collisionality, both through computation with the MISK code [R14-1-2] and through experimental observation of proximity to marginal stability [R14-1-3]. The experimental trend of stability as measured by resonant field amplification (RFA) via MHD spectroscopy from a database of NSTX discharges showed a general consistency with expectation from theory. Theory predicts that collisions have the competing effects of both dissipating mode energy and damping stabilizing kinetic effects [R14-1-2]. In the experiment, there was little change in RWM stability with collisionality for marginally stable plasmas [R14-1-3]. In contrast, plasmas which have a stabilizing resonance between rotation and ion motion can in theory benefit from a reduction in collisionality, which allows those resonant effects to be stronger. Correspondingly, as collisionality was reduced in the experiment for plasmas with greater stabilization by kinetic resonances, there was a decrease in RFA amplitude (indicating the plasma was becoming even more stable) [R14-1-3].

Additionally, the underlying instabilities that were primarily responsible for disruption at reduced density in NSTX were characterized. It was found that rotating MHD modes that slow and lock to the wall were the primary cause of disruptions at low density. In many experiments, it was observed and that disruptive early n=1 modes could be avoided by early gas fuelling that most likely resulted in modification of the edge temperature and therefore the resistivity [R14-1-4]. The timing and magnitude of fueling has a profound impact on discharge evolution, will be optimized in NSTX-U. Slower current ramps with the larger solenoid in NSTX-U may facilitate reduced fueling and the improved solenoid design and reduced error fields may further improve lower-density startup. Finally, the extra and/or more flexible torque deposition profile from the newly added neutral beam system on NSTX-U may reduce the prevalence of mode locking.

Analysis of such rotating MHD was carried out during FY2014 using the MARS-K code for modes observed early in the plasma current flat-top phase while the density was still relatively low. Figure R14-1-2a shows the onset of such an n=1 mode near t = 0.376s in shot 138065 with an effective/observed initial mode growth-rate $\gamma_{eff} \sim 1\ ms^{-1}$. This mode is in fact the second large n=1 mode to become unstable and then decay away early in this shot. Generally, the onset of such modes can lead to reduction in neutron rate, core rotation flattening, β saturation, and if driven too hard with high NBI heating power, can lead to β and more global rotation collapse, mode-locking, and disruption. The beam power is held constant at 3MW for the times shown in Figure R14-1-2, and prior to the onset of the n=1 mode at t = 0.376s, the β_N is rising approximately linearly in time after t=0.3s. Figure R14-1-2b shows that the n=1 instability does not lead to disruption for this particular shot, but rather leads to saturation in the β_N (thick black line) from t = 0.376s to t ~ 0.45s until the mode amplitude is less than ~1G (measured at the vessel wall) and energy confinement is apparently improved and β_N again begins to rise.

The β_N limit for an n=1 rotating ideal kink stabilized by a conducting wall ("ideal wall mode" - IWM) [R14-1-5] in the limit of low rotation is shown by the solid green curves in Figure R14-1-2b. Interestingly, the predicted values for marginal stability are approximately a factor of two higher (β_N = 7-8) than the experimentally observed marginal β_N values ~ 3.5 at mode onset. (Note that the dashed curves in this figure are the corresponding no-wall limits.) The solid orange

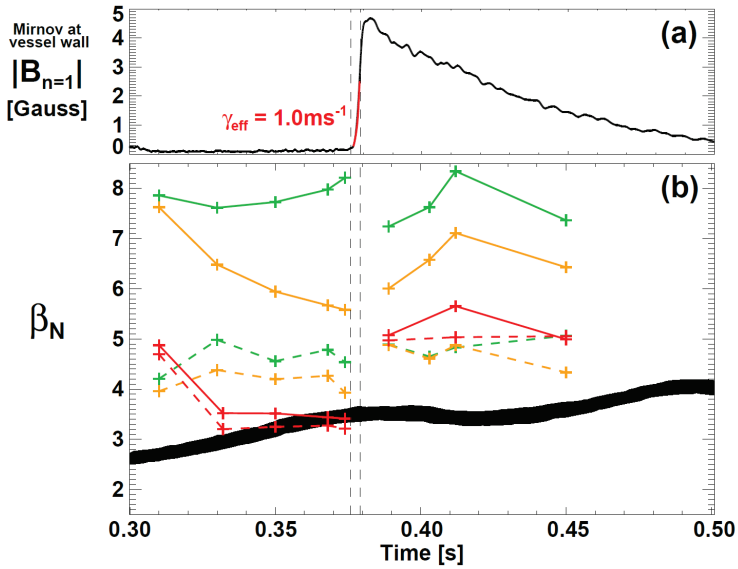

Figure R14-1-2. *(a) Mirnov amplitude of an n=1 mode during the early flat-top phase of shot 138065, (b) time history of experimental β_N (black), β_N limits from MARS-K with conducting-wall (solid) and no-wall (dashed) at low rotation and ideal plasma (green), experimental rotation and ideal plasma (orange), and experimental rotation with kinetic thermal and NBI fast-particle distributions (red).*

curves in Figure R14-1-2b show the IWM β_N limit including plasma rotation, and it is found that the rotation and/or rotation-shear is systematically destabilizing with a $\Delta\beta_N$ and as large as -2 and marginal β_N value ~ 5.5 at mode onset. The solid red curves in Figure R14-1-2b show the IWM β_N limit including plasma rotation and a slowing-down distribution for NBI fast-ions in the calculation of the MARS-K kinetic pressure, and the predicted marginal β_N value ~ 3.4-3.5 just prior to mode onset is in good agreement with the observed value. The measured and predicted mode frequencies (f ~ 26kHz) just prior to mode onset are also in good agreement (not shown) only if the plasma rotation and NBI slowing-down distribution are included.

SXR analysis finds that the mode can be characterized as kink/IWM for the first 0.5-1ms after mode onset, but at later times the mode has a tearing-mode/island structure. Thus, it appears that rotation and fast-ion effects reduce the ideal-wall limit, and tearing modes are triggered as the β_N is increased toward the reduced limit. It is also noteworthy that by 10-15ms after mode onset, all calculated IWM limits shown in Figure R14-1-2b are above the experimental β_N value. From this we infer the kink-triggered tearing mode modifies the equilibrium profiles in such a way that IWM limits are not subsequently exceeded while the tearing mode is present, and this may explain in part why this tearing mode can slowly decay rather than cause a larger disruption. These analysis results are consistent with observations that higher fueling and density can help stabilize such modes, since higher density reduces the toroidal rotation and rotation shear at fixed NBI torque and power, and higher density also reduces the fast-ion pressure fraction.

Tools to avoid low density or collisionality disruptions in NSTX-U must be developed. In support of this goal efforts were made to consider both density and rotation control schemes. First, for density control, real-time density measurements via the FIReTIP diagnostic will be utilized, along with supersonic gas injection, and the addition of a cryo-pump in later years. For rotation control, it is necessary to understand neoclassical toroidal viscosity (NTV) at low collisionality, as well as exploring how 3D fields from the present mid-plane coils or future non-axisymmetric control coils (NCC) can reduce plasma rotation.

Previous studies already showed that the core-to-edge NTV ratio could be varied by an order of magnitude with either partial or full NCC coil sets in NSTX-U, and more precise calculations performed this year with PENT code and new targets also confirmed this prediction. The capability of NTV variability can become even greater if the existing midplane coils are combined with the NCC. In order to fully investigate the large number of possibilities with all the coils, stellarator optimizers were coupled to IPEC-PENT and used to search the optimized field configuration without coil constraints (see also the NCC section of the 3D field research in the Macroscopic Stability chapter). The study shows that core or edge NTV inside the pedestal can be driven most efficiently when the perturbations are orthogonal to the field lines, and that the presently designed partial NCC combined with the midplane coils can produce a similar configuration, demonstrating the advantages of the present NCC design at the fundamental level.

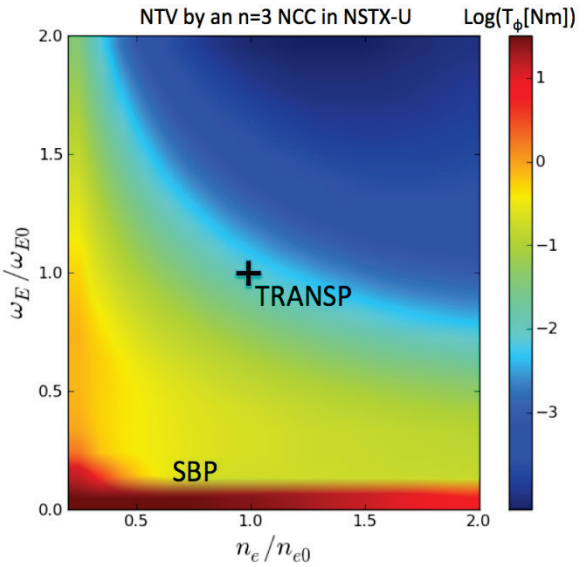

Figure R14-1-3*. NTV prediction by IPEC-PENT when an optimized n=3 NCC configuration is used and kinetic profiles are varied from nominal TRANSP runs. SBP marks roughly the level of rotation and density where SBP behavior is expected.*

The optimized NCC is expected to be an even more powerful tool for rotation control in the regime of the reduced collisionality. As illustrated in Figure R14-1-3, IPEC-PENT calculations show that the substantial enhancement of NTV is expected when the density is reduced while keeping thermal pressure constant, and also that the superbanana plateau (SBP) regime can be reached only by 20~30% reduction of the density if the rotation level is sufficiently low. Similar predictions can be made, generally in a number of other field configurations possible by NCC and midplane coils, which will be tested in NSTX-U and utilized in the rotation control system by combining appropriate the input torque and momentum diffusion/pinch models.

References

[R14-1-1] S.P. Gerhardt et al., Nucl. Fusion **52**, 083020 (2012)
[R14-1-2] J.W. Berkery et al., Phys. Rev. Lett. **106**, 075004 (2011)
[R14-1-3] J.W. Berkery et al., Phys. Plasmas **21**, 056112 (2014)
[R14-1-4] S.P. Gerhardt et al., Nucl. Fusion **53**, 043020 (2013)
[R14-1-5] J.E. Menard et al., "Rotation and Kinetic Modifications of the High-beta Tokamak Ideal Wall Limit", submitted to Phys. Rev. Lett. (2014)

FY2014 Research Milestone R(14-2): Develop models for *AE mode-induced fast-ion transport (Target - September 2014. Completed – September 2014)

Milestone Description: *Good confinement of fast ions from neutral beam injection and fusion reactions is essential for the successful operation of ST-CTF, ITER, and future reactors. Significant progress has been made in characterizing the Alfvénic modes (AEs) driven unstable by fast ions and the associated fast ion transport. However, models that can consistently reproduce fast ion transport for actual experiments, or provide predictions for new scenarios and devices, have not yet been validated against a sufficiently broad range of experiments. In order to develop a physics-based parametric fast ion transport model that can be integrated in general simulation codes such as TRANSP, results obtained from NSTX and during collaborations with other facilities (MAST, DIII-D) will be analyzed. Information on the mode properties (amplitude, frequency, radial structure) and on the fast ion response to AEs will be deduced from Beam Emission Spectroscopy, Reflectometers, Fast-Ion D-alpha (FIDA) systems, Neutral Particle Analyzers, Fast Ion Loss Probes and neutron rate measurements. The fast ion transport mechanisms and their parametric dependence on the mode properties will be assessed through comparison of experimental results with theory using both linear (e.g., NOVA-K) and non-linear (e.g., M3D-K, HYM) codes, complemented by gyro-orbit (ORBIT) and full-orbit (SPIRAL) particle-following codes. Based on the general parametric model, the implementation of reduced models in TRANSP will then be assessed. For instance, the existing Anomalous Fast Ion Diffusion (AFID) and radial fast ion convection models in TRANSP could be improved by implementing methods to calculate those transport coefficients consistently with the measured (or simulated) mode properties. Further improvements will also be considered, for instance to include a stochastic transport term or quasi-linear models.*

Milestone R(14-2) Report

Significant progress has been made during FY-14 to develop and validate reduced models for AE-induced fast ion transport. Two complementary approaches have been developed to compute the fast ion response to a given set of instabilities, namely through quasi-linear theory and via a reduced, "probabilistic" model for fast ion evolution in phase space.

The fist approach is based on the 1.5-dimensional quasi-linear theory of energetic particle profile relaxation following radial transport induced by instabilities [R14-2-1]. A *critical gradient* model (CGM) has been implemented to reconstruct the radial fast ion profile which leads to a balance between the mode's drive, proportional to the local radial gradient, and damping mechanisms from interaction with the background plasma [R14-2-2]. Linear mode properties are computed through the NOVA-K code and used as input to the model to extract the spatially-varying critical gradient, from which the radial profile is computed. Initial validation work has been performed in collaboration

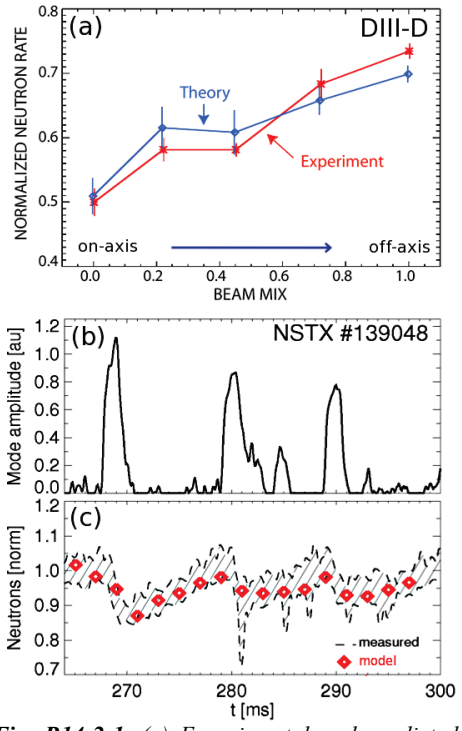

Fig. R14-2-1. *(a) Experimental and predicted (through CGM model) neutron rate on DIII-D for different mixes of NB injection. (b-c) Neutron rate prediction via the "kick" model for a NSTX discharge with bursting TAE avalanches.*

with DIII-D, exploiting the different combinations of on- and off-axis Neutral Beam (NB) injection available on DIII-D. Results show good agreement between the CGM model and experiments, for instance in terms of predicted neutron rate [R14-2-3], see Fig. R14-2-1a. Additional dedicated experiments have been performed during the FY14 DIII-D National Campaign for further validation of the model. In addition, the CGM model is now being tested for NSTX scenarios featuring weakly chirping TAE modes which eventually end up in a large burst (or *avalanche*). A specific goal of the ongoing validation work for NSTX plasmas is to explore the range of validity of the model. For example, the concept of "critical gradient" may not apply to transient events such as avalanches, which can happen on time scales much shorter than the typical evolution time of the fast ion distribution. Inclusion of the CGM model in TRANSP will be considered after completion of the validation work.

A second approach employs a probability distribution, $p(\Delta E,\Delta P_\zeta)$, to advance an ensemble of particles in phase space coordinates following a MonteCarlo scheme [R14-2-4]. (Here E and P_ζ are energy and toroidal angular momentum of the fast ions). Under the effects of resonant instabilities, fast ions suffer correlated variations (or "kicks") in energy and P_ζ, which are described by p. The probability p can be computed via simulations with particle-following codes such as ORBIT, or (when available) directly from theory. Experimental data on mode amplitude, for instance from reflectometers or Mirnov coils, are used to rescale p as the discharge evolves. So far, the model has been successfully verified against complete ORBIT simulations, and then applied to NSTX scenarios with strong TAE avalanches. For these initial tests, a stand-alone version of the NUBEAM module of TRANSP has been used. Results confirm that TAE avalanches can indeed cause a large redistribution of fast ions (see Section on Energetic Particle Physics Results). Redistribution happens primarily in energy, with only modest particle losses from the core plasma. Nevertheless, the net energy loss from the fast ions to the modes is capable of producing a significant drop in the neutron rate, consistent with experimental results, see Fig. R14-2-1(b-c). Moreover, since TAE resonances mostly affect strongly co-passing fast ions, noticeable effects are also observed on the NB-driven current profile, which is depleted in the central plasma region thus affecting the overall NB current drive efficiency. The capability of the model to discriminate between fast ions based on their phase space coordinates represents a significant improvement with respect to the crude diffusive/convective transport models presently implemented in TRANSP. The "kick" model is being implemented in the NUBEAM module of TRANSP, and it will be used to quantitatively assess AE effects on fast ion confinement and NB current drive for both NSTX and (predicted) NSTX-U scenarios with different levels of AE activity.

References

[R14-2-1] N. Gorelenkov et al., Nucl. Fusion **45**, 226 (2005)
[R14-2-2] K. Ghantous et al., Phys. Plasmas **19**, 092511 (2012)
[R14-2-3] W. W. Heidbrink et al., to be presented at the 25th IAEA Fusion Energy Conference (St. Petersburg RU, Oct. 2014)
[R14-2-4] M. Podestà et al., Plasma Phys. Control. Fusion **56**, 055003 (2014)

FY2014 Research Milestone R(14-3): Develop advanced axisymmetric control in sustained high performance plasmas (Target - September 2014. Completed – September 2014)

Milestone Description: *Next step tokamaks and STs will need high-fidelity axisymmetric control. For instance, magnetic control of the plasma boundary and divertor impact the global stability, power handling, and particle control from poloidally localized pumps. Control of the current and rotation profiles will be critical for avoiding resistive wall modes and tearing modes, thus maximizing the achievable β. The 2nd neutral beamline for NSTX-U will provide considerable flexibility in the neutral beam driven current profile, while additional divertor coils will allow a wide range of divertor geometries; it is thus an appropriate facility for the development of these critical control techniques. As part of this milestone, realtime control algorithms for the snowflake divertor will be designed; these will likely use methods for rapid tracking of multiple X-points, and additions will be made to the ISOFLUX boundary control algorithm to target specific divertor quantities for control. These divertor control algorithm will be prepared for use in NSTX-U, and may be tested in DIII-D. For profile control, a real-time Motional Stark Effect diagnostic will be developed for NSTX, and the data provided to the NSTX-U implementation of rtEFIT for constrained reconstruction of the current profile; the feasibility of real-time rotation measurements in NSTX-U will be determined and that system implemented as appropriate. Real-time control algorithms will be developed for the current profile using the various neutral beams as actuators; integrated modeling of the current profile evolution with codes such as PTRANSP and TSC will be used for system identification. Similarly, algorithms for control of the rotation profile will be developed, using the neutral beams and magnetic braking as actuators. This profile control development may be based on existing DIII-D control algorithms, but with NSTX-U specific constraints. The ability of the proposed non-axisymmetric control (NCC) coils to provide improved actuator capability for rotation control compared to the existing mid-plane coils will be addressed using NTV calculations. The feasibility of simultaneous rotation, current, and β control will be assessed. This research will provide a considerable head start developing the required control algorithms for NSTX-U, as well as provide valuable guidance on the axisymmetric control designs for next-step tokamaks and STs, including ITER.*

Milestone R(14-3) Report:

Research in support of the R14-3 milestone can be divided into a 4 topical areas: i) model based β_N+l_i control and β_N+q_0 control using TRANSP as a "flight simulator", ii) model based full q-profile control development, iii) model based rotation profile control development, and iv) studies of the neoclassical toroidal viscosity (NTV) from the proposed NCC coils. These topics will be discussed in that order below.

R14-3, Topic #1: Model Based Control using TRANSP as a Flight Simulator

While modern control algorithms are typically developed from reduced models of the underlying physical process, it is advantageous to use full physics models to test the final control design. However, the creation of these full-physics models is typically outside the scope of a control development task. In order to circumvent this dilemma, a method of using the existing full-physics models in the TRANSP [R14-3-1] code as a "flight simulator" has been developed.

In these studies, the "expert file" mechanism within TRANSP is used. In this method, previously used for debugging new physics models in TRANSP, external blocks of FORTRAN code can be

called at appropriate times during the execution of TRANSP. These blocks of code can modify internal code variables, and in this way, be used to execute control loops.

In the example tested during this period, a combined β_N+q_0 controller has been developed. This controller uses two PID loops, with one loop actuating the neutral beam power to adjust β_N and the other actuating the outer plasma-wall gap to adjust q_0 [R14-3-2]. Both of these control loops, as well as code to automatically scale the electron temperature to achieve the correct H_{98} in the presence of heating power and density variations, are contained within the expert file.

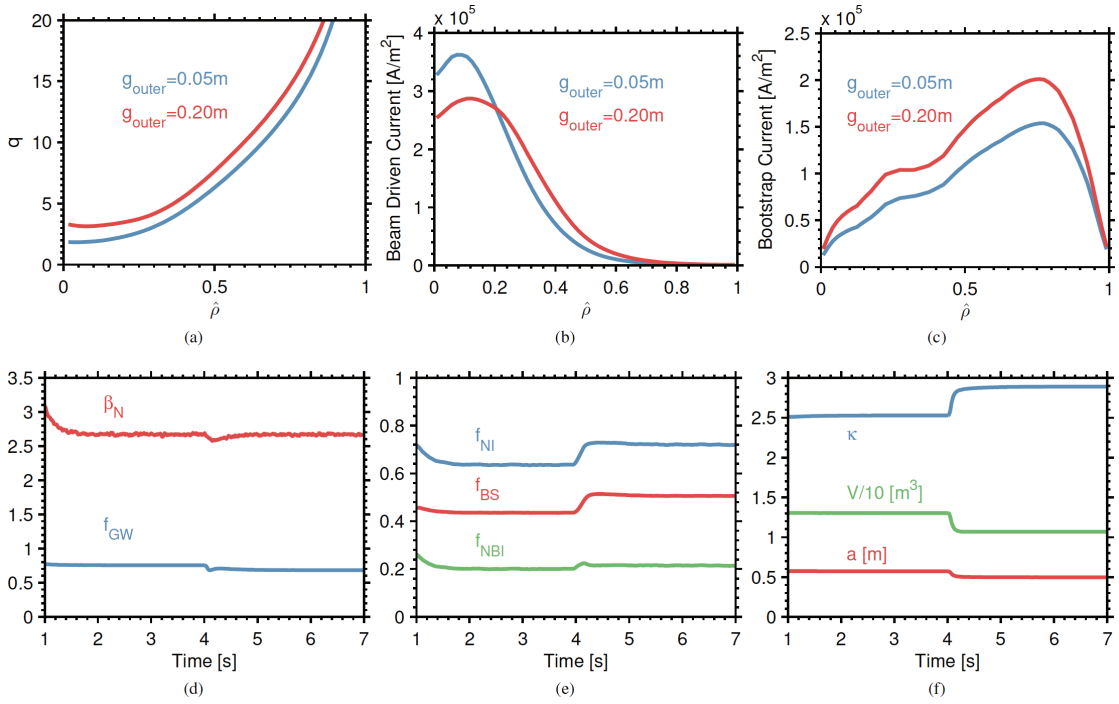

Fig. R14-3.1*: Examples of controlling q_0 and β_N using the beam power and outer gap as actuators. In frames a) and b), the targets are shown in red, while the results of the closed loop TRANSP control simulation are shown in blue.*

An example use of this controller is shown in Fig. R14-3.1. As can be seen by inspecting the red traces in frames a) and b), there are step changes requested in both the values of q_0 and β_N. These changes in the requests are matched by the TRANSP computed evolution in the plasma quantities, shown in blue; note that q_0 responds on the current diffusion time scale, while β_N responds on the much faster energy confinement time scale. These changes in β_N and q_0 are driven by the changes in the requested outer gap and input power, as shown in frames d) and e). This example shows that TRANSP is now fully functional as a tool for control development.

This critical capability will continue to be used to further refine this particular control capability. Furthermore, it will be applied to many of the other control development tasks in the coming period, including full current profile control, rotation profile control, and future efforts in shape control. In this way, control development exercises can continue to benefit from updates to the physics models in TRANSP.

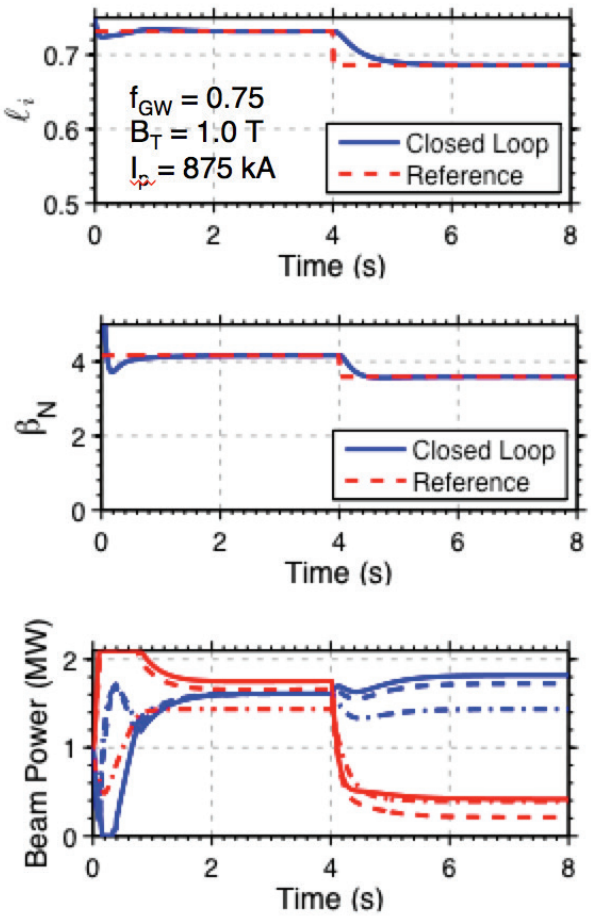

Fig R14-3.2: *Example of combined β_N+l_i control. Shown are (top) l_i, (middle) β_N, and (bottom), the powers of individual beams.*

In addition to this work, reduced models for the current profile evolution in NSTX have been developed (see next section for more descriptions of these models). It is anticipated that the first year of NSTX-Upgrade operations will not have MSE-constrained rtEFITs; hence, while detailed q-profile data will not be available in realtime, reasonable realtime β_N and l_i measurements should be available (these parameters being independently calculable from the equilibrium of a shaped plasma [R14-3-3]). As a consequence, these reduced models have been used to construct a β_N+l_i controller; this choice is also highly appropriate given the strong role that l_i plays in determining the vertical stability of the configuration. This controller will use a Kalman filter observer to determine l_i, using data from the available rtEFITs as well as models for the current profile evolution. An example of these simulation results is shown in Fig. R14-3.2, using the reduced model, Kalman filter, and control scheme implemented in MATLAB. Step changes in β_N and l_i can be accommodated by changing which beams are active, as shown in the bottom frame. Future research will determine the range of simultaneous control of these variables given the available actuator constraints, as a function of background parameters such as the plasma current and toroidal field.

Note that this work was done by ORISE post. doc. Mark Boyer, who is assigned to PPPL.

R14-3, Topic #2: Full Current Profile Control Development

An ultimate goal of the NSTX-Upgrade physics program is to implement full control of the current profile using actuators such as the neutral beams, plasma density, plasma β, and boundary shape. In order to progress towards this goal, a study of full current profile control has been undertaken by Lehigh University researchers (Prof E. Schuster and students) under a subcontract with PPPL.

In these studies, a reduced models for all the relevant processes in the current diffusion process are considered [R14-3-4, R14-3-5]. These include physically realistic models for the bootstrap current [R14-3-6], neutral beam current drive, and plasma resistivity, consistent with transport expectations. These models are formed in such a way that they can be easily manipulated to form control oriented models, e.g. the spatial and temporal parts of the models can be cleanly separable. These models are then used to form a linear-quadratic-integral (LQI) controller for the current profile, using the neutral beams and plasma current as actuators. In particular, the variable $\theta(\hat{\rho},t) = \partial\psi/\partial\hat{\rho}$ is used as the controlled variable, where ψ is the poloidal flux and $\hat{\rho}$ is the normalized minor radius. This can be directly related to the safety factor profile as $q(\hat{\rho},t) = B_{\phi,0}\rho_b^2\hat{\rho}/\theta(\hat{\rho},t)$, where ρ_b is the minor radius of the last closed flux surface. These reduced models and controllers are implemented in MATLAB for the examples provided below; inclusion of these controllers in the TRANSP flight-simulator mode will be done in the future.

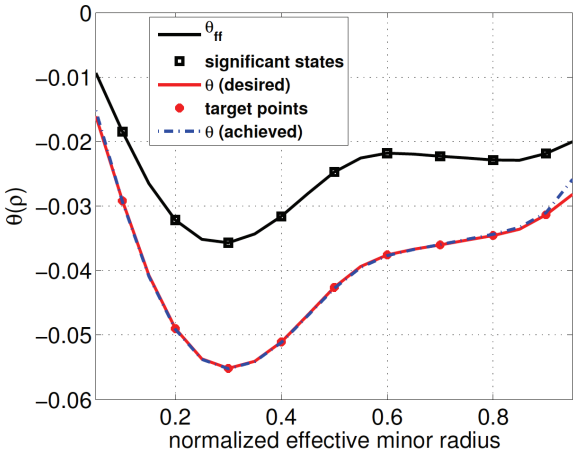

Fig. R14-3.3: *Feedforward, target, and achieved profiles of the controlled variable $\theta(\hat{\rho})$.*

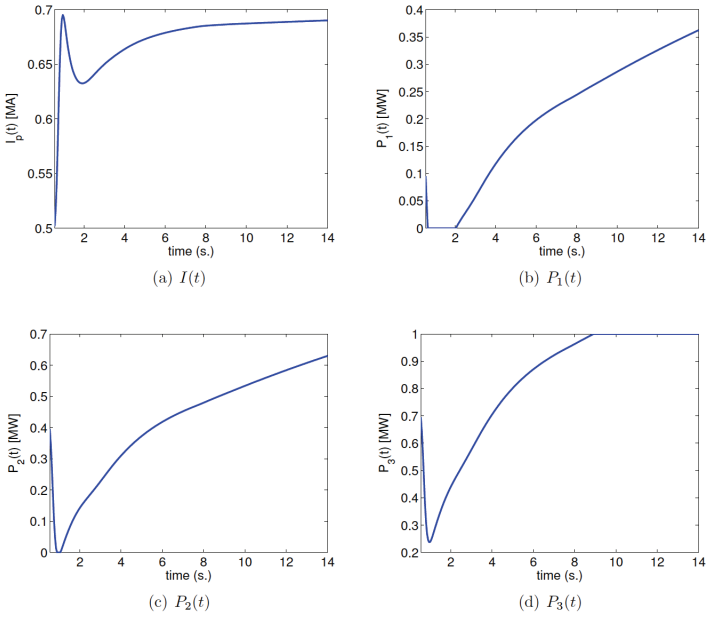

Fig. R14-3.4: *Time evolution of the plasma current and three (of six) neutral beam powers, determined by the feedback controller in order to achieve the target $\theta(\hat{\rho})$ profile in Fig. R14.3-3.*

Numerous numerical studies have been completed to demonstrate the proper functioning of this control scheme; a few examples are presented here. In the first example, a pre-programmed (feed-forward, or ff) trajectory of the beam heating powers and plasma currents is used to define a feed-forward $\theta(\hat{\rho})$ profile at the end of the simulation period (t=14 s); this is the profile that would be achieved in the absence of feedback, and is shown in black in Fig. R14-3.3. This feedforward case has a plasma current of I_P =500 kA. A target $\theta(\hat{\rho})$ profile is also defined, which the feedback algorithm tries to achieve; this target case has a plasma current of I_P=700 kA.

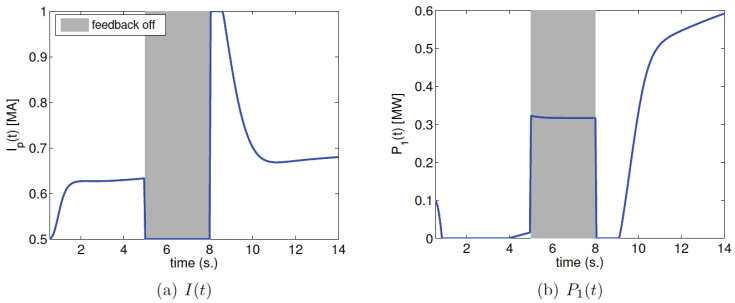

(a) $I(t)$ (b) $P_1(t)$

Fig. R14-3.5: *Time evolution of the plasma current and first neutral beam power, for the simulation where control is frozen for 5<t<8.*

Fig. R14-3.4 shows the trajectories of the plasma current and three (of six) neutral beam powers, determined by the feedback controller to achieve the target value of the $\theta(\hat{\rho})$ profile. The controller sends the plasma current towards the target value of 700 kA, and adjusts all the beam powers. The resulting $\theta(\hat{\rho}, t = 14\ s)$ profile is shown as a dashed blue line in Fig. R14.3-3, closely matching the target and demonstrating the capabilities of the controller.

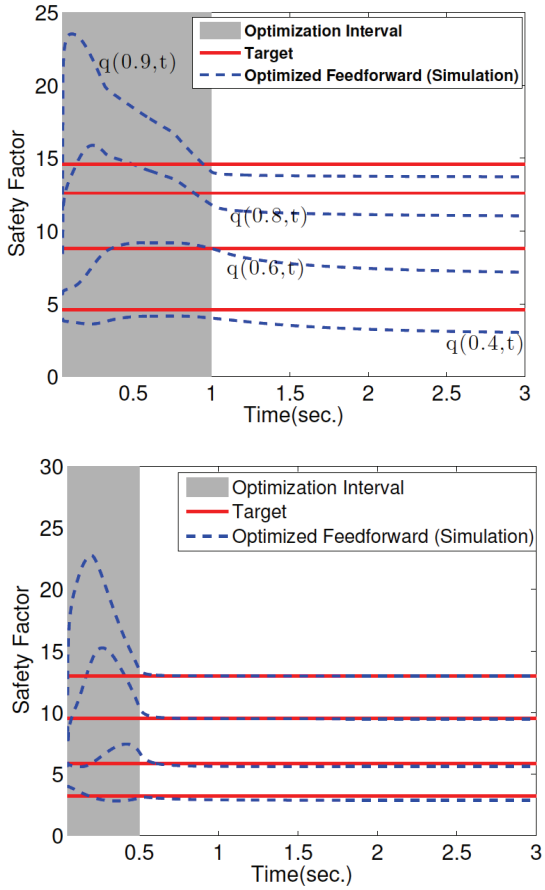

Fig. R14-3.6: *Time evolution of the safety factor at 4 locations, under (top) the constraint to achieve a given target by 1 s, and (bottom) the constraint to achieve the target state within 0.5 seconds and achieve stationarity afterwards.*

As a second demonstration, the same target $\theta(\hat{\rho})$ profile and feedforward trajectories were used, but the feedback control was turned off during the phase 5< t [s]<8. The resulting evolution of the plasma current and first neutral beam power are shown in Fig. R14-3.5. The controller progresses along trajectories similar to the previous example, until control is turned off. When control is turned back on, the controller rapidly responds to the deviations that occurred during the control-off phase, and rapidly brings the equilibrium back to the target. The final actuator states are very close to those achieved in the case without the control pause, and the final $\theta(\hat{\rho})$ is close to the target, indistinguishable from the blue dashed curve in Fig. R13-4.3. This demonstrates the robust disturbance rejection capabilities of the controller.

Finally, the control-oriented models developed as part of this study can be used to optimize the development of high performance scenarios for NSTX-U, by defining optimal feed-forward actuator trajectories. A Sequential Quadratic Programming (SQP) technique is used to optimize the trajectories, with constraints on the degree to which the target state is achieved and the proximity of the state to stationarity.

As an example of this capability, the optimizer has been configured to achieve a target q profile by 1 second, with no constraint on stationarity. The results are shown in the top frame of Fig. R14-3.6, where the target q-profile is nearly achieved in the desired time, though the result continues to evolve due to lack of a stationarity constraint. On the other had, the example in the bottom frame shows an example where the optimizer is configured to achieve the given q-profile within 0.5 s, with a further weight on stationarity. This goal is admirably achieved.

As noted above, future work in this area will involve incorporating TRANSP in closed loop simulations with these control techniques. The implementation of these controllers in the plasma control system (PCS) will be defined, and the feedforward optimization techniques will be tested against NSTX-U data.

R14-3, Topic #3: Rotation profile control

The rotation profile plays a critical role in determining the transport level and stability of the plasma to large disruptive MHD modes such as the resistive wall mode [R-14-3-7, R14-3-8] and neoclassical tearing mode [R14-3-9, R14-3-10]. As a consequence, the control of the rotation profile is an important topic. This has been addressed via a collaboration between the Princeton University (PU) Mechanical and Aerospace Engineering group led by Prof. C. Rowley, PPPL, and the NSTX-U Columbia University collaboration, with PU graduate student Imene Goumiri leading the effort. The neutral beam torque and, uniquely, neoclassical toroidal viscosity (NTV) [R14-3-11, R14-3-12, R14-3-13] from 3D coils are used as actuators in this rotation control study.

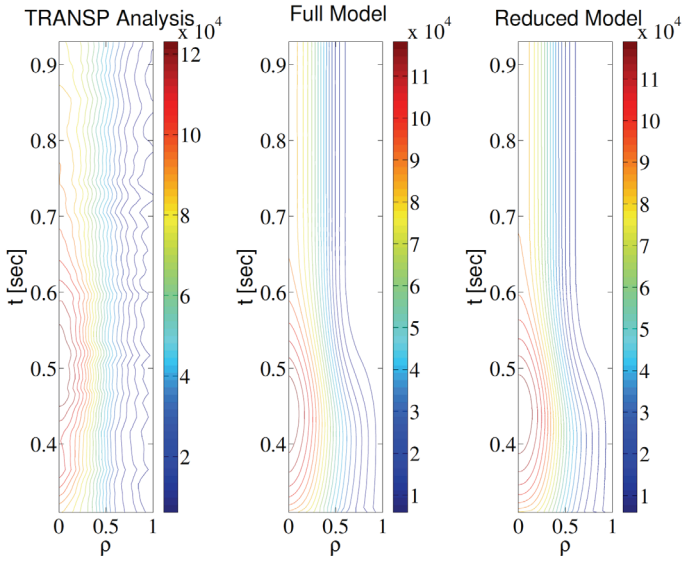

Fig. R14-3.7*: The time evolution of the rotation profile is shown, under three different analysis techniques. See text for details.*

As for the current profile control studies, the control development begins with reduced models for the relevant physical processes and actuators. The neutral beam torque is broken into a spatial part and a temporal part, with the temporal action including the effect of the fast particle slowing down time. The NTV model includes both a spatial profile function, an amplitude function proportional to the square of the 3D coil current, and a dependence on the rotation frequency, the latter of which introduces interesting non-linearities into the system. The perpendicular momentum diffusivity profile (χ_ϕ) is taken from an NSTX discharge. The toroidal momentum diffusion

equation [R14-3-14] is simplified by eliminating terms that are unimportant to this problem, and then further reduced using a Bessel function decomposition in order to make it more amenable for control development.

Fig. R14.3-7 shows the results of this model reduction exercise. The left frame shows the rotation profile for an NSTX discharge, as processed by TRANSP in analysis mode. The center frame shows the model prediction solving the simplified momentum diffusion equation before Bessel function reduction, using the model diffusivity profile and beam torque model. While the dynamics are not exactly the same between the left and center frames, the profile shapes and magnitudes are quite comparable. The differences are due to effects not present in the model, for instance, MHD instabilities that damp the rotation transiently. The right frame shows the solution of the reduced model with four Bessel modes, and it is clear that only four modes are required to reproduce the dynamics of the system.

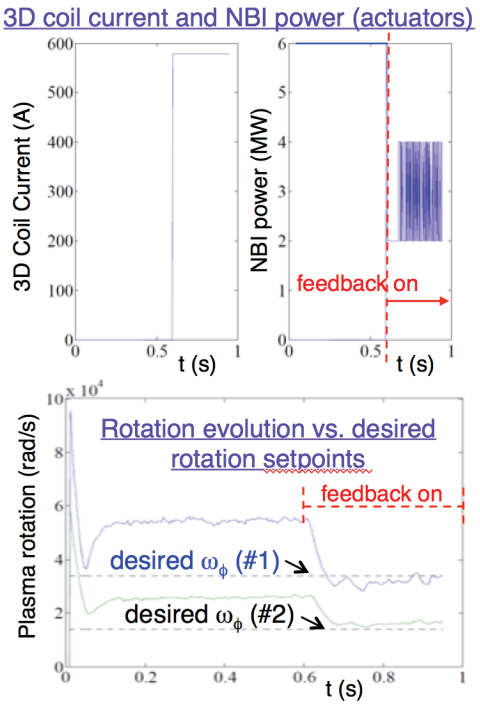

Fig. R14-3.8: *Example of rotation profile control with neutral beam modulation as the actuator. The pre-programmed 3D coil current, producing NTV, is shown on the top left. The neutral beam power is shown in the upper right. The plasma rotation at the two locations is shown in the bottom frame, and quickly approaches the target values once feedback is turned on.*

Having demonstrated the utility of the reduced model, control design has been completed using the NSTX actuators. The plasma state is estimated using a Kalman filter and an integrator with anti-windup control is implemented in a Linear Quadratic Regulator (LRQ) control scheme. An example of rotation control at two points on the profile is shown in Fig. R14.3-8, when the closed loop simulation is implemented in MATLAB.

In this case, a pre-programmed pulse of n=3 currents is imposed at t=0.6 s, resulting in an NTV torque on the plasma. The desired rotation values are shown in the bottom frame, with the rotation substantially faster than desired before control is turned on. When feedback is applied at t=0.6 s, the neutral beam power is immediately reduced by the controller, resulting in the plasma rotation dropping to values near the desired set points. This demonstrates the effective nature of the proposed control scheme.

Future work will involve implementing these control schemes within the TRANSP expert file framework, so that the control can be simulated with full physics models. Additionally, the models will be updated to include the NSTX-Upgrade actuators and beam modulation constraints. The final results of this study will be a rotation control design appropriate for implementation on NSTX-U.

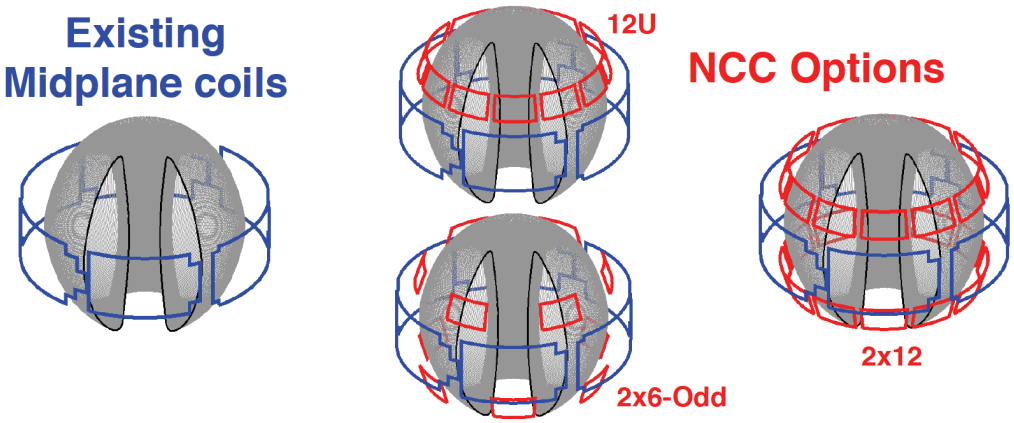

Fig. R14-3.9: *Images of the existing midplane coils in NSTX, and three potential options for the NCC coils.*

R14-3, Topic #4: NTV from the Existing Midplane Coils and the Proposed NCC Coils

The rotation control development, as well as NSTX experience [R14-3-8], has clearly demonstrated the utility of NTV for controlling the plasma rotation profile. However, it is known that different coils sets, and the excitation of different toroidal mode numbers in the applied 3D fields, can produce different levels and profiles of NTV torque. In this study, we assess the different NTV capabilities of the existing midplane coils and various potential configuration of the proposed non-axisymmetric control coils (NCC). Fig. R14-3.9 shows various examples of the coil options, with the 12U (12 coils in the upper location) and 2x6-Odd (6 coils upper and lower, staggered toroidally) configurations designed as intermediate steps in a phased implementation of the full 2x12 option; the existing midplane coils will be referred to as the MID coils below. This work was executed as a collaboration between PPPL and the NSTX-U Columbia University collaboration.

The first figure of merit under consideration is related to the ability to apply non-resonant n=1 fields (useful for rotation control), while not applying resonant n=1 fields (which tend to drive locked modes and can lead to disruptions). Here, the non-resonant n=1 field is quantified by the NTV torque that is applied while the resonant part is indicated by the resonant field components squared. This yields a figure of merit

$$F_{N-R} = T_{NTV} / \sum_{\psi_{N<0.85}} \partial B_{nm}^2$$

It is desirable to scan a large range in this quantity, to provide experimental flexibility, while also providing a large maximum value of $F_{N\text{-}R}$ in order to provide rotation control with n=1 fields without leading to dangerous locked modes.

Fig. R14-3.10 shows this quantity for a range of 3D field configuration. The $F_{N\text{-}R}$ from the known PF-5 non-circularity and the midplane coils (MID) are shown on the left, and provide a baseline level for consideration. The 12U configuration produces a single $F_{N\text{-}R}$ value that is not particularly different than the existing MID coil. However, the 2x6 odd configuration produces a range of $F_{N\text{-}R}$ values, depending on the toroidal phase difference between the n=1 fields applied by the upper

and lower coil rows, and has a maximum value much larger than for the MID coils. The full 2x12 coil set has a similar range of possible $F_{N\text{-}R}$. Hence, we infer that for rotation control with n=1 fields, the 2x6 and 2x12 options are of similar viability, and both are far better than the existing MID coils.

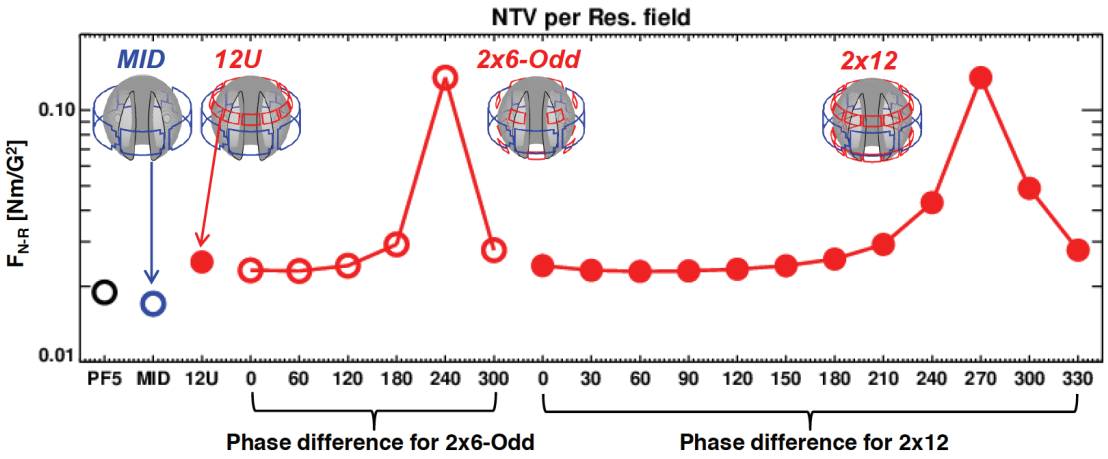

Fig. R14-3.10: *The quantity $F_{N\text{-}R}$ as a function of various 3D field configurations. See text for further details.*

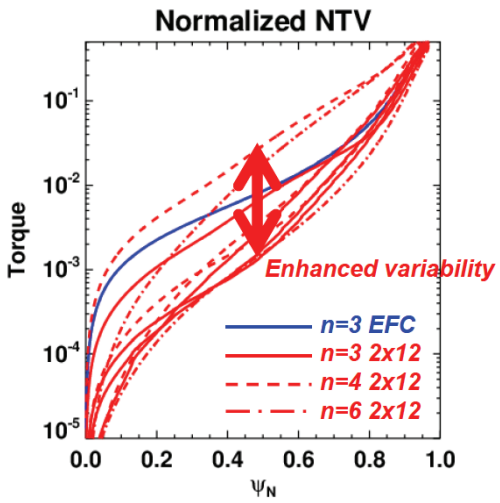

Fig. R14-3.11: *NTV torques normalized to unity at the edge, for a range of applied 3D fields. Blue shows the n=3 profile from the MID coils, while red shows various possibilities with the full 2x12 NCC coils. See text for further details.*

A second comparison can be made of the ability to apply n>2 fields for rotation control. This is shown in Fig. R14-3.11, where a large number of NTV profiles (in particular, the volume integral of the NTV torque density starting from the magnetic axis) have been normalized to unity at the edge. The blue curve shows the profile for the existing MID profiles. The red curves show various possible profiles created by the 2x12 NCC coil. It is clear that by varying the toroidal mode number and toroidal phase between the upper and lower coils, it is possible to create a large range of torque profiles with the full NCC coils. This capability, if implemented on NSTX-U, will provide an important additional actuator for controlling the rotation and rotation shear in the outer portion of the plasma.

ITER and FNSF Implications

These studies have a number of important implications for next step fusion devices. The development of control within the TRANSP framework allows sophisticated control models to be developed with minimal physics model development on the part of the control engineer. TRANSP is already used for many ITER simulations [R14-3-15, R14-3-16, R14-3-17], and so this opens an avenue for advanced ITER control development. Current profile control will be critical for ensuring the stability of ITER steady state scenarios, and the control work done for NSTX will contribute to the physics basis and confidence level for these control techniques. Finally, control of the rotation profile will be important for next step devices, especially if they are operating a high β. ITER will be equipped with 3D field coils, and this control development is opening up new means of controlling the rotation profile in that device.

References

[R14-3-1] R. J. Hawryluk, et al., "An Empirical Approach to Tokamak Transport", in Physics of Plasmas Close to Thermonuclear Conditions, ed. by B. Coppi, et al., (CEC, Brussels, 1980), Vol. 1, pp. 19-46.
[R14-3-2] S.P. Gerhardt, et al., Nuclear Fusion **52**, 083020 (2012).
[R14-3-3] L.L.Lao, et al., Nuclear Fusion **25**, 1421 (1985).
[R14-3-4] Y. Ou, et al., Fusion Engineering and Design **82**, 1153 (2007).
[R14-3-5] J. E. Barton, et al., "Physics based Control-oriented Modeling of the Safety Factor Profile Dynamics in High Performance Tokamak Plasmas", *52nd IEEE Conference on Decision and Control*, pp. 4182-4187, 2013.
[R14-3-6] O. Sauter, et al., Phys. Plasmas **6**, 2834 (1999).
[R14-3-7] J.W. Berkery, et al, Phys. Rev. Lett. **104**, 035003 (2010).
[R14-3-8] S.A. Sabbagh, et al., Nuclear Fusion **50**, 025020 (2010).
[R14-3-9] S. P. Gerhardt, et al., Nuclear Fusion **49**, 032003 (2009).
[R14-3-10] Y. Park, et al., Nuclear Fusion **53**, 083029 (2013).
[R14-3-11] K.C. Shaing, et al., Phys. Fluids **31**, 2249 (1988).
[R14-3-12] W. Zhu, et al., Phys. Rev. Lett **96**, 225002 (2006).
[R14-3-13] J.K. Park, et al., Phys. Rev. Lett. **102**, 065002 (2009).
[R14-3-14] J.D. Callen, et al., Nuclear Fusion **49**, 085021 (2009).
[R14-3-15] R.V. Budny, et al., Nuclear Fusion **48**, 075005 (2008).
[R14-3-16] R.V. Budny, Phys. Plasmas **17**, 042506 (2010).
[R14-3-17] R.V. Budny, Nuclear Fusion **52**, 013001 (2012).

Additional NSTX-U Research Achievements in FY2014

Beyond the completion of the FY2014 research described above, additional important scientific results were obtained during the FY2014 period and are described below.

Boundary Physics Research Results

Boundary physics research can be broadly divided into two categories: pedestal and ELM physics, as well as scrape-off layer (SOL) and divertor physics. While these areas are clearly coupled, the topics can be divided along these lines for presentation clarity.

A. Section BP-PED: Pedestal and ELM Studies

1. Collaborative studies on Alcator C-Mod: Kinetic Ballooning Modes

During FY 14, NSTX-U researchers published results [BP-PED 1] in which it was shown that edge instabilities limit the increase of the pedestal temperature. These first of its-kind detailed measurements on this edge instability on Alcator-Mod were made possible using a suite edge diagnostics and a magnetic probe placed near the separatrix. Figure BP-PED-1 displays the measured density fluctuation using the O-mode reflectometer at different radii. The left panel indicates the radii probed by the measurements.

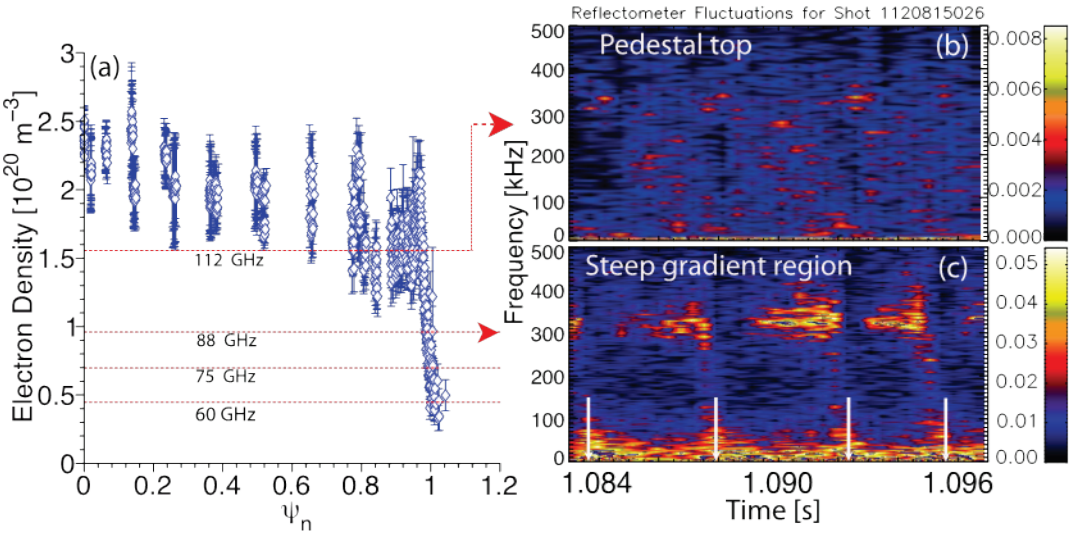

Figure BP-PED-1: *Radial localization of the coherent fluctuations. (a) Density profile and overlayed are the vertical lines indicating the density cutoff corresponding to each probing frequency. (b) Spectrogram of the reflectometer signals for the 112 GHz channel probing the pedestal top. (c) This panel shows inter-ELM coherent fluctuations. Note the white vertical lines at the bottom of this panel represent the ELMs.*

On the right panel, two examples of spectrograms of the fluctuations showing the onset of fluctuations near 300 kHz until the next ELM. The absence of fluctuations at the pedestal top suggests that the density fluctuation is localized in the steep gradient region. These density fluctuations are observed to have a magnetic signature as shown in figure BP-PED-2. This figure BP-PED-2 (a) shows the spectrogram of fluctuations measured using a double-head magnetic probe inserted 2 cm from the separatrix. It is clearly observed that after an ELM there is prompt

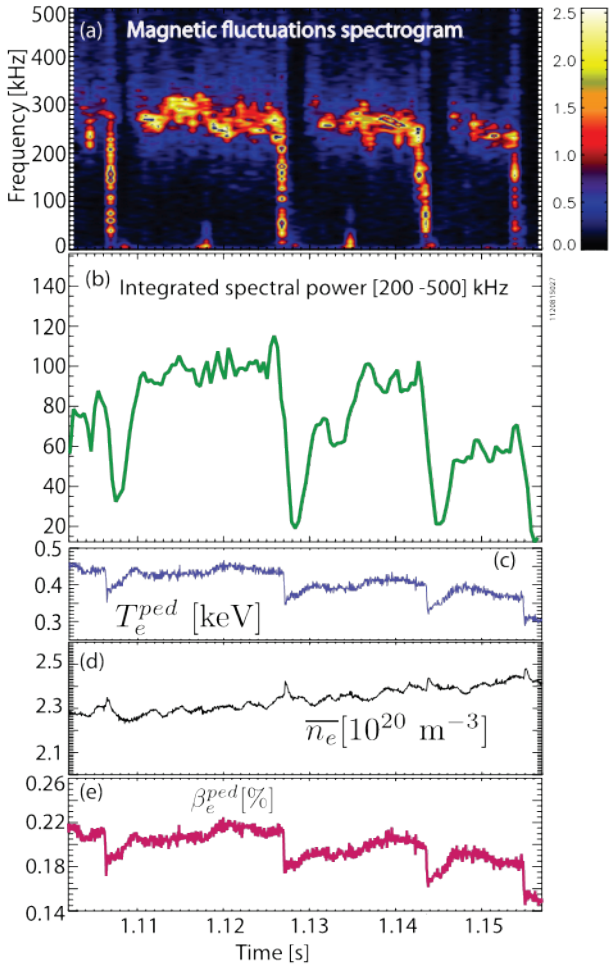

Figure BP-PED-2: *(a) Magnetic fluctuations spectrogram displaying the inter-ELM fluctuations sustained for 10 - 20 ms. (b) Integrated spectral amplitude obtained from integrating the above spectrogram between 200 and 500 kHz. (c) Edge temperature evolution measured using the ECE. (d) Line-averaged density evolution. (e) Estimate of the pedestal electron beta evolution.*

drop in edge temperature indicated in figure BP-PED-2 (c) followed by increase of the edge temperature. This increase is associated with the onset of an edge instability that saturates until the next ELM. In the last panel of this figure, we show that the onset of the fluctuations is correlated with the increase of electron beta. While a subset of measurements was shown here, these fluctuations were observed on other diagnostics probing the density. The combination of these various diagnostics allowed the characterization of the fluctuations to be of ion-scale consistent with KBM. The characteristic of this instability was corroborated using gyrokinetic calculations in the edge. The edge pedestal was determined to be ballooning unstable.

In summary, the work performed on Alcator C-Mod during NSTX-U outage will be extended on NSTX-U to probe the pedestal evolution with dedicated magnetic probe placed near the edge. The experience was valuable in showing the existence of an instability limiting the edge pedestal parameter. Extending to low-aspect ratio and to machines that are near the peeling boundary will provide valuable implications for ITER since ITER is predicted to be peeling unstable.

2. Investigation of ELM evolution patterns with BES in NSTX

Investigations of ELMs typically rely on slow observations of D_α intensity, ELM frequency, and stored energy loss. Also, growing experimental evidence suggests linear peeling-ballooning models accurately capture ELM onset conditions. In contrast, ELM perturbed fields, radial structure, saturation mechanisms, and filament dynamics require nonlinear models and verification with fast measurements. To gain insight into nonlinear ELM dynamics, here we analyze fast measurements of ELM events to identify possible patterns in the time-series data.

We assembled a database of 51 ELMs drawn from 25 shots covering 8 days. The ELM events are distinct and isolated, so the analysis does not include so called "grassy" ELMs. Identifying groups of similar ELM events is a two-step process. First, time series similarity metrics are developed and applied to the ELM database. A suitable similarity metric should reproduce intuitive expectations of similar or dissimilar time series data. Second, cluster analysis algorithm is applied to a matrix of similarity quantities. Cluster analysis is an unsupervised machine learning technique, and cluster analysis can identify groups of similar observations, if any. For our application, "observations" are similarity metrics that quantify the similarity or dissimilarity among ELM time-series data.

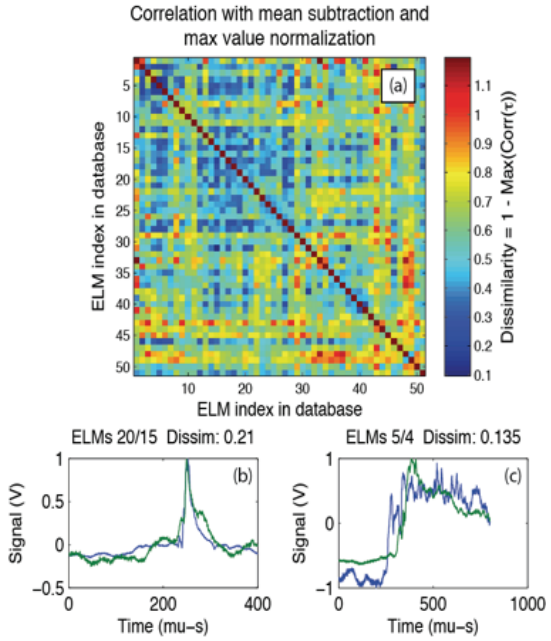

Figure BP-PED-3: *(a) Similarity matrix for a database of 51 ELMs using a correlation similarity metric; (b, c) ELM time-series data for ELMs with high similarity (low dissimilarity)*

Figure BP-PED-3a shows the similarity matrix for 51 ELMs using a correlation similarity metric. Figures BP-PED 3b and BP-PED 3c show that the correlation metric correctly measures high similarity (small dissimilarity) for ELM events that appear similar. Other candidate similarity metrics include the total Euclidean distance between time series, the dynamic time warping path length, and the difference between wavelet decomposition coefficients.

The ELM order in Figure 1a is basically random, but we can apply hierarchical clustering to identify ELM groups with high similarity. Hierarchical clustering is best known from genomics for connecting gene expression and functional pathways. Figure BP-PED-4a shows the linkage diagram for hierarchical cluster analysis for the ELM similarity matrix in Figure BP-PED 3a, and Figure BP-PED 4b shows the similarity matrix reordered to reflect the cluster results. The boxes in Figure BP-PED 4b highlight two groups of ELMs with similar evolution characteristics. Figure BP-PED 4c shows the group of fast, non-oscillatory ELMs, and Figure BP-PED 4d shows the group of slow, oscillatory ELMs. We note that these ELM characteristics and groupings are not discernable from traditional slow measurements like D_α intensity, stored energy loss, and ELM frequency. Furthermore, linear stability calculations of the peeling-ballooning mode do not capture ELM evolution dynamics.

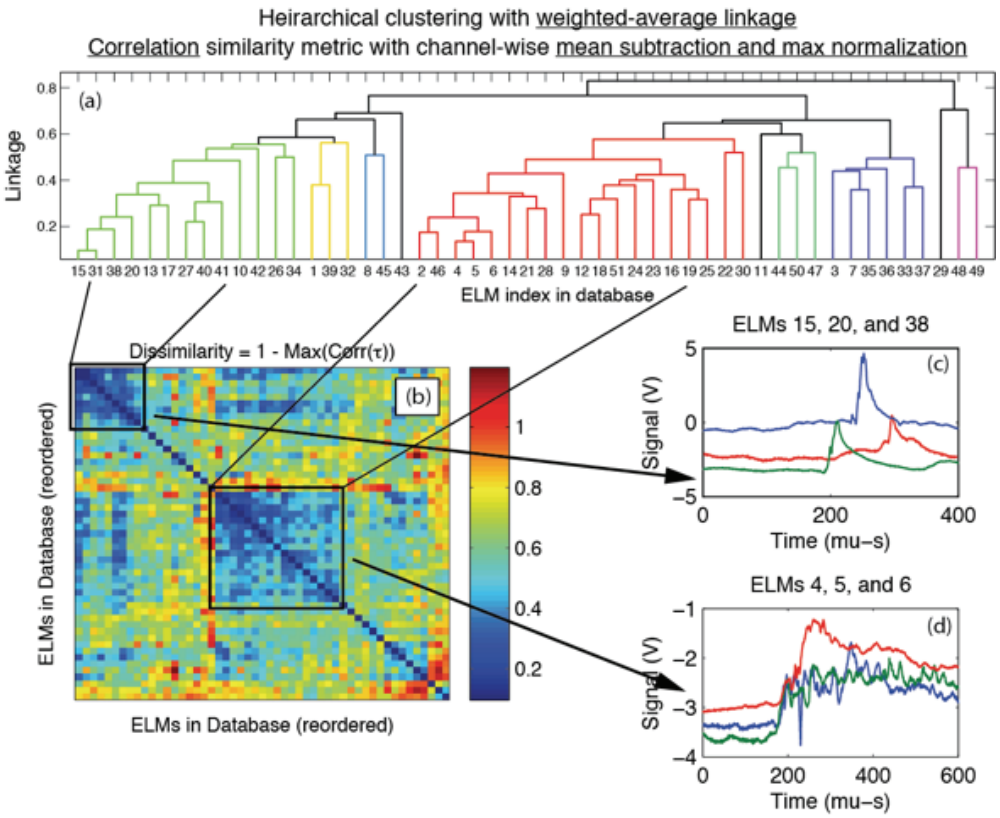

Figure BP-PED 4*: a) Hierarchical cluster results for the ELM database in Figure 1a; b) The ELM database reordered to reflect cluster results; c and d) example ELMs from the identified ELM groups*

The results in Figure BP-PED 4 correspond to the correlation similarity metric with a weighted-average linkage algorithm, but other similarity metrics and linkage algorithms give similar results. For instance, the dynamic time warping similarity metric produces similar results showing two ELM groups. We will continue exploring similarity metrics and cluster analysis algorithms to ensure the results are robust, and we will continue investigating properties of the ELM groups identified in this analysis. For instance, we will search for plasma parameters that distinguish the two ELM groups, and we will determine if nonlinear MHD simulations of ELM can reproduce the characteristics of the ELM groups.

3. Dependence of recycling and edge profiles on lithium evaporation in high triangularity, high performance NSTX H-mode discharges

Lithium wall conditioning (‘dose’) was routinely applied onto plasma facing components (PFC) between discharges in NSTX, partly to reduce recycling. Here, the effects of a pre-discharge lithium evaporation scan in highly shaped discharges are compared [BP-PED 2] with previously analyzed trends in moderately-shaped discharges. Because the lithium evaporators have a variable radial deposition profile, it is important to confirm such trends with different strike point configurations. Overall the trends are similar between strongly and moderately shaped discharges, indicating that the benefits of lithium conditioning should apply to the highly shaped plasmas planned in NSTX-U.

While many devices have reported performance improvements with lithium conditioning [BP-PED 3-4], including e.g. recent long pulse advances in EAST [BP-PED 5], the continuous improvement of plasma confinement and edge stability with *increasing* levels of lithium conditioning has been clearly documented in NSTX [BP-PED 6]. Those first studies were conducted in discharges with a 'weaker' boundary shaping than typical in NSTX, namely an intermediate-level average triangularity ($\delta \sim 0.46$), low elongation ($\kappa \sim 1.8$), and relatively low squareness shape. Numerous studies have shown that strongly shaped discharges exhibit good performance in NSTX, and thus highly shaped discharges were chosen as the baseline configurations for NSTX-U. In this paper, we present trends from an experiment in NSTX in which pre-discharge lithium evaporation was systematically increased in highly shaped discharges ($\delta \sim 0.6$-0.7, $\kappa \sim 2.2$, high squareness), as envisioned for NSTX-U. These highly shaped discharges represented the first set into which lithium was introduced in this particular run period.

The centroid of the lithium deposition onto the lower divertor plasmas facing components (PFCs) from the LiTERs was on the inner-horizontal set of tiles, as shown in Figure BP-PED 5; there was a Gaussian distribution of the deposition, with a full width of 23° in the poloidal cross section. Figures BP-PED 5a and BP-PED 5b illustrate the geometry of the inner and outer strike points with the centroid of LiTER deposition for the strongly shaped and weakly shaped discharges respectively. It is clear that the centroid is very near the outer strike point in strongly shaped discharges, and in the private flux region in weakly shaped ones. Thus it can be expected that this geometric difference could lead to a different effect on plasma discharges.

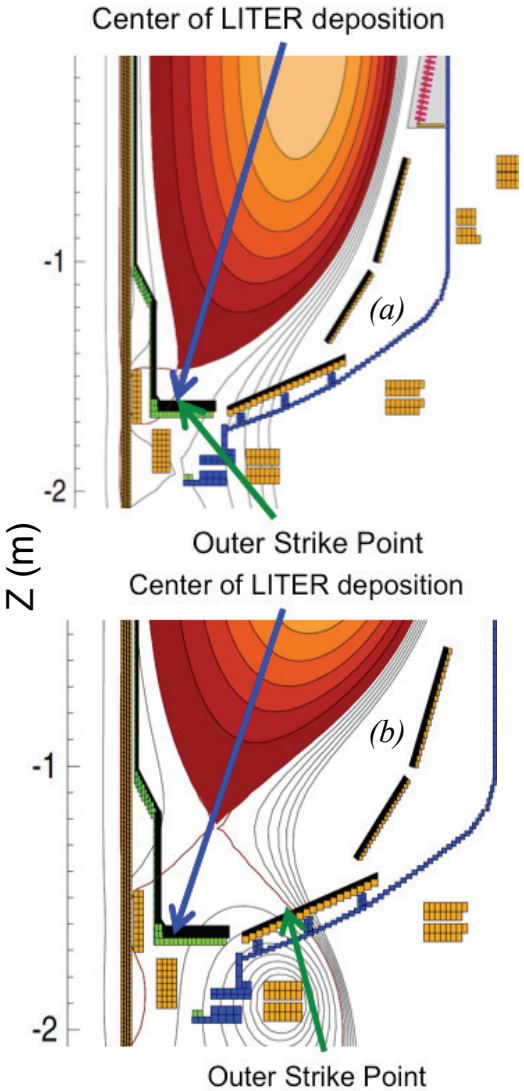

Figure BP-PED 5: *comparison of high and low δ shapes (a and b) with centroid of lithium evaporator deposition.*

The trends of lower and upper divertor D_α, confinement relative to H97L scaling, and midplane neutral pressure with increasing lithium dose, are shown in Figure BP-PED 6. The plots are color coded: the orange stars are from the present high shaping study, while the black diamonds are from the previous study in weakly shaped discharges. The trends are, overall, rather comparable. A few points are noted. First, both datasets show a sharp decrease

in lower divertor D_α, followed by a flattening at higher lithium dose (panel (a)). We interpret this as the transition from the high recycling to sheath limited heat transport regimes. This transition occurs at lower lithium dose for the highly shaped discharges. This is qualitatively consistent with expectations, in that the strongly shaped discharges have the centroid of lithium deposition much closer to the outer strike point than the weakly shaped discharges. In other words, it takes less lithium dose to cause this transition. The final fractional reduction in lower divertor D_α is also larger in the highly shaped discharges (90% reduction, compared with ~ 70% in the weakly shaped discharges). There are other factors related to the X-point geometry, of course, but these differences seem qualitatively understandable. Second, the relative confinement improvement trend is similar, but the magnitude may be slightly lower in the highly shaped discharges (panel (c)). Additional data, including data at higher lithium dose, would be needed to determine if there were a real difference in the trends; for now, the plan is to conduct experiments over a wide range of lithium dose in NSTX-U. Finally the magnitude of the neutral pressure is markedly lower (by up to 50%) in the highly shaped discharges. The highly shaped discharges were closer to true double-null configuration, and thus may have had better isolation between the midplane and divertor than the lower shaped discharges, which were biased more strongly toward the lower divertor.

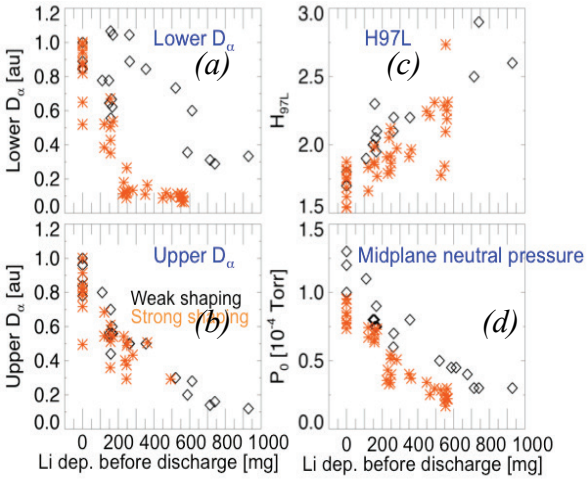

Figure BP-PED 6: *dependence of various quanities on pre-discharge lithium evaporation: (a) lower divertor D_α, (b) upper divertor D_α, (c) H97L confinement quality factor, and (d) midplane neutral pressure. High and low δ discharges are color coded. Panels (a), (b), and (c) are taken near 300msec, while panel (c) is evaluated at the peak of the stored energy during the discharge.*

In summary, discharge performance increased nearly continuously with increasing lithium dose in highly shaped discharges, as observed in previous NSTX studies in lower shaped discharges. The modest differences in the observed trends can be qualitatively understood by the more efficient deposition of lithium near the outer strike point in the highly shaped discharges. These results bode well for the use of lithium conditioning onto graphite PFCs in NSTX-U, which will be equipped with four lithium evaporators, to coat *both* the lower and upper divertors, extending the capability as compared with NSTX.

4. Non-axisymmetric Magnetic Field Modeling for ELM control

Numerical modeling of the proposed NSTX-U internal off-axis Non-axisymmetric Control Coil (NCC) and the external equatorial plane Resistive Wall Mode (RWM) Error field Correction (EFC) coil is being carried out with a set of 3D vacuum magnetic perturbation field and resistive MHD codes by General Atomics in collaboration with NSTX-U team members. Here, an

ensemble of 3D magnetic field codes are used to model the structure of the vacuum perturbation fields everywhere inside the NSTX-U vessel based on high fidelity non-axisymmetric coil models. In addition to producing high resolution field line trajectory plots (TRIP3D and TRIP3DGPU), spectral decomposition plots (SURFMN) and magnetic field or vector potential input data for 3D MHD codes (PROBE_G), these codes are used to analyze simulations of the plasma response to the vacuum perturbation fields generated by the M3D-C[1] MHD code.

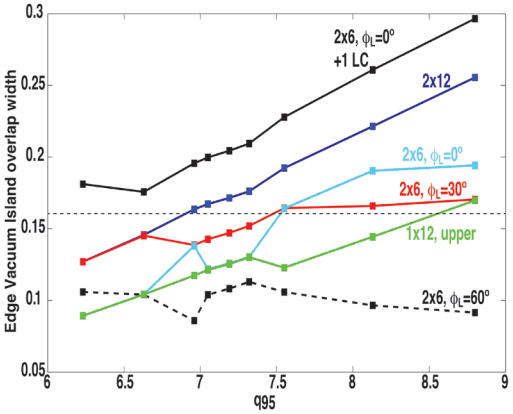

Figure BP-PED 7: *Variation in the width of the edge region covered by overlapping magnetic islands as a function of q95 and NCC configuration. The dashed line at 0.165 indicates the VIOW found in DIII-D to correlate with ELM suppression.*

As a prerequisite for plasma response simulations with M3D-C[1], a series of NSTX-U equilibria were generated where the central plasma pressure was varied from 84.3 to 127.0 kPa. This resulted in a q_{95} variation between 6.23 and 8.8. Using these equilibria and the SURFMN code, the width of the edge region covered by overlapping magnetic islands was studied and compared to similar calculations of the DIII-D I-coil perturbation field during ELM suppression. A correlation between the edge vacuum island overlap width (VIOW) was found in DIII-D when the VIOW exceeded ~0.165 in normalized poloidal flux [BP-PED 7-8]. Figure BP-PED-7 shows variations in the edge VIOW associated, with several configurations of the NCC being considered for installation in NSTX-U during 2017, as a function of q_{95} for the nine β-scan equlibria mentioned above. In these simulations, only the NCC is used with an n = 3 square wave perturbation field and 1 kAt in each coil. Six NCC configurations are compared in Figure BP-PED 7: 1) two poloidal rows consisting of 12 coils toroidally (2x12 – solid dark blue line), 2) one upper poloidal row with 12 toroidal coils (1x12 upper – solid green line), 3) two poloidal rows consisting of 6 coils toroidally with no toroidal shift of the lower poloidal row (2x6, ϕ_L=0º – solid light blue line), 4) two poloidal rows consisting of 6 coils toroidally with a 30º toroidal shift of the lower poloidal row (2x6, ϕ_L=30º – solid red line), 5) two poloidal rows consisting of 6 coils toroidally with a 60º toroidal shift of the lower poloidal row (2x6, ϕ_L=60º – dashed black line) and 6) two poloidal rows consisting of 6 coils toroidally with no toroidal shift of the lower poloidal row and one additional coil in the lower row (2x6, ϕ_L=0º +1 LC – solid black line). The addition of a 7th coil in the lower row creates multiple n≠3 harmonics, which significantly enhance the edge VIOW.

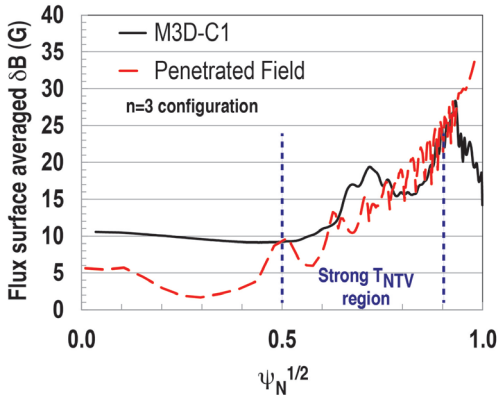

Figure BP-PED 8: *Flux surface averaged δB from a single fluid M3D-C[1] simulation (solid black) and NTVTOK (dashed red) is NSTX 133726.*

In addition to the NCC modeling done with SURFMN, the M3D-C^1 code is being used, in collaboration with Columbia University, to model the MHD plasma response to the RWM/EFC coil in NSTX discharge 133726. Here, the surface averaged δB field from M3D-C^1 is compared to δB values determined using NTVTOK code calculations of the NTV torque density base on toroidal rotation measurements in NSTX. As can be seen in fig. BP-PED 8, good agreement is found between the single fluid M3D-C^1 and NTVTOK fields in the region between $0.5 < \psi_N^{1/2} < 0.9$. Note that outside of this region (at both lower and higher ψ_N), the instantaneous NTV torque density measurement made in the experiment shows a sufficiently weak magnitude, and so conclusions regarding the strength of the field perturbation can only be drawn within this region. In this case, the M3D-C^1 simulation has a core mode, which may be contributing to a larger average δB in the core than the NTVTOK calculation (dashed red in Figure BP-PED 8). Results from these simulations will be presented at the 2014 IAEA FEC [BP-PED 9] and the analysis will be extended to include additional physics effect that are included in M3D-C^1.

5. Calculation of Plasma Response in NSTX for Fast Ion Orbit Loss Analysis

The plasma response to applied n=3 fields in NSTX discharge 138146 was calculated using M3D-C^1, in order to simulate the effect of the perturbed fields on fast ion orbit loss rate. The ion loss rate was calculated using the SPIRAL code, which has been modified to read M3D-C^1 output using the same libraries that are used by TRIP3D and TRIP3D-MAFOT. In the experiment, the neutron rate was observed to drop roughly 10% when n=3 fields were applied for approximately 4 ms. Using the plasma response fields calculated by M3D-C^1, it was found that the reduced neutron rate predicted from the calculated beam ion loss rate and a constant fuelling rate calculated with NUBEAM matches the experimental data well [BP-PED 10]. A comparison of the predicted neutron rate using vacuum fields, plasma response fields from the ideal-MHD IPEC code, and plasma response fields from the two-fluid M3D-C^1 code is shown in figure BP-PED 9. It is found that the models that include plasma response result in a significantly greater predicted ion loss rate than the vacuum model.

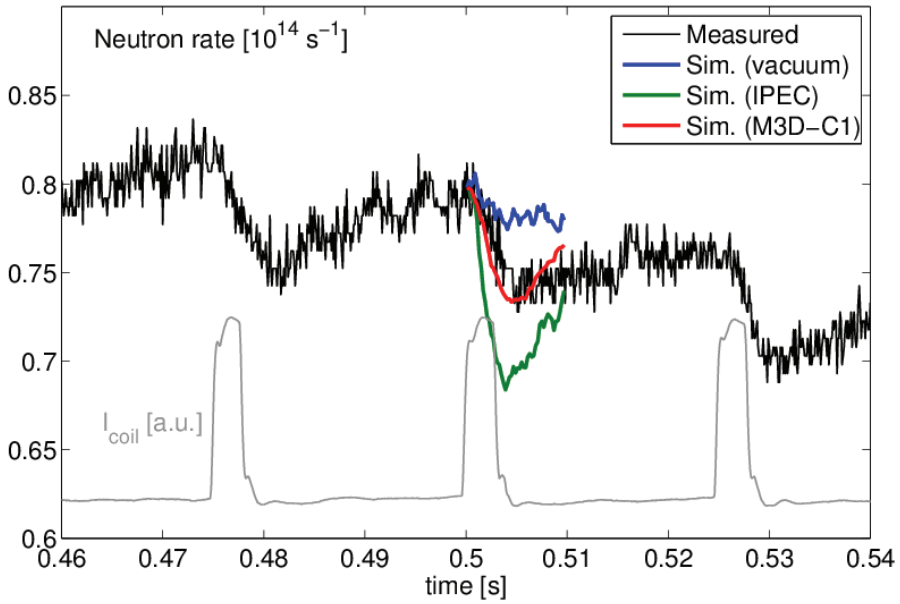

Figure BP-PED 9: *The effect on the neutron rate is calculated using NUBEAM and SPIRAL, taking the perturbed magnetic fields from the n=3 coils without plasma response (blue), with plasma response calculated by IPEC (green), and with plasma response calculated by M3D-C[1] (red). Figure reproduced from [BP 10].*

6. Update on cryo-pump design studies

Given the challenges with particle control in NSTX, and the anticipation that these difficulties will be greater in NSTXU, a significant effort has gone into designing a divertor cryo-pumping system [BP-PED 11] to be installed following the first two years of operation. The initial physics design was performed based on a semi-analytic pumping model [BP-PED 12] combined with projections of the divertor plasma parameters in NSTXU, and confirmed with Monte-Carlo neutral transport simulations using the EIRENE code [BP-PED 13]. Recent effort to develop the cryo-pump design has involved working with engineers at PPPL to make the overall design of the system more realistic and ensure that the physics and engineering requirements are simultaneously met.

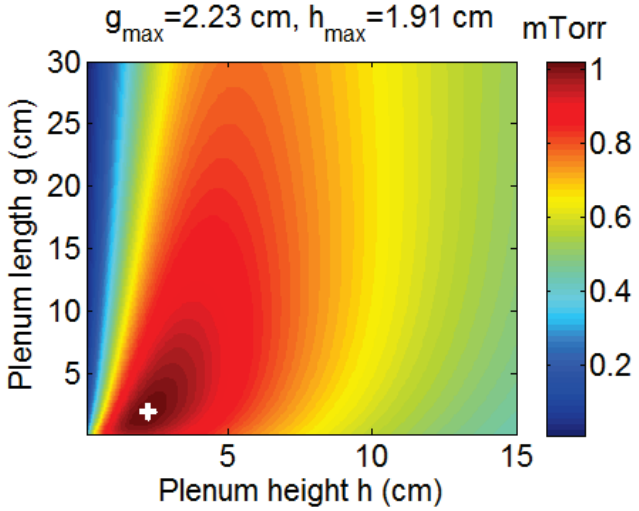

Figure BP-PED 10*: Projected plenum pressure using modified pumping geometry as entrance height and length are varied*

Based on initial feedback from engineering, the physics design of the cryo system was modified to take into account several changes. First, the cryo ring was relocated from a major radius of 1.2m to 0.9m, with a gas seal added at R=0.95 to reduce conductance out of the pumping plenum. This reduces the pumping speed from an estimated 24 m^3/s (based on the DIII-D systems), to 18 m^3/s. The second major alteration of the physics design was to account for the presence of a baffle blocking line-of-sight access of fast neutrals from the plasma to the cryo ring. This affects the vertical build of the plenum, and can also affect the net pumping speed by reducing conductance through the plenum to the pump (i.e., reduce pressure at the ring). The estimates of the pumping capability were redone taking these changes into account, and the geometry of the plenum entrance re-optimized as shown in Figure BP-PED 10. The impact on the optimized pumping entrance is modest, with a duct height of 2 cm and length of 2.2 cm (compared to 2 and 2.5 cm in previous optimization). Further, it is still the case that the plenum pressure is reduced only modestly as the length and height are increased together, so that a larger plenum entrance can be implemented initially to ensure flexibility in the shapes that can be pumped. Finally, the overall impact on performance was to reduce the pumped flux by ~15%; this is still anticipated to provide adequate pumping during high power, long pulse NSTXU discharges.

Recent effort has also been made to ensure that the space taken up by the plenum does not

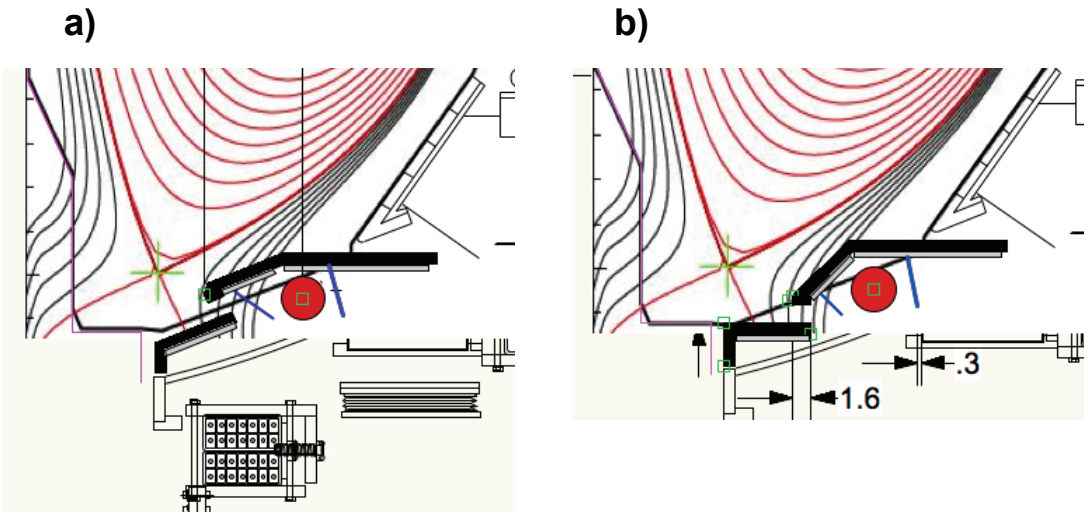

Figure BP-PED 11: *a) original design with angled plate near plenum entrance, and b) new design with horizontal plate*

interfere with the achievable plasma shapes in NSTX-U. In the original design [BP-PED 11], an angled target plate was assumed near the plenum entrance, as was the case in NSTX. This geometry results in significant penetration of the upper shelf of the plenum into the plasma scrape-off-layer, as illustrated in Figure BP-PED 11a. An improvement to this has been made by modifying the plate on the outboard side of the CHI gap to be horizontal. This allows the shelf above the plenum to have a steeper incline as shown in Figure BP-PED 11b, resulting in less penetration into the SOL. The new geometry has other anticipated advantages as well. It allows a reduced-size neutral line-off-sight baffle within the pumping volume thereby reducing the expected impact on neutral transport to the cryo ring. Further, the horizontal plate has more clearance from the vacuum vessel, which may make baking this component easier. While a full

engineering design remains to be done, these recent changes illustrate the effort to make the cryo design more consistent with the expected engineering requirements.

7. Edge gyrokinetic modeling of the effect of lithium on edge instabilities

Linear gyrokinetic simulations using the GS2 code [BP-PED 14] comparing discharges without lithium and with thick lithium PFC coatings showed significant destabilization of electron temperature gradient (ETG) modes at the foot of the pedestal with lithium [BP-PED 15] (Figure BP-PED 12a). This is due to an increase in ηe (the ratio of temperature and density gradients) driven by the change in density gradient induced by lithium. Based on this it has been postulated that ETG may play a critical role in the stabilization of ELMs that is observed with lithium. The essential picture is that lithium reduces recycling and thus the edge density, but that due to stiff ETG onset the Te profile is unable to increase in response to the reduced density. This would reduce the edge pressure gradient and hence bootstrap current, which has been calculated to be key to the stability to peeling-ballooning modes with lithium [BP-PED 16].

The plausibility of this picture depends on whether ETG is capable of driving an experimentally relevant amount of electron heat transport, and hence play a role in setting the Te profile. To study this, the GS2 simulations have been extended to include nonlinear calculations. The simulations were electrostatic with adiabatic ions, which anticipated to be sufficient for ETG simulations. Extensive resolutions checks have been done, which are necessary due to the sharp variation in the magnetic geometry present at the plasma edge. The calculated electron heat fluxes are shown in Figure BP-PED 12b as a function of electron temperature gradient, with the

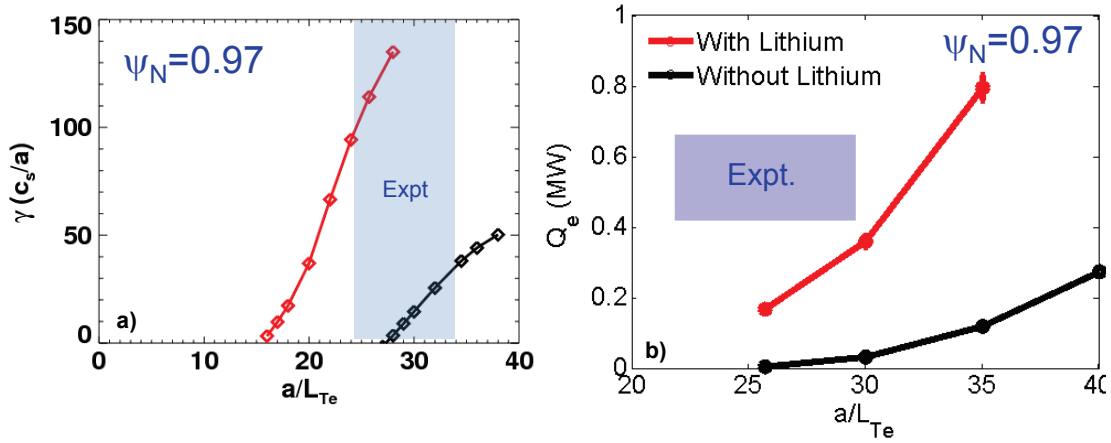

Figure BP-PED 12*: a) linear and growth rate and b) nonlinear electron heat flux as temperature gradient is varied.*

experimental values indicated by the shaded box [BP-PED 17]. It is found that with lithium, ETG provides ~1/3 to 1/2 of the experimental electron heat flux at the nominal temperature gradient with lithium. Further, with a modest increase of the temperature gradient by ~20%, ETG can provide the full electron heat flux with lithium. In contrast, without lithium ETG does not appear to be a significant transport mechanism. These nonlinear simulations support the picture that the changes to ETG stability induced by lithium through the density profile may play a key role in keeping the edge T_e profile fixed, even as the density is reduced, contributing to ELM stability.

8. References for Section BP-PED

[BP-PED 1] Diallo, A., *et al. Phys. Rev. Lett.* 2014 **112** 115001
[BP-PED 2] Maingi, R., *et al. J. Nucl. Mater.* 2014 submitted
[BP-PED 3] Snipes J., E.S. Marmar, and Terry J. L., 1992 *J. Nucl. Mater.* **196-198** 686
[BP-PED 4] Mansfield D. K.*, et al.*, 2001 *Nucl. Fusion* **41** 1823
[BP-PED 5] Guo H. Y.*, et al.*, 2014 *Nucl. Fusion* **54** 013002
[BP-PED 6] Maingi R.*, et al.*, 2011 *Phys. Rev. Lett.* **107** 145004
[BP-PED 7] Fenstermacher, M.E. et al. *Phys. Plasmas* **15** (2008) 056122.
[BP-PED 8] Evans, T.E., *et al. Nucl. Fusion* **53** (2013) 093029.
[BP-PED 9] Sabbagh, S.A. *et al.,* 25th IAEA FEC, Saint Petersburg, Russia, 2014.
[BP-PED 10] Bortolon, A., "Mitigation of Alfvenic Activity by 3D Magnetic Perturbations on NSTX." 41st Meeting of the EPS, Berlin, Germany, June 23–27, 2014.
[BP-PED 11] Canik, J.M., *et al*, "Physics design of a cryo-pumping system for NSTX-U", Bulletin of the APS-DPP, Providence, Rhode Island, (2012) 261.
[BP-PED 12] Maingi, R., *et al, Nucl. Fusion* **39** (1999) 1187.
[BP-PED 13] Reiter, D., *et al*, *Fusion Science Techn.* **47** (2005) 172 and www.eirene.de
[BP-PED 14] Kotschenreuther, M. *et al*, *Comp. Phys. Comm.* **88** (1995) 128
[BP-PED 15] Canik, J.M. *et al*, *Nucl. Fusion* **53** (2013) 113016.
[BP-PED 16] Maingi, R. *et al*, *Phys. Rev. Lett.* **103** (2009) 075001.
[BP-PED 17] Canik, J.M., *et al*, "Changes to edge gyrokinetic stability with lithium coated PFCs in NSTX", Bulletin of the APS-DPP, Denver, CO, (2013) 146.

B. Scrape-off-layer physics

1. Edge turbulence studies via gas-puff imaging

Significant progress on edge turbulence was made by continuing analysis of the Gas Puff Imaging (GPI) data from the NSTX run of 2010. Work was also done to re-install and upgrade the GPI diagnostic for NSTX-U.

A new paper was published [BP-DSOL 1] which examined in detail the perturbing effects of the small pulsed deuterium gas puff used for GPI on the edge plasma and edge turbulence in NSTX. This gas puff caused little or no change in the line-averaged plasma density or total stored energy, or in the edge density and electron temperature up to the time of the peak of the gas puff. The radial profile of the Dα light emission and the edge turbulence within this gas puff did not vary significantly over its rise and fall, implying that these gas puffs did not significantly perturb the local edge plasma or edge turbulence (see Figure BP-DSOL 1). The edge plasma measurements were also compared with modeling by DEGAS 2, UEDGE, and with simplified estimates for the expected effects of this gas puff.

In a second paper [BP-DSOL 2], the close physical proximity of the GPI and BES diagnostics on NSTX is used to directly compare fluctuation measurements and to study the local effects of the GPI in H-mode plasmas without large ELMs. Strong cross-correlation between GPI and BES is observed, and strong cross-coherence is seen for frequencies between 5-15 kHz. Also, the probability distribution functions of fluctuations measured inside the separatrix exhibit only minor deviations from a normal distribution for both diagnostics, and good agreement between correlation length estimates is found. While the two instruments agree closely in many respects, the relative BES fluctuation levels can be up to a factor of 5 larger than GPI at a similar minor radius. The BES mean intensity is also found to be sensitive to the GPI neutral gas puff, and normalized fluctuation levels between 4-10 kHz are observed to increase during the GPI puff in some cases.

A comprehensive analysis was done in FY14 of the NSTX GPI database of 2010, which includes 140 shots covering the whole range of NSTX operation (~4 GB of data). These GPI images of the edge and SOL plasma near the outer midplane were systematically analyzed to form a database of the radial and poloidal turbulence structure and motion as a function of radius for each shot. This database was being examined for empirical scalings; for example, with increased stored plasma energy there is a reversal of the poloidal velocity of the turbulence inside the separatrix, but little or no variation in the radial velocity in the SOL. These edge/SOL turbulence variations are being compared with theoretical expectations for drift wave and blob physics, in collaboration with Lodestar.

The GPI diagnostic of 2010 has been re-installed re-calibrated inside the vessel this year in preparation for the FY15 run, and an improvement in the ex-vessel GPI optics using a zoom lens should allow a variable-sized field of view in FY15. The collaboration with the EAST tokamak on GPI diagnostic development (supported by NSTX) has resulted in two new papers in the last

year [BP-DSOL 3, BP-DSOL 4].

Finally, a new paper was published on edge and SOL studies of NSTX with Langmuir probes [BP-DSOL 5]. Radial turbulent particle fluxes peak near the last closed flux surface (LCFS) in L-mode and are suppressed in H mode (80%–90% lower) mostly due to a reduction in density fluctuation amplitude and of the phase between density and radial velocity fluctuations. Profiles of normalized fluctuations feature levels of 10% inside LCFS to ~150% at the LCFS and SOL. The L-H transition causes a drop in the intermittent filaments velocity, amplitude and number in the SOL, resulting in reduced outward transport away from the edge and a less dense SOL.

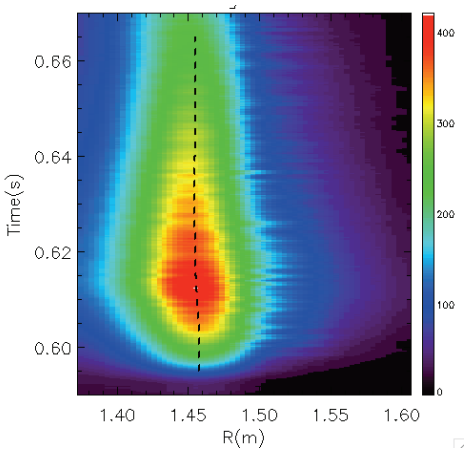

Figure BP-DSOL 1*: Radial profile of the Dα light emission from the GPI gas puff vs. time. This profile does not vary with respect to the separatrix position (dashed black line), implying that this gas puff did not significantly perturb the local edge plasma.*

2. Scrape-off-layer turbulence and transport

SOL turbulence and transport investigations of NSTX plasmas have been carried out at Lodestar using a newly improved physics model, now embodied in the SOLT turbulence code. The new model includes finite ion pressure and ion diamagnetic drifts. These effects are important for describing the physics of H-modes where mean flow shear, driven by the ion diamagnetic pressure, is thought to play a fundamental role in edge turbulence and transport [BP- DSOL 6]. The pedestal gradient and the scrape-off-layer (SOL) heat flux width are critical quantities for both NSTX-U and ITER. It is well known that the pedestal gradient, together with the pedestal width, determines the peak pedestal pressure and hence the overall fusion performance of ITER. On the other hand, the SOL heat flux width, together with the peak power, determine the survivability of the divertor target plates. Our modeling suggests that in selected NSTX discharges the pedestal gradient width and the SOL heat flux width are inversely related by turbulent transport. Large-scale turbulent convection connects the gradient-driven fluctuations in the pedestal with the heat flux across the separatrix. For the wider pedestal (post-Li), and hence the weaker fluctuations, the SOL heat flux width is reduced in comparison to the steeper pedestal (pre-Li), and hence stronger fluctuations, case. This work grows out of ongoing simulations [BP-DSOL 7] of pre and post lithium H-mode discharges which show dramatic changes in the pedestal gradients. Qualitative trends in both the simulated heat flux width and the fluctuation

levels agree with experimental data. The modeling of these discharges has been accepted for presentation at the upcoming IAEA conference [BP- DSOL 8].

One important issue remains to be resolved: the poloidal flow velocities of turbulent structures in the simulations are too fast when compared with NSTX GPI data. Ad-hoc flow damping in the simulation improves the comparison, but it is not clear if known physical damping mechanisms, such as ion-neutral friction, are strong enough to explain the results. (Neutral densities near the plasma boundary around the machine are not well diagnosed.) A comprehensive database of GPI structure velocities (as described in the previous section) is being analyzed, in addition to further simulations, to address this issue.

3. Analysis of Midplane Neutral Density Profiles

A new technique for inferring neutral density profiles from the tangentially viewing Edge Neutral Density Diagnostic has been developed and applied to discharges from the 2010 run campaign. The conventional "S/XB" method is accurate only in the narrow region in which both the electron impact excitation rate of the atoms and their neutral density are significant. This new method is a hybrid approach in which a DEGAS 2 neutral transport simulation is used to augment the experimental procedure, extending the spatial range over which useful densities can be obtained. Relative to previous studies employing codes to estimate neutral densities, this method promises reduced uncertainties and fewer assumptions. The former statement stems from the successful use of a similar technique to quantitatively simulate the neutral gas cloud in NSTX midplane gas puff imaging (GPI) experiments [BP- DSOL 9].

The Edge Neutral Density Diagnostic (ENDD) uses an absolutely calibrated camera with a tangential view through the edge of the NSTX plasma, providing radial Balmer-β emission profiles with 2 mm spatial resolution and an exposure time of 3.7 ms per frame. As in the GPI simulations, the experimental input to DEGAS 2 consists of the EFIT magnetic equilibrium (for the geometry) and midplane plasma profiles from Thomson scattering and CHERS for the shot and time of interest. The primary difference between the present technique and that described in [BP- DSOL 9] is that the neutral source is not known here. To motivate a simple and general characterization of that source, we argue that the atoms contributing to the ENDD signal are most likely penetrating in from the far SOL at a nearby poloidal location. This leads us to assume a vertically uniform source of deuterium molecules coming off of the vacuum vessel walls with a flux of arbitrary magnitude.

The volumetric source of D_β photons is accumulated in each computational zone along the path of the penetrating atoms; a synthetic ENDD image is constructed from these data in post-processing. The resulting radial profile is then compared with that from the experimental data. The ratio of the peak emission rate in the ENDD signal to that of the DEGAS 2 simulated signal provides an overall scale factor that can then be applied to all of the DEGAS 2 output, and to the neutral atom and molecular densities in particular.

This method has been applied to the H-mode phases of two 2010 NSTX shots, 139412 and 142214. Shot 139412 had relatively low triangularity (0.3) and exhibited considerable ELM activity; the selected time is during a lull in that activity. Shot 142214 had medium triangularity (0.6) and was ELM free. The resulting simulated ENDD profiles are similar to those observed [BP- DSOL 10], confirming the validity of our approach to inverting the ENDD data, and of the characterization of the D_2 source. The resulting radial profiles of the D and D_2 densities at midplane are shown in Fig. BP-DSOL 2. The simulated neutral densities at the vessel wall also compare well with those obtained from midplane micro-ion gauges [BP- DSOL 10].

To assess the sensitivity of this method to the assumption of a uniform source along the vacuum vessel wall, we considered a simulation in which the source flux varied by a factor of 10 over the vertical range of the problem. The simulated ENDD profile differed from that of the baseline simulation by no more than 3%; the density profiles differed on average by only about 10%. We expect that such deviations are smaller than the overall uncertainties in the density profiles.

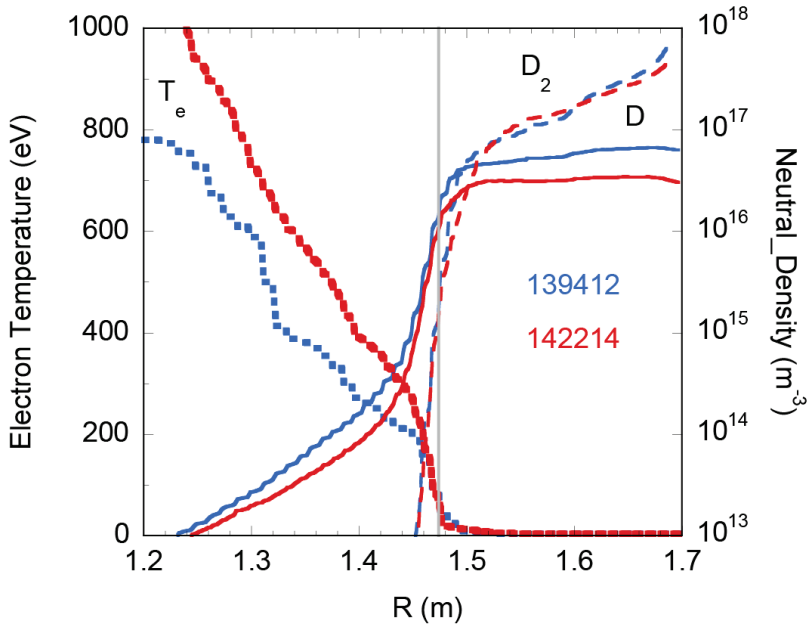

Figure BP-DSOL 2: *Inferred deuterium atom (solid lines) and molecule (dashed lines) midplane density profiles for shots 139412 and 142214. The electron temperature profiles (dotted lines) are provided for reference. The gray line indicates the separatrix location.*

4a. Divertor Physics – Modeling of Snowflake Divertor Experiments

Modeling of NSTX snowflake divertor (SFD) experiments with UEDGE has demonstrated the ability to capture observed physics behavior, including partial detachment [BP-DSOL 11]. Good agreement with heat flux data is achieved (Figure BP-DSOL 3), and partial detachment is captured in the SFD case. Simulations indicate that saturation of the lithium pumping mechanism occurred in the SFD, increasing target recycling to 0.97 vs. 0.91 in the companion conventional divertor (CD) discharge. Density scans have been performed to provide insight into detachment physics. Increased divertor volume in the SFD plays the leading role in reducing parallel heat flux. A significant role is also played by neutral gas power loss to the outer divertor target, a loss that is magnified by the increased wetted area of the SFD.

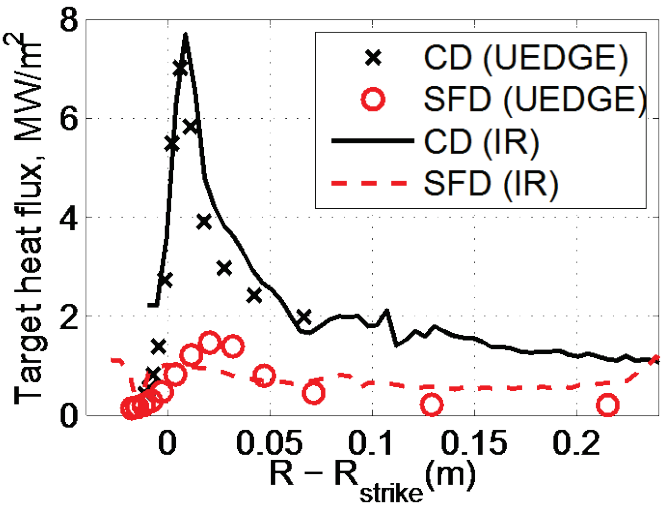

Figure BP-DSOL 3: *Modeled and IR-thermography-based heat fluxes for NSTX conventional and snowflake divertor configurations.*

Initial UEDGE modeling of the NSTX-U SFD [BP-DSOL 12] indicated that SFD divertor optimization is necessary to achieve favorable neutral confinement and thus avoid sheath-limited outer target plasma conditions. In pursuit of this optimization, several different SFD configurations have been modeled and compared [BP-DSOL 13]. In SFD cases A, B, C, and D, the secondary X-point is translated horizontally from a location near the outer strike point (case SFD-A) to a location 1.25 mm (measured at the outer midplane) beyond the separatrix (in SFD-D). Modeling of these four SFD cases and a companion CD case shows that SFD-C and -D configurations enable highly radiating, partially detached divertor conditions at relatively low core/separatrix densities, and also provide a "gradual" detachment as density is increased (Figure BP-DSOL 4). This favorable result is attributed to improved neutral confinement as flux surfaces are tilted with respect to the target in SFD-C and -D. The results shown in Figure BP-DSOL 4 are for a scenario with $P_{NBI} = 12$ MW and $I_p = 1$ MA.

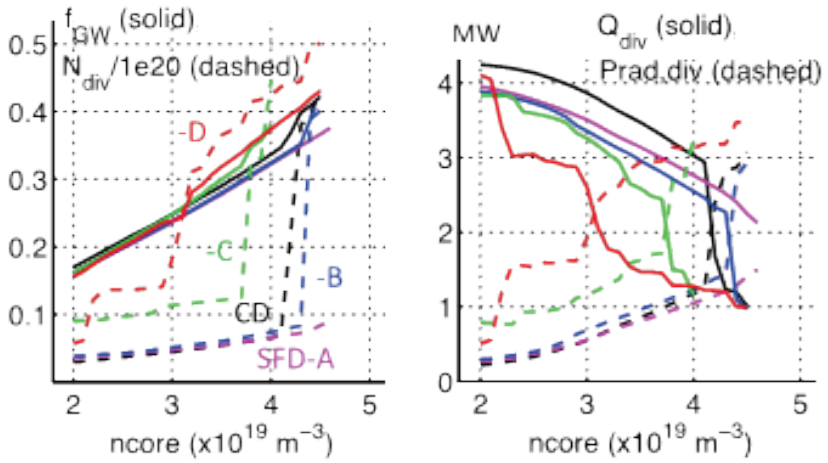

Figure BP-DSOL 4: *UEDGE density scan results for NSTX-U snowflake and conventional divertor configurations. Left panel: Greenwald fraction (f_{GW}) and total divertor density (N_{div}) as a function of core density. Right panel: total power transmitted to the divertor (Q_{div}) and power radiated in the divertor ($P_{rad,div}$).*

For ST-FNSF, UEDGE modeling has been performed to examine divertor concepts, including a conventional divertor (CD), conventional with vertical target (CD-VT), snowflake (SFD), and "super-snowflake" (super-SFD) [BP-DSOL 13]. (Here, "super-snowflake" refers to a snowflake with the outer divertor leg extended to large major radius as in the Super-X divertor [BP-DSOL 14].) Simulations indicate that control of neutral behavior is crucial to achieving low target temperature compatible with low sputtering yields. By managing neutral behavior with target tilt (CD-VT) or leg-extension with baffling (super-SFD), scenarios are found with acceptable target temperature (<50 eV) and heat flux (<10 MW/m^2). In the CD-VT, neutrals are directed toward the outer strike point, promoting high density and low temperature (T_e ~ 20 eV) across the outer target. In the super-SFD, outer strike point detachment is seen (T_e ~ 2 eV) with the upstream location of the ionization front set by the position of the cryopump duct.

4b. Upgrades to UEDGE for modeling snowflake divertors in NSTX-U

Both NSTX and DIII-D experiments have been operated in snowflake divertor configurations showing reduced peak power to the divertor plates. It is planned that NSTX-U will also use this type of divertor configuration. Until now, detailed modeling of the snowflake has been hampered the requirement to keep the second X-point slightly outside the computational domain, i.e., the logic within UEDGE did not allow for a general placement of two X-points, especially if they were close together. This difficulty has very recently been overcome, and UEDGE can treat both snowflake minus, snowflake plus, and exact snowflake configurations.

The upgrade to UEDGE had two components. The first is to provide the logic that connects cells in throughout the 2-X-point region via indirect addressing. Such logic requires distinguish 3 types of configurations - two for the snowflake minus and one for the snowflake plus, which are identified by the poloidal angle between the X-points as introduced in the paper by Ryutov et al. [BP-DSOL 15]. The second advance that enabled the upgrade is a more general mesh generator that can deal with the various configurations. An example of a UEDGE solution obtained with two X-points in the divertor region is shown in Figure BP-DSOL 5 for DIII-D geometry, but the same can now be done for NSTX-U. Note the four divertor legs denoted by circled numbers in the clockwise direction about the X-points; there is substantial density in each leg. More detailed comparisons with NSTX and DIII-D data is planned.

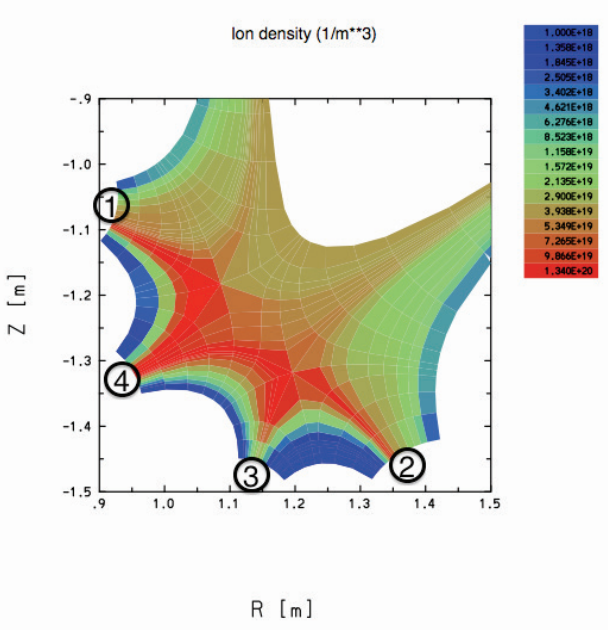

Figure BP-DSOL 5: *Example of a UEDGE solution with two X-points, (DIII-D geometry.)*

5a. Diagnostic preparation: Absolutely Calibrated Tangential Imaging of Divertor

Work is currently underway to upgrade the lower divertor tangential imaging system of NSTX [BP-DSOL 16], adapting it to the NSTX-U device and being able to perform absolutely calibrated measurements. The largest difficulty when performing the calibration for this imaging system resides not on the calibration itself but in maintaining this calibration throughout the several month long experimental campaign. Coatings inevitably develop through the campaign on the vacuum interface window and other invessel optics such as mirrors. The final design, developed by engineers Robert Ellis and Howard Feder of PPPL, was approved and the hardware is currently under fabrication and procurement. In order to monitor the transmission and reflection of the in-vessel window and mirror, a target plate made of sand-blasted stainless steel is inserted in field of view. This plate acts as a diffuse Lambertian source. Illumination is provided through a re-entrant illumination probe carrying a 1/8" diameter fiber light guide inserted by means of a bellows mechanism. A CAD drawing of the hardware being built is shown in Fig. BP-DSOL 6. In this figure the re-entrant tube with the vacuum interface window is shown together with the vacuum mirror (gold color plate) and the calibration target plate (grey plate). The actuators for both the mirror and target are also shown. The yellow colored tube on the bottom is the illumination probe which is usually kept retracted (and not inserted as shown here).

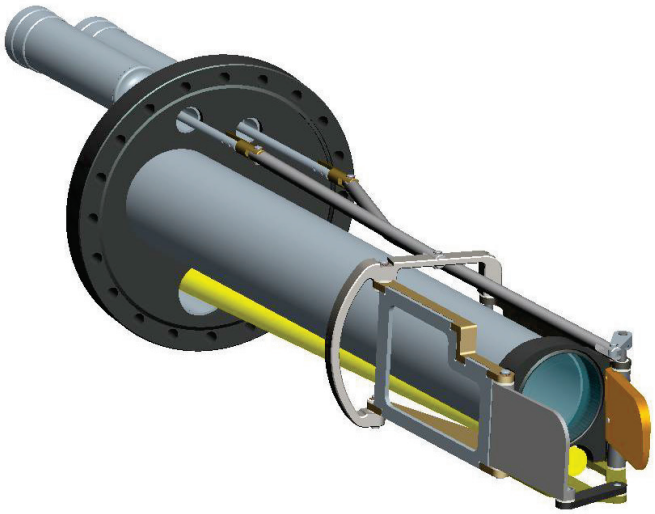

Figure BP-DSOL 6: CAD Drawing of re-entrant hardware for the lower dome access port at Bay F. The mirror is deployed and the calibration target plate is retracted.

The absolute calibration is performed while there is manned access to the vessel, before and after the experimental campaign, the measurement of the optics transmission/reflection is done on some days after the day's experiments have finished.

The preparation of software is underway. The "forward" problem, that is calculating the ray paths lengths in the NSTX-U, has been completed for the expected geometry of the hardware being built. The images in Fig. BP-DSOL 7 show a sequence of artificial images of MARFE-like toroidal structures, similar to those seen in NSTX [BP-DSOL 17], moving along the center column of NSTX-U and reaching the bottom divertor surface tiles. The development of software for the inversion for 2-D images into 2-D emission profiles in the R-Z plane is currently underway. This inversion uses a nonnegative least squares (NNLS) [BP-DSOL 18] algorithm to restrict the emission cells to positive values.

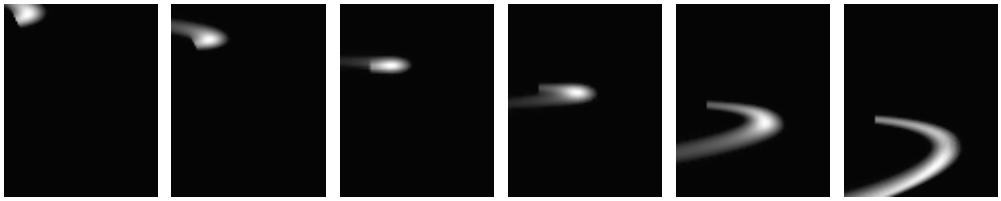

Figure BP-DSOL 7: *Sequence of artificial images showing a MARFE like structure moving in the lower divertor region. Structure has 8 cm and 4 cm FWHM in R and Z.*

5b. Boundary diagnostic development through LLNL collaboration

Results and accomplishments in the area of diagnostic operation and development are summarized as follows. Ten edge diagnostics are being prepared for day-1 operation on NSTX-U. Theses diagnostics include

1) 30 spectrally filtered edge impurity emission system (EIES) detectors
2) the Lyman-alpha diode array (LADA) divertor radiometer

3) the divertor vacuum ultraviolet spectrometer SPRED
4) the ultraviolet-visible-near-infrared spectrometers VIPS and DIMS
5) Upgraded one-dimensional filtered camera arrays with divertor and midplane views
6) Divertor filtered imaging cameras, including the CIDTEC camera with image splitting capabilities
7) Near-infrared divertor spectrometer
8) Extreme ultraviolet (EUV) spectrometer MonaLisa (Metal Monitor and Lithium Ion Spectrometer Assembly)
9) EUV spectrometer LoWEUS
10) EUV spectrometer XEUS

Upgrade of the EIES (filterscope) diagnostic includes re-routing and installing new fiberoptic bundles and upgrading the data acquisition system. The upgrade of the one-dimensional camera arrays includes new Teledyne Dalsa cameras with increased time resolution and sensitivity, and a new image relay and splitter system that enables additional shielding of the cameras and simultaneous measurements at three wavelengths.

A layout of the spectrometer mount on NSTX-U at Bay J horizontal divertor port has been developed for the divertor VuV spectrometer SPRED. A new detector was tested and mounted on the SPRED spectrometer image intensifier. The divertor SPRED will be used on NSTX-U for understanding spectral composition of divertor radiated power in impurity-seeded and snowflake radiative (partially detached) divertor experiments

The intensified radiation-tolerant CIDTEC camera diagnostic package from Alcator C-Mod has been brought back to PPPL, to be used on NSTX-U. Based on this package, a new NSTX-U diagnostic for two-dimensional two-color measurements of impurity emissions has been developed. These measurements will be important for plasma-surface interaction studies with coated high-Z plasma-facing components presently envisioned for NSTX-U. A new optical image splitter and new image relay optics are developed for divertor imaging, to be used with the CIDTEC and Phantom cameras on NSTX-U.

The new EUV grating spectrometer MonaLisa has been designed and built at Livermore. The instrument will measure core impurity concentration and impurity time evolution and will focus on such elements as lithium and molybdenum. It is now fully assembled and aligned. It is waiting testing on the Livermore EBIT facility, which generates similar EUV photon intensities as those expected from NSTX-U core plasma. The installation of the instrument has been coordinated with NSTX-U staff, and a port has been identified to mount the new instrument together with the two existing LLNL spectrometers LoWEUS and XEUS. Co-location of all three instruments on one NSTX-U port is more economical space-wise, however, it has required designing a new stand that accommodates all three instruments without mutual interference. Such a stand has been designed at LLNL and the design was handed over to PPPL. Princeton engineering has agreed to build the stand. Once PPPL has completed the stand, MonaLisa will be shipped and installed on NSTX-U. Recently, we have procured a new CCD camera detector for recording the spectra. Together with the spectrometer, the camera is awaiting testing.

Finally a conceptual design was carried out for a divertor Thomson scattering diagnostics for NSTX-U, which remains a high priority boundary physics upgrade after completion of the NSTX-U construction project [BP-DSOL-19].

5c. Boundary diagnostic development through UT-K collaboration

First wall lithium coating will be strong part of the experimental program of NSTX-U. Nevertheless, many physics and operational aspects are still to be clarified. Examples are the complex chemistry at play at the wall surface during plasma exposure, which involves complex chemical bounds between D, Li, O, C and elements from refractive substrates; or the issue of material erosion, migration and redeposition, which connects with the improvement of plasma performance with lithium evaporation.

The collaboration program with University of Tennessee Knoxville (FOA collaborative program 2012-2015), aims to advance the understanding of these issues, through accurate characterization of the surface characteristics, especially regarding spatial distribution of lithium layer within the vessel.

The collaboration supports one postdoctoral scientist on site, and will bring to NSTX-U a multi-channel spectroscopic diagnostic that will provide spatially and temporally resolved measurement of visible and UV emission from near-wall regions, permitting to characterize the near-wall processes by monitoring the abundance of atomic (e.g. C, Li, O) and molecular species, (Li_2, CD, LiD, Li oxides) within a single plasma discharge and throughout the campaign.

The spectroscopy diagnostic (UTKSPEC) consists of two collection optics assemblies, each housing an imaging objective lens and a holder for 16 optic fibers heads. The first assembly, equipped with a 105 mm, F/4.2 lens (Tochigi Nikon), will be installed at a Bay G bottom port and will provide 16 lines of sights, measuring the upper divertor, from R=0.45 to 0.90 m. The second will be installed at an equatorial Bay J port, with a 60 mm, F/4 lens (CoastalOpt-Jenoptics) that provides the larger field of view required to cover the central stack from Z=0 to Z=1.20 m. The collected radiation will be spectrally analyzed in the diagnostic acquisition room (DARM) adjacent to the main experimental chamber, where the two 40 m long bundles of 16 fibers (Polymicro, FPBI) will be connected to a dedicated multi-channel Czerny-Turner spectrometer (Princeton Instruments Isoplane 320 mm, F/4.6, coma corrected), through a patch panel.

In order to maximize the opportunity of measuring radiation from atomic and molecular impurity species, the optical elements are chosen as to ensure efficient transmission in from ultra-violet (350nm), through the near infrared (1200 nm): Sapphire vacuum windows, high OH fused silica fibers, and UV graded imaging objectives. The spectrometer houses 3 interchangeable gratings (3600, 2400, 1200 g/mm) to cover spectrum from UV (higher resolution) to NIR (lower resolution) and mounts a dedicated high speed, high quantum efficiency CCD camera (Princeton Instruments ProEM512B), with Excelon coated CCD, for enhanced QE and “etaloning”-free imaging in the NIR.

The UTK program, in close collaboration with the ORNL group, also comprises the staged installation of two new infrared cameras, to extend the pre-existing thermography imaging coverage. The cameras will be installed at Bay G bottom and Bay J equatorial ports to provide measurement to couple with the spectroscopy lines of sights (i.e. upper divertor and central stack). This extended IR imaging capability will enable, not only to study heat flux deposition, but also to measure the tile surface temperature, a key element for modeling of surface evolution, sputtering and erosion rates.

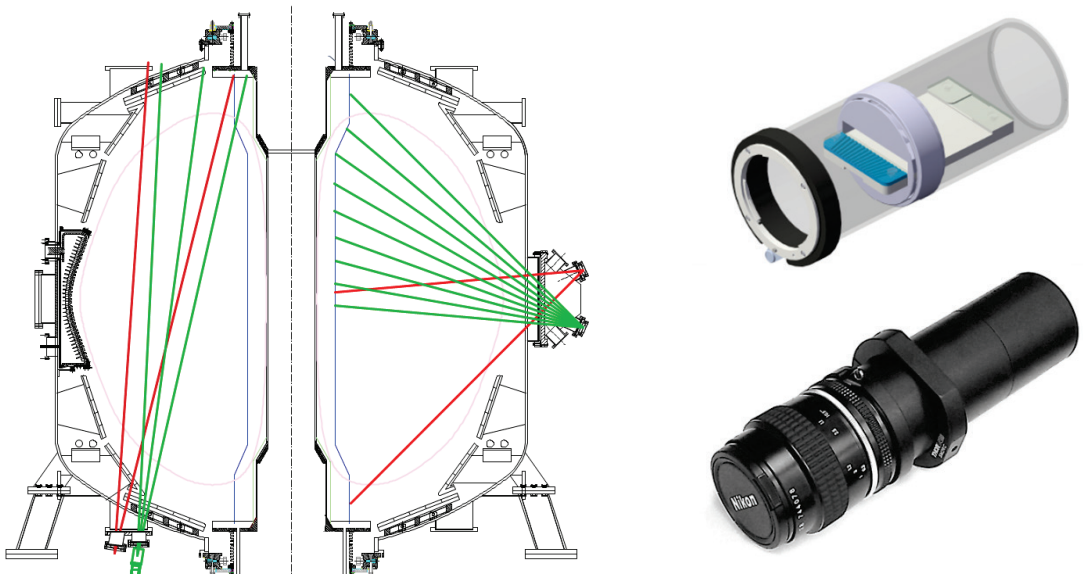

Figure BP-DSOL 8. *Left: schematic of the lines of sight of the UTK spectroscopy (green) and the IR thermography field of view (red). Access from the equatorial plane (bay J) and machine bottom (bay G) allow covering the central column and the upper divertor regions. Right: CAD model of the light collection optics, where the lens mount (black) and the fiber holder assembly (blue) are visible. The bottom picture shows the actual assembly, mounting a Nikon objective.*

6. ELM heat flux analysis - Broadening of heat flux profile with increasing number of ELM filaments

ELMs represent a challenge to future fusion devices, owing to cyclical high peak heat fluxes on divertor plasma facing surfaces. One ameliorating factor has been that the heat flux characteristic profile width has been observed to broaden with the size of the ELM, as compared with the inter-ELM heat flux profile [BP-DSOL 20], so that the 'wetted area (A_{wet})' increases with the ELM size. In contrast, the heat flux profile has been observed to narrow during ELMs under certain conditions in NSTX. It is shown that the ELM heat flux profile width increases with the number of filamentary striations observed, *i.e.,* profile narrowing is observed with zero or very few striations [BP-DSOL 21]. The impact of striations on the 2-D and 1-D radial heat flux profiles during ELMs is shown in Figure BP-DSOL 9. Both profiles in 1(a) and 1(b) were taken at ELM peak times. The number of striations caused by an ELM can be simply counted by comparing both 1-D and 2-D data during the ELM to those before the ELM. Figure 1(a) is for an ELM with no striations observed other than the peak heat flux at the strike point, while figure 1(b) shows four or five striations caused by ELM filaments. It is clear even from these data that the footprint broadens with the number of striations. ELM dynamics exhibit moderate variability during ELMs and across multiple ELMs. The ELM heat flux can evolve in such a way that both A_{wet} expansion and contraction can be observed during the evolution of a single ELM.

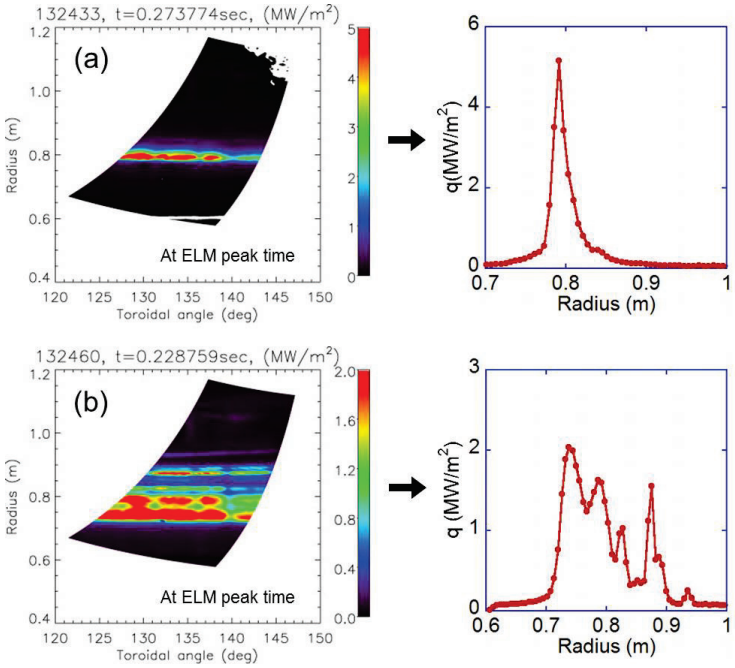

Figure BP-DSOL 9: *Example of 2-D divertor heat flux profiles (left plots), along with the mean 1-D radial profiles (right) at ELM peak times. (a) is for an ELM with no striation except that for strike point and (b) is for an ELM with ~5 additional striations.*

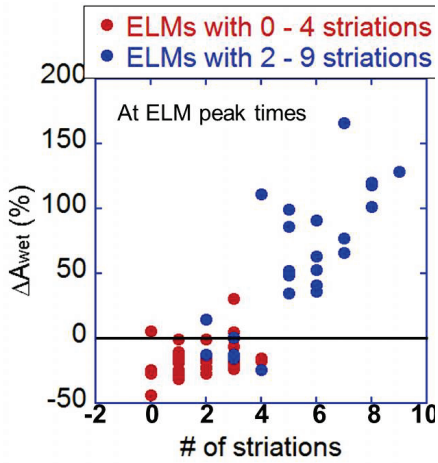

Figure BP-DSOL 10: *Change of wetted area by ELMs with respect to the value immediately before each ELM, as a function of the number of striations observed in the heat flux profiles.*

Figure BP-DSOL 10 is a summary of A_{wet} change as a function of the number of striations observed in the profile for a total of 62 ELMs. Each data point was taken at the ELM peak time,

and there are two groups of data shown in the figure. The red points represent ELMs with 0 – 4 striations, from discharges of weaker shaping (κ~1.9, δ~0.5), which show profile contraction, *i.e.,* $\Delta A_{wet} < 0$, for most of the data. The blue points are for ELMs with 2 – 9, from discharges of stronger shaping (κ~2.5, δ~0.75), and indicate the profiles broadened, *i.e.,* $\Delta A_{wet} > 0$, for many of the data points. It is clear from the combined dataset that the 3 – 4 striations represent the threshold between heat flux profile contraction or expansion.

Because NSTX often lies on the long wavelength current-driven mode side of ideal MHD instabilities, few filamentary structures can be expected under many conditions. ITER is also projected to lie on the current driven low-n stability boundary, and therefore detailed projections of the unstable modes expected in ITER and the heat flux driven in ensuing filamentary structures is needed.

7. References for Section BP-DSOL

[BP-DSOL 1] S.J. Zweben, *et al., Plasma Phys. Contr. Fusion* **56** (2014) 095010

[BP-DSOL 2] Y. Sechrest, D. Smith, T. Munsat, and S. J. Zweben, "Cross-diagnostic Characterization of Edge Fluctuations in NSTX", to be submitted in FY2014

[BP-DSOL 3] G.S. Xu, L.M. Shao, S.C. Liu, *et al., Nuclear Fusion* **54**, 013004 (2014)

[BP-DSOL 4] L.M. Shao, G.S. Xu, S.C. Liu, *et al., Plasma Phys. Cont. Fusion* **55**, 105006 (2013)

[BP-DSOL 5] J. A. Boedo, J. R. Myra, S. Zweben, *et al., Phys. Plasmas* **21**, 042309 (2014)

[BP-DSOL 6] K. Miki, P. H. Diamond, O. D. Gurcan, *et al.*, *Phys. Plasmas* **19**, 092306 (2012); and refs. therein.

[BP-DSOL 7] D. A. Russell, D.A. D'Ippolito, J.R. Myra, *et al.*, presented at the 2014 Transport Task Force Workshop, San Antonio, Texas, April 22 – 25, 2014.

[BP-DSOL 8] D. A. Russell, D.A. D'Ippolito, J.R. Myra, *et al.*, 25th IAEA Fusion Energy Conference, Saint Petersburg, Russian Federation, 13–18 October 2014.

[BP-DSOL 9] B. Cao, D. P. Stotler, S. J. Zweben, *et al.*, *Fusion Sci. Techn.* **64**, 29 (2013).

[BP- DSOL 10] D. P. Stotler, F. Scotti, R. E. Bell, *et al.*, "Midplane Neutral Density Profiles in NSTX", presented at the 21st International Conference on Plasma Surface Interactions (May 26 – 30, 2014, Kanazawa, Japan); submitted to J. Nucl. Mater.

[BP-DSOL 11] E.T. Meier et al., submitted to *J. Nucl. Mater.* (2014)

[BP-DSOL 12] E.T. Meier et al., *Contrib. Plasma Phys.* **54** (2014) 454]

[BP-DSOL 13] E.T. Meier et al., in preparation for IAEA / *Nucl. Fusion* (2014)

[BP-DSOL 14] P.M. Valanju et al., *Phys. Plasmas* **16** (2008) 056110

[BP-DSOL 15] D. D. Ryutov, M. A. Makowski, and M. V. Umansky, *Plasma Phys. Controlled Fusion* **52**, 105001 (2010

[BP-DSOL 16] A.L. Roquemore, *et al.*, *Rev. Sci. Instrum.* **75** (2004), 4190.

[BP-DSOL 17] R. J. Maqueda, R. Maingi, K. Tritz, *et al.*, *J. Nucl. Mater.* **363-365** (2007) 1000.

[BP-DSOL 18] C. L. Lawson and R. J. Hanson, "Solving Least Squares Problems", *SIAM* (1995), 160.

[BP-DSOL 19] A. G. McLean et.al., Accepted for publication in Rev. Sci. Instrum. 85, (2014)

[BP-DSOL 20] T. Eich *et al*., *J. Nucl. Mater.* **415**, S856 (2011)

[BP-DSOL 21] J-W. Ahn *et al*., submitted to *Nucl. Fusion* (2014)

Materials and PFC Research for NSTX-U

Introduction

The Materials and PFC (M&P) research program on the NSTX-U exists to perform the critical research needed to address the fundamental question of what materials are suitable to a fusion plasma experiment and, eventually, a fusion power plant. In the context of the NSTX-U program, this practically means gaining an understanding of the existing materials and wall-conditioning techniques (carbon PFCs + boronization and lithiumization) in use in the machine so that incremental upgrades to reactor-relevant systems (e.g. high-Z tungsten/molybdenum and flowing liquid lithium) will provide the greatest knowledge gain and minimize the operational learning-curves.

The research program in M&P has been divided into three main thrust areas: surface science to support long-pulse operation, tokamak induced material migration and vapor-shielding physics. Each of these thrusts addresses needs of both solid and liquid plasma-facing components with-respect to future power reactors. In the case of surface science, it is necessary to have an accurate understanding of hydrogen and impurity uptake in high-Z systems with and without low-Z coatings. The focus is on lithium coatings on high-Z substrates in order to assess fuel retention which is a critical question for the continued usage of lithium in next-step experiments such as the FNSF which is expected to make use of tritium fuel. The question of retention in a low-Z layer is as important as understanding where those layers are created and destroyed inside the tokamak device. In order to address this area of tokamak-induced material transport, state-of-the-art codes such as OEDGE and WallDYN have been obtained and are being modified for use with the NSTX and NSTX-U machines. These codes will provide an interpretative modeling framework which can be used to build predictive capabilities that will be tested in the NSTX-U during this 5-year plan. The question is applicable to both liquid and solid PFCs as these will determine the lifetime of critical components due to erosion/redeposition processes in the case of solid components and the locations of net material supply and recovery in the case of liquid-metal PFCs. Finally, the ultimate temperature limits of a lithium surface greatly impacts the technological and plasma-control choices associated with the use of lithium in a future power reactor. Lower temperature limits (e.g. 400C) will necessitate the use of fast-flowing systems or alternative methods of reduced plasma power fluxes. On the other hand, higher temperatures may provide a means of accessing a self-shielding regime termed *continuous vapor-shielding*. Already experiments have demonstrated operation of a linear plasma source on a 1000C target without contaminating the plasma source. Understanding the near-surface forces and impurity transport for a lithium vapor cloud has the possibility of improving our understanding of off-normal erosion of high-temperature tungsten PFCs and whether such events and abnormal erosion yields will terminate a discharge.

Progress in each area is continuous in the past year due in part to the capabilities present at the PPPL, collaborator institutes and the active collaboration with the Dutch Institute for Fundamental Energy Research (FOM-DIFFER). This progress is detailed below.

Surface Science Experiments on D Retention in Li Films on TZM

Two surface science laboratories have been established at PPPL to advance the scientific understanding of plasma-lithium surface interactions, aid the development of liquid metal plasma facing components with superior performance for long pulse discharges and provide the pathway to advanced PFCs for FNSF. Deuterium retention in ultrathin lithium films (three monolayers thick) on molybdenum substrates was studied in ultrahigh vacuum environments to elucidate the chemistry at the Mo-Li interface [Fig. MP-1]. The lithium films were exposed to deuterium ions from an electron cyclotron resonance (ECR) plasma source. Retention was measured using temperature programmed desorption (TPD) by monitoring the evolution of deuterium from the lithiated surface as the sample was heated. [MP-1]

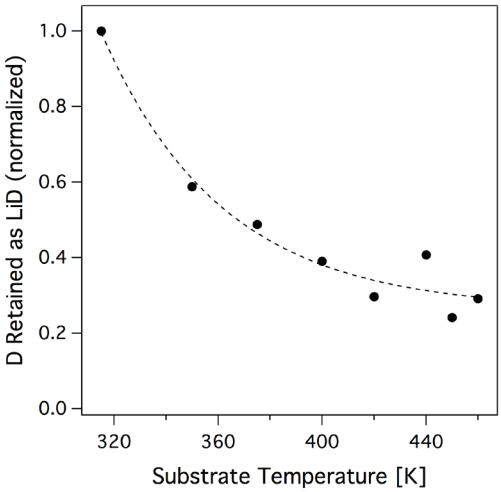

Figure MP-1: *The amount of deuterium retained as LiD in a 3 ML Li film as measured for ion bombardment at different substrate temperatures using TPD. The decrease in relative D retention with increasing substrate temperature is described well by an exponential fit.*

This work has shown that D is retained in metallic Li films as LiD and less LiD was formed by ion bombardment at increasing substrate temperatures above 300 K. Figure MP-1 shows that the relative D retention drops exponentially with temperature up to 400 K. These results are relevant to results on the Lithium Tokamak Experiment (LTX) in which the D pumping ability of liquid Li films declined more rapidly than solid Li films [Ref. MP-2]. Experiments conducted on ultrathin oxidized lithium films indicated that the amount of D retained in the lithium oxide film was 2.5 times higher than the amount of D retained as LiD in the metallic Li film. However, lithium oxide retains D as LiOD, which is less thermally stable than LiD. These results highlight the importance of maintaining a metallic Li layer and shows that oxygen can be detrimental to D retention in Li films on TZM at elevated temperatures.

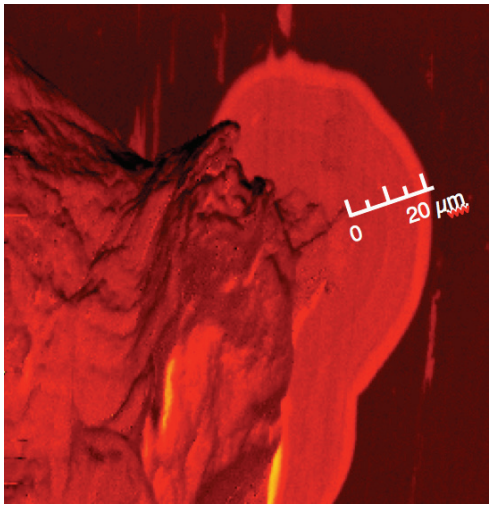

Figure MP- 2: *False color image of the spreading of lithium onto stainless steel, observed by the Scanning Auger Microprobe.*

Wetting will be a key factor in the design and operation of liquid metal plasma facing components foreseen for NSTX-U. We have made initial measurements of wetting of lithium on a stainless steel surface using a Scanning Auger Microprobe. This spreading of lithium onto the stainless steel surface occurred at room

temperature (i.e. from solid lithium) after the surface had been cleaned by an argon ion beam [Fig. MP-2]. This work will be extended to Mo and W substrates at elevated temperatures to understand the fundamental surface chemistry of wetting of candidate materials for liquids plasma facing components.

Material Analysis and Particle Probe (MAPP)

The Materials Analysis and Particle Probe (MAPP) is a unique diagnostic that allows *in situ* analysis of samples exposed to tokamak plasmas. The implementation of MAPP on NSTX-U is a collaborative effort including researchers and graduate students from the University of Illinois at Urbana-Champaign, and the Program in Plasma Physics at PPPL. Testing of MAPP prior to installation on NSTX-U continued on the Lithium Tokamak eXperiment (LTX) during the past year. Samples of plasma-facing component (PFC) materials that included stainless steel and a molybdenum alloy (TZM) were coated by evaporation of lithium from a reservoir inside LTX. They were then withdrawn into an analysis chamber, where they were studied using X-ray photoelectron spectroscopy (XPS). A series of XPS measurements were taken over a span of several days, and changes in the fractions of lithium compounds on the samples were monitored (Fig. MP-3). This provided information on the "passivation" of lithium coatings on PFCs, which is an important indicator of plasma performance.

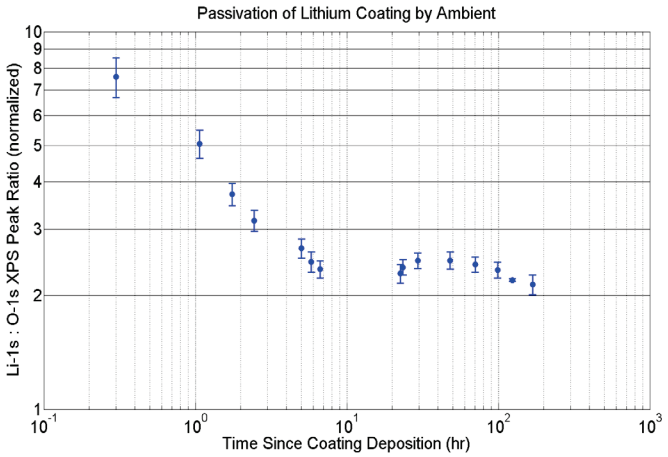

Figure MP- 3: *Normalized ratio of Li-1s to O-1s XPS peaks is plotted against time since a 50 nm lithium coating was evaporatively deposited on a 316 stainless MAPP sample at 25 °C. The sample is serving as a proxy for cold LTX shells, and the lithium coating is passivation due to reaction with the vacuum ambient. This result suggests near-complete formation of Li_2O within about 5 hours of coating deposition.*

Activities related to the installation of MAPP on NSTX-U included a successful "fit-up" of the analysis chamber and bellows drive on a lower dome port. Progress was also made on remote control of the surface analysis diagnostic. For XPS, this included the safety interlock systems and providing power for the X-ray source and microchannel plate detectors. Remote control was also implemented for scanning the electrostatic analyzer voltage for determining electron energies. For TDS, remote control is operational for the residual gas analyzer and the four sample heaters, whose temperatures can be set separately. A remotely-controllable ion source was also implemented, and initial tests have been performed for "depth profile" with ion bombardment.

Deciphering the PMI surface chemistry of lithium-based PFCs and its effect on high-performance plasmas in NSTX

Work in 2013-2014 included preliminary studies of lithium thin-films on various high-Z substrates including Mo and W. Studies of D, He and D/He particle bombardment of Li thin-films were conducted both in laboratory facilities at Illinois with in-situ diagnosis and at the Pilot-PSI and Magnum-PSI facilities in DIFFER. Furthermore, high-flux and high-fluence exposures of lithiated graphite were also conducted at DIFFER. In these experiments we identified how lithium coatings on tungsten can survive plasma fluences of order 10^{25} cm^{-2} that resulted in no fuzz formation even at relatively high temperatures near 800 C. Furthermore, lab experiments at UIUC also demonstrated that for those conditions at room temperature, lithium coatings survived and were integrated in the tungsten matrix. This was found for cases with D, He and combined He/D irradiation. Fig. MP-4 shows SIMS results that demonstrate the survival of a thin-film of lithium about 100-nm in thickness.

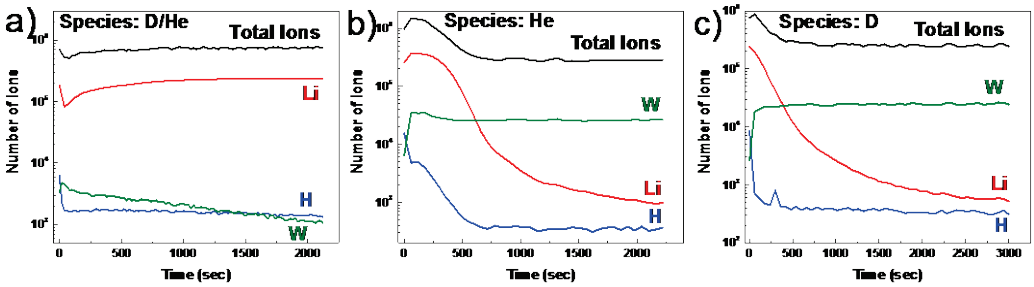

Figure MP- 4: *Dynamic TOF-SIMS data showing depth profiles for tungsten samples coated with 100nm of Li and exposed to Pilot-PSI plasmas: (a) 10% He-D plasma, (b) He plasma and (c) D plasma.*

In addition, experiments with lithiated graphite having a 1-μm lithium coating also demonstrated that deuterium retention still persisted even for exposure to 10^{24}-10^{25} cm^{-2} fluences indicating that for plasma shot conditions in NSTX-U, lithium conditioning will still enable deuterium particle control at the edge.

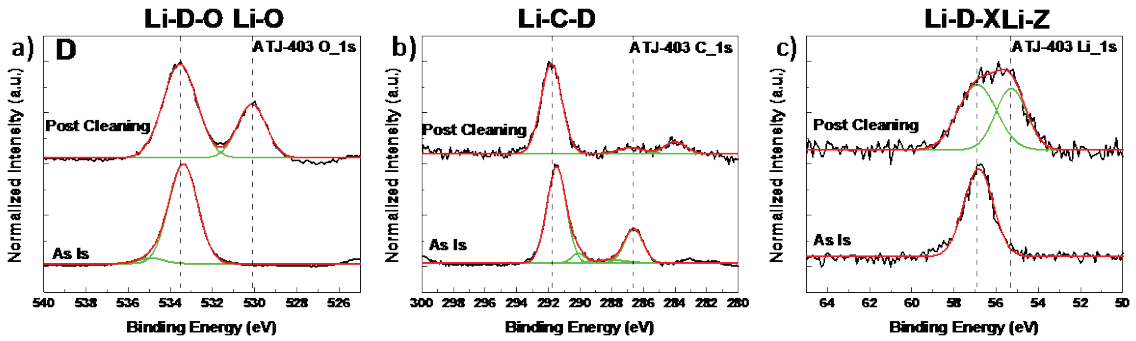

Figure MP- 5: *XPS spectra of lithiated graphite after exposure to D plasma in Pilot-PSI: (a) O1s spectra showing Li-D-O complexes, (b) C1s spectra and (c) Li1s spectra.*

OEDGE and WallDYN modeling of the NSTX and NSTX-U

The OEDGE (OSM + EIRENE + DIVIMP) code suite has been applied to study global erosion and migration patterns in the NSTX geometry. A fully carbon wall has been simulated as a first step, and the scaling of gross carbon erosion with various parameters has been examined. Special attention has been paid to gross erosion from the outer wall, which can be a large source of impurities due to the negligible probability of prompt redeposition. Simulations show that the gross erosion rate from the outer wall, integrated toroidally and poloidally, decreases slightly with increasing divertor electron temperature, as seen in Figure MP-6. This result runs contrary to naïve 1D particle flux and power flux scalings, which scale with $T^{1/2}$ and $T^{3/2}$, respectively. Since the gross erosion rate at the wall depends strongly on how many neutrals reach the wall from the outer strike point, the simulated behavior can be explained by increasing neutral opacity being dominant over increasing neutral flux recycled from the divertor target. Scaling studies of carbon walls with reduced recycling coefficients have shown that, despite the large discrepancy in surface area, the recycling behavior of the region near the strike point has considerably more influence over the outer wall erosion rate than the recycling behavior of the wall itself. In addition, a scaling study of the effect of a D_2 puff (similar to the Gas Puff Imaging diagnostic) has shown that such a puff will increase the outer wall erosion rate by 0.1-1.0 mg/s.

Initial steps have been taken to apply the WallDYN mixed material evolution code to NSTX-U. WallDYN will allow for the calculation of time-resolved surface concentrations and impurity erosion fluxes for a fully mixed C/Li/Mo environment. The calculations made by WallDYN will be directly comparable to experiments carried out on NSTX-U in 2015/2016, allowing for the fine-tuning of the computational model and the eventual development of predictive capability.

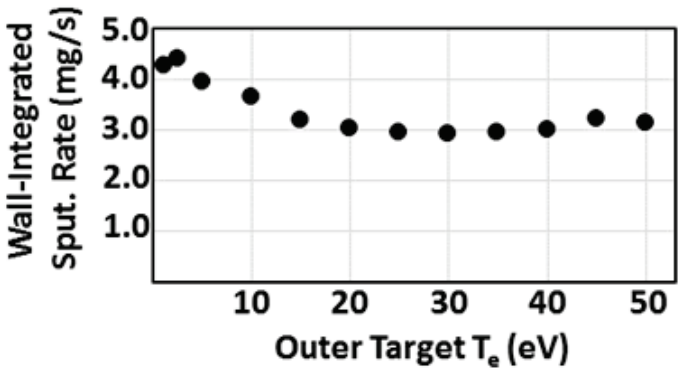

Figure MP- 6*: Gross erosion calculated by OEDGE, integrated along the outer wall, as a function of divertor target plasma temperature.*

In parallel with the computational effort, plans have been made for establishing diagnostic support for material migration experiments during the first year of NSTX-U operation. A set of 3 quartz crystal microbalances will be set up in recessed areas along the outer wall, allowing shot-to-shot measurements of erosion and deposition with a sensitivity of 0.7 nm. The MAPP system (described above) will allow shot-to-shot analysis of the composition of deposited material, in addition to its quantity. An array of witness plate samples will provide wide poloidal coverage of campaign-integrated erosion/deposition at the vacuum vessel wall. A probe head to measure parallel and perpendicular SOL flows at the outboard midplane is in the initial stages of development.

Thermogravimetric Analysis (TGA) diagnostic development

The utilization of QCM diagnostics for mass transport effects is effective but limited in that mass fluxes alone do not distinguish between codeposited fuel and eroded PFC material. The MAPP diagnostic can make compositional measurements of non-hydrogenic components of deposited films and via thermal desorption spectroscopy (TDS), can measure the amount of fuel on a given sample. An alternative approach for measuring the mass of volatile species in a layer is to perform thermogravimetric analysis (TGA) on the samples. In this method, the mass of the sample is monitored while undergoing thermal desorption, similar to the TDS process. An existing QCM system was modified to allow bake-out capability up to 400C with an additional sample heating system capable of reaching over 900C. In addition, a replacement piezoelectric material, gallium ortho-phosphate ($GaPO_4$), was identified to enable operation at such high temperatures. The method was qualitatively demonstrated in tests in the Lithium Technology Development laboratory where carbon-hydrogen codeposits were degassed at elevated temperatures and a net mass loss was measured before and after the desorption process. The co-deposits were created in-situ with a magnetron sputtering system operating with a graphite target and hydrogen working gas. While confirming the basic premise of the method, several improvements in the technique and apparatus were identified as necessary to make the technique more quantitative. In the present operation at room temperature with a temperature ramp to achieve outgassing, the temperature-dependent crystal frequency was identified as a critical parameter necessitating an improved temperature measurement of the QCM front-face. Alternatively, the $GaPO_4$ crystals can be operated at an elevated temperature to minimize the fuel codeposition quantity and measure the non-volatile mass change more directly. If further development proves successful, the technique could be applied to existing QCM devices with minor modifications.

High-temperature erosion of lithium PFCs in high-flux tests

Lithium coatings are applied to the walls of many current plasma confinement devices to enhance performance and protect the underlying solid walls. Li-coated high-Z substrates are planned for use in NSTX-U and are a candidate plasma-facing component (PFC) for a DEMO reactor. However Li evaporation and the strong enhancement of the Li sputter yield at elevated temperatures observed on low-flux experiments [MP-3] implies that the maximum Li temperature permitted on such devices may be unacceptably low. Thus it is crucial to characterize gross Li erosion rates under high-flux plasma bombardment. Recently thin (< 1 μm) Li films on TZM molybdenum substrates were studied in the Magnum-PSI linear plasma device capable of ion fluxes > 10^{24} m^{-2} s^{-1} and Li surface temperatures $\leq$ 800 °C. Predictions of temperature-dependent Li erosion rates were obtained from SDTrimSP simulations of collisional Li sputtering, the thermal-spike model of temperature-enhanced sputtering [MP-4], and Langmuir law evaporation rates. Measured Li erosion rates were reduced by a factor > 1000 from these predictions [MP-5].

Two modifications were proposed to the Li erosion model to interpret this strongly suppressed Li yield. First, erosion is reduced in part due to the preferential sputtering and lithium deuteride (LiD) formation that occurs when D atoms are implanted in and adsorbed on a Li surface. Second, an alternative model of thermal sputtering involving the creation of surface adatoms [MP-6] was analyzed and tested. Li erosion behavior was measured during bombardment with a noble gas (Ne) that does not chemically react with Li was found to agree well with predictions. Next the ratio of the total D fluence to the surface Φ to the areal density of the Li coating ρ was varied to quantify the differences in the Li erosion behavior between the low-fluence ($\Phi/\rho \ll 1$) and high-fluence ($\Phi/\rho \gtrsim 1$) regimes for macroscopically thick (500 μm) Li coatings [MP-7]. The time-dependent ratio of D to Li atoms on the target surface was inferred using the results of molecular dyanamics (MD) simulations of D diffusion in liquid Li. The adatom-model of mixed-material Li/D thermal erosion was applied to the resulting data; see Figure MP-7. This model provides good agreement to the measured Li erosion rate during these discharges if a reduction of the Li thickness to 25 μm via macroscopic melt motion is assumed. This implies that temperature limits for lithium-coated PFCS in a fusion reactor environment may be significantly higher than previously envisioned.

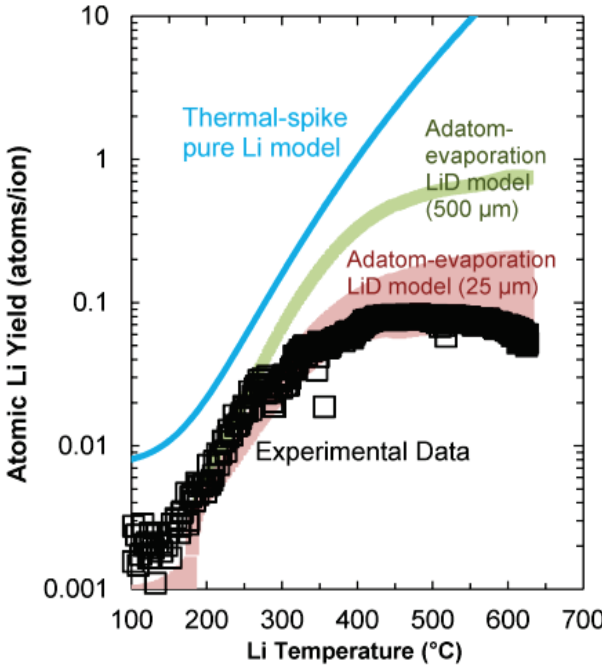

***Figure MP-** 7: Inferred atomic Li yields during 20 eV D→Li bomardment in Magnum-PSI. Predictions of the adatom-evaporation LiD model and thermal-spike pure Li model are overlaid.*

Stable vapor-cloud production and analysis in divertor-like plasmas

Once issues associated with erosion rate are determined, the question of the near-surface plasma interacting with the emitted lithium vapor becomes important. Last year, experiments demonstrated the production of a stable cloud of lithium vapor in front of a lithiated sample during exposure to the Magnum-PSI plasma device. A model has been developed to describe the pre-sheath region of the plasma directly in front of the target. A control-volume integral is applied to the mass and momentum fluid equations, including ionization and friction effects, in the pre-sheath region, shown in figure MP-8. As the sheath region is of order 10 microns thick and the ionization mean-free path of lithium is approximately 300 microns in these plasmas, it is appropriate to consider the pre-sheath effects themselves. If one assumes an electrically connected plasma, for which, the Bohm sheath criteria is applicable, the potential well of the pre-sheath region can be analyzed including ionization and friction losses [MP-8]. The result indicates that the momentum loss terms have the tendency to *increase* the potential drop through the pre-sheath region and thereby create the scale length of this region. The magnitude of the pre-

sheath drop is of order $0.5T_e$ which, for these plasmas, is about 1eV. The resulting scale length calculated from the atomic physics rates is about 3mm which is comparable in size to the observed emission region. The magnitude of the potential well is significant for lithium emission from the liquid surface as previous measurements of lithium emission indicates energies at or below 1eV [MP-3]. This means that the potential well alone is sufficient to recover a large fraction of the emitted particles providing a stabilizing effect. This trapping effect provides an additional means of preventing lithium from contaminating further parts of the experimental device; it further indicates the need to re-evaluate the temperature limits of liquid lithium PFCs. Additional analysis and model development is underway.

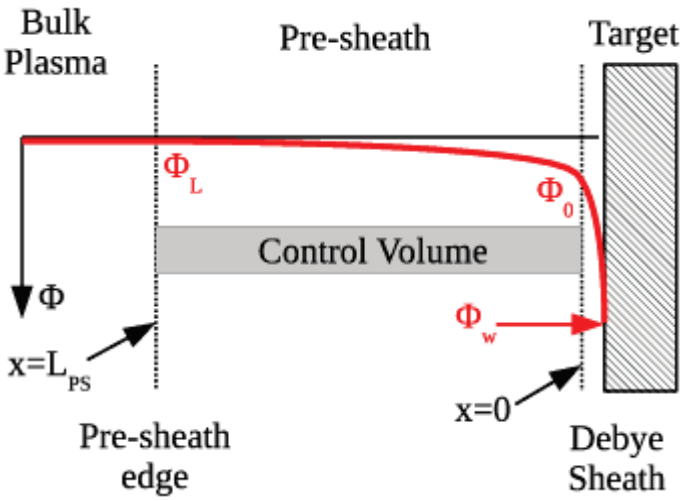

Figure MP- 8: Diagram indicating transition from the bulk plasma to the target and the region of the control volume. A cartoon representation of the electric potential variation through the transition region to the sheath is also shown.

References

[MP-1] A.M. Capece, J.P. Roszell, C.H. Skinner, B.E. Koel submitted to J. Nucl. Mater., (2014)
[MP-2] J.C. Schmitt, et al., J. Nucl. Mater. **438** (2013) S1096.
[MP-3] R.P. Doerner et al., J. Nucl. Mater. 290-293 (2001) 166-172.
[MP-4] J.P. Allain et al., Phys. Rev. B 76, 205434 (2007).
[MP-5] T. Abrams et al., Fus. Eng. Des. (2014), dx.doi.org/10.1016/j.fusengdes.2014.06.005
[MP-6] R.P. Doerner et al., J. Appl. Phys. 95 (2004) 4471.
[MP-7] T. Abrams et al., J. Nucl. Mater., *in press*.
[MP-8] M.A. Jaworski, et al., in preparation.

Macroscopic Stability Research

Macroscopic stability research during FY2014 progressed along many lines of research within three key areas: stability, 3D fields, and disruptions. This research is all aimed at enabling long-pulse high performance in NSTX-U. Advanced passive stability understanding and active feedback control will be integrated into a disruption avoidance system, allowing us to sustain macroscopic stability in the new low collisionality regime of NSTX-U. Understanding 3D field effects will provide a physics basis for optimizing stability through new capabilities of equilibrium profile control. Finally, understanding disruption dynamics, and development of techniques for disruption prediction, avoidance, and mitigation in high-performance ST plasmas will be greatly beneficial to future devices.

Stability

Resistive wall mode stability theory and calculations

Validated and benchmarked calculations of kinetic resistive wall mode (RWM) stability are important for disruption avoidance in ITER and other high performance tokamaks by providing a confidently predicted RWM stable operating region. In Ref. [MS-RWM-1] such calculations were benchmarked between three leading codes, MARS-K [MS-RWM-2], MISK [MS-RWM-3], and PENT [MS-RWM-4]. Good agreement was found between the code calculations for two Solov'ev analytical equilibria and a projected ITER equilibrium [MS-RWM-1], including the most important stabilizing kinetic effect: resonances between the plasma rotation and frequencies of thermal particle's motion [MS-RWM-5]. However, several important physics considerations were not included in that effort, including: non-resonance rotational effects [MS-RWM-6] collisions [MS-RWM-7], and isotropic energetic particles [MS-RWM-8]. The benchmarking effort presented in Ref. [MS-RWM-1] was continued, while including these three additional pieces and presenting a more realistic projection of ITER stability.

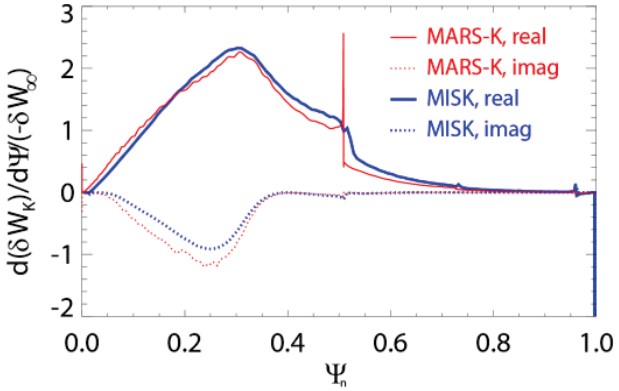

***Figure MS-RWM-1**: $d(\delta W_K)/d\Psi/(-\delta W_\infty)$ vs. Ψ for l=0 trapped alpha particles in the ITER case at the nominal rotation, as calculated by MARS-K and MISK.*

Due to ITER's relatively low plasma rotation and collisionality, collisions and rotational effects were both found to have little impact on stability, and rotational effects also will not self-consistently affect the ITER RWM eigenfunction. Alpha particles, in contrast, were found to be very important to stability. Without alpha particles, ITER is projected to be unstable to the RWM, but the expected level of alphas is calculated to provide a just sufficient level of stability, which agrees with a previous result [MS-RWM-8]. Figure MS-RWM-1 shows good agreement between

the MARS-K and MISK contributions to δW_K vs. Ψ from the trapped, $l=0$ bounce harmonic component for alpha particles, a previously un-benchmarked portion of the codes.

Additionally, a significant new capability was added to the MISK code when the effect of anisotropy of the plasma pressure on the resistive wall mode stability energy principle was derived and implemented [MS-RWM-9]. The fluid anisotropy was treated as a small perturbation on the plasma equilibrium, which allows a relatively simple treatment of the problem. Fluid treatment with CGL pressures is akin to consideration of the high frequency mode rotation limit. More complete treatment leads to kinetic terms in addition to anisotropy corrections to the fluid terms. Specifically, the shear Alfvén, fast magneto-acoustic, and kink fluid terms are relatively simply modified and these corrections are small. The kinetic effects depend upon $\partial f/\partial \varepsilon$ and $\partial f/\partial \Psi$, while the anisotropy correction to the fluid pressure-driven ballooning term depends upon $\partial f/\partial \chi$, where f is the distribution function, ε is the energy, Ψ is the flux function, and χ is $v_{||}/v$, the pitch angle variable. Expressions for these terms for a perturbed bi-Maxwellian distribution function for thermal particles were derived.

For thermal particles with larger perpendicular energy than parallel, the ballooning destabilization term is reduced, while for $T_{||} > T_{\perp}$ it is enhanced. This leads to a reduction of the fluid growth rate of the RWM for $T_{||}/T_{\perp} < 1$ and an increase for $T_{||}/T_{\perp} > 1$. The stabilizing kinetic effects of the trapped thermal ions can also be enhanced for $T_{||}/T_{\perp} < 1$. Together these two effects can lead to a modest increase in resistive wall mode stability.

DIII-D experiments: Unification of kinetic RWM stability physics in tokamaks

A dedicated experiment was recently run on DIII-D (S.A. Sabbagh, J.W. Berkery, J.M Hanson, et al. "*MP2014-22-07: Testing kinetic RWM stabilization theory at marginal stability in high beta, tearing mode stabilized plasmas*") to test kinetic RWM stabilization physics proposed in several NSTX publications [MS-RWM-10 - MS-RWM-14] with the goal of unifying the physics understanding of kinetic RWM marginal stability conditions between devices. The experiment was successful and analysis of the data is ongoing, but substantial progress has already been made in comparing experimental observations and kinetic RWM stability analysis between the devices.

Prior experiments have shown that unstable RWMs cause disruptions – full current quenches that terminate the plasma, and major thermal quenches that rapidly drop the plasma stored energy by 50 – 80%. Such disruptions observed in this experiment, caused by rapidly growing RWM activity, appear to be at points of RWM marginally stability (full analysis for all representative cases are underway). RWM instability doesn't occur when significant tearing modes (TM) appear, and so the present experiment was designed to create significant periods during which the plasma was stable to large tearing modes that would otherwise preclude RWM destabilization. As tearing modes are planned to be stabilized in ITER and future tokamaks, one must be concerned with what instabilities limit plasma performance when TMs are avoided or controlled. Another important observation in this experiment is that RWM activity can itself trigger tearing modes. A unification of the underlying kinetic RWM stability physics between NSTX and DIII-D will give

the greatest confidence to confidently extrapolate results to future devices for disruption avoidance.

High β_N, q_{min} plasmas were chosen to study kinetic RWM stability characteristics in this DIII-D experiment because for several reasons. These plasmas are candidates for steady-state, high β_N operation and are therefore important to the DIII-D program and future tokamak operation. These plasmas can also operate at high $q_{min} > 2$ which eliminates the 2/1 rational surface and therefore precludes destabilization of the significant 2/1 tearing mode. In this condition, 3/1 tearing modes were observed to be destabilized, but ECCD control was used to successfully suppress this mode, allowing an investigation of the RWM marginal stability point over a wide range of plasma rotation profiles. RWM marginal stability crossings were found for three different rotation profiles and plasma conditions:

1. Induced by profile peaking at moderate β_N and high rotation
2. Found at high β_N and low rotation
3. Found at high β_N and high rotation

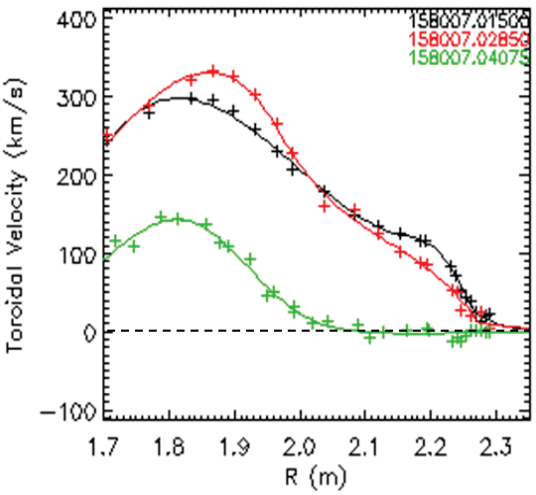

Figure MS-RWM-2: *Rotation profiles in DIII-D near different RWM marginal stability conditions.*

Plasma rotation profiles representing these conditions are shown in Figure MS-RWM-2. The unique 1 ms charge exchange recombination (CER) spectroscopy capability in DIII-D and magnetics showed that radially extended ELMs, also named "global bursting MHD events" because the modes are not edge localized, sometimes correlate with crossing the RWM marginal stability point - either moving toward instability or *toward stability* - but a trigger that initiates RWM growth was sometimes not found. The high time-resolution CER show that the thermal and rotation collapses presently appear to be caused by RWM mode growth rather than a loss in rotational torque balance.

Representative detail of approaching and crossing the RWM marginal stability point were produced in the three different rotation profile and β_N conditions mentioned above. Here, we examine just one condition in detail for the sake of brevity. Figure MS-RWM-3 illustrates a 50% thermal collapse during RWM activity. The lower right-hand side magnetic spectrogram shows that a 3/1 tearing mode stabilizes before the large thermal collapse (time period highlighted in yellow). This stabilization of the tearing mode (not mode locking) is confirmed by the ECE and MIR diagnostics. During the next time interval (highlighted in green), the frequency of ELMs decreases and β_N rises, even though NBI power has been automatically decreased via real-time β_N control. The $n = 1$ RWM sensor amplitude then begins to rise during this period of approximately 60 ms, indicating resonant field amplification of the stable $n = 1$ RWM field perturbation rising to about 5G. After this point, there is a strong increase in the $n = 1$ RWM field perturbation. The

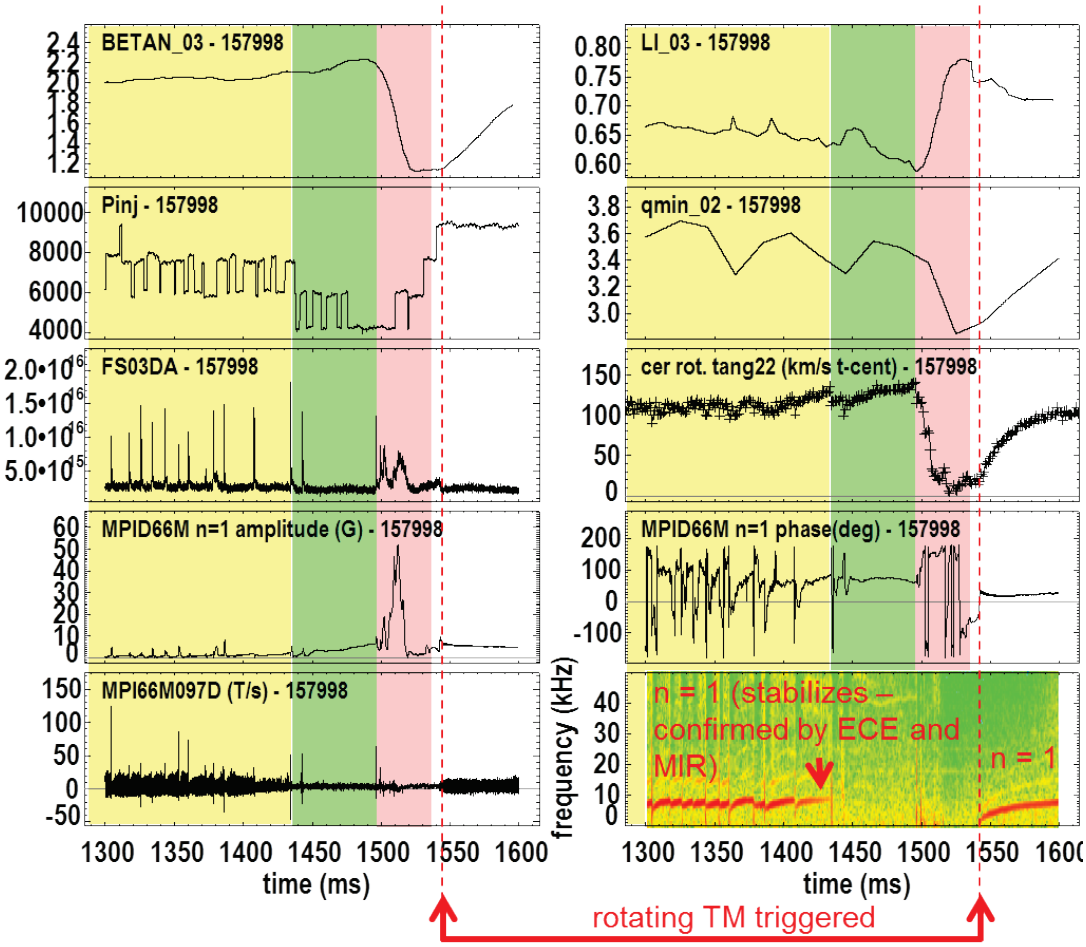

Figure MS-RWM-3*: Illustrative plasma parameter waveforms approaching an RWM marginal stability point in DIII-D.*

detail of this increase is shown in Figure MS-RWM-4, which shows a zoomed-in view of the time period highlighted in red in Figure MS-RWM-3. Three bursts are observed in the D_α signal (upper left frame in the figure) which would generically be called "Edge Localized Modes" (ELMs), however, this is literally a misnomer, as these events are found to be radially extended modes, and are therefore not "edge localized". They otherwise share common characteristics with ELMs, including toroidal and poloidal localization. The 3D magnetics arrays in DIII-D show the mode to be ballooning, as the mode amplitude is observed to increase as the mode propagates through the device midplane. These characteristics, especially the radially extended eigenfunction, suggest that these events are closer to "X-Events" in DIII-D [MS-RWM-15], or "3D ballooning modes" in TFTR [MS-RWM-16], but the presently observed radially extended MHD bursts are significantly less perturbative to the plasma than either. The toroidal and poloidal mode spectrum for a toroidally/poloidally localized mode is expected to be broad, which is measured, but these spectra vary significantly when comparing different instances of these events. The 1 ms CER diagnostic data shows an orderly decrease of the plasma toroidal rotation as the strong n = 1 RWM that causes the strong β_N collapse unfolds. The middle two frames of Figure MS-RWM-4 show the n = 1 RWM amplitude and phase. During the initial drop in rotation apparently caused by the first bursting event (yellow highlight), the n = 1 amplitude changes a

small bit, but doesn't show strong growth, the RWM apparently rotates in the co-NBI direction, and the plasma rotation itself partially recovers within 3 ms. The next bursting event (red highlight) shows a strong increase in the n = 1 amplitude in a short period ~ 2 ms which is near the expected RWM growth time. This strong increase in n = 1 amplitude leads to a strong decrease in plasma toroidal rotation, which would be caused by neoclassical toroidal viscosity (NTV) if (as expected) the observed global perturbation is ideal. The next period (highlighted by green) interestingly shows damping of the n = 1 RWM amplitude after a smaller MHD burst, and finally strong RWM growth occurs during the time of the second red highlighted region, without an obvious trigger.

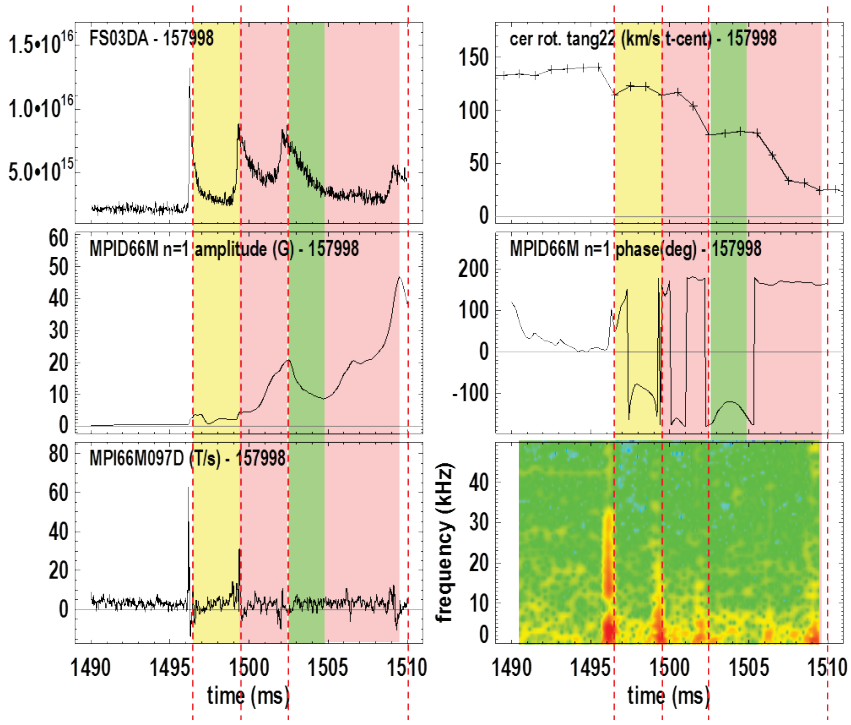

Figure MS-RWM-4: *Illustrative plasma parameter waveforms approaching an RWM marginal stability point in DIII-D (zoomed in view of Figure MS-RWM-3).*

The unique 1 MS CER data indicates that RWM instability is caused by peaking of both the ion temperature, and plasma toroidal rotation during this time interval (Figure MS-RWM-5). Direct analysis of the kinetic RWM stability of this plasma await the completion of the equilibrium reconstructions of this discharge. The stability of similar discharges used to design the experiment have been completed, and are shown in the next section.

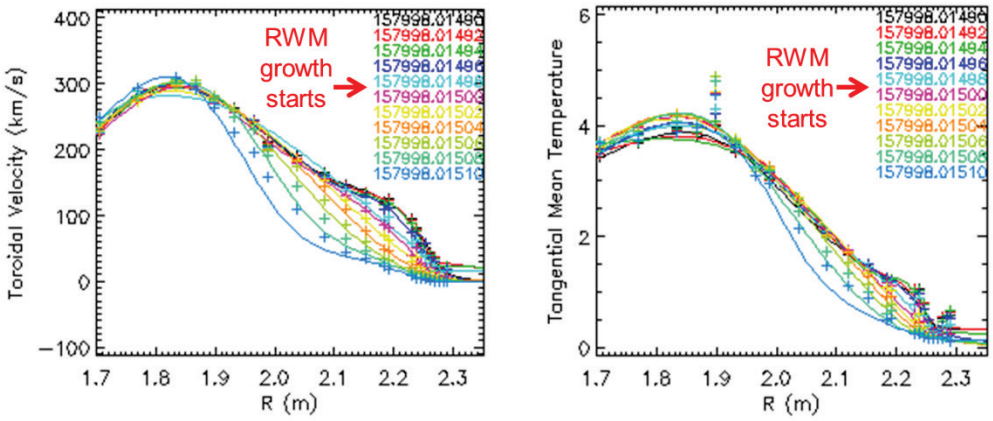

Figure MS-RWM-5: *High time-resolution CER data showing profiles of plasma rotation and ion temperature during the n = 1 RWM growth, showing a peaking of both profiles.*

This especially illustrative example yields two new hypotheses to potentially explain the dynamic shown last few figures. First, a simple model of kinetic RWM stabilization has been long proposed by Boozer [MS-RWM-17] and can qualitatively explain the detail shown. Details of this hypothesis are explained by Figure MS-RWM-6. The figure shows a contour plot of RWM sensor signals (toroidal angle vs. time), also showing the field perturbation (in Gauss) in the upper frame

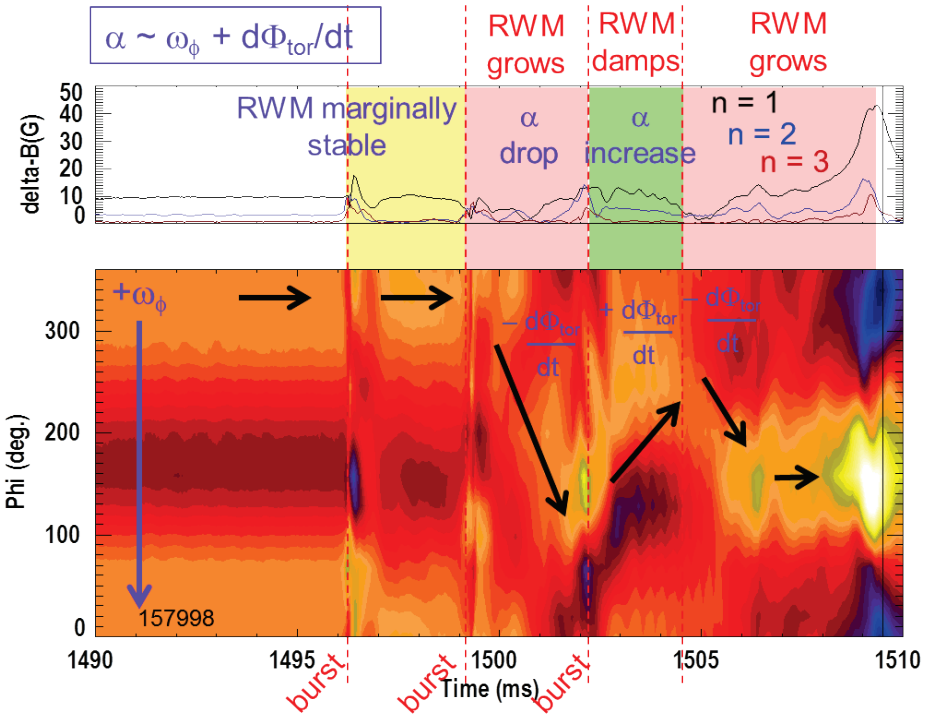

Figure MS-RWM-6: *Contour plot of RWM sensor signals (toroidal angle vs. time), showing the δB perturbation (in Gauss) in the upper frame for n = 1, 2 and 3 field components. Time intervals highlighted by yellow, red and green correspond to time intervals similarly highlighted in Figure MS-RWM-4.*

for n = 1, 2 and 3 field components. Time intervals highlighted by yellow, red and green correspond to time intervals similarly highlighted in Figure MS-RWM-4. In the Boozer theory, the RWM is stabilized by the differential rotation between the plasma rotation and the RWM rotation, with a difference symbolized by the parameter "α". Higher α signifies a higher differential rotation between the mode and plasma rotation, which increases stability, with the opposite being true for lower α. When the plasma is at RWM marginal stability, small changes in α can bring the equilibrium across the marginal point. We then notice a drop in α in Figure MS-RWM-6 as the plasma enters the following time interval highlighted in red. This is because the RWM phase is observed to decrease during this period, meaning that it spinning with the plasma rotation at a faster pace, and therefore decreasing the differential rotation with the plasma. This could change the RWM stability from stable to unstable since the plasma is expected to be at marginal stability in the yellow highlighted time interval. In the next time interval highlighted in green, there is an observed temporary reversal in the sign of the change in the RWM phase, which indicates an increase in α, and therefore increased stability. This correlates with the hypothesis that the plasma has now moved back over the marginal point to again become RWM stable. In the next time interval, again highlighted in red, there is another reversal in sign of the RWM phase change vs. time, which again means a drop in α and theoretically reduced stability, which again correlates with RWM growth in the experiment.

A second new and provocative hypothesis arises from these observations – that the plasma is becoming non-linearly destabilized by the bursting MHD events that occur. The following qualitative explanation follows from work of Bagaipo, et al. on the non-linear destabilization of MHD interchange modes [MS-RWM-18]. Again, consider the illustration in Figure MS-RWM-6 and examine the following highly simplified qualitative illustration of non-linear MHD interchange destabilization shown in Figure MS-RWM-7. Following the same progression through the highlighted time intervals in Figure MS-RWM-4 as done in the prior paragraph, before the yellow highlighted region (before the first MHD burst), we expect we are near the RWM linear stability boundary, but we are still linearly stable (see Figure MS-RWM-7 – we are in the "RWM stable" region). Since an MHD burst has not occurred yet, the blue region in this figure labelled "RWM non-linearly unstable" does not exist. Then, after the first MHD burst in Figure MS-RWM-4, a region of RWM non-linear instability exists, but as the mode is not growing strongly, showing that the plasma does not cross into the RWM non-linearly unstable

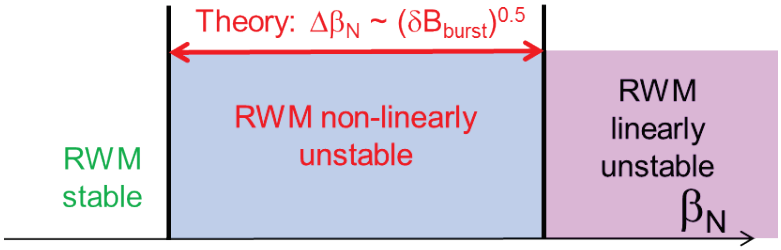

Figure MS-RWM-7*: Simple qualitative illustration of non-linear RWM destabilization hypothesis.*

region. Note that the size of the RWM non-linear unstable region scales in theory with the amplitude of the field perturbation generated by the bursting MHD event that is superposed in

time and space with the RWM activity. Therefore, as the field perturbation generated by the bursting MHD event dies away on a fast timescale (magnetics and other diagnostics indicate the timescale to be ~ 1 ms), the non-linearly destabilized region also reduces to zero. By the time of the next highlighted time interval (first red interval in Figure MS-RWM-4), the plasma rotation and ion temperature profiles have now increased in peakedness to bring us closer to RWM linearly unstable point, and when the second MHD burst occurs, the observation of the strongly growing RWM is consistent with the amplitude of the MHD burst moving the plasma into the RWM non-linearly unstable region. Further supporting evidence of this hypothesis is shown in Figure MS-RWM-4 as it appears that the growth rate of the unstable RWM may be decreasing as the green highlighted time interval is approached, correlated to the field perturbation generated by the second bursting MHD event dying away and the related vanishing of the non-linear unstable region. Then, as the green highlighted time interval is reached, the third bursting event observed apparently not have sufficient field perturbation amplitude to create a significant RWM non-linear unstable region. By the time of the second red highlighted time interval, the plasma finally crosses into the linearly unstable RWM region, and the mode strongly grows continually.

Comparison of NSTX and DIII-D kinetic RWM stabilization physics

Kinetic RWM analysis of the exact equilibria that reach the marginal RWM stability point in the experiment described above await the computation of the experimental kinetic equilibrium reconstructions. However, the high β_N, high q_{min} target plasma used in the experiment was taken directly from DIII-D shot 150312, and that plasma has been analyzed for kinetic RWM stability. We expect that the stability analysis of this target at high β_N will be similar to the experimental marginal stability crossing found in the present experiment. The results are summarized here, and are initially compared to RWM unstable plasmas in NSTX to determine the dominant physical stabilization mechanisms. The MISK code was used to compute the kinetic RWM stability for DIII-D shot 150312 at the observed experimental RWM marginal stability point with $\beta_N = 3.5$, $q_{min} = 2.8$. In this case, changes of the kinetic stabilization due to the peaking of the plasma toroidal rotation profile appear to be the dominant cause for the decrease in kinetic RWM stability. The rotation profile evolution and the computation of the crossing of the kinetic RWM marginal stability at the time of a rapid, 60% collapse in the experimental value of β_N is shown in Figure MS-RWM-8.

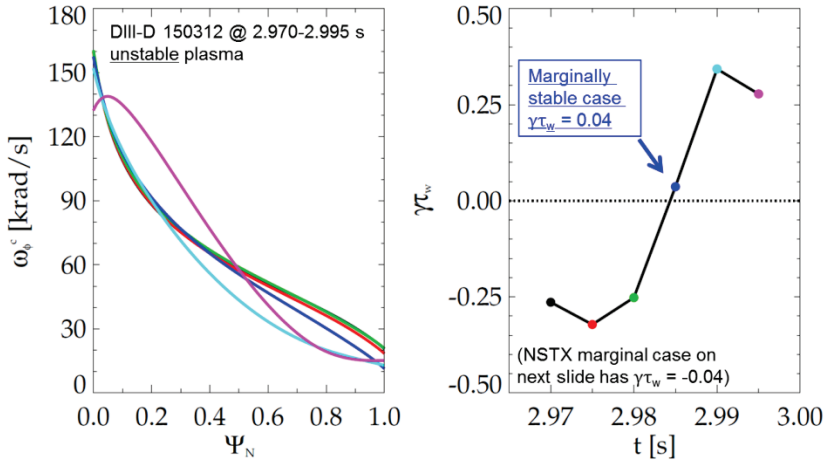

Figure MS-RWM-8: *(left) Plasma rotation profile evolution and (right) computed kinetic RWM stability using the MISK code for DIII-D high β_N, high q_{min} plasma suffering a major β_N collapse at t ~ 2.990s. RWM normalized growth rate $\gamma\tau_w > 0$ indicates instability.*

In addition, the present DIII-D experiment has found that reducing q_{min} below 2 experimentally increases the RWM stability of this plasma. The q_{min} variation was also examined for similar DIII-D plasmas in preparation for the present experiment, and the theoretical RWM stability analysis also shows increased stability, which is a combination of both an increase in the ideal and kinetic components of the stability functional δW.

The kinetic RWM stabilization physics of an NSTX plasma experimentally exhibiting an unstable RWM was compared to the equivalent analysis shown above for the recent DIII-D experiment. Many NSTX equilibria that have reached marginally stability have been analyzed for kinetic RWM stability. Here, we choose a plasma at "intermediate" levels of plasma rotation in NSTX, and with moderately high β_N, which appear to be the least stable combination at relatively high rotation in NSTX [MS-RWM-14], and most analogous to the DIII-D plasma. The evolution of β_N and n = 1 RWM amplitude are shown in Figure MS-RWM-9 for an NSTX plasma in these conditions that disrupts due to the RWM, along with the theoretically computed kinetic RWM growth rate. The reconstructed equilibria approaching the time of disruption are found to approach the theoretically computed kinetic RWM marginal stability point.

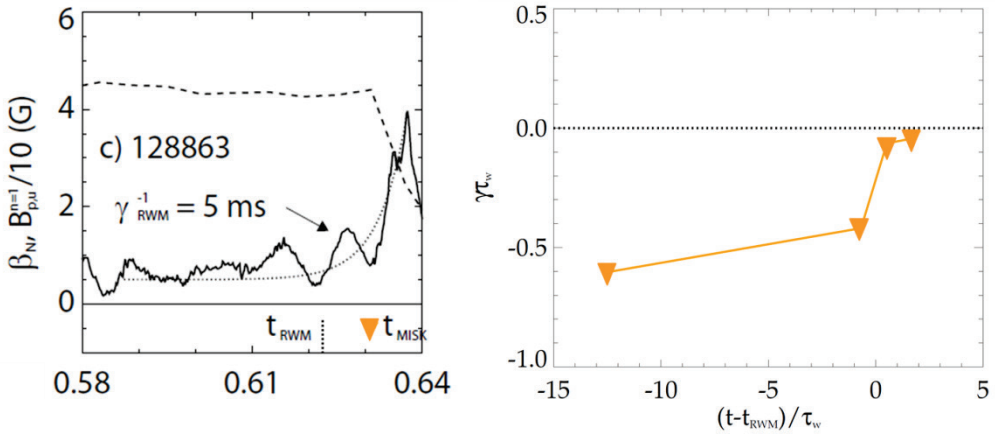

Figure MS-RWM-9: *(left) evolution of β_N and n = 1 RWM amplitude and (right) theoretically computed kinetic RWM growth rate for an NSTX high β_N plasma suffering a full current quench disruption.*

Analysis of the DIII-D and NSTX experimental results summarized above is beginning to provide a unified understanding of kinetic RWM stability physics in tokamaks based on the kinetic RWM stabilization physics model. The unstable and/or marginally stable modes were found at significant levels of plasma rotation in both devices, and share common dynamics observed during mode growth and rotation. Kinetic RWM stabilization theory is broad enough to explain the observed RWM destabilization in both devices, and an important complementarity has been found in the analysis to date that are part of the underlying theory: stabilization can be dominated by bounce orbit resonance in DIII-D for higher rotation plasmas, but is dominated by ion precession drift resonance in NSTX. This is illustrated for stable plasmas in DIII-D and NSTX, as well as the RWM unstable plasmas shown above. Figure MS-RWM-10 shows a comparison of the MISK-calculated imaginary part of the kinetic component of the RWM stability functional δW_K for RWM stable plasmas in DIII-D and NSTX vs. scaled experimental rotation. Here, the abscissa value of $\omega_\varphi/\omega_\varphi^{exp}$ = 1 corresponds to rotation profile measured in the experiment, and values less than unity correspond to rotation profiles that are scaled self-similarly to lower speeds to extrapolate the analysis. Here, we focus on the experimentally accessed rotation profiles ($\omega_\varphi/\omega_\varphi^{exp}$ = 1). At this relatively high rotation in DIII-D, the stabilizing resonance between the bounce motion of the ions and the plasma rotation is dominant, whereas in comparison NSTX case, the kinetic stabilization due to the ion precession drift resonance is stronger than the bounce resonance stabilization.

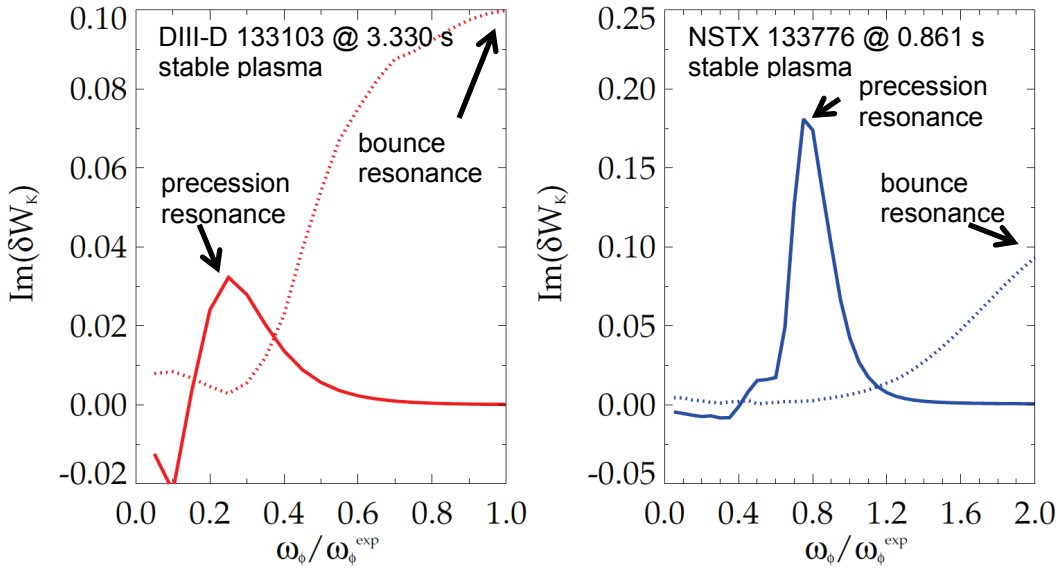

Figure MS-RWM-10: *Im(δW_K) vs. scaled experimental rotation DIII-D and NSTX, as calculated by MISK.*

A similar comparison of the physics components that create the kinetic stabilization in DIII-D and NSTX is shown in Figure MS-RWM-11 for the unstable plasma described earlier in this section. It is again found that bounce resonance stabilization dominates the DIII-D plasma at the relatively high experimental rotation profile, while ion precession drift stabilization is stronger than the bounce resonance stabilization in NSTX. Continued analysis will compare DIII-D experimental plasmas at the significantly reduced plasma rotation profile shown in Figure MS-RWM-2, and also at intermediate β_N and increased pressure peaking factor, which are also similar to analogous NSTX plasmas exhibiting unstable RWMs.

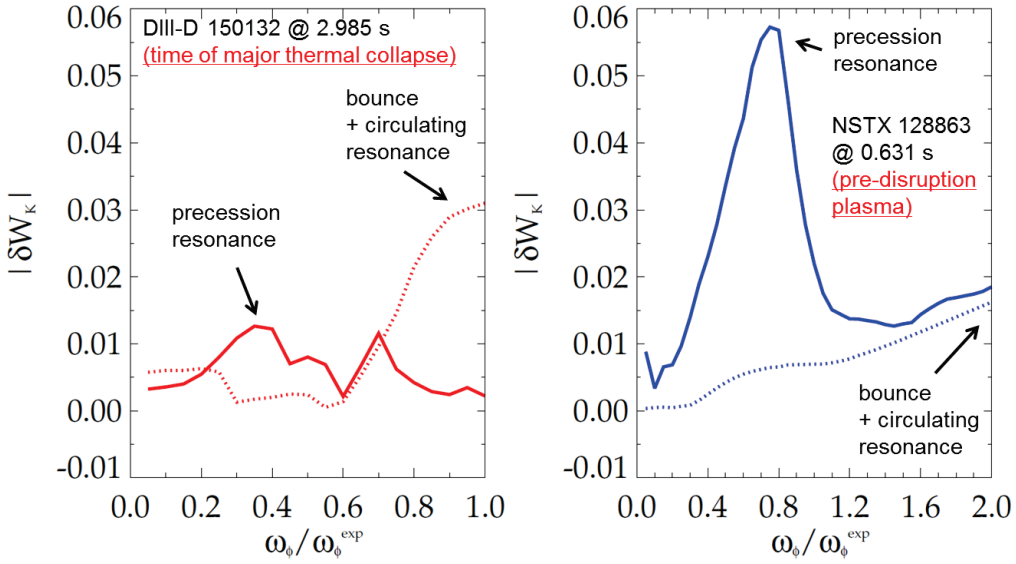

Figure MS-RWM-11: *Kinetic RWM stability functional $|\delta W_K|$ vs. scaled experimental rotation in DIII-D and NSTX, as calculated by the MISK code.*

Rotation and kinetic modifications of the high-beta tokamak ideal wall limit

The impact of toroidal rotation and drift-kinetic effects on the tokamak ideal wall mode stability limit was considered theoretically and compared to experiment for the first time [MS-RWM-6]. It was shown that high toroidal rotation can be an important destabilizing mechanism primarily through the angular velocity shear, and that drift-kinetic damping can potentially stabilize rotation-driven instabilities. These results were obtained using the unique parameter regime accessible in NSTX of high toroidal rotation speed relative to the thermal and Alfven speeds and high kinetic pressure relative to the magnetic pressure. The inclusion of rotation and kinetic effects was found to significantly improve agreement between measured and predicted stability characteristics, and an example of such results is shown in Figure R14-1-2 in the summary for Research Milestone R(14-1): "Assess access to reduced density and collisionality in high-performance scenarios."

RWM control performance calculations with the proposed NCC and realistic sensors

The active RWM control performance of a feedback system utilizing the proposed upgrade of the existing external RWM control coils set was evaluated as part of the NSTX-U Five Year Plan. Those calculations were extended to examine the optimal RWM active control performance (using proportional gain) afforded by three different possible configurations of a new non-axisymmetric control coil (NCC) supplemented by the existing RWM coil. This coil upgrade is proposed to be installed on NSTX-U within the next five years. The results of the highest performance NCC design option chosen are compared to the performance of the existing external midplane RWM coils in Figure MS-RWM-12. As the purpose of the calculations shown in this figure are to compare the optimal control performance of the configurations, "optimal" sensors were used in the calculations. As we now enter the next phase of the upgraded RWM feedback

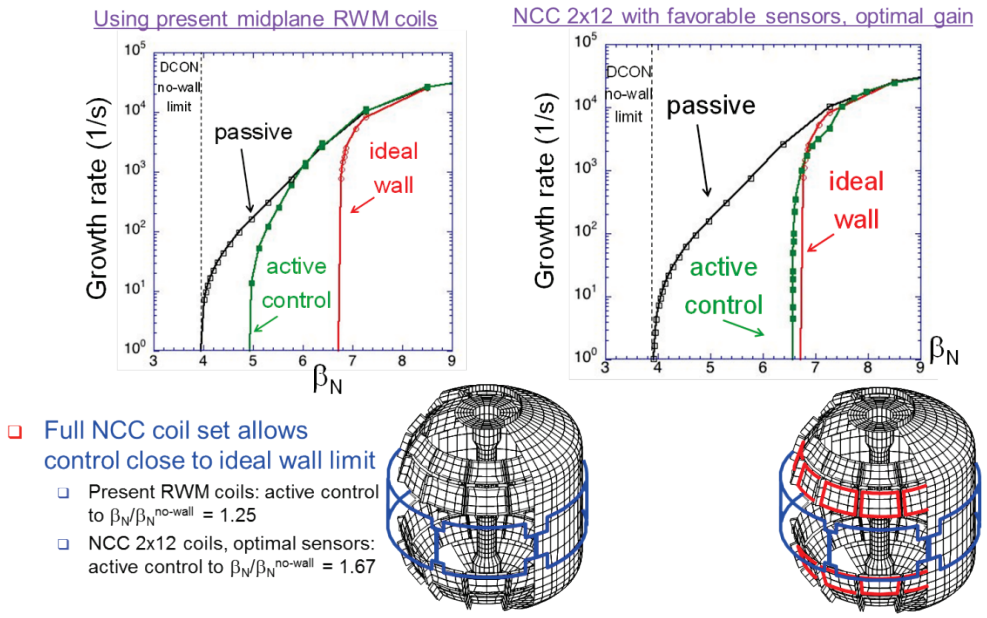

Figure MS-RWM-12*: Active RWM control performance using optimized sensors and proportional gain for projected NSTX-U plasmas comparing (left) the present external RWM coils and (right) the addition of the full NCC coil set.*

system design, a realistic set of sensors needs to be considered. The initial calculations show that care must be taken to choose sensor locations that minimize the coupling to the eddy currents created in the passive stabilizer plates due to the AC field created by the NCC during RWM feedback. Due to these initial findings, direct comparisons have first been made using a subset of the existing RWM sensors on NSTX-U that measure the poloidal component of the control field. Different combinations of the existing RWM sensors and the planned NCC coils have been chosen in this initial set of calculations, with the present best case scenario of utilizing sensors below the device midplane to control NCC coils above the midplane reaching a controllable β_N value of 5.42. This value is considerably better than the value $\beta_N = 4.9$ projected for the external RWM coils alone when using optimal sensors (Figure MS-RWM-12 (left)), and is closer to the controllable β_N value of 6.1 reached using the combination of optimal sensors controlling the NCC coils above the midplane. However, this controllable β_N value is still significantly below the optimal value of $\beta_N = 6.56$ computed using optimized sensors and all coils (Figure MS-RWM-12 (right)). These calculations continue, moving forward to consider the best placement of a new set of realistic sensors to further improve the RWM control performance, aiming to approach the performance found using optimized sensors.

References

[MS-RWM-1] J.W. Berkery et al., Phys. Plasmas **21**, 052505 (2014)
[MS-RWM-2] Y.Q. Liu et al., Phys. Plasmas **15**, 112503 (2008)
[MS-RWM-3] B. Hu and R. Betti, Phys. Rev. Lett. **93**, 105002 (2004)
[MS-RWM-4] N.C. Logan et al., Phys. Plasmas **20**, 122507 (2013)
[MS-RWM-5] J.W. Berkery et al., Phys. Rev. Lett. **104**, 035003 (2010)
[MS-RWM-6] J.E. Menard et al., "Rotation and Kinetic Modifications of the High-beta Tokamak Ideal Wall Limit", submitted to Phys. Rev. Lett. (2014)
[MS-RWM-7] J.W. Berkery et al., Phys. Rev. Lett. **106**, 075004 (2011)
[MS-RWM-8] J.W. Berkery et al., Phys. Plasmas **17**, 082504 (2010)
[MS-RWM-9] J.W. Berkery et al., "*The Effect of an Anisotropic Pressure of Thermal Particles on Resistive Wall Mode Stability*", submitted to Phys. Plasmas (2014)
[MS-RWM-10] S.A. Sabbagh, J.W. Berkery, R.E. Bell, et al., Nucl. Fusion **50**, 025020 (2010)
[MS-RWM-11] J.W. Berkery, S.A. Sabbagh, R. Betti, et al., PRL **104**, 035003 (2010)
[MS-RWM-12] J.W. Berkery, S.A. Sabbagh, H. Reimerdes, et al., Phys. Plasmas **17**, 082504 (2010)
[MS-RWM-13] S.A. Sabbagh, J.-W. Ahn, J.P. Allain, et al., Nucl. Fusion **53**, 104007 (2013)
[MS-RWM-14] J.W. Berkery, S.A. Sabbagh, A. Balbaky, et al., Phys. Plasmas **21**, 056112 (2014)
[MS-RWM-15] A. Turnbull, L.L. Lao, T.H. Osborne, et al., PPCF **45**, 1845 (2003)
[MS-RWM-16] Y. Nagayama, S.A. Sabbagh, J. Manickam, et al. PRL **69**, 2376 (1992)
[MS-RWM-17] A. H. Boozer, Phys. Plasmas **6**, 3180 (1999)
[MS-RWM-18] J. Bagaipo, P. Guzdar, A. Hassam, et al., Phys. Plasmas **18**, 122103 (2011)

3D Field Physics Research

Analysis of Experimental NTV

Experiments conducted on NSTX utilizing rapid changes (significantly faster than the momentum diffusion time) of $\delta \boldsymbol{B}$ best isolate the torque profile exerted on the plasma by neoclassical toroidal viscosity (NTV). The measured angular momentum damping and the theoretically computed T_{NTV}, created by a range of experimentally applied 3D field spectra and plasma parameters were analyzed, including configurations with dominant $n = 2$ and $n = 3$ field components (Figure MS-3D-1). This figure compares the theoretically computed T_{NTV} profile vs. minor radial coordinate to the measured change in the plasma angular momentum density, dL/dt, as $\delta \boldsymbol{B}$ is rapidly changed. The analysis computes $\delta \boldsymbol{B}$ fully in 3D, and uses the complete Shaing formulation of T_{NTV} valid for all collisionality regimes and the superbanana plateau regime for both ions and electrons as implemented in the NTVTOK code [MS-3D-2]. The calculation includes the effect of flux surface displacement, $\boldsymbol{\xi}$. A standard decomposition of $\delta \boldsymbol{B}$ into in-surface and normal components is made to first order in the displacement, $\delta B = \vec{b} \bullet \left(\vec{B} / B \right) + \left(\vec{\xi} \bullet \nabla B \right)$. The large radial variations of the theoretical T_{NTV} shown in Figure MS-3D-1 are due in part from this, and appear in other published models of $\boldsymbol{\xi}$. In contrast, such large radial variations of T_{NTV} are not observed experimentally. Rather, T_{NTV} is experimentally found to be radially extended, without strong localization of the torque as is observed in resonant braking by magnetic islands. Solution of the momentum diffusion equation shows that the charge exchange recombination spectroscopy diagnostic could discern details of the ω_ϕ evolution caused by these strong radial variations if they existed. Experiments at low A yield unique information as the maximum computed displacement $|\boldsymbol{\xi}| = 0.3$cm is smaller than either the ion banana width or gyroradius suggesting that finite-orbit effects will average T_{NTV} over such spatial scales. Figure MS-3D-1 shows that averaging the ion T_{NTV} profile over the banana width more closely matches the measured dL/dt profile. This work directly supports the near-term application of NTV for model-based, closed-loop $\omega_\phi$control in NSTX-Upgrade, described in the next section. Another critical and advanced area of research regarding T_{NTV} profile computation is the evaluation of the plasma response. A major issue is that the full plasma displacement $\boldsymbol{\xi}$ and its plasma-induced amplification are not directly measured in detail in any experiment and the development of first-principles models is still an active research area. Models tested against experiment in this work include the vacuum field assumption for $\boldsymbol{\xi}$, and various physics models in the M3D-C[1] resistive MHD code. The M3D-C[1] calculation (See

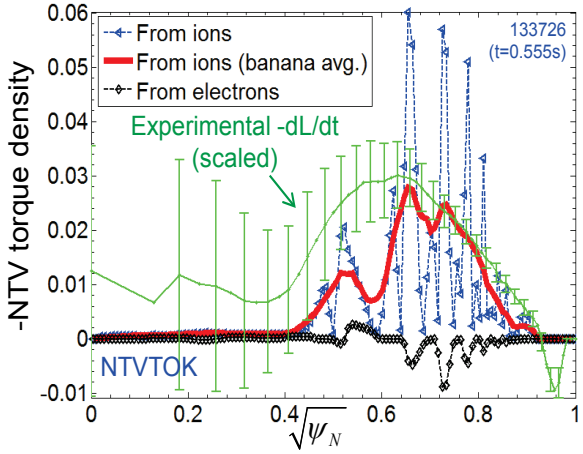

Figure MS-3D-1: *T_{NTV} profile components for an n = 3 field configuration in NSTX, computed from (i) ions using the vacuum field assumption, (ii) ions using banana width-averaging, (iii) electrons. The measured (-dL /dt) profile is shown in green.*

Figure BP-PED 8 in the boundary physics highlights section) shows the computed averaged $|\delta \boldsymbol{B}|$ from M3D-C[1], compared to the banana width-averaged vacuum field assumption model for the NSTX plasma in Figure MS-3D-1. Analyses show the M3D-C[1] single-fluid model produces a flux surface-averaged $|\delta \boldsymbol{B}|$ magnitude consistent with the experimentally measured T_{NTV} in the region of the plasma where T_{NTV} is strongest.

Rotation feedback controller using NTV as an actuator

The NSTX-U rotation feedback controller that will use the six neutral beam sources and, for the first time, non-resonant Neoclassical Toroidal Viscosity (NTV) induced torque as actuators, is currently being designed and tested. This controller was written in the past year, and is now being tested in open-loop fashion using existing NSTX data, and closed-loop fashion using computed NSTX-U plasma projections using the TRANSP code. The controller uses the momentum force balance equation to evolve for the plasma rotation frequency, ω_φ, which is decomposed into Bessel function states. The model for the NTV torque was developed from a substantial database of NSTX experimental results [MS-3D-3] and related theoretical analyses such as shown in the prior section. Two illustrative examples of this work of shown in Figure MS-3D-2. The left-hand panel shows an open-loop comparison of the rotation controller reproducing the plasma rotation of a TRANSP reconstruction of NSTX shot 133743. The right-hand panel of the same figure shows a closed-loop feedback simulation using the rotation controller to match a target plasma toroidal rotation profile by applying a primarily $n = 3$ field to the plasma using the existing NSTX

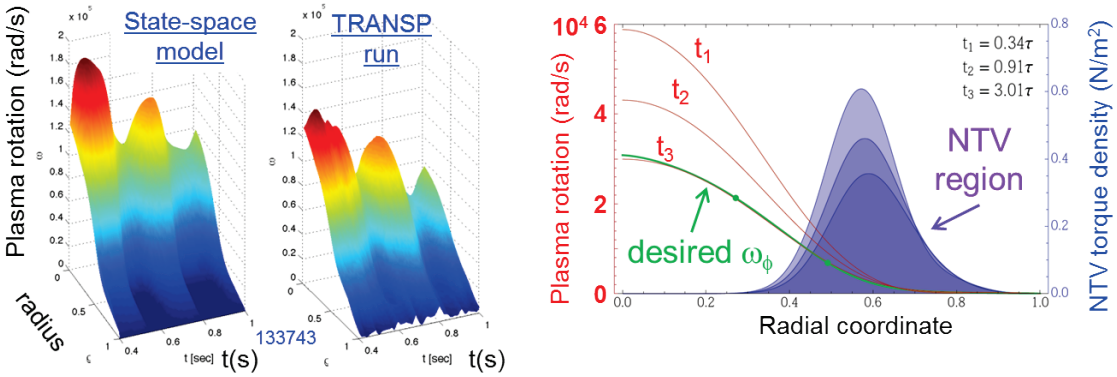

Figure MS-3D-2: *NSTX-U state-space ω_φ controller with NTV as an actuator.*

RWM coils. The control output is the needed current in the 3D RWM coils to produce a desired plasma rotation profile. The desired rotation profile is shown in green in this plot, and the time evolution of the rotation profiles toward this target profile is shown by three discrete rotation profiles labelled t_1 through t_3. These are normalized to the momentum diffusion time "τ" in this plot. Both the strength, and the radial profiles of the $n = 3$ NTV torque density are shown in this figure as well at each of these times. As shown, the desired rotation profile is reached in a time of approximately 3τ, since in this case, the action of the NTV torque occurs directly in the outer region of the plasma, then mostly relies on momentum diffusion to alter the rotation profile in the core to reach the target rotation profile.

Long-pulse NTV experiments on KSTAR supporting rotation feedback control design

We conducted a dedicated set of experiments on the KSTAR superconducting tokamak within the past year (S.A. Sabbagh, Y.S. Park, Y.M. Jeon, et al. "Long-Pulse Low Rotation Plasmas for ITER Applicability and Instability Characterization in High Normalized Beta Plasmas above the ideal No-wall Limit") which have shown strong n = 2 NTV non-resonant magnetic braking in KSTAR, reducing the plasma rotation to 40% of the maximum value run in these high performance plasmas. The rotation profile pedestal is reduced, altering ω_ϕ toward an L-mode profile shape while maintaining H-mode energy confinement. Analysis of these experiments finds the expected theoretical scaling of T_{NTV} with $\delta \boldsymbol{B}^2$, and strong dependence on ion temperature ($\sim T_i^{2.5}$) compatible with the "1/ν" regime of NTV theory [MS-3D-4]. These experiments have demonstrated the important and favorable observation for rotation profile control - a lack of hysteresis on the ω_ϕ profile when altering the rotation by non-resonant NTV, as the profiles reach the same steady-state profile for a given applied 3D field independent of the initial ω_ϕ. This is conclusively illustrated in Figure MS-3D-3, which shows two long-pulse plasmas, one in which the 3D applied field is stepped up in time, and one in which it is stepped down in time. In both cases, the duration of the step is much greater than the momentum diffusion time, which allows the plasma toroidal rotation profile ample time to settle into a steady state after each increase in the 3D applied field magnitude. In the shot indicated by the solid lines, rotation is monotonically decreased at each step. In the shot indicated by the dashed lines, the rotation is first decreased to the minimum of the series of 3D field steps, and then increases in magnitude as the 3D field is decreased from the initial maximum value taken in the first step. Regardless of whether rotation is increasing or decreasing – as will naturally occur repeatedly in a plasma rotation controller with an NTV actuator – the steady-state rotation profile is the same at each level of the applied 3D field current. This substantially increases confidence that the planned non-resonant NTV actuation will allow successful plasma rotation control in NSTX-U with closed-loop feedback.

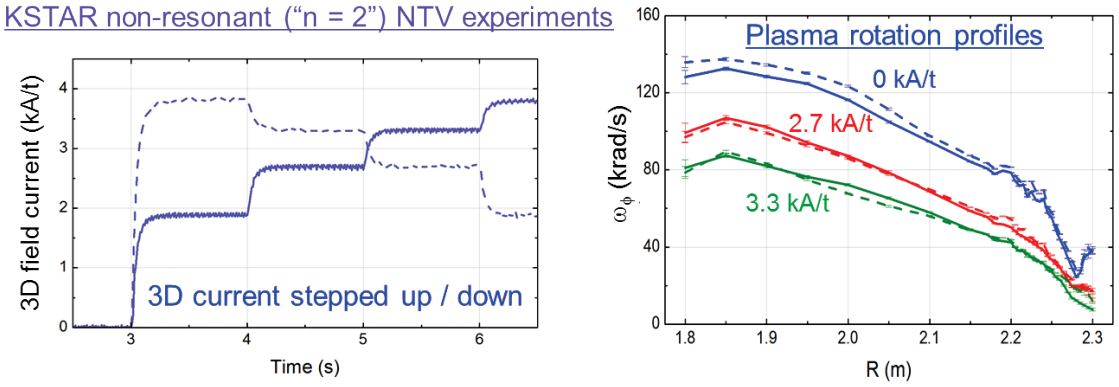

Figure MS-3D-3: *(left) 3D field current in the In-Vessel Control Coils, showing clear increase and decrease in current, taken in steps, and (right) resultant plasma toroidal rotation profiles are shown to be the same for a given level of applied 3D field current, regardless of whether the rotation is slowing, or increasing toward these steady-state profiles (note: error bars are shown).*

Theory comparison and numerical benchmarking of NTV torque

Systematic comparison and numerical benchmarking have been successfully carried out [MS-3D-5] among three different approaches of neoclassical toroidal viscosity (NTV) theory and the corresponding codes: IPEC-PENT is developed based on the combined NTV theory but without geometric simplifications [MS-3D-6]; MARS-Q includes smoothly connected NTV formula [MS-3D-7] based on Shaing's analytic formulation in various collisionality regimes; MARS-K, originally computing the drift kinetic energy, was upgraded to compute the NTV torque based on the equivalence between drift kinetic energy and NTV torque [MS-3D-8]. The derivation and numerical results both indicated that the imaginary part of drift kinetic energy computed by MARS-K is equivalent to the NTV torque in IPEC-PENT.

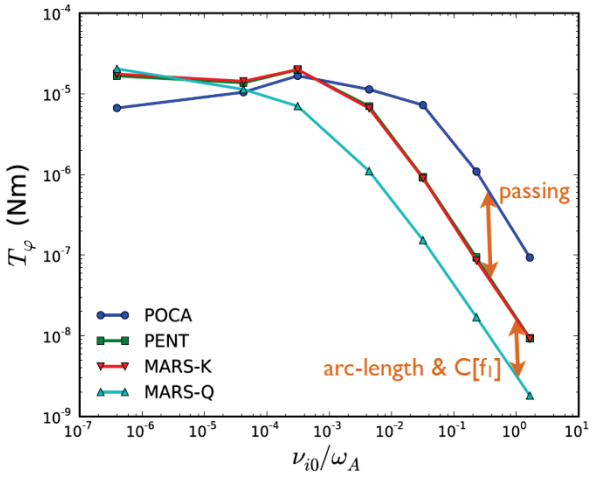

Figure MS-3D-4: *SBP comparison among four different NTV codes. Qualitatively all agree, but there are quantitative differences due to different approximations for geometry and collisionality.*

In the benchmark of precession resonance between MARS-Q and MARS-K/IPEC-PENT, the agreement and correlation between the connected NTV formula and the combined NTV theory in different collisionality regimes were shown for the first time. However, there are often quantitative differences by a few factors, as Figure MS-3D-4 shows the expected superbanana-plateau (SBP) behaviour in the low collisionality by all three codes but with some differences depending on the collisionality. The additional comparison with POCA particle code [MS-3D-9], which calculates NTV with the least approximation, shows that MARS-K and IPEC-PENT agree better to POCA possibly due to the geometric generalization. The geometric simplification in MARS-Q has been removed in NTVTOK [MS-3D-2], which will also be compared with other codes in the future. The difference in high collisionality between POCA and other codes is presently understood by incomplete orbit trajectories of most of particles due to frequent colliding, which can make the path integral of the semi-analytic codes less precise. In the benchmark of other resonances, IPEC-PENT, MARS-K, and POCA shows the bounce-harmonic resonance can greatly enhance the NTV torque when *E x B* drift frequency reaches the resonance condition. The enhancement can easily reach to an order of magnitude especially in the low collisionality, indicating that it is important to include bounce-harmonic resonances in the simulation for NSTX-U.

Full particle simulation for NTV

Another important progress has been made in the particle simulation study of the 3D field, with a global full-f drift-kinetic particle-in-cell simulation using XGC0 (X-point included Guiding-Center) code, which was originally designed for neoclassical transport study in the realistic tokamak geometry including separatrix, limiter, and divertor. The code solves the drift-kinetic equation in the whole tokamak volume eliminating a local assumption in the POCA code, and has been extended to 3D neoclassical transport study [MS-3D-10]. The 3D version of XGC0 code has been successfully tested to simulate and analyze the evolution of temperature, density, toroidal flow, and radial electric field in the 3D magnetic perturbations considering vacuum approximation and ideal plasma response.

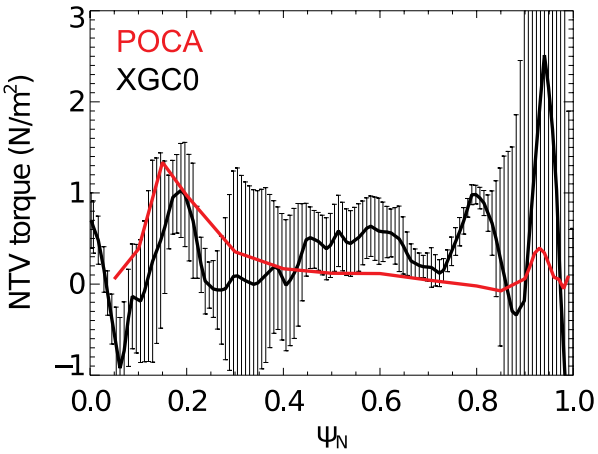

Figure MS-3D-5: *NTV profiles by POCA calculation and XGC0 damping rate, applying 3D field by IPEC.*

The first application was made to the study of toroidal flow damping by non-resonant magnetic perturbation in DIII-D. It is found that self-consistent treatment of radial electric field via multi-species particle simulation is essentially required to achieve the temporal evolution of plasma potential and toroidal flow in the 3D field. The XGC0 ion simulation indicates that ions can move out by non-resonant 3D field to further steepen the negative potential well at the pedestal, and thus the toroidal flow can be accelerated. However, inclusion of electron species shows enhanced electron transport by 3D field to significantly relax the negative radial electric field, which results in damping of the toroidal flow as observed in the experiment. NTV torque profile estimated from the toroidal rotation evolution well captured dominant damping area at the core (ψ_N~0.2) and pedestal in spite of some qualitative discrepancies in detained profile and a factor of 2 quantitative differences (Figure MS-3D-5). Large statistical errors in the pedestal indicate the sensitivity of the kinetic response at the pedestal to the applied 3D field, which could be compensated by increasing test particle number.

Another important issue in the 3D neoclassical transport is the modification of pedestal structure by the resonant magnetic perturbation, which is directly connected to ELM suppression mechanism. The XGC0 simulation for the resonant magnetic perturbation discharge with ELM suppression in DIII-D is being performed to find a consistent kinetic feature of the pedestal to experimental observations such as the particle pump-out effect by 3D field. It is confirmed that the evolutions of radial electric field and plasma flow are the complicated functions of 3D field and kinetic plasma response, thus they are very sensitive to the initial plasma conditions and pedestal structure. In particular, the ideal plasma response computed by IPEC prevents the magnetic islands from opening at the pedestal, thus results in different transport and pedestal structures than stochastic field by the vacuum approximation.

NCC modelling

Figures of Merit	Favorable values	MID	12U	2x6-Odd	2x12
EF (n=1), $F_{N-R} = \frac{T_{NTV}}{\sum_{\psi_N<0.85} \delta B_{mn}^2}$	High $F_{N\text{-}R}$	0.07	0.13	1.24	1.24
NTV (n≥3), $F_{N-N} = \frac{T_{NTV}(\psi_N < 0.5)}{T_{NTV}(\psi_N < 1)}$	Wide $\Delta F_{N\text{-}N}$	1.00	1.44~ 6.08	1.75~ 11.33	6.38~ 59.4
RMP (n≥3), $F_{N-C} = \frac{T_{NTV}}{(C_{vacuum}, \psi_{N=0.85})^4}$	High $F_{N\text{-}C}$	0.25~ 0.30	0.31~ 1.04	0.43~ 0.77	1.18~ 3.53
	Wide $\Delta F_{N\text{-}C}$	1.00	2.20~ 12.3	10.4~ 17.4	888~ 14400
RWM (n=1), $F_{\beta} = \frac{\beta_{active}}{\beta_{no-wall}}$	High F_{β}	1.25	1.54	1.61	1.70

Table MS-3D-1. *NCC performance comparison table, based on defined FOMs. Note here that NCCs were used alone without the midplane coils except for the RWM analysis. FOM values for 2MA target is marked as purple.*

Part of the NSTX upgrade includes a set of in-vessel 3D perturbative coils (NCC coils) designed with multiple physics metrics for error field, RWM, rotation control by NTV, and RMP characteristics. Extensive studies done in the past already show the increase of figures of merits over an order of magnitude when partial/full NCC is applied compared to the midplane coil only. This year the analyses have been updated with more precise calculations using IPEC-PENT, leading to the similar conclusion. The physics advantages by NCC are somewhat decreased when targets are varied from 1.5MA to 2MA, but still remained significant, especially in RMP characteristics. Although partial and full NCC is expected to provide significant flexibility for each physics merit, it will be important to know what's theoretical max performance and how close the present NCC is to those idealized coils without any constraints. The goal is to assess physics benefits of potentially improved coil sets within to drive subsequent engineering analysis. The IPECOPT code was developed for this purpose from STELLOPT, and applied to optimize core and edge NTV torque, and will be extended to analyse other figures of merit. The IPECOPT code utilizes experimentally validated models: the IPEC code computes the perturbed equilibrium model, the PENT code then calculates the NTV torque based on this perturbed equilibrium, and the IPECOPT code reuses the optimization machinery of STELLOPT, including a choice of the Levenberg-Marquardt, Genetic Algorithms, Differential Evolution, or Particle Swarm techniques.

This application of stellarator tools to 3D tokamak already yielded interesting and important insights. For both n=1 and n=3, as shown in Figure MS-3D-6 for an example, IPECOPT shows that the optimized field for the edge torque inside the pedestal is typically the field orthogonal to the equilibrium field lines almost everywhere. The ideal patterns shown in Figure MS-3D-6 also indicate that the spatial coil coverage must be sufficient at least in the outboard side, in order to minimize the pitch-aligned field lines that can be too easily amplified. Indeed, the preliminary investigation shows that NCC can produce roughly 50% of the ideal patterns if the midplane coils are combined and cover the central area nearby the midplane. More systematic optimization with the coils is planned, using IPECOPT with designed NCC and also other virtual coils.

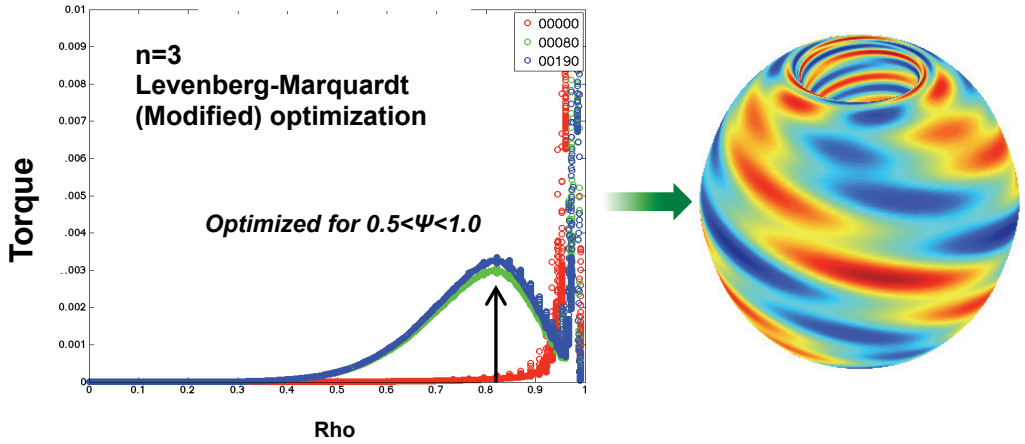

Figure MS-3D-6: *Torque profile optimized by IPECOPT for edge torque and the magnetic fields (not constrained by engineering concerns) that create it.*

Development of resistive DCON to study layer physics

To calculate the outer region solution of singular MHD modes (e.g. tearing modes), Resistive DCON (RDCON) has been developed based on the well-established ideal DCON and the asymptotic matching method which allows non-vanishing large solutions. Resistive DCON extends the finite element method developed by Pletzer & Dewar (1991) [MS-3D-11] to compute the outer region matching data for toroidal plasmas. The new method, so called resonant Galerkin method, uses the C1 hermite cubic basis function and introduces the small solutions as the extra basis function which greatly improves the convergence of outer region solution.

The developed arbitrary high order large and small solutions allow resistive DCON to calculate resistive MHD stability with high beta values, which is important for the application of the code to NSTX experiments. A very robust convergence of matching data (Δ value) is achieved even in the challenging NSTX plasmas due to the resonant Galerkin method. In order to determine the growth rate of resistive instability and to reconstruct the corresponding global solution, the asymptotic method requires that the outer region solution needs to match with the inner layer solution. The DELTAR code is used as the inner-layer model which is derived from the resistive single fluid MHD. The dispersion relation to match the large and small solutions between the outer and the inner regions in full toroidal geometry is derived. The vacuum region has been successfully implemented in RDCON for free boundary calculation. A systematic benchmark

between resistive DCON and MARS-F has been carried out. A very good agreement between resistive DCON and MARS-F has been achieved by comparing the eigenfunction, Δ' value, and the growth rate, where the circular tokamak equilibrium and DIII-D like equilibrium are considered. A benchmark with realistic NSTX and DIII-D equilibria is undergoing.

To achieve the relaxed perturbed equilibrium, it requires flattening the pressure gradient at the singular surface due to the opened island. The degenerate power series for large and small solutions also has been developed.

Study of kinetic effects in 3D plasma response

A quantitative interpretation of the experimentally measured high pressure plasma response to externally applied n = 1 three-dimensional (3D) magnetic field perturbations, across the no-wall Troyon β limit, is achieved. The key to success is the self-consistent inclusion of the drift kinetic resonance effects in numerical modeling using the MARS-K code [MS-3D-12], where the drift kinetic effects are derived from the perturbed drift kinetic theory and associated with distorted particle orbits by 3D fields. The external coils, the resistive wall, and the vacuum are all included in the MARS-K simulation. This work resolves an outstanding issue of the ideal magneto-hydrodynamic model, where ideal MHD theory finds a very high (almost singular) amplification near the no-wall β limit, denoted as β^{NW}. The large plasma response driven by the external perturbation is due to the ideal potential energy approaching zero when β approaches β^{NW}. In contrast, empirical experiments [MS-3D-13, MS-3D-14] show the plasma response increases along with β across the ideal β^{NW}. This disagreement between ideal MHD theory and experiments has been studied by the MISK code based on the potential energy analysis [MS-3D-15]. Now, this subject is studied through a quantitative comparison between the accurate modeling results by MARS-K and experimental results in NSTX [MS-3D-16] and DIII-D [MS-3D-17] plasmas. Since the drift kinetic effects can dramatically modify the plasma response structure, the results also highlight the importance of solving the model equations self-consistently. It is only in a self-consistent calculation that the kinetic effects can modify the plasma response structure (i.e. displacement).

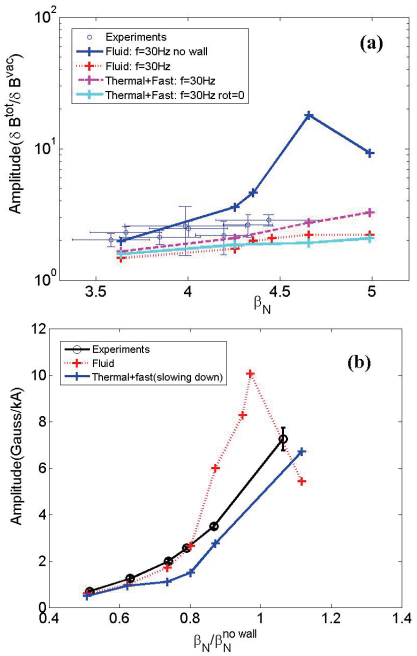

Figure MS-3D-7: *The amplitude of plasma response measured at the magnetic sensor is plotted as the function of β_N for fluid and kinetic plasma response. The β_N^{NW} in NSTX (a) and DIID (b) are around 4.6 and 2.25 respectively.*

The kinetic plasma response solved by MARS-K includes the kinetic effects contributed by the thermal particles and the energetic particles (slowing down distribution). Figure MS-3D-7 shows the amplitude of kinetic plasma response in both NSTX and DIII-D plasmas agrees with the

experiment measurements. The kinetic plasma response keeps the finite amplitude near the no-wall beta limit. As for the NSTX case, it is noted that the plasma response may be strongly coupled to the resistive wall. Therefore, the fluid case of plasma response (solved only with ideal MHD) with-wall (red line) shows a strong suppression of amplitude comparing with the no-wall case (blue line). Moreover, both 'fluid' cases show a large phase value when β_N approaches or exceeds β_N^{NW}, which is largely different from the small phase observed in NSTX experiments. As for the kinetic plasma response, it not only gets an agreement of amplitude but also keeps a relatively small phase as in the experiments. Since NSTX plasma can achieve much stronger fluid rotation than a DIII-D plasma, it is important to investigate this effect in the kinetic plasma response calculation. Figure MS-3D-7(a) clearly shows kinetic plasma response with the fluid rotation (dashed line) has much larger amplitude than the case without rotation (cyan line). It indicates that the fluid rotation could cause the destabilizing effect of the plasma which is consistent with the results in a NSTX Ideal Wall Mode study [MS-3D-14]. In both experiments, the perturbed energy analysis shows the modification of plasma response is mainly contributed by the precession, bounce, and transit resonances of thermal ions.

The internal response structure measured by soft X-ray in DIII-D experiments is also compared with MARS-K results. For the case near the no-wall limit, we note the fluid response largely overestimates the amplitude of the internal perturbation. The phase of the fluid response also disagrees with measurements. The kinetic response, on the other hand, generally shows very good quantitative agreement with experiments, for both amplitude and phase. Therefore, the self-consistent drift kinetic model leads to quantitative agreement not only for the measured 3D field amplitude and toroidal phase, but also for the measured internal 3D displacement of the plasma.

References

[MS-3D-1] S.A. Sabbagh, R.E. Bell, T.E. Evans, et al., IAEA FEC (2014) EX/1-4.
[MS-3D-2] Y. Sun., Y. Liang, K.C. Shaing, et al., Nucl. Fusion **51**, 053015 (2011)
[MS-3D-3] W. Zhu., S.A. Sabbagh, R. Bell, et al., Phys. Rev. Lett. **96**, 225002 (2006)
[MS-3D-4] Y.S. Park, S.A. Sabbagh, W.H. Ko, et al., IAEA FEC (2014) EX/P8-5.
[MS-3D-5] Z. Wang et al., Phys. Plasmas **21,** 042502 (2014)
[MS-3D-6] J.-K. Park et al., Phys. Rev. Lett. **102**, 065002 (2009)
[MS-3D-7] K. Shaing et al., Nucl. Fusion **50**, 025022 (2010)
[MS-3D-8] J.-K. Park, Phys. Plasmas **18**, 110702 (2011)
[MS-3D-9] K. Kim et al., Nucl. Fusion **54** 073014 (2014)
[MS-3D-10] G. Park et al., Phys. Plasmas **17** 102503 (2010)
[MS-3D-11] A. Pletzer et al., J. Plasma Physics **45** 427 (1991)
[MS-3D-12] Y.Q. Liu et al., Phys. Plasmas **15**, 112503 (2008)
[MS-3D-13] S.A. Sabbagh et al, Nucl. Fusion **46**, 636-644 (2006)
[MS-3D-14] A.M. Garofalo et al, Phys. Plasmas **10**, 4776 (2003)
[MS-3D-15] J.W. Berkery et al, Phys. Plasmas **21**, 056112 (2014).
[MS-3D-16] J.-K. Park et al, Phys, Plasmas **16**, 082512(2009)
[MS-3D-17] M.L. Lanctot et al., Phys. Plasmas **17**, 030701 (2010)

Disruption Studies

Progress in 3D nonlinear simulations of disruptions, saturated modes, and soft beta limits in NSTX using M3D-C1

We have applied the M3D-C1 [MS-DIS-1,MS-DIS-2] extended magnetohydrodynamics code to model several discharges in NSTX in which the ideal and/or resistive β-limits are approached and exceeded at some point in the discharge. The goal is to understand when and by what mechanism exceeding the stability limits leads to a disruption, and by what mechanism the plasma self-limits itself by some form of enhanced transport when it does not.

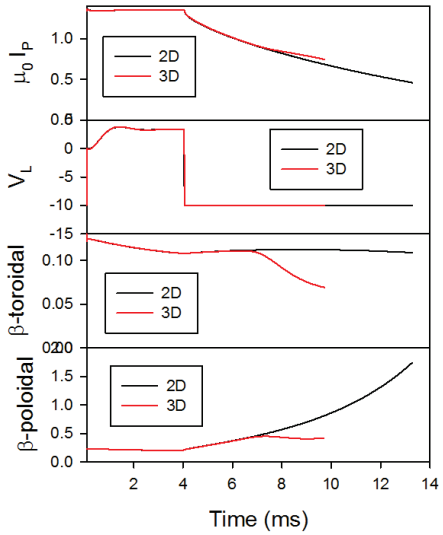

Figure MS-DIS-1. *Traces of scalar quantities for 2D and 3D simulation of NSTX shot 129922 starting at time 860 ms.*

Figure MS-DIS-1 shows some of the global quantities vs. time for two M3D-C1 time dependent simulations of NSTX shot 129922 starting at time 860 ms into the discharge (denoted here as time t = 0), near the termination of the discharge. The curves in black (2D) used an axisymmetric version of the code, whereas the curves in red (3D) used the full 3D version of M3D-C1 with 32 cubic Hermite finite elements used to represent the toroidal variation of each (R,Z) node. Both versions had identical transport coefficients chosen to match experimental profiles. Before t = 4 ms, a current controller was used to apply a loop voltage at the boundary to keep the plasma current constant in time. At t = 4 ms, the controller was turned off and the loop voltage was suddenly reversed and decreased to -10V, similar to what happens when the OH coil currents are brought to zero at the end of the discharge.

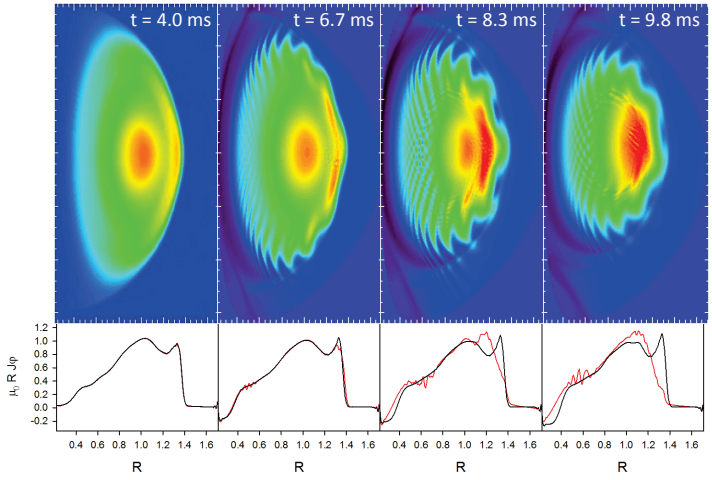

Figure MS-DIS-2: *Snapshots of 2D slices of the toroidal current at several times. Red curves show midplane profiles for 3D calculation, while black curves show results for corresponding 2D calculation.*

It is seen from Fig. MS-DIS-1 that when the loop voltage is reversed, the plasma current, I_P, begins to decrease, as expected. The trajectories of the plasma current, β_T, and β_P are nearly identical for the 2D and 3D calculations until approximately t = 7 ms, at which time the β_T and β_P in the 3D calculation begin to decrease and level off, respectively, while those in the 2D calculation remain level and increase.

Figure MS-DIS-2 shows 2D slices from the 3D calculation of the plasma toroidal current at several times during the current ramp-down. It is clear that a high poloidal mode number instability develops at about 6.7 ms and continues to grow before it begins to saturate at around 9 ms. Fourier analysis of the output shows that the mode with toroidal mode n = 8 has the maximum amplitude and growth rate. Comparison of the midplane profiles of the 3D and the 2D run shows that the primary effect of the 3D modes is to shift the outboard current peak inward, while reducing the amount that the current reverses on the inboard side.

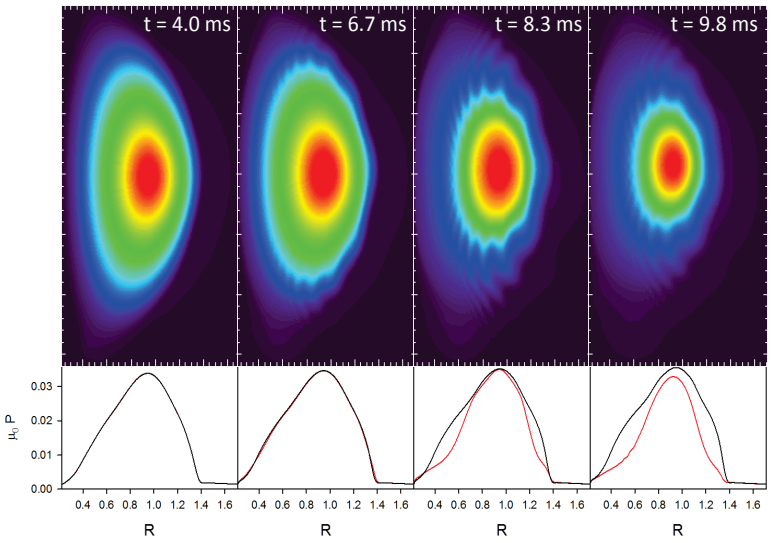

Figure MS-DIS-3: *The analogue of Figure MS-DIS-2, except for pressure contours. Red curves show midplane profiles for 3D calculation, while black curves show results for corresponding 2D calculation.*

In Fig. MS-DIS-3 we show the corresponding 3D slices and midplane profiles of the plasma pressure. In comparing the 2D (black) and 3D (red) mid-plane profiles, we see that the primary effect of the 3D mode was to reduce the pressure near the plasma boundary, with very little effect near the axis. This sequence is presently being redone at higher resolution because the highest mode number that was well resolved was the most unstable (n = 8).

MGI valve development and testing

During the past year we made progress in two areas related to developing disruption mitigation systems. We successfully built and tested an electromagnetic MGI valve for installation on NSTX-U [MS-DIS-3], which is described here. We also developed the concept of an Electromagnetic Particle injector in much more detail [MS-DIS-4], which will be described in the next section.

Figure MS-DIS-4 shows the main features of the valve. The primary plenum holds the gas to be injected into the vessel. The lower part of the piston makes an O-ring seal with the flange that would connect to the NSTX-U vessel. The piston shaft slides along the Lip Seals that are located in the cavity shown in the figure.

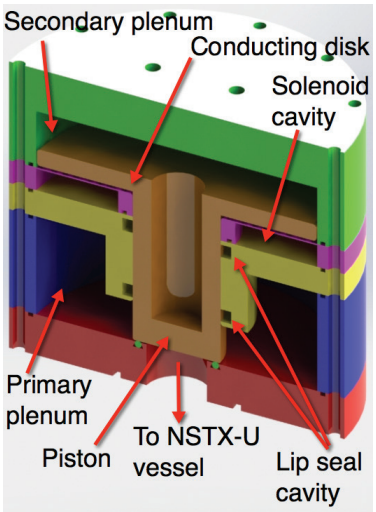

Figure MS-DIS-4: *Components of the Version 4 MGI valve. It measures 12.7 cm in diameter and is 12.7 cm long.*

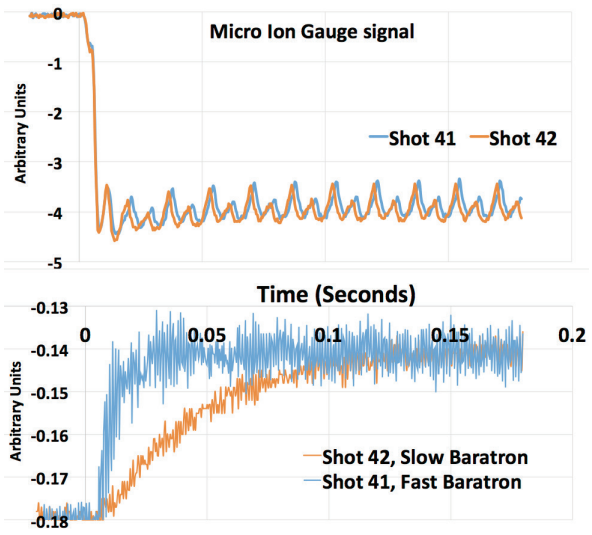

Figure MS-DIS-5: *Vessel gas pressure measurements using a Micro Ion Gauge (MIG) and Baratron to compare the Baratron response to the faster MIG response time.*

The top part of the piston is attached to a large flat conducting disk and is located in the secondary chamber. The gas pressure in the secondary plenum tends to push the piston against the lower sealing O-ring, while the gas pressure in the primary plenum acts on the area between the O-ring and the outer edge of the piston and tends to open the O-ring seal by pushing the piston up. Thus for a given pressure in the primary plenum, the pressure in the secondary plenum can be adjusted so that there is just enough over pressure from the secondary plenum to make a good O-ring seal. The primary advantage is that the requirements on the power supply to operate this valve are nearly independent of the pressure in the primary plenum. The design has been used on JET for operation at pressures up to 34 atm. NSTX-U test cell pressure limits for gas systems is limited to about 5000 Torr, but it is planned to increase this limit during 2016. The pancake solenoid contains 21 turns of 1.4 mm diameter magnet wire. A 0.5 mF capacitor charged to <1 kV is used to drive the coil. The quarter cycle current pulse width is about 100 µs, with peak currents of about 2 kA at 770 V. The rapidly changing current in the pancake coil induces eddy currents on the lower part of the flat surface of the conducting disk, which causes the disk to move away from the solenoid. This causes the O-ring seal on the lower part of the valve to open and causes the primary chamber to partially empty, before the lower seal is re-established. In order to retain a high gas flow-rate only part of the primary chamber volume is allowed to empty. To inject more gas, the desired operating condition would require the primary plenum pressure to be further increased.

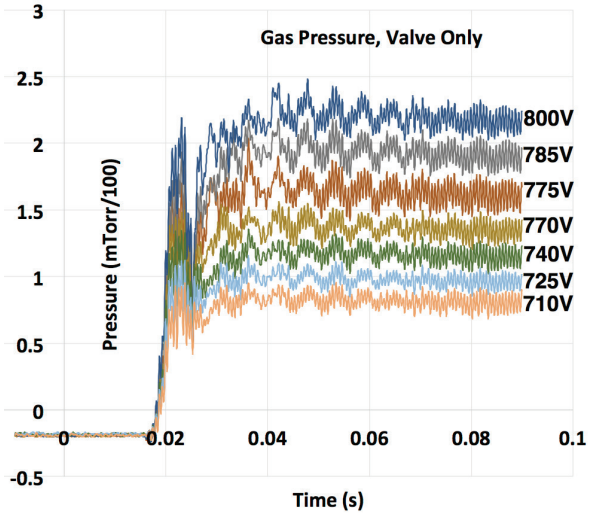

Figure MS-DIS-6: *Shows the time response of the version 4 valve as measured by the fast Baratron signal as the operating voltage is increased from 710 V to 800 V.*

Initial experiments were conducted at low gas throughput of 3-4 Torr.L nitrogen injections so that the time response of the pressure rise in the 1.3 m^3 test chamber could be measured with a fast micro ion gauge. This was then compared to the time response seen by the Baratron operated in the standard 'slow' mode and in the 'fast' mode. Figure MS-DIS-5 shows the results of this comparison. For 5000 Torr in the primary chamber and 300 V operating voltage for the version 1

valve, the micro gauge shows the pressure in the vessel to rise in about 4 ms. The fast Baratron signal shows it to increase on a slightly longer time scale, and the slow Baratron takes over 50 ms to respond to the pressure increase in the vessel. These measurements show that the valve opens on a sufficiently fast time-scale. Figure MS-DIS-6 shows the time response of the version 4 valve as measured by the fast Baratron signal as the operating voltage is increased from 710 V to 800 V. At 710 V, 125 Torr.L of nitrogen is injected with an effective pressure rise time of less than 3 ms. This is consistent with the thermal velocity of nitrogen molecules. At 770 V, the amount of injected gas increases to 220 Torr.L. For these experiments the valve was operated at a primary plenum pressure of 7000 Torr. In future tests it is planned to increase this pressure to at least 15,000 Torr.

Electromagnetic Particle Injector

Predicting and controlling disruptions is an important and urgent issue for the International Thermonuclear Experimental Reactor (ITER). Tokamaks and STs rely on substantial amounts of plasma current to sustain the plasma discharge, so have the potential to disrupt. Methods to rapidly quench the discharge after an impending disruption is detected are essential to protect the vessel and internal components. The warning time for the onset of some disruptions could be less than 10 ms, which poses stringent requirements on the disruption mitigation system. In this proposed method, a cylindrical boron nitride projectile containing a radiative payload composed of boron nitride or beryllium particulate matter, and weighing about 12 g is accelerated to velocities on the order of 1-2 km/s in less than 2 ms in a linear rail gun accelerator. The capsule is then injected into the tokamak discharge in the 3 to 6 ms time scale, where the radiative payload is dispersed. The device referred to as an Electromagnetic Particle Injector (EPI) has the potential to meet the short warning time scales, for which an ITER disruption mitigation system must be built. The system is fully electromagnetic, with no mechanical moving parts, which ensures high reliability after a period of long standby, as needed for satisfying the demanding needs of a prompt-acting reactor disruption mitigation system.

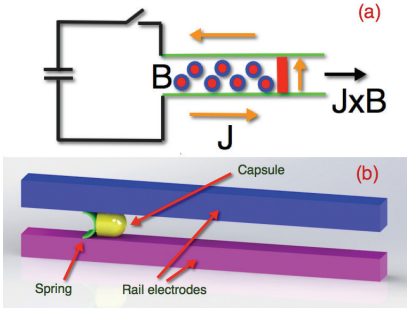

Figure MS-DIS-7: *(a) Cartoon showing rail gun operating principles. (b) Electrode configuration for initial NSTX-U level test of the EPI concept.*

The primary advantage of the device referred to as an Electromagnetic Particle Injector (EPI) is its potential to meet the short warning time scales, for which an ITER disruption mitigation system needs to be built. Figure MS-DIS-7a describes the injector operating principle. The projectile is placed between two conducting rails separated by about 1 to 2 cm. The length of the rails would be about 1 m long. The projectile is placed in front of a conducting spring, as shown in Figure MS-DIS-7b. A capacitor bank is connected to the back end of the rails. Discharging the capacitor bank causes the current to flow along the rails as shown in Figure MS-DIS-7a. The $J \times B$ forces resulting from the magnetic field created in the region between the rails, and the current along the spring armature accelerates the projectile.

Because of the compact nature of the injector and its simple geometry, a test of the concept could be conducted on NSTX-U. Parameters for such a device, whose primary objectives are to verify the system response time, attainable velocity parameters and successful dispersion of the capsule payload inside the NSTX-U plasma are also shown in Table 1. Case A is for a low power test to verify the system response time. A 20 mF capacitor bank charged to 1.5 kV accelerates a 2 mg projectile to 0.4 km/s in about 0.7 ms in an accelerator that is 20 cm long. As the operating voltage is increased to 2 kV and the bank size increased to 30 mF, the velocity increases to almost 1 km/s in 1 ms, in an accelerator that is about 50 cm long. NSTX- Case A should be adequate for a test on NSTX-U, while Case-B would serve as in intermediate off-line test towards developing an ITER-scale injector. Typical parameters for an ITER-scale injector are also shown in Table MS-DIS-1. The calculated voltage waveform for all these cases show that for the chosen capacitor bank size, the energy in the capacitor is depleted on the acceleration time scale. The peak acceleration currents for the four cases range from 80 kA for the low power NSTX-U case to a maximum of about 350 kA for the ITER cases.

Injector Parameters	ITER-A	ITER-B	NSTX-A	NSTX-B
Capsule Diameter (cm)	2	2	1	1
Capsule Length (cm)	3.25	3.25	2.2	2.2
Capsule Mass (g)	12	12	2	2
Injector Length (m)	1	1.2	0.20	50
Bank Capacitance (mF)	100	90	20	30
Bank Voltage (kV)	3	4	1.5	2
External inductance (μH)	2	3	2	2
Capsule Velocity (km/s)	1	1.5	0.4	1
Acceleration Time (ms)	1.5	1.5	0.7	1

Table MS-DIS-1: *Electromagnetic Particle Injector parameters.*

A cylindrical capsule would be fabricated out of thin (~ 0.5 to 1 mm thick) boron nitride, with a rounded front end. The actual wall thickness needs to assessed experimentally by the strength requirements needed for the capsule to travel through a bent guide tube between the injector and the ITER vessel. The cylindrical shape in combination with a rounded front end is chosen to allow the capsule to easily travel through the guide tube with a shallow bend to avoid direct streaming of neutrons back to the injector. The hollow shell pellet would be filled with boron nitride powder, although for ITER applications beryllium powder could also be considered. For NSTX-U applications, the capsule would be fragmented prior to injection into NSTX-U using a shatter plate, or by introducing sharper bends in the guide tube itself to fracture it inside the guide tube. For ITER applications, while such systems could be deployed, the much larger, and much more energetic nature of an ITER plasma may require that much of the capsule be injected nearly intact so that the particles penetrate deep within the plasma, and not be ablated at the plasma edge. These are details that need theoretical investigations to calculate the ablation rate of different sized particles in an ITER plasma environment and the minimum required velocities for

these particles to penetrate sufficiently deep into the plasmas, to determine if shattering the pellet before injection into an ITER discharge is a viable option.

References

[MS-DIS-1] S. C. Jardin et al., J. Phys.: Conf. Series **125** 012044 (2008)
[MS-DIS-2] S. C. Jardin et al., Computational Science and Discovery **5** 014002 (2012)
[MS-DIS-3] R. Raman, et al., Review of Scientific Instruments **85**, 11E801 (2014)
[MS-DIS-4] R. Raman, et al., "Fast Time Response Electromagnetic Disruption Mitigation System", 41st EPS Conference on Plasma Physics, P5.015

Transport and Turbulence Physics Research

NSTX transport and turbulence studies in FY2014, in the absence of operation, have focused on analyzing existing data and performing experiment-theory comparisons.

1. Thermal Transport

The unique features of ST operation result in a fusion plasma regime distinct from that of conventional aspect ratio tokamaks. In particular, because of the strong toroidal rotation, large ρ_i/a and strong toroidicity and shaping, it is crucial, while highly challenging, to use global gyrokinetic simulations to address turbulence and transport physics. Nonlinear global gyrokinetic simulations of an NSTX L-mode plasma using the GTS code [TT-1] have shown, for the first time, that a drift wave Kelvin-Helmholtz mode can be destabilized by strong toroidal rotation shear. This shear flow mode is characterized by finite $k_{||}$ and broader $k_{\square}$ than the ITG mode, which is also found to be present in the L-mode. Figure TT-1 shows the perturbed electric potential for the combined ITG and Kelvin-Helmholtz modes, which co-exist. The strong ExB shear can, at the same time, reduce the low-k fluctuations and associated transport linearly by changing the unstable mode family members and structure, and nonlinearly by modifying the fluctuation amplitude and spectrum. However, even at the reduced level, the remaining low-k fluctuations, while contributing weakly to the observed highly anomalous electron thermal transport, can produce a significant ion thermal transport relevant to the experimental level in the outer core region. Figure TT-2 shows the comparison of the experimentally inferred electron (right) and ion (left) thermal diffusivities along with the values predicted by the GTS code and neoclassical calculations of ion thermal diffusivity. For the ions, the inferred and predicted profiles are within a factor of two in the outer core (the total predicted ion thermal transport is the combination of values from the GTS and neoclassical calculations).

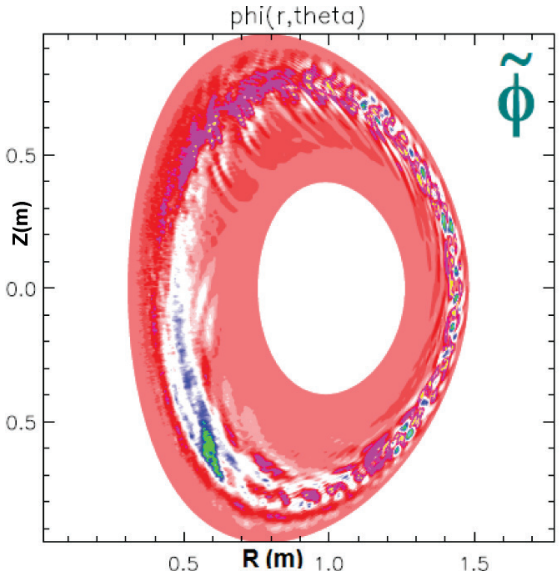

Figure TT-1 *Nonlinear GTS result showing electric potential perturbation for combined ITG/Kelvin-Helmholtz modes in an L-mode plasma.*

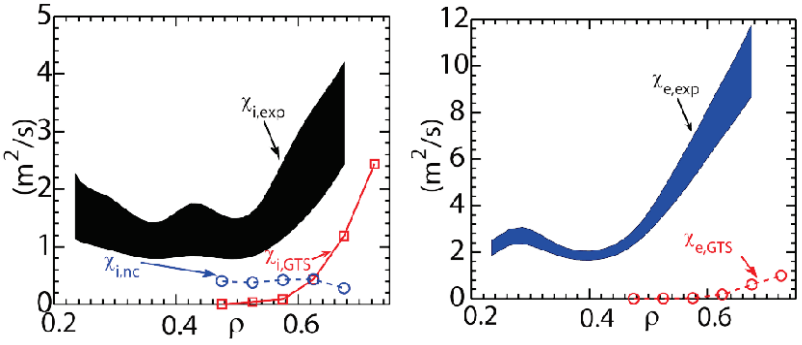

Figure TT-2 *Comparison of experimental and GTS predicted thermal diffusivity for ions (left panel) and electrons (right panel).*

Representative H-mode discharges were studied in detail as a basis for a time-evolving prediction of the electron temperature profile using an appropriate reduced transport model. For a high collisionality discharge, the time evolution of characteristic plasma variables such as β_e, ν_e^*, the MHD a parameter and the gradient scale lengths of T_e, T_i and n_e were examined as a prelude to performing linear gyrokinetic calculations using GYRO [TT-2] to determine the fastest growing microinstability at various times and locations throughout the discharge. The inferences from the parameter evolutions and the linear stability calculations were consistent. Early in the discharge, when β_e and ν_e^* were relatively low, ballooning parity modes were dominant. As time progressed and both β_e and ν_e^* increased, microtearing became the dominant low-k mode, especially in the outer half of the plasma. There are instances in time and radius where other modes, at higher k_θ, may be important for driving electron transport, in addition to the microtearing. Given these results, the Rebut-Lallia-Watkins (RLW) electron thermal diffusivity model, which is based on microtearing-induced transport [TT-3,TT-4], was used to predict the time-evolving electron temperature across most of the profile. The results indicate that RLW does a good job of predicting T_e for times and locations where microtearing was determined to be important, but not as well when microtearing was predicted to be stable of subdominant [TT-5].

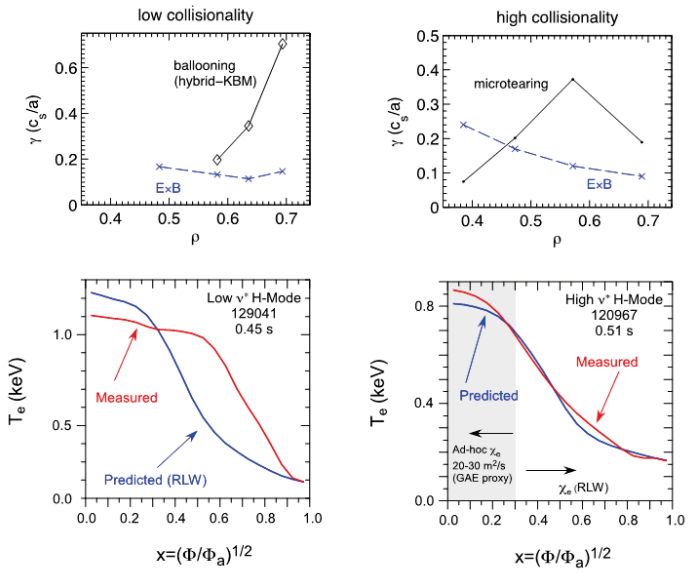

Figure TT-3 *Linear growth rates (top) and measured vs predicted T_e using the RLW model (bottom) for a low (right) and high (left collisionality H-mode discharge.*

Shown in Fig. TT-3 is a comparison of the linear growth rates (top panels) and predicted and measured T_e profiles (bottom panels) at representative times for two discharges at low and high collisionality respectively. For the low ν_e^* (left panels), the dominant microinstabilities have ballooning parity, and are identified as a hybrid TEM/KBM. For this discharge, the RLW model does a poor job of predicting the T_e profile. However, for the higher ν_e^* discharge (right panel), where microtearing is calculated to be dominant, RLW does an excellent job in matching the T_e profile in the region from x=0.2 to 0.8. Inside of 0.2, an ad-hoc χ_e was used as a proxy for transport induced by GAE/CAE modes in the very core, and x=0.8 was chosen as the boundary. Identifying the reduced model that is able to predict electron temperatures in this unique ST parameter regime can lead to higher confidence extrapolations to future STs, such as FNSF and NSTX-U, where microtearing may be unstable.

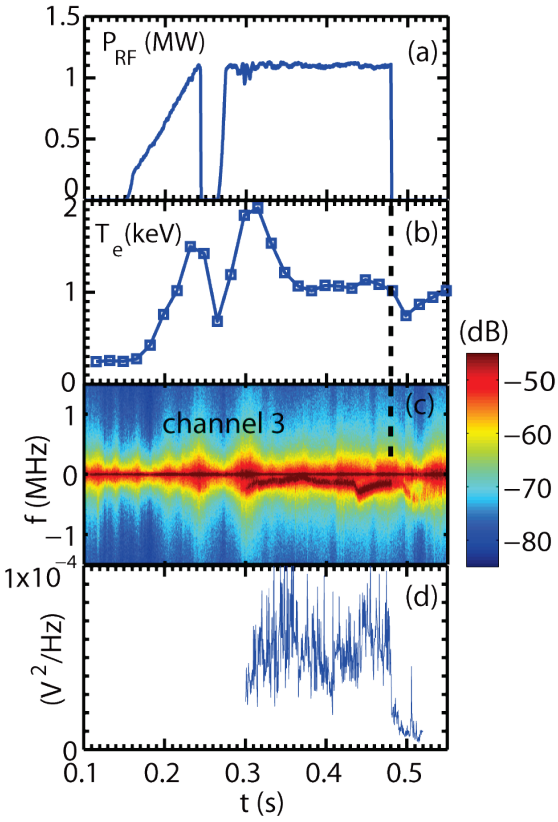

Figure TT-4 *The time traces of (a) injected RF power and (b) maximum T_e; (c) Spectrogram of signal from the channel 3 of the high-k scattering system; (d) Time trace of the peak spectral power of the scattered signal. A black vertical solid line extends from (b) to (c) denotes the time point at which the RF heating is terminated, i.e. t=479.6 ms.*

Highly non-linear electron thermal transport was observed in a set of RF-heated L-mode plasmas [TT-6]. It was observed that electron-scale turbulence spectral power, as measured by a high-k collective microwave scattering system (high-k scattering system) [TT-7] at r/a~0.6, was reduced significantly following the cessation of RF heating (see Fig. TT-4). The scattered signal measured the microwave high-k scattering system, i.e. the spectral peaks at f<0 shown in Fig. TT-4(c), can be distinguished easily from the stray radiation, i.e. the central peak at f=0, from about t=300 ms to 550 ms, and we can see that a sudden drop in scattered signal power at almost the same time as the RF cessation at t=479.6 ms shown in Fig. TT-4(a). This drop can be seen more clearly in Fig. TT-4(d), where the time trace of the peak spectral power of the scattered signal in Fig. TT-4(c) is plotted. The results clearly show a time delay of about one to two ms between the RF cessation and the drop of about a factor of seven in measured electron-scale turbulence, indicating a causal relation between the two. In addition, the drop in turbulence spectral power happened on a 0.5 to 1 ms time scale, which is too fast for the standard local transport paradigm to provide a satisfying explanation. This is because that, while the drop in turbulence was on a fast time scale, there was virtually no change in the local equilibrium quantities that would be expected to drive the turbulence (e.g., a/L_{Te}, a/L_{Ti}, a/L_{ne}) on this time scale; the changes in these quantities occurred on confinement time scales (e.g., tens of ms). The power balance analysis has shown about a factor of two decrease in the electron thermal transport after the sudden drop in turbulence. Linear stability analysis has shown that both ion- and electron-scale microinstabilities are unstable in the high-k measurement region, and that, linearly, the profiles are well above marginal stability. Two explanations are being explored for this non-linear response through nonlinear local and global gyrokinetic simulations. The first is one of high profile stiffness, so that even nearly-negligible changes in driving gradients can lead to large changes in turbulence and transport. The second is on of flux-driven transport, which would inherently be a non-local phenomenon. A decrease in local heat flux, due to changes in some other region of the plasma, leads to a decrease in the turbulence responsible for the transport.

First detailed measurements of changes of high-k turbulence across the L-H transition have also been made with the high-k scattering system [TT-7,TT-8]. The high-k turbulence measurement (for $3 \lesssim k_\perp \rho_s \lesssim 12$) was carried out in an NSTX discharge with I_p=1.1 MA, B_T=5.5 kG and NBI heating power of 2-6 MW. The measurement region is located at R=135.5-140 cm (r/a≈0.71-0.81) and is at smaller radius than the location of the Edge Transport Barrier (ETB) in the H-mode phase ($R \gtrsim 143$ cm, $r/a \gtrsim 0.89$). It is observed that before the high-k turbulence is suppressed to its minimum at about t=365 ms with the L-H transition occurring at about t=350 ms, it gradually decreases from about t=350 to 365 ms, during which time there are intermittent periods of about 0.5-1 ms having close to minimum high-k turbulence [see Fig. TT-5(a) and (c)]. This "dithering" phase (from about t=350 to 365 ms) of high-k turbulence coincides with similar "dithering" behavior seen in the D_α signal for the same time period, although no set phase relations between the two is identified (low-f activity was seen to be relatively benign after the L-H transition). The measured wavenumber spectra show that the suppression of the high-k turbulence occurs only at lower wavenumbers, namely $k_\perp \rho_s \lesssim 9$. It was after this period of dithering that the ETB at r/a>0.9, typical of the H-mode, was fully established. The suppression of high-k turbulence is found to be consistent with the decrease in maximum ETG linear growth rate from gyrokinetic stability analysis using measured equilibrium profiles. However, such a consistency cannot explain the observed intermittency in the high-k turbulence since equilibrium profiles are not expected to change much on the 0.5-1 ms time scale of the high-k quiescent periods and nonlinear effects must play an important role. In addition, low-k turbulence measurements from Beam Emission Spectroscopy (BES) diagnostic [TT-9] at the same location exhibited similar temporal intermittency as the high-k turbulence [see Fig. TT-5(b) and (c)].

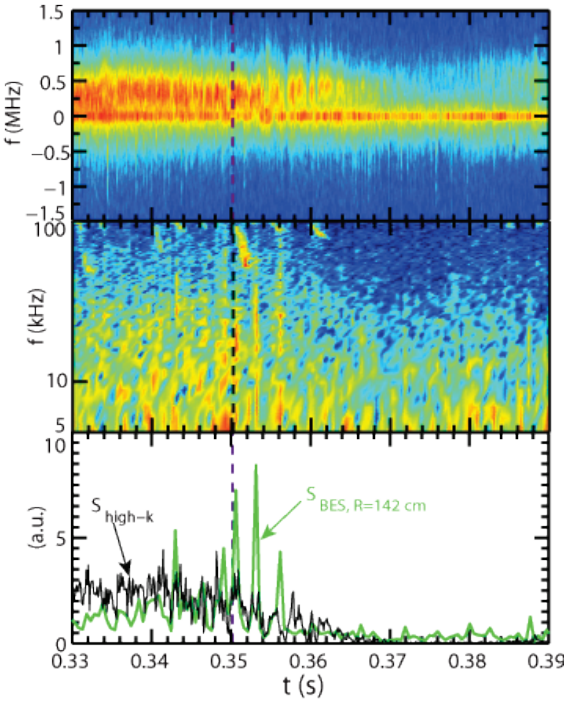

Figure TT-5 *(upper panel) Spectrogram of the signal from the channel 3 of the high-k scattering system; (middle panel) Spectrogram of the signal from a BES channel at R=142 cm; (lower panel) Integrated spectral power of the scattered signal from the channel 3 of the high-k scattering system (black) and integrated BES fluctuation power from 8 kHz to 45 kHz to avoid MHD activities at higher frequency (green).*

2. Momentum Transport

Linear gyrokinetic analysis has been used to study the source of anomalous momentum and impurity transport in NSTX. While many microinstabilities were considered, it is expected that only ion-scale ballooning instabilities contribute to the transport of momentum and impurities. In NSTX H-mode plasmas, perturbation experiments indicated the existence of a significant inward momentum pinch [TT-10,TT-11]. However, only microtearing or KBMs are predicted to dominate in these plasmas, and simulations indicate only a small outward pinch (Fig. TT-6), which is insensitive to parameter variations. Gyrokinetic calculations for L-mode plasmas indicate that the inward momentum pinch is also small and weakly dependent on many parameters. Initial global, nonlinear gyrokinetic simulations have been performed for an L-mode plasma using GYRO [TT-2], GTS [TT-3] and XGC-1 [TT-12]. The results for all three codes show a significant inward residual stress contribution in the absence of flow shear (Fig. TT-7), which would contribute to the overall momentum balance.

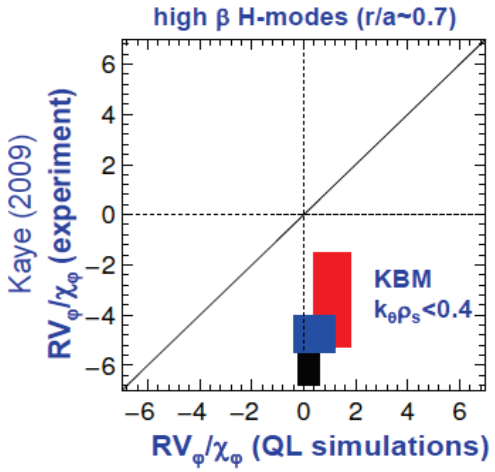

Figure TT-6 *Comparison of momentum pinch (RV_ϕ/χ_ϕ) from perturbative H-mode experiments as well as quasi-linear gyrokinetic predictions.*

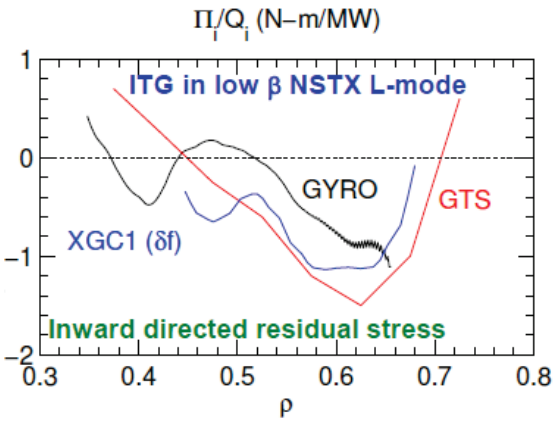

Figure TT-7 *Predictions of momentum flux due to residual stress contributions from global, nonlinear gyrokinetic simulations (in the absence of flow and flow shear) using GYRO, GTS and XGC-1.*

3. Particle and Impurity Transport

NSTX-U researchers contributed to control room profile analysis and between-shots gyrokinetic simulations of the DIII-D National Fusion Science Campaign experiment "Controlling H-mode particle transport with ECH" (Oct. 2013) led by D. Ernst (MIT). Gyrokinetic simulations show density gradient driven trapped electron modes (TEM) are the only unstable drift modes in the inner half-radius (Fig. TT-8). Particle transport driven by TEMs increases strongly with electron temperature when local ECH is applied, reducing the core electron density gradient. Despite a reduction in density gradient, the growth rates increase due to doubling of T_e/T_i, which reduces the threshold density gradient of the TEM. Ongoing analysis will contribute to an IAEA 2014 oral (Ernst), and also provides a basis for studying density profile control in NSTX-U using RF heating.

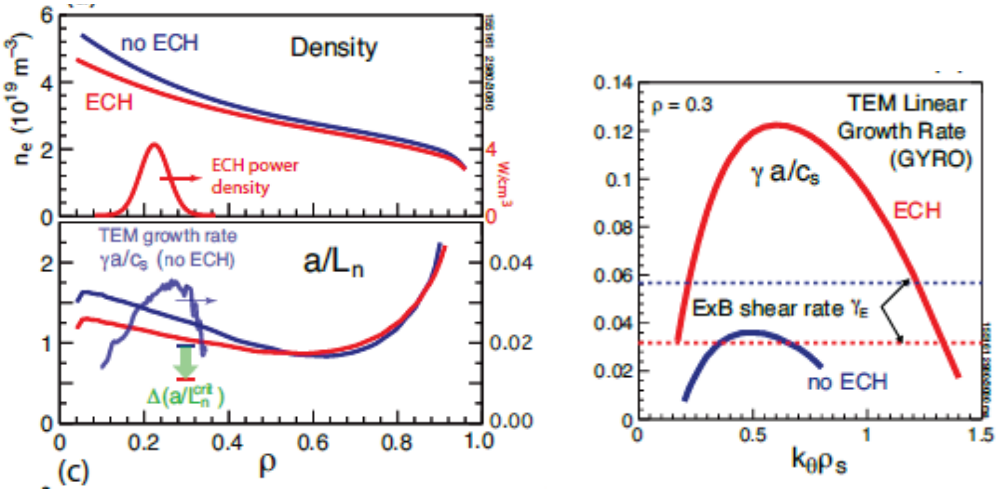

Figure TT-8 *(left) Density profiles without and with ECH heating in the core of DIII-D QH modes. (right) Corresponding profiles of normalized density gradient (a/Ln), as well as linear TEM growth rates for the case w/o ECH. (right) Core (ρ=0.3) linear growth rate spectra and E×B shearing rates (γ_E).*

For impurity transport, the linear gyrokinetic calculations indicate an inward carbon pinch when KBMs dominate, which is inconsistent with experimental observations [TT-13]. Consequently local linear theory does not appear to explain impurity transport in NSTX. While non-local effects could be important and are being investigated, the influence of centrifugal effects are also being examined using the GKW code in collaboration with University of Bayreuth.

Understanding the mechanism of impurity flushing during 3D fields-triggered ELMs and quantifying their effect is important to determine their applicability in NSTX-U. ELM-free H-mode discharges in NSTX were characterized by core accumulation of impurities. This was the result of near neoclassical levels of impurity transport, an edge inward impurity pinch and the absence of impurity flushing mechanisms (e.g., ELMs) [TT-13]. Accumulation of metallic impurities led to high levels of core radiated power (up to 50% of the injected power) while accumulation of carbon prevented the achievement of density control in discharges with lithium conditioning where the deuterium inventory was otherwise generally controlled. One of the leading strategies under consideration to achieve density control in the NSTX-Upgrade is the combined use of lithium coatings for deuterium control and the triggering of ELMs to flush impurities from the core plasma. Non-axisymmetric magnetic perturbations (n=3) were applied in NSTX to trigger ELMs (f_{ELM}=10-62.5 Hz) in order to mitigate core impurity buildup while maintaining the positive effects of lithium on energy confinement [TT-14, TT-15, TT-16].

The response of kinetic plasma profiles to ELMs triggered by 3D fields and the inter-ELM impurity transport was therefore studied in H-mode discharges in NSTX. For ELMs triggered at 10 Hz, carbon impurity flushing was observed following the ELM crash for normalized volumetric radii (R_{VOL}) larger than 0.6. Up to a 30% drop in the carbon density was observed at the pedestal top. Comparable effects were observed in the T_e, n_e, T_i, v_Φ profiles following the ELM crash. While carbon profiles recovered within the 10 Hz ELM cycle, the increase in the

triggering frequency led to a reduction in the overall core carbon inventory, progressively affecting carbon density profiles at inner radii. In particular, the carbon inventory for $0.5< R_{VOL} <1.0$ decreased by up to a factor of 2 with the increase in the ELM frequency while no decrease was observed in the carbon inventory inside $R_{VOL} \sim 0.5$. The impurity transport code MIST was used to simulate the carbon transport during and following the ELM crash, similarly to what carried out in other devices (e.g., ASDEX-Upgrade [TT-17]). The equilibrium v/D ratio is inferred from the steady state carbon density profiles and the absolute levels of the transport coefficients are scaled by the neoclassical diffusivity, consistently with what done in Ref. [TT-13]. Transient perturbations to the steady state particle diffusivity D and convective velocity v are applied to reproduce the response of the carbon density profile to the ELM. The profile recovery following the ELM crash is used to estimate absolute values of the transport coefficients. Preliminary results indicate the need for an inward (convective) transport perturbation for $R_{VOL}<0.6$ to drive carbon flux upward the core peaked carbon density profiles and reproduce the experimentally observed increase in core carbon density immediately following the ELM crash. An outward (diffusive and/or convective) transport perturbation for $R_{VOL}>0.6$ is instead needed to reproduce the ELM flushing effect at the edge.

4. Diagnostic development

The University of Wisconsin-Madison maintains and operates the BES system that measures density fluctuations in the core, pedestal, and SOL regions. BES measurements of ion-scale fluctuations and instabilities contribute to several areas including turbulence and transport, edge physics, and macroscopic/MHD instabilities.

Two significant upgrades to the BES system were performed in 2014 in preparation for NSTX-U operation. First, the BES detector inventory expanded from 32 to 48 channels. The detector expansion improves utilization of fixed BES sightlines and reduces the need to manipulate delicate optical fibers. All 48 detectors are presently at PPPL, and alignment and installation activities are ongoing. Second, UW and PPPL Engineering jointly designed a new fiber assembly for 2D BES measurements spanning the pedestal region. The UW Physical Sciences Lab has nearly finished fabricating the 2D assembly (http://www.psl.wisc.edu/archives/3114). As shown in Fig. TT-9, the 2D configuration includes 54 fiber bundles in an approximate 9x7 configuration, and the configuration spans r/a~0.4 to the scrape-off-layer. The 2D configuration will facilitate more sophisticated studies of turbulence and transport including zonal flows dynamics, Reynolds stress measurements, and velocimetry.

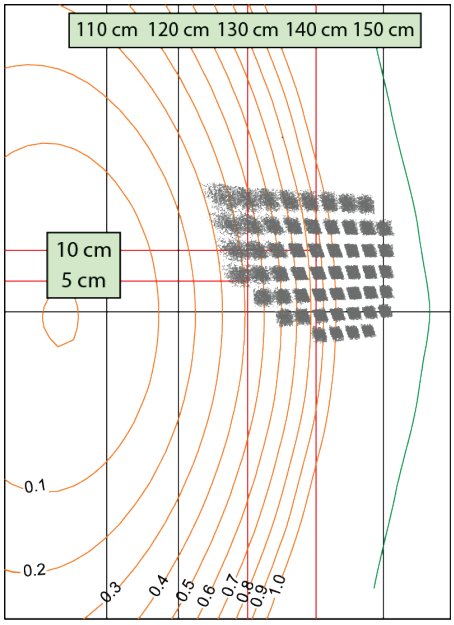

Figure TT-9 *New 2D fiber configuration for BES measurements on NSTX-U.*

References

[TT-1] W.X. Wang et al., Phys. Plasmas, **17**, 072511 (2010).
[TT-2] J. Candy and R. Waltz, J. Comput. Phys., **186**, 545 (2003).
[TT-3] P.H. Rebut and M. Brusati, Plasma Phys. Controlled Fusion, **28**, 113 (1986).
[TT-4] P.H. Rebut, P.P. Lallia and M.L. Watkins, The critical temperature gradient model of plasma transport: applications for JET and future tokamaks (Proc. 12th IAEA Conference on Plasma Physics and Controlled Nuclear Fusion Research, Nice, France, 1988), 1988, IAEA-CN_50/D-4-1.
[TT-5] S.M. Kaye et al., accepted for publication in Phys. Plasmas (2014).
[TT-6] Y. Ren et al., to be submitted to Phys. Plasmas.
[TT-7] D. R. Smith et al., Rev. Sci. Instrum. **79**, 123501 (2008).
[TT-8] Y. Ren et al., to be submitted to Nucl. Fusion.
[TT-9] D. R. Smith et al., Rev. Sci. Instrum. **81**, 10D717 (2010).
[TT-10] W.M. Solomon et al., Phys. Rev. Lett., **101**, 065004 (2008).
[TT-11] S.M. Kaye et al., Nucl. Fusion, **49**, 045010, (2009).
[TT-12] S. Ku, C.S. Chang and P.H. Diamond, Nuclear Fusion **49**, 115021 (2009).
[TT-13] F. Scotti, et al., Nucl. Fusion **53**, 083001 (2013).
[TT-14] J.M. Canik, et al, Phys. Rev. Letter **104** , 045001(2010).
[TT-15] J.M. Canik et al., Nucl. Fusion **50**, 034012 (2010).
[TT-16] J.M. Canik, et al., Nucl. Fusion **50**, 064016 (2010).
[TT-17] T. Pütterich et al., J. Nucl. Mater. **415**, S334-S339 (2011).

Energetic Particle Research

Following the two main Thrusts for EP research on NSTX-U over the FY14-18 time period, research in FY14 has focused on improving predictive tools for fast ion transport and assessing requirements for mitigation/suppression of EP-driven instabilities. The main results obtained in the past year fall into three categories: experimental work, joint theory/experiments work and code development for improved analysis and simulations. The major outcomes from each category are briefly summarized below.

1. Classification of stability domains

Classification and quantification of the stability domain for EP-driven instabilities is a necessary step to establish validated predictive capabilities for fast ion transport. At low frequency (f<50kHz), the stability of kink-like modes (including fishbones) was characterized numerically through the M3D-K code [EP-1]. For the NSTX case analyzed in detail, a transition was observed from unstable non-resonant kinks at the lowest $\beta_{fast}/\beta_{total}<0.15$ to fishbones at higher $\beta_{fast}/\beta_{total}$. The important role of the minimum value of the *q* profile has been assessed, with fishbones destabilized even at higher $q_{min}>1.1$-1.2. Numerical results are now being compared with a more extended database from NSTX discharges spanning $0.1<\beta_{fast}/\beta_{total}<0.6$ and $1<q_{min}<2$ [EP-2].

At frequencies up to the TAE range, stability boundaries for Alfvénic modes (AEs), Energetic Particle modes (EPMs) and other kink-like instabilities have been empirically characterized in terms of fast ion to Alfvén velocity ratio *vs.* fast ion to total plasma pressure (or beta) ratio [EP-3], see Fig. EP-1. A database has been constructed, based on shots for which TRANSP runs were performed. Each shot was divided into 50 ms intervals. For each interval, the dominant beam-driven activity was characterized and plasma parameters were collected into a database. Overall, it is found that TAE avalanches are present for $\beta_{fast}/\beta_{total}>0.3$ and quiescent plasmas only for $\beta_{fast}/\beta_{total}<0.3$. A more quantitative assessment of the TAEs stability, including their saturation level, is under way by studying the multi-mode scenarios commonly observed on NSTX through the M3D-K code [EP-4]. Preliminary results show strong modification of the mode dynamics, including frequency chirping and amplitude modulation, when multiple modes are included self-consistently in the simulation.

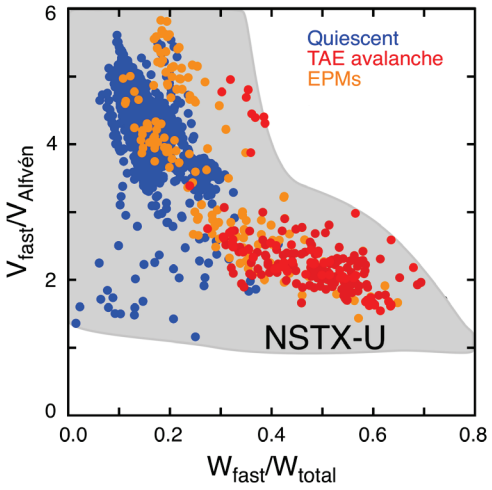

Figure EP-1: *Stability diagram for various EP-driven instabilities on NSTX (from Ref. [EP-3]). The expected parameter range for NSTX-U is shown by the shaded area.*

At even higher frequency, near the ion cyclotron frequency, work has continued to characterize Compressional and Global AEs (CAEs/GAEs). Simulations through the hybrid MHD code HYM have confirmed and extended previous results, showing coupling of CAEs to kinetic Alfvén

waves (KAWs) [EP-5]. Since KAWs are strongly damped on the thermal plasma, this would provide an efficient mechanism for dissipation of fast ion energy, driving the CAEs, to electrons (cf. Sec. on Transport and Turbulence Physics Research). In addition to HYM, new tools are being developed to study these high frequency modes, see below.

2. Study of multi-mode physics – towards "mode control"

For all classes of EP-related modes mentioned above, modifications of mode stability caused by different mechanisms are observed experimentally and can provide the basis to develop mode control schemes. In addition to mode-mode coupling phenomena (e.g. between kinks and CAEs/GAEs) and to the mitigation of high frequency GAEs by 3D fields reported in the past [EP-6][EP-7], new studies have been performed to look at modifications of mode dynamics correlated with High Harmonic Fast Wave (HHFW) injection [EP-8]. For a series of NSTX discharges at low current, I_p~300kA, HHFW heating with P_{rf}=2MW is found to simultaneously suppress fishbones, TAEs and GAEs (Fig. EP-2). The timescales for mode suppression at HHFW onset, and for the modes to recover after HHFW heating could provide hints on the mechanism of mode suppression. Both GAE and TAE activity persist for 40-50 ms after the start of HHFW heating. The strong frequency chirping of both the TAE and GAE appears to be quickly suppressed, although in both cases, frequency chirp does reappear. The delay in suppression after start of HHFW heating suggests that it either takes some time to modify the fast ion distribution responsible for exciting TAEs and GAEs, or there are variations in the equilibrium plasma parameters, during this interval, which affect the AE stability.

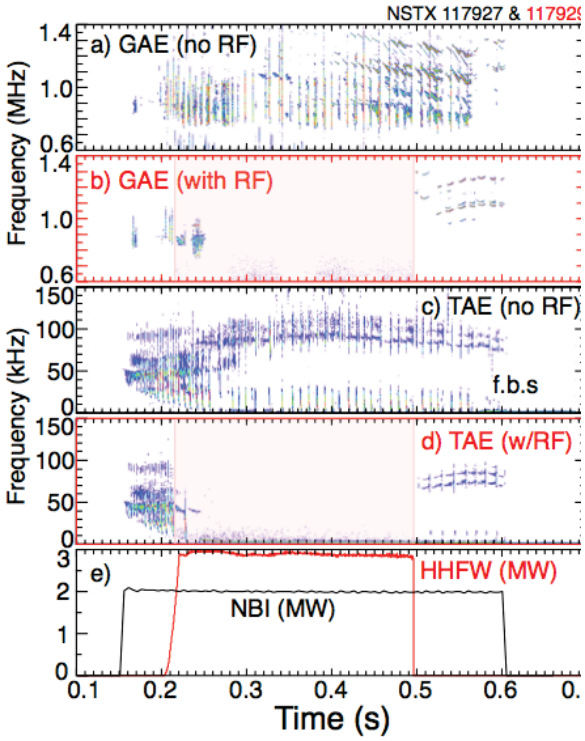

Figure EP-2: *Spectrograms showing GAE frequency range a) w/o RF, b) with RF, TAE frequency range c) w/o RF, d) with RF and e) NBI and HHFW power waveforms. (from Ref. [EP-8]).*

3. Development of "reduced models" for fast ion transport

The substantial modification of fast ion dynamics and confinement properties caused by their interaction with instabilities motivates the development of tools to improve both data analysis and simulation capabilities. An important line of research that has made substantial progress in FY14 is the development of reduced models for fast ion transport, which enable more accurate simulations of EP behavior in the presence of instabilities. The need for *reduced* models – as opposed to *first-principle* models – arises from the need of long-time-scale, integrated simulations in which fast ion behavior is taken into account along with other quantities (e.g. thermal plasma, sources and sinks) in a self-consistent way for the entire duration of a discharge.

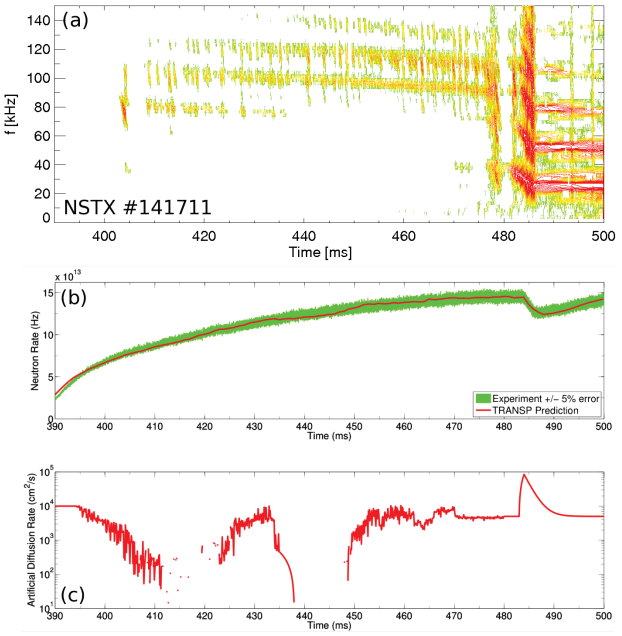

Figure EP-3: *(a) Spectrogram from Mirnov coils showing TAE activity which culminates in an avalanche at t~485ms. (b) Measured and predicted (TRANSP) neutron rate. The anomalous fast ion diffusivity shown in (c) is required to match the experimental values. (from ref. [EP-9]).*

Two different models have been developed in FY14 as part of the NSTX-U R14-2 Research Milestone (see dedicated Section), namely a Critical Gradient model (CGM) and a probabilistic "kick" model. After its initial validation for DIII-D plasmas, the CGM has been applied for further validations against NSTX scenarios with multiple unstable TAE modes which transition from weakly bursting/chirping separable instability regimes to coupled TAE avalanches (Fig. EP-3) [EP-9]. For this analysis, an effective fast ion diffusion rate has been derived from TRANSP. A relatively small diffusivity $<1 m^2/s$ is required to match the measured neutron rate when TAE activity is weak, whereas it spikes to $>8 m^2/s$ during a TAE avalanche, indicating that the instabilities are likely to be strongly coupled. Implications for the radial fast ion pressure or density profiles evolution are now under assessment via the CGM model. The model is being employed in order to understand the ways it is applied to fusion experiments and whether time averaging of its predictions is required.

The study of TAE avalanches effects on the fast ion distribution and other associated quantities, such as the NB-driven current, have also provided an initial benchmark for the newly developed "kick" model [EP-10]. Results for a discharge with repetitive TAE avalanches indicate a substantial redistribution of fast ions in space and energy. The latter is, in fact, responsible for most of the observed reduction in the neutron rate. Moreover, the model can resolve the effects of TAE avalanches on NB-driven current redistribution, which requires resolving the fast ion dynamics in phase space (energy, pitch) in addition to the spatial variables. A comparison with commonly used diffusive models presently available in TRANSP shows clear differences in the computed NB driven current profile (Fig. EP-4), which confirms that the details of EP evolution in phase space are indeed important for quantitative predictions.

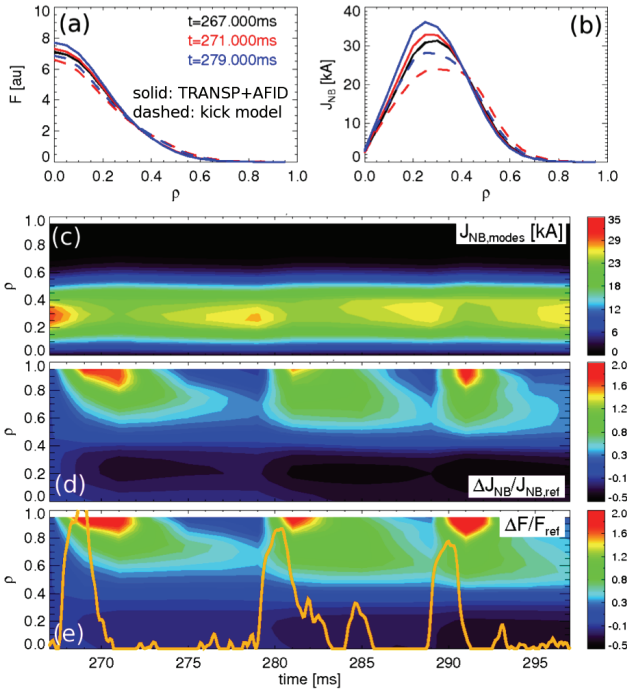

Figure EP-4: *Effects of TAE avalanches on fast ion and NB-driven current profiles (ρ: normalized toroidal flux). (a) Fast ion profile before, just after and 10 ms after the first TAE burst. (b) Same as in (a) for the NB-driven current profile. (c) NB-driven current profile. (d-e) Relative variation of NB-driven current and fast ion profiles normalized to the no-modes reference case. The solid line in (c) shows the mode amplitude. (from Ref. [EP-10]).*

The development of reduced models has proceeded in parallel with improvements to other numerical tools for EP simulations in FY14.

4. NOVA codes improvements

The suite of NOVA codes has been upgraded with an improved equilibrium solver, which accounts for toroidal rotation and (anisotropic) EP pressure effects through a "pressure coupling" scheme [EP-11]. This is a task emerged recently from realistic applications of the linear AE stability analysis for such applications as critical gradient model (see above, section 3).

The effects of plasma rotation have been included in the NOVA–K post-processor to compute realistically the thermal ion Landau damping and fast ion drive, which include such important stabilizing effects as ion finite Larmor radius (FLR) and finite orbit width (FOW) effects. The improved computation scheme reduces ion Landau damping by up to an order of magnitude with respect to the case where rotation is neglected. These effects are especially important for the level of agreement CGM has when validated against the experimental data. Modifications of NOVA-K led to significantly improved agreement with the experimental data, especially in the plasma center where ion Landau damping does not allow sufficient EP profiles relaxation.

5. ORBIT improvements

An important aspect for wave-particle interaction studies is the characterization of which portions of EP phase space are involved in the interaction and which modes mostly contribute to the energy exchange. Particle following codes such as ORBIT [EP-12] are well suited for this task. The ORBIT code has been extensively used for EP studies on NSTX. It also represents a crucial step in the implementation of the reduced "kick" model, by providing the probability distribution $p(\Delta E, \Delta P_\zeta)$, which contains the information on wave-particle interaction in phase space.

Recent upgrades to ORBIT enables more intensive simulations over short times, e.g. to follow fast ion dynamics over time scales comparable to, or exceeding, the slowing-down time. Multi-threaded parallelism has been introduced in the core of the code, with the goal of achieving the largest performance improvement while minimizing changes made to the source code [EP-13]. Compiler directives have been introduced in the most compute-intensive parts of the code, which constitutes the stable core that seldom changes. Standard OpenMP directives are used for shared-memory CPU multi-threading while newly developed OpenACC directives and CUDA Fortran code are used for Graphics Processing Unit (GPU) multi-threading. Initial tests shows that the fully-optimized CUDA Fortran version is >50 times faster than the original code.

Applications for the improved ORBIT code (along with TRANSP simulations utilizing the new "kick" model) will include projections of EP modifications by AEs on NSTX-U, for instance as a function of different mixes of on- vs. off-axis NB injection.

6. Exploring the use of RF codes for AE antenna simulations

A set of AE antennae has been recently installed on NSTX-U to study mode stability properties through active spectroscopy and enable a detailed comparison with stability codes such as NOVA-K, M3D-K and HYM. In this regards, the possibility to extend the use codes originally designed for RF studies to EP studies has been explored in FY14 [EP-14]. In particular, the AORSA and TORIC full wave codes may be suitable to study antenna-driven modes in the ω_{ci} frequency range. The advantage with respect to other EP simulation codes is that full wave RF codes retain effects such as full power absorption by species, full finite-Larmor-radius (including $\omega \sim \omega_{ci}$ range) and the possibility to use either a measured or predicted (e.g. by TRANSP) fast ion distribution as input. As an initial result, TORIC simulations have shown similarities with HYM predictions on the coupling between ω_{ci} modes and KAWs (Fig. EP-5), suggesting that AORSA and TORIC can be used to optimize the AE antenna operations and to guide design improvements for CAEs/GAEs stability studies.

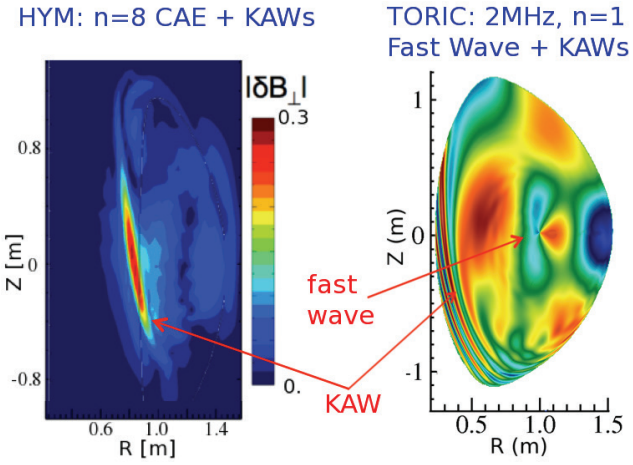

Figure EP-5: *HYM and TORIC results for $\omega \sim \omega_{ci}$ modes showing coupling to kinetic Alfvén waves (KAWs). Modes are driven by fast ions in HYM and by an external antenna in TORIC.*

7. Implementation of 3D Halo model in TRANSP

Another important achievement in FY14 for improved theory/experiment comparisons is the implementation of a new 3D "halo" model in TRANSP, which enables more accurate interpretation and simulations of charge-exchange-based diagnostics (e.g. NPA, ssNPA, FIDA). The effects of so-called halo neutrals are important, since halo density can be of the same order of the NB neutral density. The new model employs a "beam-in-a-box" model (Fig. EP-6a), which encompasses both NB and halo neutrals. Halos are thus modeled as a localized population, contrary to the previous model used in TRANSP. Initial simulations of E//B NPA signal confirm the importance of 3D halos. The total (localized) neutrals along the NPA line of sight increase by ~80%, leading to a similar enhancement in the reconstructed emissivity (Fig. EP-6b). The new model has been compared with the FIDASim code [EP-15], and a broader assessment of the two methods is ongoing to quantify the effects of different cross-section libraries available in TRANSP on NB deposition and simulation of charge-exchange reactions.

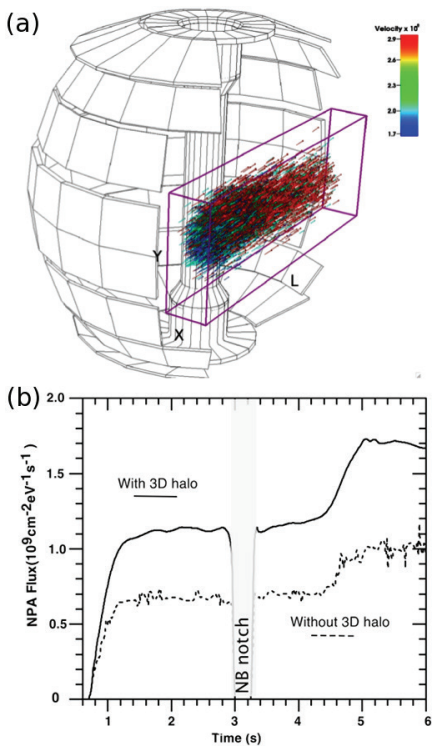

Figure EP-6: *(a) Beam-in-a-box scheme for new 3D halo model in TRANSP. (b) E//B NPA simulations showing a ~80% flux enhancement when the new halo model is used.*

References

[EP-1] F. Wang et al., Phys. Plasmas **20**, 102506 (2013)
[EP-2] G. Dong, to be presented at APS-DPP Meeting (2014)
[EP-3] E. Fredrickson et al., Nucl. Fusion **54**, 093007 (2014)
[EP-4] G.-Y. Fu et al., TTF Meeting, San Antonio TX (2014)
[EP-5] E. Belova et al., APS-DPP Meeting (2013)
[EP-6] E. Fredrickson et al., Phys. Plasmas **20**, 042112 (2013)
[EP-7] A. Bortolon et al., Phys. Rev. Lett. **110**, 265008 (2013)
[EP-8] E. Fredrickson et al., EPS Meeting (2014)
[EP-9] J. Lestz, to be presented at APS-DPP Meeting (2014)
[EP-10] M. Podestà et al., Plasma. Phys. Control. Fusion **56**, 055003 (2014)
[EP-11] N. Gorelenkov, TTF Meeting, San Antonio TX (2014)
[EP-12] R. B. White et al., Phys. Fluids **27**, 2455 (1984)
[EP-13] A. Qu et al., PPPL Report #4996 (2014)
[EP-14] C. K. Phillips et al., APS-DPP Meeting (2013)
[EP-15] W. W. Heidbrink et al., Commun. Comput. Phys. **10**, 716 (2011)

Wave Heating and Current Drive

Experimental work

Diagnostics for NSTX-U

RF studies will be greatly improved by upgrades to the diagnostic coverage in NSTX-U. Using a new dedicated set of Langmuir probes and an infrared camera viewing the antenna, it is anticipated that an improved understanding of the mechanism underlying the field-aligned losses of HHFW in the SOL and also interactions between neutral beam generated fast ions and fast waves will be achieved.

An array of RF-dedicated Langmuir probes has been designed, constructed, and installed in the NSTX-U vacuum vessel. Langmuir probes on NSTX showed a marked change in characteristics when the probe lay underneath the RF spiral [RF-1, RF-2]; however, it could not be determined whether this effect was due primarily to plasma heating, RF rectification, or both. The new probes have been designed to acquire data fast enough to resolve an RF cycle. The fast acquisition will provide a window into the physics behind RF-induced changes to Langmuir-probe characteristics and will hopefully definitively identify the change in characteristic as due to either heating or rectification. Also, the probes have been positioned in NSTX-U to fall under the most intense portion of the RF spiral. Analysis of NSTX probe data suggests that, if RF rectification is primarily responsible for the change in Langmuir probe characteristic, then the heat flux to the divertor tile at the probe location was enhanced by a factor of ~ 2. Estimates of the total power lost to the divertor region obtained in this fashion suggest that RF sheath losses could be a substantial contributor to the losses in the RF spiral.

RF Test Stand

The HHFW antenna used on NSTX, like all ICRF antennae, operates at high voltages and sometimes arcs. This arcing can potentially damage the antenna components and generally limits the power applied to the plasma. Understanding the exact location and cause of these arcs could lead to an improved antenna design and greater applied power. To facilitate such studies, two antenna straps have been installed in an RF test stand. The general setup of the test stand is as follows. The antenna straps are tuned to match the 50 ohm transmission line using two stub tuners. Diagnostics include a network analyzer, high-voltage probes in the transmission line, directional couplers, a residual gas analyzer (RGA), which measures the rise in gas pressure in the test stand as a result of an RF pulse, a fast visible-light camera for detecting arcs, and an infrared (IR) camera for determining the Ohmic heating of antenna components during an RF pulse.

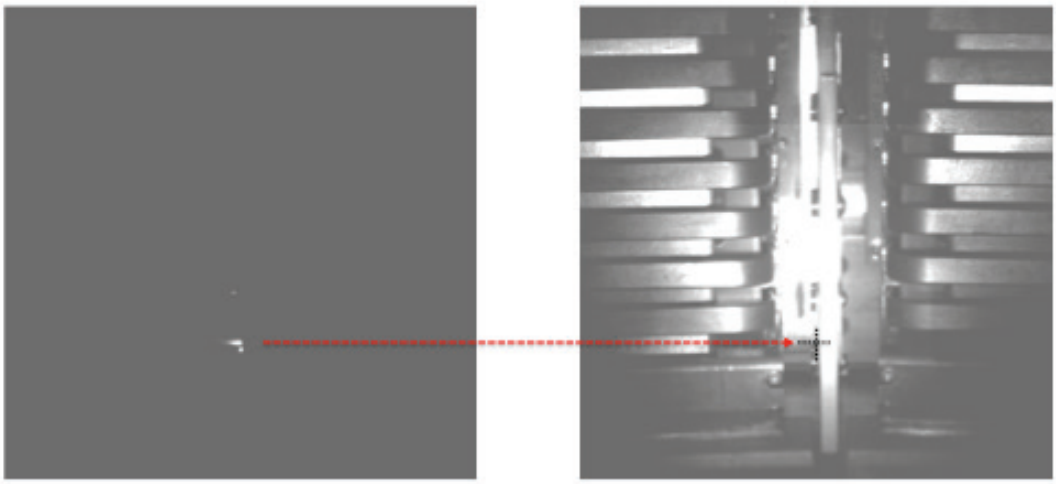

***Figure RF-14**: (LEFT) Location of arc in between the two antenna straps towards the low-voltage end at the bottom of the straps. (RIGHT) A picture of the antenna in which the straps, Faraday bars, and boron nitride septum can be seen. The light in this figure is from external illumination, not arcs.*

The visible-light camera located arcing towards the low voltage point of the antenna structure, as shown in Fig. RF-1. The location of this arc was somewhat surprising, as arcing was suspected to occur towards the high-voltage point of the antenna strap. This arcing was successfully eliminated by adding an additional grounding point between the antenna box and the vessel wall. The high voltage standoff improved up to ~ 46 kV for 55 ms RF pulse lengths; this standoff is much higher than that found on NSTX for vacuum operation (~ 25 kV). Moreover, any arcs occurring after the installation of the additional grounding point were observed towards the high-voltage end of the strap. The additional ground point has been implemented on the NSTX-U antenna structure and could lead to substantial improvement of the high-voltage standoff.

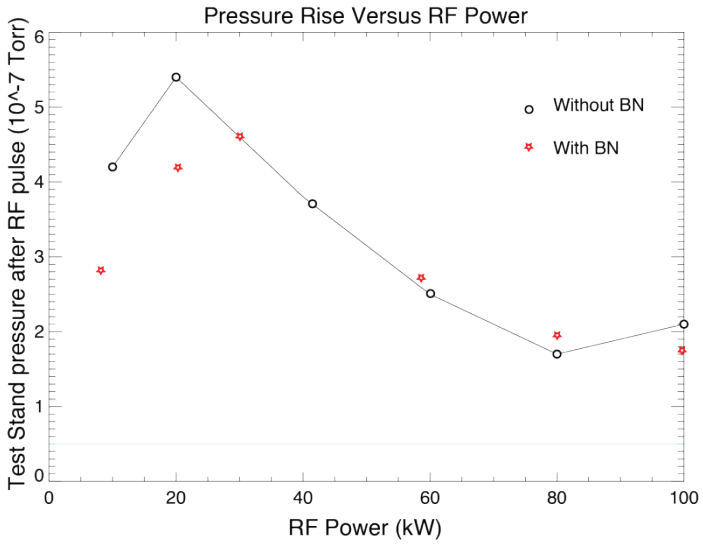

***Figure RF-15**: The pressure rise in the test stand in not a monotonic function of applied RF power. The base pressure is 0.5 * 10^{-7} torr.*

Despite the improvements made with the installation of the additional grounding point, the pressure rise in the test stand persists. It is possible this pressure rise is due to outgassing of the antenna components as a result of Ohmic heating. In Fig. RF-2, this pressure rise is plotted as a function of applied RF power and is found to be non-monotonic, which could be an indication of multi-pacting conditions as well.

Further insight into the origin of the pressure rise will be obtained using an infrared camera to observe Ohmic heating of the antenna structure. Initial results on the test stand show relatively intense IR emission from the edges of antenna faraday shield structure. While the measurements of IR emission have not yet been converted to temperature due to complication of IR reflections, the initial results are in qualitative agreement with Microwave Studio calculations that predict relatively large current densities in the edge of the Faraday cage. In the future the goal will be to locate where large Ohmic heating could lead to excessive out-gassing and then improve the antenna design to avoid this. This future work entails converting the IR-emission measurements to temperatures and making quantitative comparisons to Microwave Studio calculations.

Modeling work

NSTX and NSTX-U HHFW Simulations

Recent experimental studies of high harmonic fast wave (HHFW) heating on NSTX have shown that up to ~ 60% of the coupled HHFW power can be lost along the open field lines in the scrape-off layer (SOL) when edge densities are high enough that the fast waves can propagate close to the launcher. The mechanism behind the loss is not yet understood [RF-1, RF-2, RF-3 - RF-5]. The power loss is estimated by using the full wave code AORSA, in which the edge plasma beyond the last closed flux surface (LCFS) is included in the solution domain [RF-6]. A collisional damping parameter is used as a proxy for the actual, possibly nonlinear, damping processes [RF-7, RF-8]. The model is applied to specific NSTX discharges to predict the effects and possible causes of this power loss. Full wave simulations demonstrate for the first time a direct correlation between the location of the fast wave cut-off layer, the large amplitude of the RF fields in the scrape-off region, and the power losses in the SOL (driven by the RF field) observed in the NSTX experiments (see Fig. RF-3). In particular, a strong transition to higher SOL power losses has been found when the FW cut-off is removed from in front of the antenna by increasing the edge density (see Fig. RF-4), consistent with the experimental observations [RF-4]. When evanescent waves become propagating waves in the SOL, due to higher density in front of the antenna, the power losses start to increase significantly, commensurate with the amplitude of the RF field found in the SOL. The fraction of the power

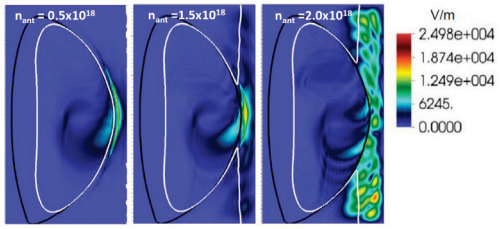

***Figure RF-3**: Electric field amplitude for different density values in front of the antenna (n_{ant}) (shown in the plots) with toroidal mode numbers $n_\phi = -21$. The white and black curves indicate the FW cut-off layer and the last closed flux surface, respectively.*

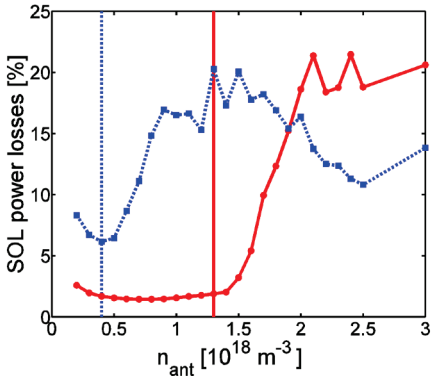

***Figure RF-4**: Fraction of power lost to the SOL as a function of the density in front of the antenna for $n_\phi = -21$ (solid curve) and $n_\phi = -12$ (dashed curve). The vertical lines represent the value of the density for which the FW cut-off starts to be "open" in front of the antenna (see Fig. RF-3).*

lost to the SOL evaluated in 3D calculations (using 81 toroidal modes to reconstruct the full antenna spectrum) is comparable to that of the dominant mode (2D, one single toroidal mode) runs. A transition in SOL power losses as a function of the density in front of the antenna is reproduced for the 3 D case, although it is less pronounced due to the contribution of the several toroidal modes. Larger SOL power losses in 3D runs with respect to the 2D runs are found for both low and high density in front of the antenna. Moreover, the full 3D shows that the absorbed power in the SOL is largest near the LCFS and near the front of the antenna, as experimentally observed [RF-2]. Full wave simulations have been also used to predict that plasmas in NSTX-U will have a wider operating SOL density range in which RF power losses in the SOL are low.

Simulation results for 28 GHz electron Bernstein wave (EBW) current drive in NSTX-U neutral beam injection (NBI) H-mode discharges

GENRAY-ADJ [RF-9] numerical simulations were run for two I_p = 1.2 MA, $B_T(0)$ = 1 T, 100% non-inductive, NSTX-U NBI H-mode plasmas, one with broad n_e and T_e profiles and the other with narrower profiles [RF-10] (Fig. RF-5). The location of the antenna was scanned in poloidal angle from the mid-plane to 70 degrees above the mid-plane, and the antenna was oriented to launch $n_{//}$ = 0.7. For cases where the antenna was within 40 degrees of the mid-plane the EBW-driven current density profile was narrow, with peak current drive densities of 0.8 MA/m^2/MW near r/a = 0.2 (Fig. RF-6). When the antenna was greater than 40 degrees above the mid-plane the location of the peak density shifted further off-axis to r/a = 0.3 - 0.6 and the current drive density fell to 0.05 - 0.1 MA/m^2/MW (Fig. RF-6). The EBW current drive efficiency is predicted to reach 40 kA/MW when the peak of the current density is located near the axis but falls to 10 - 15 kA/MW when current is driven out at r/a = 0.6 - 0.7. The current drive efficiency was found to be similar for the broad and narrow profile cases, but for a given antenna poloidal location the EBW-driven current density peaked further off axis for the case with narrower n_e and T_e profiles.

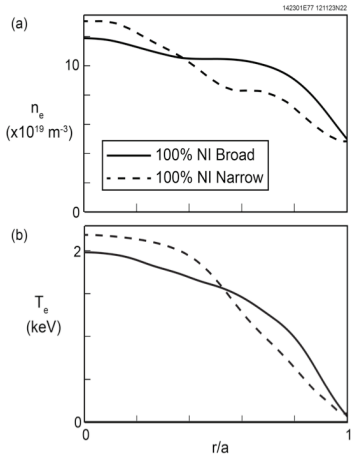

***Figure RF-5**. (a) n_e profiles and (b) T_e profiles used for modeling EBWCD in NSTX-U 100% non-inductive H-mode plasmas.*

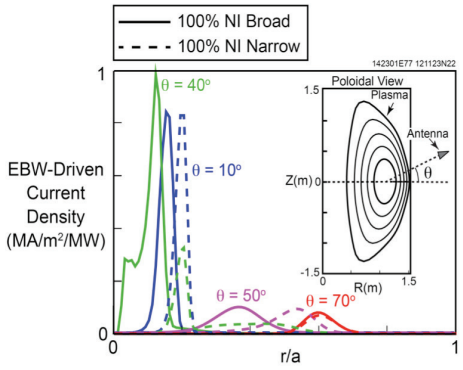

***Figure RF-6**. EBW driven current density versus normalized minor radius (r/a) for two $B_T(0)$ = 1 T, I_p = 1.2 MA NSTX-U 100% NI H-mode plasmas for the antenna oriented to launch $n_{//}$ = 0.7.*

In support to future EBW studies, a Synthetic Aperture Microwave Imaging diagnostic (SAMI) [RF-11] will be installed on NSTX-U in 2015 to measure the EBW to slow X-mode to O-mode (B-X-O) double mode conversion efficiency and

to determine under what conditions the B-X-O conversion efficiency is a maximum. Also SAMI will be used to measure how stable the angular mode conversion efficiency window is when edge density fluctuations are present. These SAMI EBW mode conversion measurements will provide valuable data for the design of an EBW heating and current drive system for NSTX-U in the future.

Cylindrical Cold Plasma Model

Both observations and numerical computations from the AORSA code show a strong relationship between the plasma scrape off layer (SOL) losses and the position of the righthand cutoff. However, interpreting the AORSA results is not simple due to the toroidal geometry, influence of the vessel wall, and the lack of distinction between plasma modes. To aid in improving the fundamental understanding of this behavior, a cold-plasma cylindrical model is being developed that will focus on the effects of cold plasma wave propagation and lacks the complications of toroidal geometry and warm-plasma effects. This model will also allow for the distinction between fast and slow wave contributions. In particular, it will address to what degree the Poynting flux remains field-aligned as power propagates away from the antenna, and will quantify the difference in the amount of power flowing in the plasma core versus the scrape-off layer.

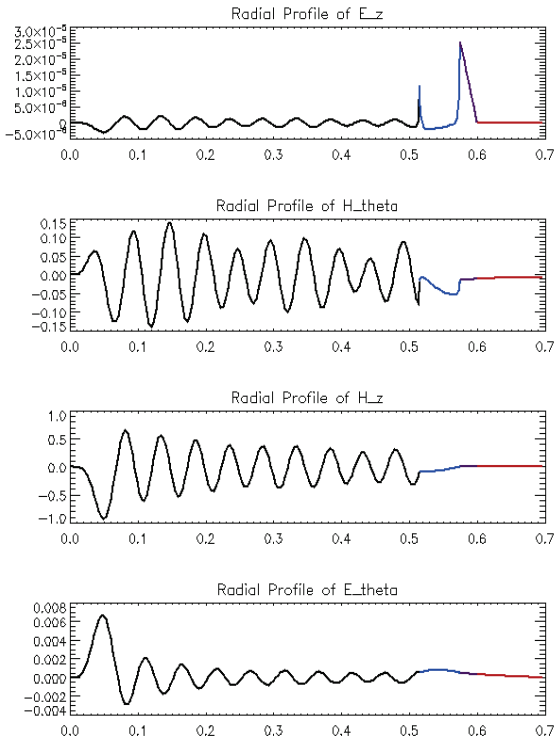

***Figure RF-7**: Radial profiles of RF fields for a cold-plasma cylindrical model for NSTX-like conditions for an m=-5 four-strap antenna. The black portion of the curves represent the core region, the blue represents the low-density annulus (SOL), the purple is the vacuum gap inboard of the Faraday screen, and the red is behind the Faraday screen.*

Last year, the axisymmetric (m=0) solution was derived and implemented in a code, with initial results presented at the 2013 APS-DPP conference [RF-12]. In FY 14, a solution valid for all azimuthal wavenumbers was derived and implemented. This involved devising new solutions to the numerical issues that arose when dealing with the cutoff slow wave. By the end of FY 14, the numerical implementation will be completed, with computed Poynting flux data available for comparison with observations and AORSA. Preliminary results are show in Figure RF-7 in terms of the radial profile of the RF field including the scrape-off layer for the m = -5 mode including all $k_{\|}$ eigenmodes for this m value.

Benchmark of ICRF codes in mid and high harmonic regimes in view of NSTX-U operation

NSTX-U is presently scheduled to operate at the beginning of 2015 with toroidal magnetic fields (B_T) up to 1 T, nearly twice the value used in the experiments on NSTX, and with NBI power up to 10 MW. The doubling of B_T while retaining the 30 MHz rf source frequency moves the heating regime from the HHFW regime (up to 10th harmonic) used in NSTX to the mid harmonic fast wave (MHFW) regime (up to 5th harmonic). Both the MHFW regime and the doubling of the NBI power can strongly affect the power absorption partitioning. In fact, the thermal and fast ions absorption can significantly increase [RF-16]. Thus, it is crucial to have an accurate evaluation of the power absorbed by fast and thermal ions. For this reason, a detailed benchmarking between different RF codes valid in the HHFW and MHFW regimes is underway. More specifically, a comparison between the full wave codes TORIC v.5 [RF-13], TORIC v.6 [RF-14], AORSA [RF-15], and the ray tracing code GENRAY [RF-16] is being performed. Preliminary results show disagreement between the codes when thermal ion absorption is significant. The reason for these discrepancies is under investigation.
This work is also in collaboration with RF SciDAC and MIT (A. Ram, P. Bonoli, and J. Wright).

Collaborations

DIII-D, EAST, and KSTAR Collaborations

It has been demonstrated that ECH and HHFW heating both have a very small heating efficiency when applied to the NB heated "ITER Baseline Scenario Regime" on DIII-D [RF-17]. PPPL contributed to this research and submitted an experimental proposal to support it (G. Taylor et al., "Energy Transport During Electron-Dominated Heating of ITER Baseline Scenario H-Mode Discharges"] to the DIII-D research forum in December 2013. Analysis of the heating characteristics suggests that this reduced efficiency is due to increases in heat, particle and momentum diffusivities, possibly in response to the changes in power deposition profiles and Te/Ti [RF-18]. This is a very important result with regard to its implications for ECH on ITER. Further insight on this poor efficiency result will be presented in a paper at the 2014 IAEA FEC meeting [RF- 19].

The research on RF edge power losses in the SOL during HHFW heating and minority ion heating regimes is being extended to include DIII-D, C-mod, EAST and KSTAR. Notably, preliminary results with the full wave AORSA code comparing edge losses vs SOL density predict that for DIII-D the HHFW edge losses have similar characteristics to those found on NSTX (losses increase substantially when the cutoff density is exceeded at the antenna), whereas for the minority regime in C-mod, EAST and KSTAR the edge losses are large at low density and decrease monotonically as the SOL density is increased to above the cutoff density [RF-20]. Future experiments will help determining if this edge loss prediction is actually observed experimentally in order to set the conditions for minimizing edge losses and optimize minority heating performance.

PPPL participated in the studies of edge losses in the minority heating regime on C-mod, comparing results for the field aligned antenna with those for the toroidally aligned antenna. Also, these edge loss studies are being extended to the minority regimes on EAST and KSTAR. Two visits to EAST and one to KSTAR have been made to setup collaborations, discuss physics issues and to determine the diagnostics required for these studies. An ICRF experiment is now planned under an approved KSTAR experimental proposal that will be run in October 2014 ("Edge power deposition during ICRF heating" by G. Taylor, N. Bertelli, J. C. Hosea, R. Perkins, H. J. Kim, S. J. Wang, B. H. Park, J-G, Kwak). A similar experimental proposal will be submitted to EAST for the next run campaign. The goal of these experiments is to understand the edge loss behavior and to ultimately optimize the long pulse ICRF heating characteristics.

A program for optimizing the ECCD stabilization of neoclassical tearing modes (NTMs) is being developed with DIII-D, KSTAR, and EAST, analyzing the experimental observations using the model of N. Bertelli [RF-21]. To extend this stabilization technique to KSTAR, an experiment is now planned under an approved KSTAR experimental proposal that will be run in October 2014 ("Optimization of NTM stabilization by ECCD and ECRH/ECCD efficiency in advanced scenario" by N. Bertelli, R. Ellis, J. C. Hosea, E. Kolemen, R. Perkins, G. Taylor, M. Joung, Y-S. Bae, H. Park). Also, an experimental proposal supporting this effort on EAST will be submitted once the ECH system is commissioned.

Helicon waves studies in DIII-D plasma by using the full-wave code AORSA were performed in collaboration with E. F. Jaeger (XCEL). In addition, an attempt was made during the last year to perform AORSA calculations for the effect of the SOL on launching helicon waves into the plasma. This effort was not successful and the code will need to be upgraded during FY15 to permit this study

Continuing Studies of the Short Wavelength Slow Mode Identified in High Resolution Simulations of the HHFW and ICRF Wave fields in NSTX and C-Mod

Over the course of a multi-year study of AORSA and TORIC-HHFW simulations of HHFW wave heating and current drive in NSTX, NSXT-U and C-Mod, mode conversion to a slow wave structure appears in the solutions if enough expansion elements are retained to resolve small-scale spatial structures. Theoretical analysis and numerical studies have indicated that the origin of the propagating slow mode can be attributed to warm electron effects, $\omega < k_{//}v_{te}$, which allow the propagation of the additional wave. However, convergence problems were found when more expansion modes were added to the solution domain and, in addition, the model predicts a smaller wavelength for the mode than was found in the simulations. Over the past year, the frequency regime was lowered to be in the vicinity or just below the ion cyclotron frequency, since the mode coupling physics is better understood there and since this range of frequencies is of interest in studying externally driven CAE modes on NSTX-U and elsewhere. While good agreement between theory and numerical simulations was found in some parameter regimes with both the AORSA and TORIC codes, convergence difficulties with the codes, particularly with high mode number resolution, still occurred. Two possible causes for the numerical difficulties were identified and some progress has been made towards resolving the issues. In the low frequency

regime, the wave field and power deposition solutions do not converge if the launched fast waves are evanescent. For example, for NSTX discharge 112705, the TORIC code converges with a launched toroidal mode number, N_ϕ, of 1 and the fast wave propagates. However, code convergence fails when the toroidal mode number is 12 and the fast wave is evanescent. This suggests that the code convergence will fail if the fast wave fields, which have a very large radial wavelength, are not sufficiently close to a global eigenmode of the system. Studies are now underway to see if some limited frequency sweeping will tune the system so that the launched waves can match an eigenmode of the system. Another possible source of the code convergence difficulties may be due to difficulties in determining the parallel wave numbers in the Cartesian coordinate system used in AORSA. Essentially, as more mode numbers are included to increase the spatial resolution needed to solve for the slow mode, the rotational transform can downshift portions of the parallel wave number spectrum and introduce modes into the field representation that are undamped. Initial studies indicated that introducing some toroidal broadening into the parallel wave number spectrum tends to suppress the appearance of spurious undamped modes that prevent the codes from converging properly. This mechanism is under further refinement, but it does not appear to affect the TORIC wave solutions as much as the AORSA solutions, since the values of the parallel wave number are better defined in the flux surface coordinate system used in TORIC. These simulations tend to require copious amount of computer time, especially for the all orders algorithm in AORSA, so 3D reconstructions of the wave fields have not yet been produced. For similar reasons, the more physically accurate method for determining power absorption and kinetic flux, has not yet been modified for use with the new plasma dispersion function developed for the electrons that includes the toroidal broadening. These studies will continue into FY2015 and conclusions will finally be published in a refereed journal. Some of these more recent results were presented in the APS-DPP 2013 poster [RF-22].

During these studies in the low frequency regime, mode conversion from the launched fast waves to the Kinetic Alfven Wave (KAW) was found to be surprisingly similar to simulations of KAW modes excited by the energetic ions from neutral beam injection in NSTX found by Elena Belova et al. As a consequnce, some detailed comparisons between these two distinct approaches to the excitation of the KAW's in NSTX and NSTX-U were initiated. Initial results indicate that the TORIC code has had convergence issues with the experimental parameters used by Belova et al in the HYM code simulations. The convergence difficulty is probably due evanescence of the fast wave for the specified parameters. By making small alterations to the applied wave frequency and other parameters such as the edge densities, which are not measured that accurately and which could affect the wave field solutions, it is possible that more quantitatively similar simulations can be constructed for the same set of experimental parameters. The ability to predict driven wave structures in the low frequency regime would be particularly valuable to the driven wave studies being lead by Eric Fredrickson and Mario Podesta on NSTX-U.

Thermal effects on Lower hybrid propagation (RF SciDAC collaboration)

In theory and modeling of lower hybrid (LH) waves it is conventional to use the cold plasma model for propagation and only to invoke finite electron temperature effects in electron Landau damping [RF-23, RF-24]. It has been found that full kinetic effects of finite temperature

electrons must be retained in the parallel contributions to the dielectric tensor to obtain accurate propagation as well as damping (see Figs. RF-8 and RF-9) [RF-25]. Counter-intuitively, the thermal corrections are not important for the high temperature (T_e > 10 keV) fusion reactor plasmas due to the short propagation path limited by strong absorption. The effect is observed if a given family of rays are sufficiently weakly damped that they encircle the magnetic axis and so are in the 'multipass' regime.

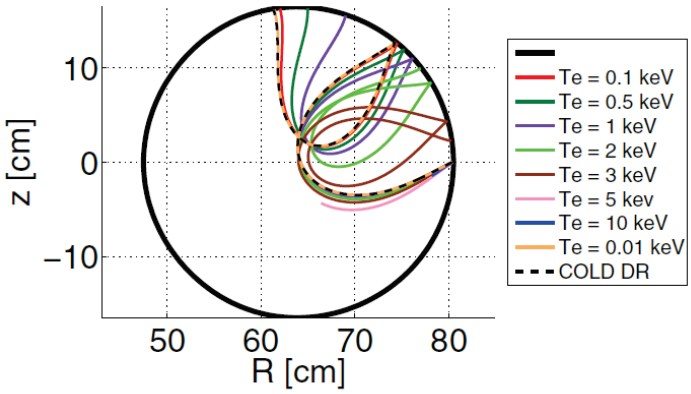

Figure RF-8. *Ray trajectories using full hot plasma dispersion relation for various temperatures compared with ray from cold plasma dispersion relation. Rays end when 99% of power is absorbed. Plasma parameters are ne = 5 × 1019 m−3, B0 = 8T, n_ = −2.5, a = 16.5 cm, R0 = 64.0 cm, δ (Shafranov shift) = −0.97 cm. Density and temperature have parabolic profiles. Rays are launched at R = 80.4 cm Z = 0 cm.*

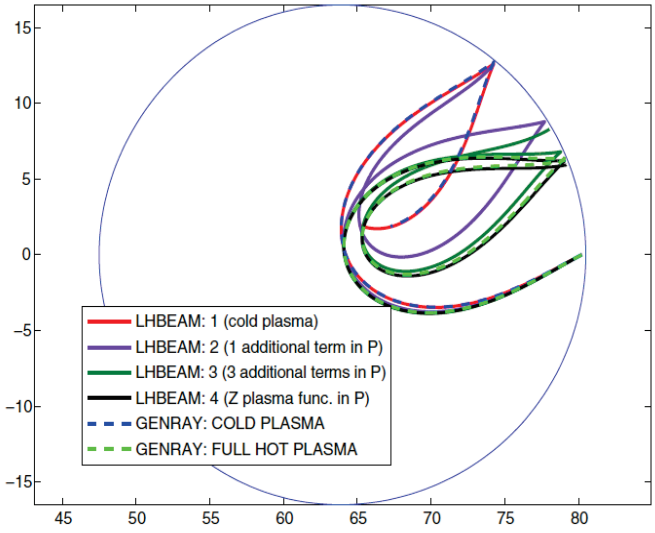

Figure RF-9. *Rays with successive thermal corrections to the parallel dielectric term, P(ζ), are calculated by the LHBEAM code [RF-26] and are compared to calculations by GENRAY using the cold plasma dielectric and the full hot plasma dielectric. Both LHBEAM and GENRAY plots for the cold dielectric are shown as a simple benchmarking validation. Plasma and wave parameters are the same as those from figure RF-8.*

References

[RF-1] R. J. Perkins et al., *Phys. Rev. Lett.* **109**, 045001 (2012).
[RF-2] R. J. Perkins et al., *Nucl. Fusion* **53**, 083025 (2013).
[RF-3] J. C. Hosea *et al*, *Phys. Plasmas* **15**, 056104 (2008).
[RF-4] C. K. Phillips *et al*, *Nucl. Fusion* **49**, 075015 (2009).
[RF-5] G. Taylor *et al*, *Phys. Plasmas* **17**, 056114 (2010).
[RF-6] D. L. Green *et al*, *Phys. Rev. Lett.* **107**, 145001 (2011).
[RF-7] N. Bertelli, *et al., AIP Conf. Proc.* **1580** (2014) 310.
[RF-8] N. Bertelli, *et al., Nucl. Fusion* **54,** (2014) 083004.
[RF-9] A. P. Smirnov, et al., Proc. 15th Workshop on ECE and ECRH, World Scientific (2009), pp. 301-306.
[RF-10] S.P. Gerhardt, et al, Nuclear Fusion **52**, 083020 (2012) ; NSTX-U cases with TRANSP ID 142301E77 and 121123N22 @ 11.9 s
[RF-11] S. Freethy, et al., Proc. 38th EPS Conf. on Plasma Physics (Strasbourg, France, 2011) paper P2.050.
[RF-12] R. J. Perkins et al., *Bull. Am. Phys. Soc.* **58** (2013), JO4.12.
http://meetings.aps.org/link/BAPS.2013.DPP.JO4.12
[RF-13] M. Brambilla, *PPCF* **44**, (2002) 2423
[RF-14] Bilato et al, *NF* **51** (2011) 103034
[RF-15] Jaeger *et al*, *PoP* **8**, 1573 (2001)
[RF-16] Smirnov et al, *Bull. Am. Phys. Soc.* **39**, 1626 (1994)
[RF-17] R.I. Pinsker et al., *Bull. Am. Phys. Soc.* **58** (2013), BP8.89.
http://meetings.aps.org/link/BAPS.2013.DPP.BP8.89
[RF-18] R.I. Pinsker et al., Proceeding of EC-18 Workshop (Nara, Japan in April 2014).
[RF-19] D. Ernst et al., IAEA FEC 2014. EX/2-3.
[RF-20] N. Bertelli et al., IAEA FEC 2014. TH/P4-14.
[RF-21] N. Bertelli et al, *Nucl. Fusion* **51** (2011) 103007.
[RF-22] C.K. Phillips et al., *Bull. Am. Phys. Soc.* **58** (2013), BP8.63
http://meetings.aps.org/link/BAPS.2013.DPP.BP8.63
[RF-23] M. Brambilla *Plasma Phys.* **18** (1976) 699.
[RF-24] Cho S and Swanson D G 1988 *Phys. Fluids* **31** (1988) 1123–9.
[RF-25] J. C. Wright and N. Bertelli, *Plasma Phys. Controlled Fus.* **56,** (2014) 035006.
[RF-26] N. Bertelli et al., *Phys. Plasmas* **19**, 082510 (2012).

Solenoid Free Plasma Start-up

We have, in the past, used the TSC code to develop initial plasma start-up scenarios for future experiments, which has shown that the NSTX-U coil configurations will easily support plasma start-up to well over the 400 kA required to couple a CHI started discharge to non-inductive current ramp-up [SFSU-1,2,3]. We have now started to use the free boundary TRANSP to model the evolution of the CHI started plasma and to study the effect of ECH heating on these target plasmas [SFSU-4]. Start-up modeling with NIMROD has been carried out using two approaches. In the first method, a simplified model is used to understand basic physics [SFSU-5,6]. In the second approach, actual coil currents from a CHI-started discharge from NSTX are used to develop a realistic model of NSTX-CHI discharges [SFSU-7]. This year we also finished the design of the CHI system for QUEST [SFSU-8] and have started procuring hardware for implementing CHI capability on QUEST later this year. We also identified suitable electrode configurations for a ST-FNSF, one of which has design features of the electrode configuration that will be tested on QUEST [SFSU-9]. These are described in the subsequent sections. The detailed work on non-inductive current ramp-up is described in a different part of the report.

TRANSP simulations

Free boundary TRANSP has been used to model the plasma discharge self-consistently after startup. A typical CHI discharge in NSTX has been used as a reference and to provide initial conditions to the TRANSP simulation. In these simulations the density evolution is prescribed, while the electron temperature profile evolution is predicted with the MultiMode (MMM) transport model, which is found to reproduce amplitude and peaking of the electron temperature profile within 10% in NSTX RF heated discharges. Simulations indicate that 1MW of EC heating, at 28GHz in O-mode, can rapidly heat typical plasmas generated by CHI. The electron temperature increases from about 10-20eV typical of CHI plasmas to about 1keV in less than 30ms (see Figure SFSU-1). For comparison the same figure also shows a simulation where the EC is not applied and the plasma is heated inductively. The Electron Cyclotron waves propagation is computed with the ray-tracing code TORAY-GA, which is

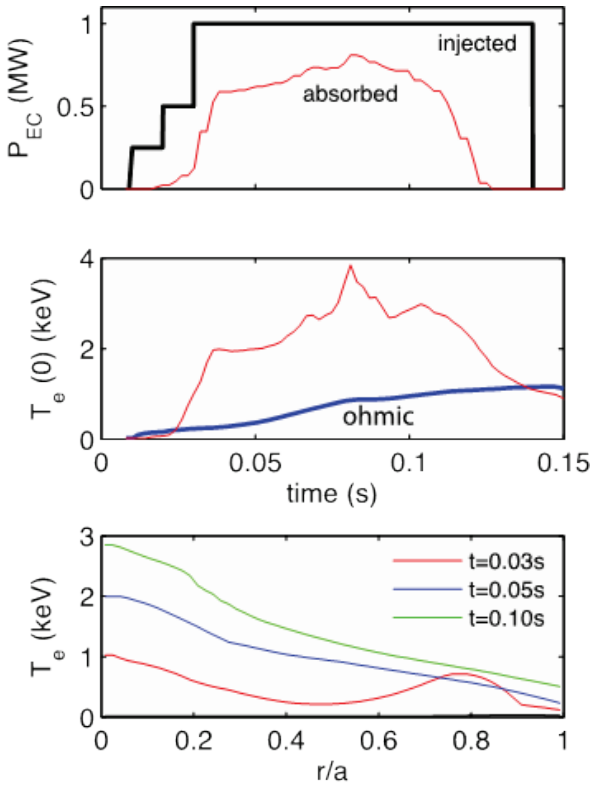

Figure SFSU-1. *(top) The time evolution of injected and absorbed EC power, (middle) electron temperature for EC and inductive heating compared, (bottom) and the electron temperature profiles at 3 times.*

implemented in TRANSP. The plasma rapidly becomes overdense to EC penetration so that only the first 100-150ms of discharge after the startup – depending on plasma conditions - offer adequate conditions for optimal heating with EC.

Simulations indicate that HHFW cannot be coupled to the CHI target plasma without EC heating. The use of EC is deemed necessary for HHFW coupling in a CHI-initiated plasma. Figure SFSU-2 shows a simulation where HHFW is injected at about 40ms and stepped up to 4MW during the EC heating time window.

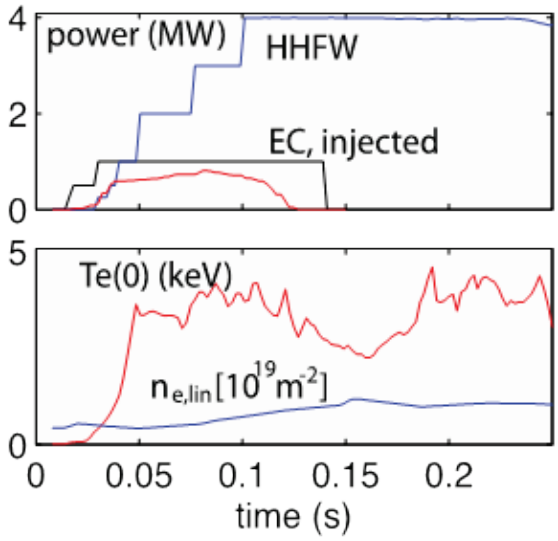

Figure SFSU-2. *TRANSP simulations of (top) power, (bottom) line-averaged density and central electron temperature for EC and HHFW heated CHI discharges.*

The combination of EC and HHFW heats the plasma up to 3-4keV and it delays the current decrease of the CHI, sustaining a non-inductive current of about 350kA. HHFW also triggers the L-H transition contributing to an increase in the bootstrap current. The use of RF is required to prepare the plasma to the Neutral Beam Injection with minimal losses. Simulations indicate that in this low-density plasma the contribution of HHFW and bootstrap current sustains about 350kA of non-inductive current. In these conditions, the neutral beams are well confined and penetrate into the H-mode plasma with minimal losses. With 10MW of NBI distributed on the two beamlines, the current is ramped-up to 900kA in about 2.5s. This is described in a different part of the report. With density between 60% and 90% of the Greenwald limit, the current is sustained with a contribution from the bootstrap current between 40% and 60% with decreasing Greenwald fraction and with confinement gain of H98~1.0-1.2.

CHI start-up modeling with NIMROD

Resistive MHD simulations using the NIMROD code are being used to model CHI start-up in NSTX; to improve understanding of the physics of injection, flux-surface closure, and current drive for CHI plasmas; and to extend these results to NSTX-U. Two approaches are taken. In the first approach, a simplified model is used to understand the basic physics of CHI plasma formation. These simulations, to be described first, use constant in time coil currents throughout the discharge. Thus no effort is made to adjust the magnitude of the vertical field as the plasma current increases. In the second set of simulations, actual coil currents from a NSTX CHI discharge are used to try to reproduce the experimental discharge itself.

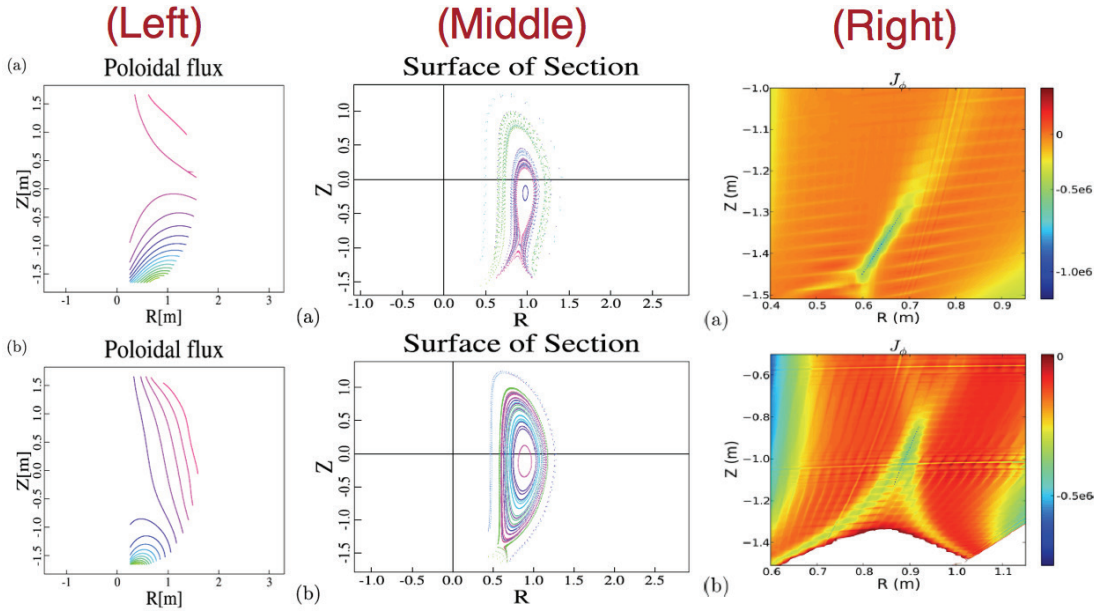

Figure SFSU-3: *(Left) Initial poloidal fluxes for (a) wide footprint, and (b) narrow footprint. (Middle) Pointcare plots for the two cases after CHI plasma formation. The much more pronounced closed flux formation for the narrow flux foot print case (b) is clearly seen. (Right) Localized current sheet formation during reconnection (a) narrow and (b) wide footprint cases.*

In previous simulations, it was found that, with large magnetic diffusivity ($\eta \sim 400$ m^2/s) (equivalent to T_e = 1eV) there was no flux closure. A small volume of closed flux forms at magnetic diffusivities of about ($\eta \sim 40 - 20$ m^2/s). The volume of closed flux surfaces increases as the magnetic diffusivity is reduced to ($\eta \sim 8$ m^2/s) (equivalent to T_e = 14 eV).

It was also found that, as the injector voltage is turned off and the evolving toroidal magnetic field decreases in the injector region, the compression from the toroidal magnetic field exerts an effective bidirectional pinch force that brings the oppositely directed fields together to reconnect. Consistent with the bidirectional pinch force, as the injector voltage is turned off, a radial pinch $E \times B$ flow is generated, where the electric field (loop voltage) in the toroidal direction induces the poloidal-field evolution that leads to reconnection.

An important result is the observation that closed flux surfaces during transient CHI can be explained through 2-D Sweet-Parker type reconnection, and 3-D non-axisymmetric modes do not appear to play a dominant role. There are similarities between the transient Sweet-Parker reconnection found here and that reported in forced-reconnection laboratory plasmas [SFSU-5,6].

Recent simulations have confirmed the role of the magnitude of the injector flux, the importance of a narrow flux foot print width, and rapid time scales required for reducing the injector voltage and (current) in increasing the magnitude of the closed flux fraction [SFSU-6]. With increasing injector flux the amount of closed flux proportionally increases, consistent with earlier TSC simulations and Zero-D models that indicated that this should indeed be the case for transient CHI discharges. Closed flux fraction also increases with the rapidity with which the injector

voltage and current are reduced, and consistent with earlier understanding that this is an important operational requirement for transient CHI. These results are described in a recent paper [SFSU-6]. Experimentally it is known that the CHI injector flux footprint width must be narrow for increasing the magnitude of the closed flux fraction. This is also seen in these recent simulations and is shown in Figure SFSU-3. Figure SFSU-3 (Left) shows the case of the wide and narrow footprint cases. The ratio of the closed current to the total plasma current is only 1.8% for the wide foot print case, but increases to >12% for the narrow footprint case (Figure SFSU-3 - Middle). In these simulations, the current sheet and X-point are formed at different locations. For the wide footprint case, the current sheet and X point are formed far from the injector gap. For the narrow footprint case, it forms near the injector gap (Figure SFSU-3 – Right). The plasma outflows in the narrow footprint case reach velocities up to 8500 m/s, much stronger than for the wide footprint case.

In the second set of simulations, experimentally measured coil currents are used to develop models. The eventual goal is to simulate experimental discharges and to develop realistic models for transient CHI start-up. Resistive MHD simulations using the NIMROD code continued during the past year with emphasis on the effects of co-injection of plasma with helicity and the effects of impurity radiation on the temperature evolution in NSTX. Some significant results are summarized below.

Previous simulations included plasma flow, required for Ohm's law including the **v**x**B** term, but the density was held approximately constant by a large density diffusivity diffusion coefficient. Analysis of earlier spheromak simulations found that this had minimal effects on the MHD physics although with a minor effect on energy conservation. The new research has included evolution of the density resulting from co-injection of plasma through the injection slot in NSTX. The flow at the slot is at the **E**x**B** velocity corresponding to the voltage across the gap; elsewhere it evolves with the full, single-fluid MHD physics used in the model.

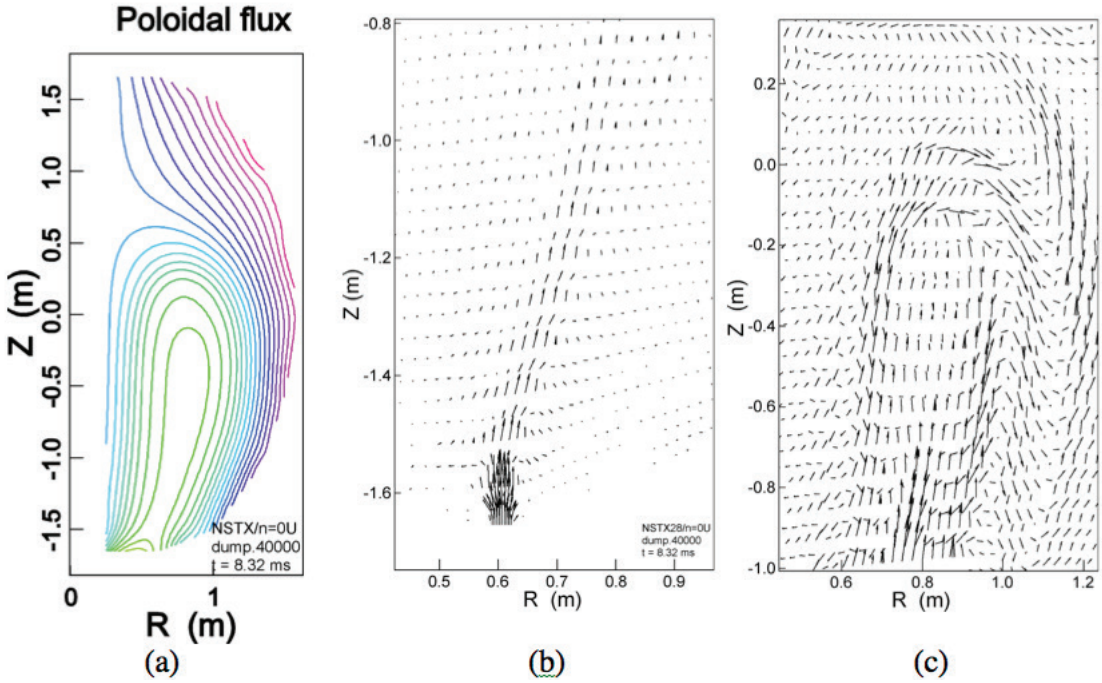

Fig. SFSU-4. *(a) Poloidal-flux bubble during co-injection of helicity and plasma. (b) Poloidal flow-velocity vectors above the injection slot. (c) Poloidal flow-velocity vectors near the top of the flux bubble. Note the different scales. The simulation assumes axisymmetry.*

High-density plasma is injected into a low-density plasma, typically an order-of-magnitude less than in the flux bubble. To ensure that the characteristics of the low-density plasma approximate a vacuum, it is maintained at a low temperature (few eV) by a large, artificial radiation term. This keeps the plasma current density in the "vacuum" low and prevents local run-away Ohmic heating results from the evolution of the magnetic field and plasma flows.

An example of poloidal flow velocity during injection is shown in Fig. SFSU-4. The velocity drops rapidly above the slot (Fig. SFSU-4a) as the flow expands. Most of the flow turns at the top of the bubble, and the flow exits the bubble primarily on the high-field side (Fig. SFSU-4b). The cross-field flow contributes to Ohm's law, $\mathbf{E}+\mathbf{v}\times\mathbf{B}=\eta\mathbf{j}$.

Following injection, flux-surface closure mechanisms are the same as in previous simulations: The reduction in flow velocity as the injector voltage drops reduces the magnetic pressure where above the slot, triggering reconnection [SFSU-5,6,7] in a Sweet-Parker process [SFSU-5,6,7]. As the flow velocity near the injection slot is determined by the voltage and the resistivity has no explicit density dependence, the density has only minor effects on the closure process. The resulting volumes of closed surfaces are similar to those in the previous simulations. These new results validate the neglect of density injection in the previous physics results.

Studies of the effects of impurity radiation have been extended. Radiation from oxygen in coronal equilibrium is used as a proxy for impurities, ionization, recycling, and other atomic processes. The simulations presented here have a large density diffusion constant, holding the density effectively constant so that Z_{eff} is unity. The effective fractional oxygen fraction, f_odens, has time and/or spatial variation in many of the simulations. As a result of the fixed density and multiple atomic processes, f_odens can be greater than 100%.

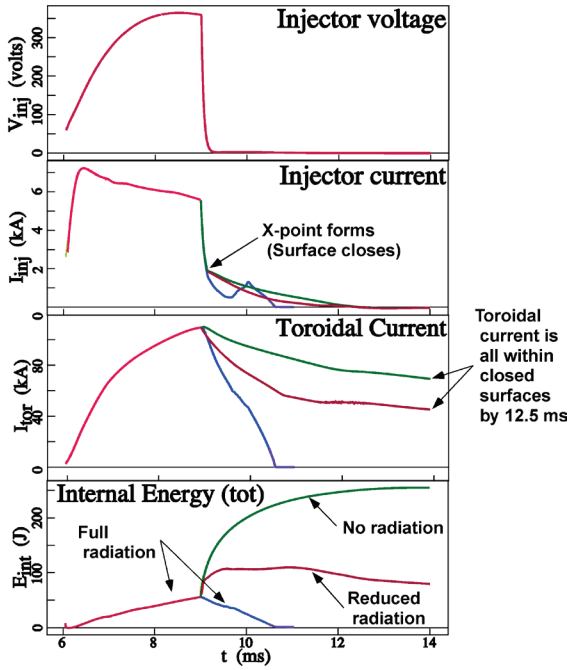

Figure SFSU-5. *Effect of impurity radiation on the discharge following injection. The radiation used to reduce the temperature to experimental levels (for discharge 119187) causes a rapid decay of the toroidal current and closed surface volume. Reducing the radiation with a 1 ms time constant is the best approximation to the experimental results.*

Figure SFSU-5 shows results for a case with f_odens=150% and the impurity radiation spatial dependence peaked in the lower-left corner of NSTX where the injection current strikes. The radiated power is taken to drop as a bigausian from the corner with scale lengths $r_{imp} = 0.45$ m and $z_{imp} = 1.0$ m. Peak temperatures during injection (< 20-30 eV) and temperature profiles are similar to those in a series of experimental discharges starting with number 119187.

Following injection (> 9 ms) the time evolution of the flux surfaces was modeled with three time dependences: The impurity radiation drops instantly at 9 ms, it drops with a 1 ms time constant following 9 ms, and it is held constant. The 1 ms drop (labeled reduced radiation in Fig. SFSU-5) provides the best approximation to the experimental evolution of the toroidal current and flux surface volume. The simulations suggest that impurity radiation is likely to be important in determining the temperature during and following injection and that pumpout of impurities following injection are critical to the observed slow decay of the magnetic flux surfaces.

CHI Implementation on QUEST

The QUEST ST is located in Kyushu University in Japan. It has a major/minor radius of 0.68/0.4 m, the estimated plasma volume is about 4.5 m^3. Features present on QUEST, that are absent on HIT-II and NSTX are: 1) It is an all metal system, an aspect which is very desirable for the CHI method as low-Z impurities could be reduced, 2) It is equipped with a high power Electron Cyclotron Resonance (ECH) heating system that will increase the electron temperature of CHI generated discharges, thereby further improving their confinement properties, and provide early data on ECH heating of CHI plasmas in support of NSTX-U experiments, 3) Improvements to the CHI installation concept would allow QUEST to explore CHI in a configuration similar to that which would be more suitable in an ST-FNSF

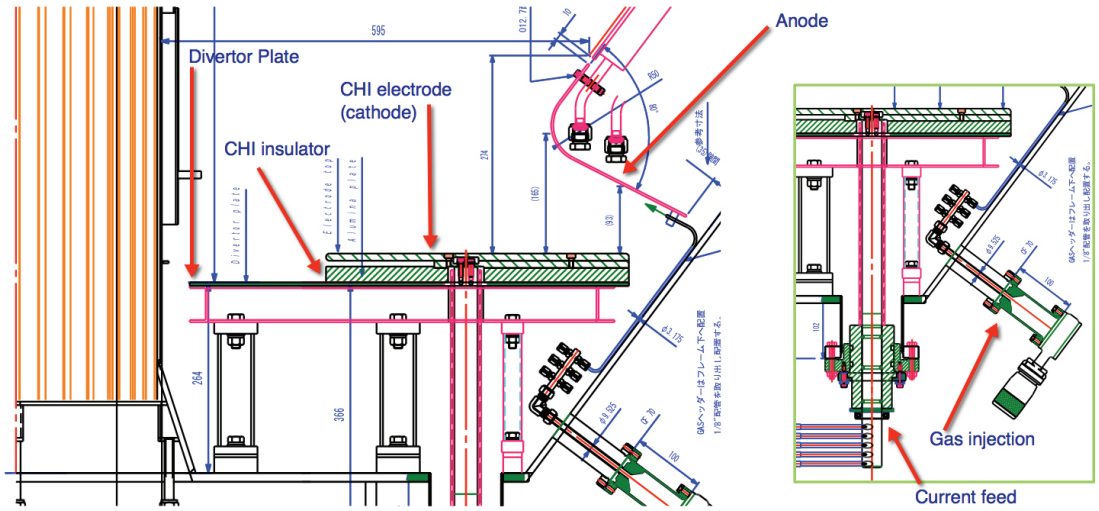

Figure SFSU-6: *The figure shows the location of the electrode assembly on top of the divertor plate. The gas would be injected in the gap between the outer edge of the electrode plate and the outer vessel structure. The gas injection ports (total 3 at different toroidal locations) would be located on the same ports that contain the cryo pumps. The injector current is fed through the current feed rods that are designed to account for the J x B forces resulting from the interaction of the injector current with the external toroidal field. There are a total of 3 current feeds at different toroidal locations. The insulator plate will be a US contribution.*

The CHI design for QUEST was finalized this year. The final design is shown in Figure SFSU-6. As part of the US/Japan collaboration effort, Kyushu University is responsible for the main changes to the machine hardware. The US will provide in-kind contributions to support this activity. These are (1) The primary alumina insulator, (2) the capacitor bank power supply and controls, and (3) the gas injection system. The insulators will be delivered to QUEST later in October 2014, and installed on QUEST later this year. Work is underway at the University of Washington for fabricating the capacitor bank power supply and the gas delivery system.

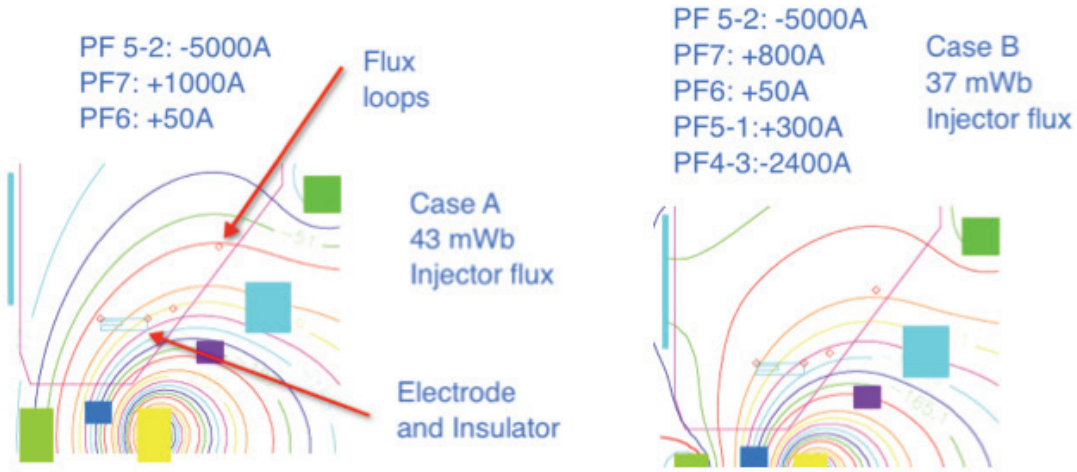

Figure SFSU-7: *The figure shows the amount of injector flux that will connect the electrode to the outer vessel. It is approximately 43mWb for the case shown on left and 37 mWb for the case shown on the right. Depending on the plasma inductance, this should result in a current generation potential of about 100-150kA during transient CHI start-up.*

Table SFSU-1 shows the calculated parameters for transient CHI for nominal operating conditions on HIT-II, NSTX and projected values for QUEST. Figure SFSU-7 shows two sets of coil currents that would be used for initiating the discharge. Because transient CHI discharges do not rely on poloidal flux amplification, the maximum closed poloidal flux in the resulting plasma discharge would be limited by the initial injector flux, as described in Reference SFSU-10. Thus, to maximize transient CHI current start-up potential, it is necessary to increase the amount of poloidal flux that connects the CHI electrodes. To inject about 28 mWb of flux injector currents of about 12 kA would be required by the CHI power supply. This can be provided by a 40 kJ capacitor bank with a capacitance of 20 mF and operated at 2 kV. The total system inductance and resistance needs to be on the order of 80 μH and 80 mOhms or less. This capacitor bank will be built by the University of Washington and by using spare parts from the NSTX-U CHI capacitor bank and parts from the HIT-II CHI capacitor bank.

Parameters	**HIT-II**	**NSTX**	**QUEST**
Major Radius: R_o [m]	0.3	0.86	0.68
Minor radius: a [m]	0.2	0.66	0.40
TF rod current: I_{TF} [MA]	0.8	2.4	1.7
Toroidal Field: B_T [T]	0.5	0.55	0.50
Toroidal Flux: ϕ_T [Wb]	0.2	2.5	0.78
Plasma normalized inductance: *li*	0.35	0.35	0.35
Nominal plasma inductance: Lp [μH]	0.07	0.19	0.15
Injector flux footprint: d [m]	0.1	0.6	0.25
Nominal Injector flux: ψ_{inj} [mWb]	8	47	28
Nominal Start-up current: I_p [kA]	0.1	250	0.15
Bubble burst current * 1.2 ; Iinj [kA]	14	4	11.3
Current Multiplication: Flux ratio	7	50	28
Max Injector flux: [mWb]	16	80	28-60

Table SFSU-1: *Representative parameters for transient CHI start-up on HIT-II, NSTX and QUEST*

Initial Studies of CHI Configuration for an ST-FNSF

Two CHI installation configurations for a ST-FNST are being considered. In the first configuration, referred to as NSTX-like, the entire blanket assembly is insulated from the vessel wall, avoiding insulator dose issues. It is also necessary to insulate the blanket piping from the vessel. Components attached to the piping would be floated above ground potential for the duration of the CHI initiation phase. Piping configurations similar to that used in the ARIES design [SFSU-11] appears easier to implement for this purpose, but requires further design optimization. In this proven NSTX-like configuration, the divertor coils permit injector flux values of >0.7Wb, at a divertor coil current of just 0.8MA•turns, << 10MA•turns limit. The injector flux connects the lower part of the vessel to the lower part of the blanket module. This permits generation of I_p >2 MA with injected current of about 100kA.

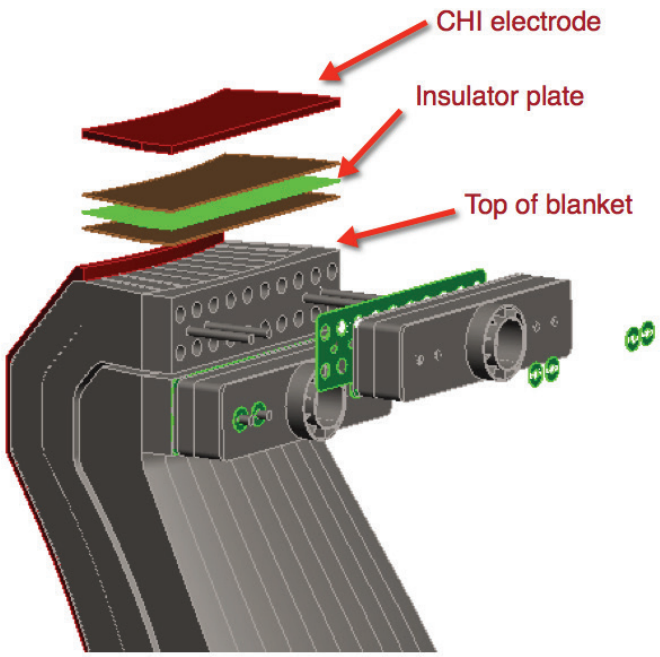

Figure SFSU-8: *Second CHI electrode concept for a ST-FNSF. The top of the blanket is largely shielded from direct neutron streaming, so the dose on the CHI insulator should be low as confirmed by MCNP calculations.*

In the second configuration, a toroidal electrode plate is attached to the top of the blanket assembly and insulated from the blanket using a toroidal insulator. This is similar in concept to the design that will be tested on the QUEST device. The ST-FNSF electrode configuration is shown in Figure SFSU-8. The injector flux connects the top of the vessel to this electrode plate. This has similarities to the ring electrode configuration used on DIII-D for CHI studies, but is much closer to the configuration that will be tested on QUEST. At similar coil currents, for this case, the injector flux doubles. However, the much-reduced gap between the electrodes triples the required injector current for 0.7 Wb flux injection to about 300 kA; however, the electrode current density of 40 kA/m^2 is still much less than the 300 kA/m^2 demonstrated on HIT-II. As part of the final design, it may be desirable to increase the electrode gap distance to reduce the injector current magnitude. The projected plasma current is based on a normalized plasma internal inductance of 0.35, as achieved on NSTX. An advantage of this design is that the blankets and piping need not be insulated, but the configuration requires experimental validation. The MCNP calculated dose on the insulator is 10^9 Gy for 6 FPY, less than the dose limit of 10^{11} Gy for the MgO insulator.

References

[SFSU-1] R. Raman, D. Mueller, S.C. Jardin, et al., Non-inductive plasma start-up on NSTX and projections to NSTX-U using transient CHI, Nuclear Fusion **53** (2013) 073017

[SFSU-2] R. Raman, T.R. Jarboe, B.A. Nelson, D. Mueller, S.C. Jardin, C. Neumeyer, M. Ono, J.E. Menard, Design Details of the Transient CHI Plasma Start-up System on NSTX-U, accepted for publication in IEEE Transactions on plasma science (2014)

[SFSU-3] R. Raman, et al., Transient CHI Plasma Start-up Simulations and Projections to NSTX-U, IAEA-FEC 2014 (accepted Synopsis)

[SFSU-4] F. Poli, et al., Modeling of fully non-inductive ramp-up towards development of advanced scenarios in NSTX-U, IAEA-FEC 2014 (accepted Synopsis)

[SFSU-5] F. Ebrahimi, E.B. Hooper, C. Sovinec and R. Raman, Magnetic reconnection process in transient coaxial helicity injection, published as a Letter, Physics of Plasmas **20**, 090702 (2013)

[SFSU-6] F. Ebrahimi, R. Raman, E.B. Hooper, C. Sovinec and A. Bhattacharjee, Physics of forced magnetic reconnection in coaxial helicity injection experiments in National Spherical Torus Experiment, Physics of Plasmas **20**, 090702 (2014)

[SFSU-7] E.B. Hooper, C. Sovinec, R. Raman, F. Ebrahimi and J.E. Menard, Resistive MHD simulations of helicity-injected startup plasmas in NSTX, Physics of Plasmas **20**, 092510 (2013)

[SFSU-8] R. Raman, Overview of potential CHI contributions to the QUEST project, 2nd Workshop on QUEST and Related ST RF Startup and Sustainment Plasma Research (Feb 24-26), Kyushu University, Japan.

[SFSU-9] R. Raman, T. Brown, L.A. El-Guebaly, T.R. Jarboe, B.A. Nelson, J.E. Menard, Design description for a Coaxial Helicity Injection Plasma Start-up System for a ST-FNSF, 21st TOFE Conference, 9-13 November (2014) (Abstract accepted)

[SFSU-10] R. Raman, D. Mueller, T.R. Jarboe, et al., Experimental demonstration of tokamak inductive flux saving by transient coaxial helicity injection on National Spherical Torus Experiment, Phys. Plasmas **18**, 092504 (2011)

[SFSU-11] X. Wang, et al., ARIES-ACT1 System Configuration, Assembly and Maintenance, FST14-797, to be published

Advanced Scenarios and Control

Profile Control

A major goal of the NSTX-U Advanced Scenarios and Control (ASC) research program is to develop control algorithm for the profiles of the plasma rotation and current. As a consequence, the significant work has occurred on the following topics i) development of TRANSP as a "flight simulator" for plasma control development with full-physics models, ii) development of a β_N and l_i controller that can be implemented with the anticipated year-1 available realtime data, iii) development of algorithms for full control of the q-profile, and iv) development of algorithms for the control of the toroidal rotation profile. These results are described in detail in the R14-3 milestone report.

Collaboration on Control Development on DIII-D

NSTX-associated researchers continued to collaborate on control topics on the DIII-D tokamak in this fiscal year. In particular, Egemen Kolemen, who is now returning to New Jersey as a Princeton University faculty member, conducted important experiments on divertor heat flux control. These included realtime control of the novel snowflake divertor configuration, demonstrating sustained high performance in advanced tokamak plasmas with large flux expansion. In a second experiment, realtime control of the detachment front was demonstrated. These results, which will provide crucial guidance for NSTX-U control design, are described in the DIII-D section of the PPPL annual report.

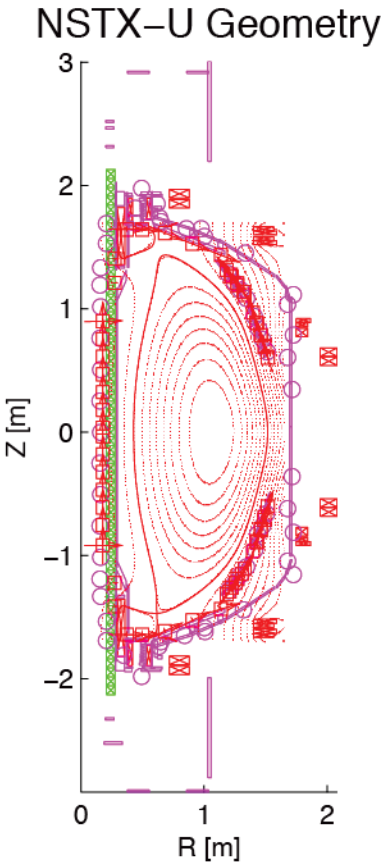

***Fig. PC-1**. NSTX-U geometry as specified in LRDFIT and implemented in TokSys*

Plasma Control (General Atomics)

NSTX-U TokSys Model Development

FY14 studies for NSTX plasma control have included developing a new TokSys model for the NSTX-U configuration, analyzing equilibria from the LRDFIT code, producing TokSys GSEQ equilibria for the new system, and analyzing the new configuration for relative vertical stability. The initial TokSys model of NSTX-U is based on conductor specifications described in the LRDFIT code. IDL scripts were written to process LRDFIT files and write the conductor geometry into files with names *_lrdfit.dat, which are later processed by matlab routines in the TokSys /define directory. To allow for flexibility in later stages, the conductors were not grouped together at this point. Fig. PC-1 illustrates the TokSys conductor configuration, along with an equilibrium derived from LRDFIT.

New NSTX-U TokSys GSEQ Equilibrium and Vertical Stability Analysis

The TokSys designeq and convergeq codes were used to produce a well-converged lower single null equilibrium with the NSTX-U coil set for a 2 MA plasma current. Figure PC-2 illustates this equilibrium along with the convergence quality for flux on the grid as well as coil currents.

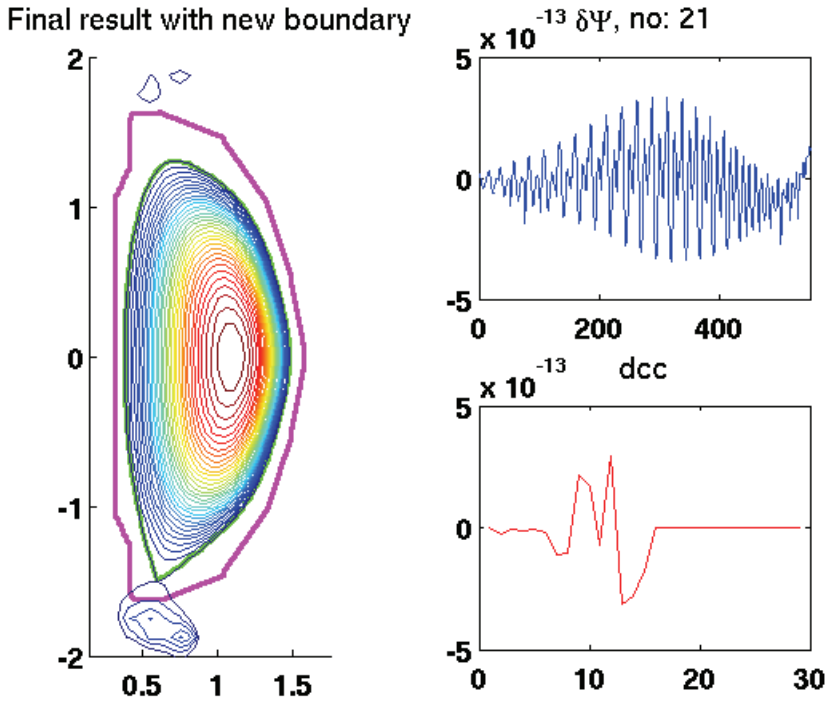

Fig. PC-2. *NSTX-U equilibrium with 2.0 MA plasma current. Panels on right show corrections to flux and coil currents in the last iteration of the solution (Wb and A respectively) as a measure of convergence quality.*

In the next step the linear nonrigid plasma response code *gspert* was applied to this NSTX-U equilibrium. It gave a vertical growth rate of about 4 rad s^{-1} with the new TokSys conductor configuration. The unstable mode is shown in Fig. PC-3 below. In this model there is a simple assumption about how the current and pressure profiles would behave during a vertical displacement event. Let *W(V)* be the thermal energy contained within a flux surface where the volume is *V*. Let *I(A)* be the toroidal current contained within a flux surface with cross sectional area *A*.

In this case the simple assumption is that:
1. *W(V)* is unaltered by the vertical displacement
2. *I(A)* is changing in a way that preserves total *Ip* and *li*

The upper panel on the right shows the approximately constant stored energy, while the lower panel on the right shows how *I(A)* is very slightly perturbed to maintain fixed *li*. The panel on the left shows how the flux is perturbed at fixed points in space when the vertical displacement begins. The predicted mode in this case is not purely vertical. Further studies will address the

form of such modes in NSTX data, and produce calculations using appropriate constraints. Experimental validation studies are anticipated in FY15.

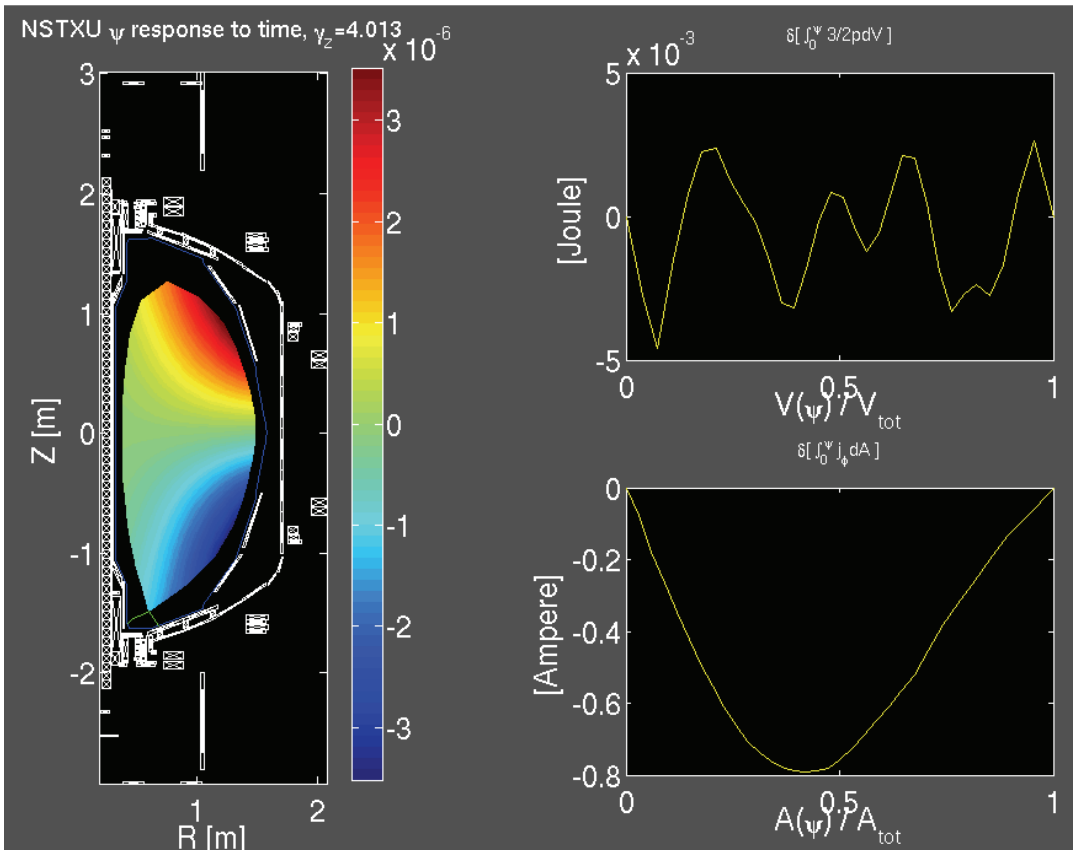

Fig. PC-3. Flux perturbation during vertical displacement event using simple assumptions for current and pressure profile responses. Panel at left shows flux perturbations on grid, while panels on right show changes in stored energy and current enclosed by flux surfaces as a function of normalized poloidal flux.

As a test of the GSEQ equilibrium code applied to the ST geometry, the equilibrium was evolved in free boundary mode as the plasma current was dropped with constant applied field. This evolution is a rough mockup of the dynamics observed in a major disruption current quench (though without self-consistent beta and li changes). Fig. PC-4 shows the results of this sequence, in which the plasma limits on the inboard surface with largely radial, minimally vertical motion. This is qualitatively consistent with typical observations in an ST major disruption with a highly balanced equilibrium such as the test case.

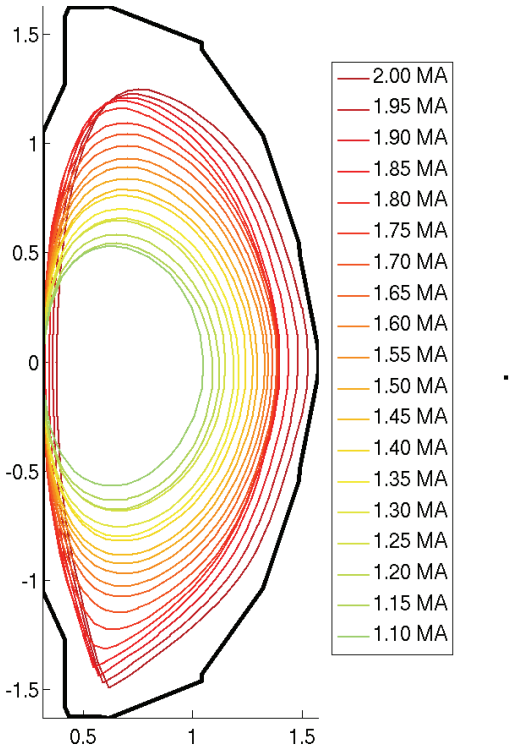

Fig. PC-4. Dropping plasma current without changing the applied vacuum field.

Note that fixing the externally applied vacuum field is similar to the result of inducing self-consistent vessel currents, which would tend to conserve flux at the vessel boundary. The computation time required for this free boundary equilibrium evolution sequence was a few seconds, indicating the usefulness of the tool for NSTX-U scenario study and equilibrium design.

NSTX-U Nonlinear Equilibrium Evolution in Vertical Displacement Event

The TokSys gsevolve code calculates the nonlinear, time dependent evolution of an ideal plasma under user-controlled constraints (e.g. fixed Ip, or fixed li). The NSTX gsevolve code was applied to an ITER similar shape NSTX-U equilibrium to produce a VDE evolution under a fixed plasma current, li, and betap constraint, with PF coil voltages held fixed. Fig. PC-5 illustrates the evolution with several snapshot plasma boundaries, corresponding to an initial growth rate of ~ 3 rad/s, in good agreement with linear calculations. However, it is notable that the instantaneous growth rate history (see Fig. PC-6) varies in distinct phases through the VDE shown in Fig. PC-5. These phases appear to correlate with changes in degree of interaction with the wall, and with the resulting plasma shape.

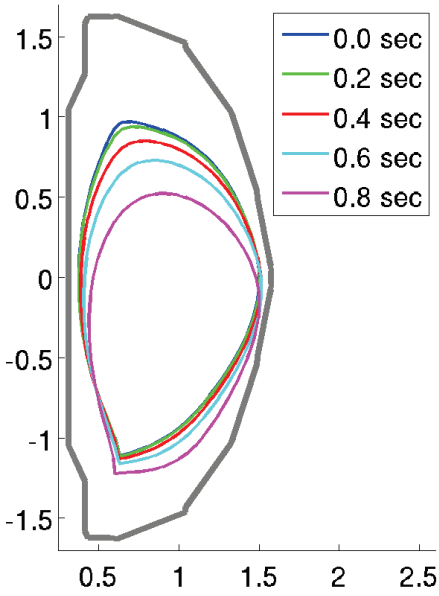

Figure PC-5. *The boundary at 5 different times during vertical displacement of ITER-similar shape in NSTX-U*

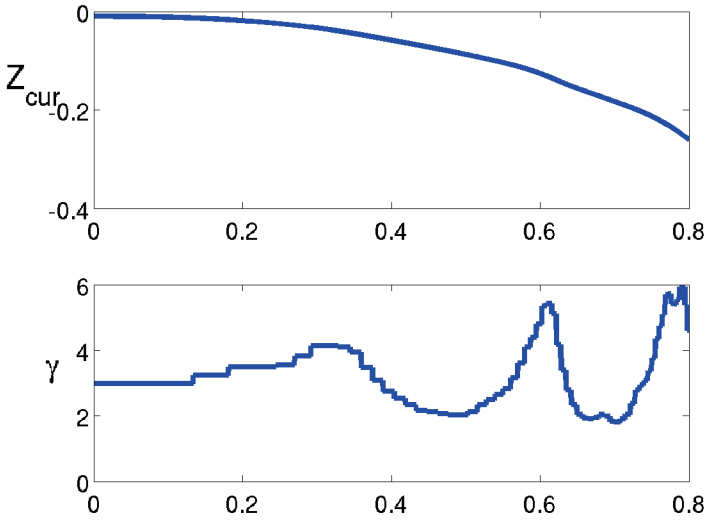

Figure PC-6. *Time evolution for Z of the current centroid and the growth rate during the vertical displacement shown in Fig. PC-5.*

NSTX-U Halo Current Modeling

A new halo current module has been partially implemented in the TokSim simulation environment for application to NSTX-U simulation, and its communication with TokSys equilibrium modules has been defined. At the center of the halo module is a 2-D magnetic diffusion model for the transfer of toroidal current from the core to the halo region (differentiated only by resistivity) over a given time step. The toroidal current is represented by filaments on a 2D grid (see Figure PC-7). Poloidal halo currents are calculated, assuming a force-free halo region, using the toroidal current and an approximation of the open field line safety factor (q_h). The communication between the halo module and equilibrium evolution is defined as shown in Figure PC-8. At a given time step, the equilibrium module must provide grid maps indicating the

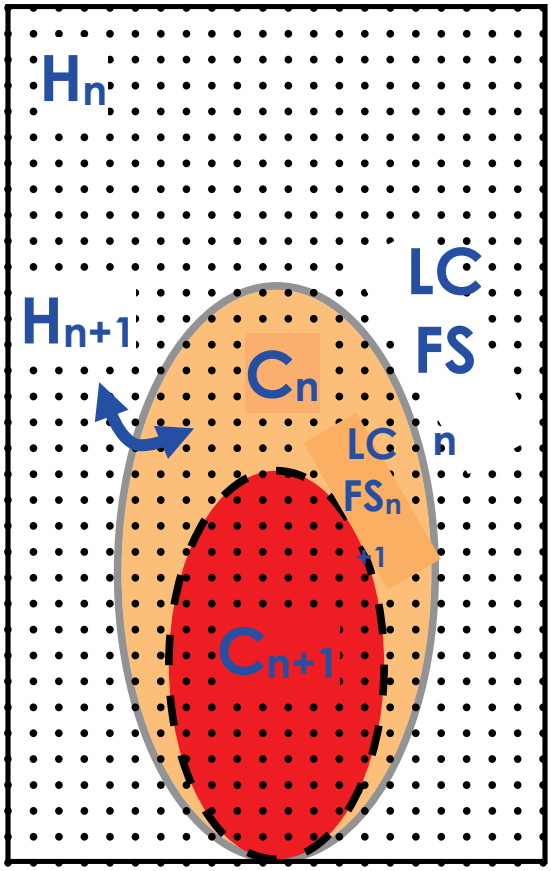

Figure PC-7: *Halo and core regions in the TokSim halo current module*

core plasma (providing the last closed flux surface (LCFS)), the ohmic drive, the poloidal magnetic field (Br,Bz), and (optionally) the core current distribution (J_c). The halo module uses the change in toroidal flux within the LCFS from one time step to the next to define the poloidal edge current, which is converted to toroidal current via q_h, and then evolves the toroidal circuit equation as described above. The halo module then feeds the new core current (0-D) back to the equilibrium module, which re-computes the equilibrium. At the next step, the halo module may either use J_c from the equilibrium module, resulting in a small 0-current gap on the grid between the previously calculated halo region and the new core region which must be rapidly filled in by diffusion, or else use Jc from the previous halo module evolution, providing continuous grid current which is slightly inconsistent with the equilibrium module.

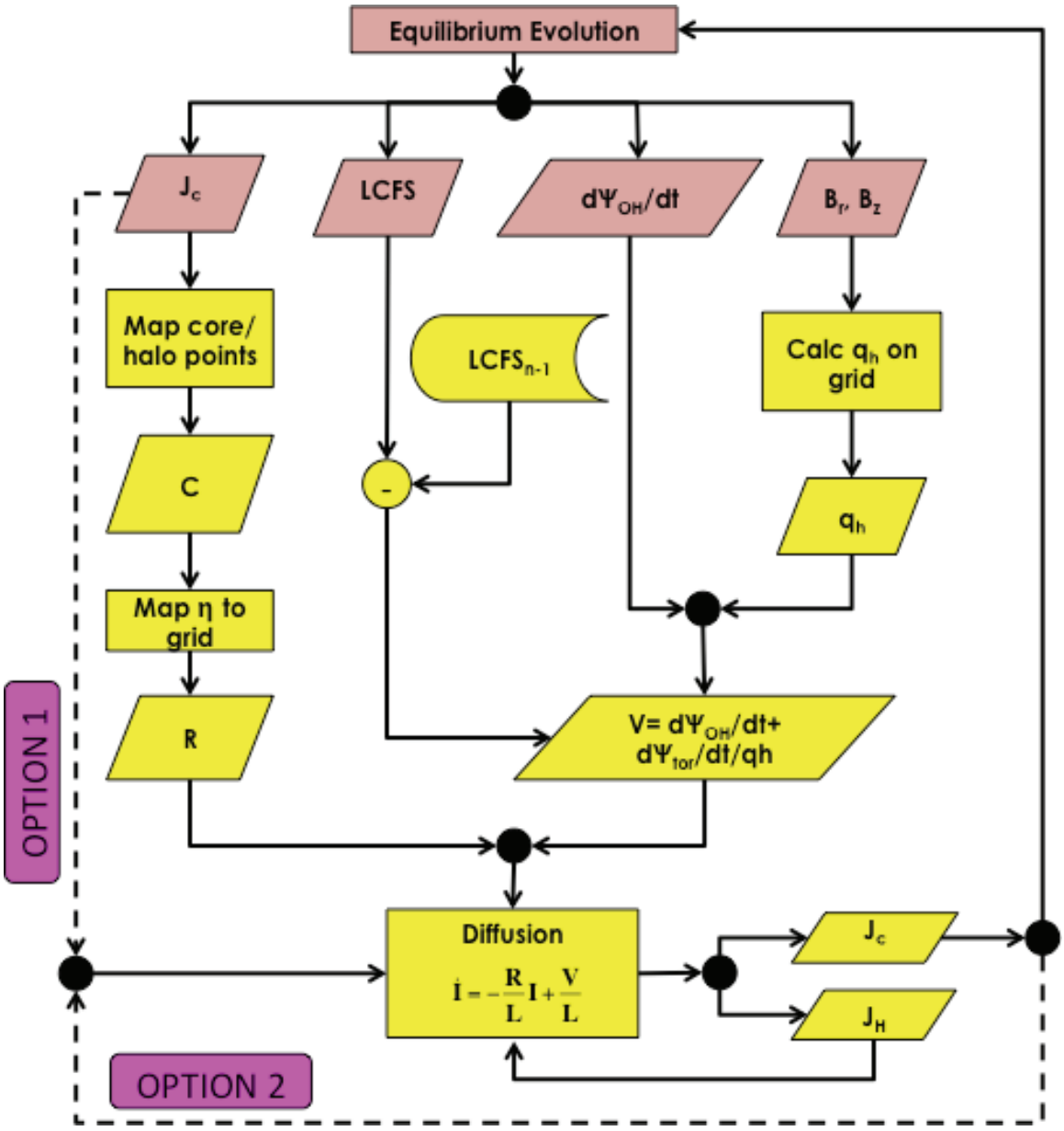

Figure PC-8: *Flow diagram of halo module functions and communication between halo module and equilibrium evolution module.*

Plasma Control System Upgrades

Significant upgrades are being done to the NSTX-Upgrade control system (NCS) in order to support the NSTX-Upgrade physics mission. Some of these upgrades are described here. Note that the plasma control system (PCS) provided by General Atomics is one of a suite of codes in the NCS.

The power supplies that powered the NSTX coils were controlled by a stand-along code known as the Power Supply Real Time Controller, or PSRTC; the coil voltage requests produced by PCS were used by PSRTC to drive the power supplies. Major upgrades to PSRTC are required to support NSTX-Upgrade operations, including the addition of new coils, the introduction of a new power supply type to support the higher TF current, and an interface to new coil protection systems. As a consequence, it was decided to transfer the PSRTC functionality to a new algorithm in the PCS, eliminating it as a stand-alone code. This will increase the integration of the power supply control with physics control, while reducing the number of standalone codes, and thus complexity, in the NCS.

A second significant upgrade involves the gas injection system. The NSTX implementation of the gas injection controls used a diverse array of hardware valve drivers, not all of which were controlled from the PCS; this prevented the supersonic gas injector or divertor impurity injectors from being used in a closed loop fashion. A preliminary design has been prepared for transitioning all valves to PCS control. This will facilitate the important research in closed loop core fueling and radiative divertor control.

Finally, specifications for upgraded plasma control software have been developed. These include a conceptual design for a discharge soft-shutdown algorithm, an improved design for the neutral beam control code and β_N control algorithm, and upgrades to the gas injection and coil current control algorithms.

Papers Published by NSTX-U Researchers (Oct. 2013 - Sept. 2014)

1. SABBAGH, SA, Ahn J-W, Allain J, et al.,
   Overview of physics results from the conclusive operation of the National Spherical Torus Experiment
   Nucl. Fusion 53 104007 (October 2013)

2. WANG F, Fu GY, Breslau JA, et al.,
   Linear stability and nonlinear dynamics of the fishbone mode in spherical tokamaks
   Phys. Plasmas 20 102506 (October 2013)

3. CANIK JW, Guttenfelder W, Maingi R, et al.,
   Edge microstability of NSTX plasmas without and with lithium-coated plasma-facing components
   Nucl. Fusion 53 113016 (November 2013)

4. MANSFIELD DK, Roquemore AL, Carroll T, et al.,
   First observations of ELM triggering by injected lithium granules in EAST
   Nucl. Fusion 53 113023 (November 2013)

5. SMITH DR, Parker SE, Wan W, et al.,
   Measurements and simulations of low-wavenumber pedestal turbulence in the National Spherical Torus Experiment
   Nucl. Fusion 53 113029 (November 2013)

6. ONO M, Jaworski MA, Kaita R, et al.,
   Recent progress in the NSTX/NSTX-U lithium programme and prospects for reactor-relevant liquid-lithium based divertor development
   Nucl. Fusion 53 113030 (November 2013)

7. BATTAGLIA DJ, Chang C-S, Kaye SM, et al.,
   Dependence of the L-H transition on X-point geometry and divertor recycling on NSTX
   Nucl. Fusion 53 113032 (November 2013)

8. LEBLANC BP and Diallo A
   Alignment of the Thomson scattering diagnostic on NSTX
   Journ. of Instrumentation 8 C11004 (November 2013)

9. JAWORSKI MA, Khodak A and Kaita R
   Liquid-metal plasma-facing component research on the National Spherical Torus Experiment
   Plasma Phys. Controlled Fusion 55 124040 (December 2013)

10. LEE KC, Domier CW, Luhmann NC, et al.,
Turbulence-induded diffusion analysis of the National Spherical Torus Experiment based on the gyro center shift
Journ. Korean Phys. Soc. 63 2102 (December 2013)

11. TAYLOR CN, Luitjohan KE, Heim B, et al.,
Surface chemistry analysis of lithium conditioned NSTX graphite tiles correlated to plasma performance
Fusion Eng. and Design 88 3157 (December 2013)

12. TAYLOR CN, Dadras J, Luitjohan KE, et al.,
The role of oxygen in retaining deuterium in lithiated graphite
J. Appl. Phys. 114 223301 (December 2013)

13. AHN J-W, Scotti F, Maingi R et al.,
Characterization of divertor footprints and the pedestal plasmas in the presence of applied n=3 fields for the attached and detached conditions in NSTX
PLASMA PHYSICS AND CONTROLLED FUSION 56 015005 (January 2014)

14. PARK YS Sabbagh SA, Bak JG, et al.,
Resistive wall mode active control physics design for KSTAR
PHYSICS OF PLASMAS 21 012513 (January 2014)
Copyright 2014 American Institute of Physics. This article may be downloaded for personal use only. Any other use requires prior permission of the author and the American Institute of Physics.

15. GRAY, TK, Canik JM,.Maingi, R et al.,
The effects of increasing lithium deposition on the power exhaust channel in NSTX
NUCLEAR FUSION 54 023001 (February 2014)

16. PARK J-K, Goldston RJ, Crocker NA, et al.,
Observation of EHO in NSTX and theoretical study of its active control using HHFW antenna
NUCLEAR FUSION 54 043013 (April 2014)

17. BOEDO, JA, Myra, JR, Zweben, S, et al.
Edge transport studies in the edge and scrape-off layer of the National Spherical Torus Experiment with Langmuir probes
PHYS. PLASMAS **21** 042309 (April 2014)
Copyright 2014 American Institute of Physics. This article may be downloaded for personal use only. Any other use requires prior permission of the author and the American Institute of Physics.

18. DAVIS WM, Ko MK, Maqueda RJ, et al.,
Fast 2-D camera control, data acquisition, and database techniques for edge studies on NSTX
FUSION ENGINEERING AND DESIGN 89 717 (June 2014)

19. ERICKSON, K, Tchilinguirian GJ, Hatcher RJ, et al.,
NSTX-U digital coil protection system software detailed design
IEEE TRANS. ON PLASMA SCIENCE 42 1811 (June 2014)

20. KIM KM, Park J-K, Boozer AH, et al.,
Calculation of neoclassical toroidal viscosity with a particle simulation in the tokamak magnetic braking experiments
NUCLEAR FUSION 54 073014 (July 2014)

21. BERTELLI N, Jaeger EF, Hosea JC, et al.,
Full wave simulations of fast wave heating losses in the scrape-off layer of NSTX and NSTX-U
NUCLEAR FUSION 54, 083004 (August 2014).

22. KIM H-S, Jeon YM, Na Y-S, et al.,
Characteristics of global energy confinement in KSTAR L- and H-mode plasmas
NUCLEAR FUSION 54 083012 (August 2014)

23. GERHARDT SP, Canik JM, Maingi R, et al.,
Progress in understanding the Enhanced Pedestal H-mode in NSTX
NUCLEAR FUSION 54 083021 (August 2014)

24. BERKERY JW, Liu YQ, Wang ZR, et al.,
Benchmarking Kinetic Calculations of Resistive Wall Mode Stability
PHYSICS OF PLASMAS **21** 052505 (May 2014)
Copyright 2014 American Institute of Physics. This article may be downloaded for personal use only. Any other use requires prior permission of the author and the American Institute of Physics.

25. BERKERY JW Sabbagh SA, Balbaky et al.,
Measured Improvement of Global MHD Mode Stability at High-beta, and in Reduced Collisionality Spherical Torus Plasmas
PHYSICS OF PLASMAS **21** 056112, 2014
Copyright 2014 American Institute of Physics. This article may be downloaded for personal use only. Any other use requires prior permission of the author and the American Institute of Physics.

26. ERICKSON, KG, Tchilinguirian, GJ, Hatcher, RE, et al.,
NSTX-U Digital Coil Protection System Software Detailed Design
IEEE TRANSACTIONS ON PLASMA SCIENCE, **42** 1811 (June 2014)

27. MEIER ET, Soukhanovskii VA, Gerhardt S, et al.,
Multi-Fluid Transport Modeling of NSTX Upgrade Standard and Snowflake Divertor Configurations
Contrib. Plasma Phys. **54**, 454 (2014)

28. KAYE SM, Guttenfelder W, Bell RE, et al.,
Reduced model prediction of electron temperature profiles in microtearing-dominated National Spherical Torus experiment plasmas
PHYSICS OF PLASMAS **21** 082510 (August 2014)

29. ZWEBEN SJ, Stotler DP, Bell RE, et al.,
Effect of a deuterium gas puff on the edge plasma in NSTX
PLASMA PHYS. CONTROLLED FUSION **56,** 095010 (September 2014)

30. FREDRICKSON E, Gorelenkov NN, Podesta M, et al.,
Parametric dependence of fast-ion transport events on the National Spherical Torus Experiment
NUCL. FUSION **54** 093007 (September 2014)

31. STAGNER L and Heidbrink WW
On geometric factors for neutral particle analyzers
REV. SCI. INSTRUM. **85** 11D803 (2014)
Copyright 2014 American Institute of Physics. This article may be downloaded for personal use only. Any other use requires prior permission of the author and the American Institute of Physics.

32. LIU D, Heidbrink WW, Tritz K, et al.,
Design of solid state neutral particle analyzer array for National Spherical Torus Experiment-Upgrade
REV. SCI. INSTRUM. **85** 11E105 (2014)
Copyright 2014 American Institute of Physics. This article may be downloaded for personal use only. Any other use requires prior permission of the author and the American Institute of Physics.

33. Bell RE
Development and operation of a high-throughput accurate-wavelength lens-based spectrometer
REV. SCI. INSTRUM. **85** 11E404 (2014)
Copyright 2014 American Institute of Physics. This article may be downloaded for personal use only. Any other use requires prior permission of the author and the American Institute of Physics.

34. RAMAN R, Jarboe TR, Nelson BA, et al.,
Design and operation of a fast electromagnetic inductive massive gas injection valve for NSTX-U
REV. SCI. INSTRUMENTS **85** 11E801 (2014)
Copyright 2014 American Institute of Physics. This article may be downloaded for personal use only. Any other use requires prior permission of the author and the American Institute of Physics.

35. ABRAMS, T, Jaworski MA, Kaita R, et al.,
Erosion and re-deposition of lithium coatings on TZM molybdenum and graphite during high-flux plasma bombardment
Accepted for publication in FUSION ENGINEERING AND DESIGN, 2014

36. GRAY TK, Canik JM, McLean AG et al.,
Measurements and interpretive 2D edge modeling of lithiated NSTX discharges
Accepted for publication in FUSION ENGINEERING AND DESIGN, 2014

37. JAWORSKI MA, Abrams T, Goldston R, et al.,
High-temperature, liquid lithium divertor target studies for NSTX-U and beyond
Accepted for publication in FUSION ENGINEERING AND DESIGN, 2014

38. ONO M, Jaworski MA, Kaita R et al.,
Radiative liquid lithium divertor concept
Accepted for publication in FUSION ENGINEERING AND DESIGN, 2014

39. SOUKHANOVSKII VA, Kaita R, McLean AG, et al.,
Divertor recycling and oxygen influxes in lithium experiments on NSTX
Accepted for publication in FUSION ENGINEERING AND DESIGN, 2014

40. MAINGI R et al.,
Enhanced confinement scenarios without large edge localized modes in tokamaks: control, performance, and extrapolability issues for ITER
Accepted for publication in NUCL. FUSION (2014)

Papers Submitted for Publication by NSTX-U Researchers (as of 9/5/14)

1. LUCIA M, Kaita R, Majeski R, et al.,
   Development progress of the Materials Analysis and Particle Probe
   Submitted for publication in REV. SCI. INSTRUMENTS, 2014

2. SOHRABI M, Barchfeld R, Domier C, et al.,
   Installation plans for the far infrared tangential interferometer/polarimeter (FIReTIP system on NSTX-U
   Submitted for publication in REV. SCI. INSTRUMENTS, 2014

3. SCHWARTZ JA, Jaworski MA, Mehl J, et al.,
   Electrical detection of liquid lithium leaks from pipes
   Submitted for publication in REV. SCI. INSTRUMENTS, 2014

4. GERHARDT SP, Erickson K, Kaita R, et al.,
   Magnetics for equilibrium reconstruction and realtime plasma control in NSTX-Upgrade
   Submitted for publication in REV. SCI. INSTRUMENTS, 2014

5. NICHOLS JH, Jaworski MA, Kaita R et al.,
   OEDGE modeling of outer wall erosion in NSTX and the effect of changes in neutral pressure
   Submitted for publication in J. NUCL. MATERIALS, 2014

6. MAINGI R, Osborne TH, Bell MG, et al.,
   Dependence of recycling and edge profiles on pre-discharge lithium dose in high triangularity, high performance NSTX H-mode discharges
   Submitted for publication in J. NUCL. MATERIALS, 2014

7. JAWORSKI MA, Abrams T, Goldston R, et al.,
   High-temperature liquid lithium divertor targets: analysis and experiments in support of NSTX-U and next-step devices
   Submitted for publication in J. NUCL. MATERIALS, 2014

8. SCOTTI F, Soukhanovskii VA, Ahn J-W, et al.,
   Lithium sputtering from lithium-coated plasma facing components in the NSTX divertor
   Submitted for publication in J. NUCL. MATERIALS, 2014

9. MEIER ET, Soukhanovskii VA, Bell RE, et al.,
Modeling NSTX snowflake divertor physics
Submitted for publication in J. NUCL. MATERIALS, 2014

10. ABRAMS T, Jaworski MA, Kaita R, et al.,
Re-deposition of lithium and boron coatings under high-flux plasma bombardment at normal and grazing magnetic incidence
Submitted for publication in J. NUCL. MATERIALS, 2014

11. GRAY TK, Canik JM, Jaworski MA, et al.,
Particle and energy transport in NSTX scrape-off layer plasmas
Submitted for publication in J. NUCL. MATERIALS, 2014

12. CAPECE, AM, Roszell, JP, Skinner, CH, et al.,
Effects of temperature and surface contamination on D retention in Li films on TZM
Submitted to J. Nucl. Mater. (2014)

13. AHN J-W, Maingi R, Canik JM, et al,
Impact of ELM filaments on divertor heat flux dynamics in NSTX
Submitted to J. NUCL. MATERIALS, 2014